Neutron Scattering and Praseodymium Suppression of Superconductivity.

A. Longmore

Oxford University

Neutron Scattering and Praseodymium Suppression of Superconductivity

by A. Longmore, Wolfson College,
submitted for the degree of Doctor of Philosophy
in October 1995.

Abstract

$PrBa_2Cu_3O_{6+x}$ is anomalous among the compounds which can be made by substituting different rare-earth ions for yttrium (Y) in $YBa_2Cu_3O_{6+x}$: it is the only compound which has the same structure as $YBa_2Cu_3O_{6+x}$, and yet does not superconduct. This unusual property makes it an important system to study, since the differences between the two compounds could produce theoretical insights into the mechanisms of cuprate, or high-temperature, superconductivity. This thesis describes neutron scattering investigations of the magnetic properties of $PrBa_2Cu_3O_{6+x}$.

I have investigated the magnetic ordering in well-characterised, single-crystal samples, both with and without Al-contamination. In the data analysis, proper account is taken of the sample mosaicity and the different intrinsic peak shapes encountered. Some of the most striking new characteristics reported here are that (i), there is a clear interaction between the Pr ions and the Cu-O_2 planes, (ii), the ordered Pr moments tilt away from the *c*-axis (as suggested previously by Mössbauer spectroscopy), and (iii), there is two-dimensional ordering in the Al-containing crystals. I show how observed trends in the magnetic ordering, as O- and Al-contents vary, may be understood in terms of charge redistribution involving the hybridisation of the Pr ions.

I have also examined the crystal field transitions of the praseodymium ion. Because of the difficulties previously encountered in measuring these in $PrBa_2Cu_3O_{6+x}$, I have used instead the compounds PrO_2 and $Y_{0.3}Pr_{0.7}Ba_2Cu_4O_8$, which contain praseodymium in a chemically similar environment. $Y_{0.3}Pr_{0.7}Ba_2Cu_4O_8$ shows the same broadening effects as $PrBa_2Cu_3O_{6+x}$; PrO_2 shows signs of mixed-valency, with temperature-dependent lifetime effects. The application of symmetry considerations and the point-charge model to the crystal field measurements is considered in some detail.

Acknowledgements

Firstly, I owe a great debt of thanks to my supervisor, Andrew Boothroyd. He has been first and foremost a friend, continually encouraging and supporting me. The fact that my thesis contains data from so many experiments and yet was finished within three years owes as much to his enthusiasm as my own. Andrew, I hope we don't lose touch - though with the number of publications we've got in mind, we should stay in touch for some time to come!

I would like to thank all my other friends here as well (some still present, some gone): Bobby, Robert, John R, Des, Dave, Paul, Sharon, Alan, Jon G, Andrew W, Andrew S, Martin, Bella, Radu, and Caelia. To an observer, it would seem as if we were a single X-ray and neutron scattering group, which is probably how we see ourselves as well. I would like to especially mention Bobby, and wish him all the best for the future.

Professor Cowley gave me a great deal of help when he explained how to include resolution effects in the Lorentz factor. That half-hour discussion ended months of head-scratching, and set the foundations for including the mosaicity and intrinsic peak shapes, which turned out to be a vital technique in analysing the elastic scattering data I've presented.

The local contacts I have been involved with, particularly Niels in Risø and Roger at RAL, have frequently assisted the experiments beyond the call of duty, and I would like to thank them - and apologise to their families for calling them at all hours!

My parents have supported me in this as in all other things - I am acutely aware that I will probably never be able to repay them for the upbringing I received, and I can only aspire to learn from them for the time when I follow in their footsteps, and have the privilege and responsibility of parenthood.

Thank you to my wife, Nicci. For you, physics became a world of electrons taking elevators, of neutron-footballs bouncing off walls of regularly planted trees, and of hills cut down the middle - you may never recover! Not only did you try and understand my work, you have been a shelter when storms raged, you put me back together when I started to fall apart, and you never left my side, even when we were apart.

Finally, there is someone I've never seen, though I've often seen his handiwork. Nor have I ever touched him - but he has touched me, and is more real than the air that I breathe. Although he died, he is not dead, nor distant, nor silent - he is alive, and his invitation can be heard by those bold enough to seek truth, truth that has stood unequalled in almost two millennia.

Table of Contents

I - Superconductivity and Praseodymium

1. Introduction

Conventional superconductivity is the name now given to the superconducting phenomena which can be understood in terms of the BCS-type theories established before 1986. At that time, superconductivity was considered a mature field - the phenomenon was well documented, and the BCS theory successfully explained its measured properties. Since then, a new class of superconductors - cuprate, or high-T_c superconductors - has emerged, with properties inexplicable within the previous theories. The most noticeable, and exciting, property of these superconductors is the temperature to which the substances can be heated whilst remaining in the superconducting phase, i.e. the 'critical' transition temperature T_c. This thesis is concerned primarily with the cuprate material $PrBa_2Cu_3O_{6+x}$, a material which has the correct structure to be a high-T_c superconductor, but does not superconduct. Rather, it is an antiferromagnetic insulator.

This is a peculiar property - $PrBa_2Cu_3O_{6+x}$ has the same structure as the successfully superconducting $YBa_2Cu_3O_{6+x}$, and though many rare-earth ion substitutions can be made for yttrium, only that of praseodymium has such a detrimental effect. Obviously, an understanding of this lack of superconductivity in otherwise ideal conditions could lead to a deeper understanding of what is, at present, a phenomenon which is not well understood.

2. Conventional superconductivity

Perhaps a good place to start any discussion on superconductivity is the field of conventional superconductivity; it provides a solid foundation of clear experimental evidence and rigorous theory that the present work on cuprate superconductors must seek to emulate.

Superconductivity has two characteristics: the lossless flow of a dc current, and the expulsion of a magnetic field (the Meissner effect). The latter is important because it shows that the superconductor is not a 'perfect' conductor, i.e. the limit of metallic conductivity tending to zero, since such a material would trap magnetic flux, rather than expel it. Before 1986, the highest temperature to which a material had been raised whilst remaining superconducting was 23.2 K for Nb_3Ge, in 1973. It was felt that this was probably close to the maximum that could ever be achieved, and to suggest that materials could superconduct above the boiling point of liquid nitrogen, 77 K, must have seemed absurd.

Part of the reason for this belief was the theoretical success in describing the conventional superconductors. The microscopic theory reached a landmark in 1956 with the concept of Cooper pairs[1]. A Cooper pair consists of two electrons with equal and opposite crystal momentum, opposite spin (hence forming a spin-singlet state, $S = 0$), and moving on the same line (i.e. no relative orbital angular momentum, s-wave). The basics of the theory are that the two electrons interact attractively via phonon coupling, and this interaction overcomes their screened Coulomb repulsion. This results in a bound state of lower energy, and hence there occurs an energy gap in the single-electron density of states at the Fermi energy E_F. The energy gap does not prevent conduction, since it moves with the Fermi surface, but it does prevent scattering since there are no available states to scatter into.

---

[1] L.N. Cooper, *Bound electron pairs in a degenerate fermi gas*, Phys. Rev. **104**, 1189-1190, (1956).

With this simple model to guide them, Bardeen, Cooper and Schrieffer created the more rigorous many-body equivalent of Cooper pairs, the BCS theory[2]. The original BCS theory assumed that the phonon interaction was isotropic, attractive and weak (in comparison to the phonon energies), and that the Fermi surface was spherical. With these simplifying assumptions they created a theory with relatively few parameters. Because all the electrons are part of the same intricately coupled many-body wave function, to scatter one electron is impossible without destroying the wave function on a macroscopic scale - to scatter one electron is to scatter all of the electrons, and so each individual electron is resilient to scattering.

One of the most simple results of the BCS theory is

$$\frac{2\Delta(0)}{k_B T_C} = 3.52 \tag{1}$$

where $2\Delta(T)$ is the size of the energy gap at the absolute temperature T. For the T_c of 23.2 K, this gives an energy gap at absolute zero of 7.0 meV. The result of allowing the phonon interaction to become comparable to phonon energies, 'strong coupling', is to increase the ratio of Equation (1) to around 4.5. The strong coupling means that the Cooper pairs have a finite lifetime, being scattered by phonons, leading to a decrease in T_c.

That phonons were in some way intimately connected to conventional superconductivity was known quite close to the advent of the field, with the observation by Frölich in 1950 of the isotope effect[3]. An investigation into different superconducting mercury isotopes revealed that $T_c \propto M^{-\frac{1}{2}}$, where M was the isotope mass. The phonon cut-off energy in Debye's theory of heat-capacities also has a dependence on M given by $\hbar\omega_D \propto M^{-\frac{1}{2}}$, and hence $k_B T_c \propto \hbar\omega_D$.

In contrast to the close connection between phonons and conventional superconductivity, magnetic excitations are to be positively avoided. The presence of

---

[2] J. Bardeen, L.N. Cooper, and J.R. Schrieffer, *Theory of superconductivity*, Phys. Rev. **108**, 1175-1204, (1957).

[3] H. Fröhlich, *Theory of the superconducting state. I. The ground state at the absolute zero of temperature*, Phys. Rev. **79**, 845-856, (1950).

magnetic moments has a devastating effect on the superconductivity, flipping the spins of the electrons and destroying the Cooper pairs.

Another example of BCS theory giving clear predictions of physical properties is the discontinuous specific heat. In the normal (i.e. non-superconducting) phase, the electronic heat capacity C_{en} is proportional to temperature, $C_{en} = \gamma T$. As temperature decreases below T_c, the heat capacity increases by an amount

$$\Delta C = 1.43\gamma T_C \tag{2}$$

caused by the gap opening at T_c.

Hence the BCS theory, based on electron-phonon coupling, provided a strong theoretical basis for superconductivity with unambiguous predictions which were consistent with experimental results.

That is, experimental results before 1986.

3. Cuprate superconductivity

In 1986, Bednorz and Müller[4] were looking at the superconducting properties of the compound $LaCu_2O_4$, doped with Ba^{2+}, Sr^{2+}, or Ca^{2+}, with the idea that the Jahn-Teller effect might enhance the electron-phonon coupling and so boost the T_c. To everyone's surprise, the substances had T_cs of over 30 K. Soon afterwards, in 1987, it was discovered that $YBa_2Cu_3O_{6+x}$ had a T_c of 93 K[5]. Thus began the field of high-T_c superconductors, where 'high' can loosely be defined as being above temperatures predicted by the conventional BCS theory. Today, the highest known T_c at ambient pressure is 135 K for Hg-Ba-Ca-Cu-O systems[6].

Table 1: Comparison of properties of conventional and cuprate superconductors.

Conventional superconductors	Cuprate Superconductors
$T_c \leq 30$ K	T_c as high as 135 K
generally isotropic	strongly two dimensional
contain wide variety of atoms	always contain Cu-O_2 planes
generally non-magnetic	always have an antiferromagnetic phase
coherence length ε between 500 Å and 10^4Å	ε between 10-30 Å in *ab*-plane, and 2-5 Å along *c*-axis
Cooper pairs are *s*-wave	Cooper pairs may be *d*-wave
Normal state properties as predicted, e.g. $\rho = A + BT^5$, for $T \ll \theta_D$	Unusual normal state properties, e.g. $\rho_{ab} = A + BT$, for $T \ll \theta_D$

---

[4] J.G. Bednorz and K.A. Müller, *Possible high T_c superconductivity in the Ba-La-Cu-O system*, Z. Phys. B **64**, 189-193, (1986).

[5] M.K. Wu, J.R. Ashburn, C.J. Torng, P.H. Hor, R.L. Meng, L. Gao, Z.J. Huang, Y.Q. Wang, and C.W. Chu, *Superconductivity at 93K in a new mixed-phase Y-Ba-Cu-O compound system at ambient pressure*, Phys. Rev. Lett. **58**, 908-910, (1987).

[6] A. Schilling, M. Cantoni, J.D. Guo, and H.R. Ott, *Superconductivity above 130K in the Hg-Ba-Ca-Cu-O system*, Nature **363**, 56-58, (1993).

The substances mentioned above all have a striking structural similarity: they contain planes of Cu-O_2, and even after almost ten years no other structural elements have been found which are so conducive to superconductivity. The properties of cuprate superconductors are briefly summarised and compared with conventional superconductors in Table 1. (The coherence length characterises the distance over which the superconducting wave function falls when moving from a superconducting to a normal region in the material; *s*-wave and *d*-wave coupling refer to the relative orbital angular momentum of the Cooper pair; ρ is the electrical resistivity of the metal in the normal state, which should follow the 'Bloch T^5 law' for very low temperatures[7].)

With the apparent failure of conventional BCS theory to explain these properties, new theories were proposed. These theories cover a broad spectrum, from being relatively minor adjustments to the original concepts of the BCS theory (BCS-type theories), to theories which challenge existing ideas at a much more fundamental level.

The BCS-type theories retain the idea that attractive interactions lead to Boson-like quasi-particles, an energy gap in the single-particle density of states, and so superconductivity. Advocates of these theories would say that nothing more radical is needed - the fundamental charge (as found by flux quanta) is still $2e$, and an energy gap apparently still exists. One of the main schools of thought is that phonons are still responsible, although their effect has in some way become boosted, for example by the strong anisotropy of the Cu-O_2 planes. Photoemission spectroscopy suggests that the ratio in Equation (1) may be increased to about 7[8], i.e. the coupling has become stronger, but the energy gap is still isotropic and the coupling is still *s*-wave. Recent

---

[7] N.W. Ashcroft and N.D. Mermin, *Solid state physics*, p526, W.B. Saunders Company (1976).

[8] For example, C.G. Olson, R. Liu, D.W. Lynch, R.S. List, A.J. Arko, B.W. Veal, Y.C. Chang, P.Z. Jiang, and A.P. Paulikas, *Photoelectron spectroscopic evidence for superconducting gap isotropy in the basal plane of the high-temperature superconductor* $Bi_2Sr_2CaCu_2O_8$, Solid State Commun. **76**, 411-414, (1990).

experiments, however, have suggested that the coupling is actually *d*-wave, in which case the energy gap would be anisotropic[9].

Another school of thought concerning BCS-type theories is that the coupling is being mediated by a completely different interaction, perhaps magnetic in origin (i.e. magnon coupling as opposed to phonon coupling). This is in contrast to conventional BCS superconductors, in which magnetism of any sort has a disruptive effect on the coupling, flipping one of the spins of the Cooper pair. The cuprates inevitably exhibit magnetic properties in the normal phase, due to the magnetic nature of copper, and so it follows that high-T_c superconductivity may be inextricably linked with strong magnetic interactions.

Among the theories which involve more fundamental reassessments of existing ideas, there is the separation of an electron's spin and charge into spinons and holons (proposed by Anderson, in whose theories the magnitude of T_c is primarily mechanism independent, and a result of the coherence between the planes), and the use of enion statistics (which necessarily violates time/parity symmetry). Evidence suggesting the need for theories more radical than the BCS-like theories are the very small coherence lengths of cuprate superconductors and their unusual normal state properties.

Ultimately, understanding of cuprate superconductivity is going to come about by the refinement of these theories to the point where they can be tested against clear experimental data. From the point of view of the experimentalist, the question that needs to be asked is 'Which experiments will produce information which will help to clarify, deepen or even challenge our understanding?' In superconductivity, a possible approach is to investigate the situations in which superconductivity does and doesn't occur. A comparison of the two situations may then produce factors which are crucial to the presence or absence of superconductivity.

This thesis, then, is concerned with $PrBa_2Cu_3O_{6+x}$, a compound which does not superconduct, in contrast to its parent compound $YBa_2Cu_3O_{6+x}$, which is a well-known superconductor. More specifically, I have investigated by neutron scattering the

---

[9] D.A. Wollman, D.J. Van Harlingen, W.C. Lee, D.M. Ginsberg, and A.J. Legget, *Experimental determination of the superconducting pairing state in YBCO from the phase coherence of YBCO-Pb dc SQUIDs*, Phys. Rev. Lett. **71**, 2134-2137, (1993).

magnetic properties of $PrBa_2Cu_3O_{6+x}$, and the magnetic ground-state crystal field transitions of the praseodymium ion in that environment, and compared the results to what is known about the superconducting members of the $RBa_2Cu_3O_{6+x}$ series. It is hoped that such a comparison may bring insight into the non-superconductivity of $PrBa_2Cu_3O_{6+x}$.

4. The anomaly of Pr cuprates

The compound $Y_{1-z}Pr_zBa_2Cu_3O_{6+x}$ 'has become one of the most studied subtopics in the field of high temperature superconductivity'[10], and given its rich phase diagram, its clear suppression of superconductivity with Pr doping, and its anything but clear other properties, this is perhaps not surprising.

4.1 The chemical structure

The chemical structure of $PrBa_2Cu_3O_7$ is shown in Figure 1; it is the same as that of $YBa_2Cu_3O_7$, with the exception that the Pr ion now occupies the central rare-earth site.

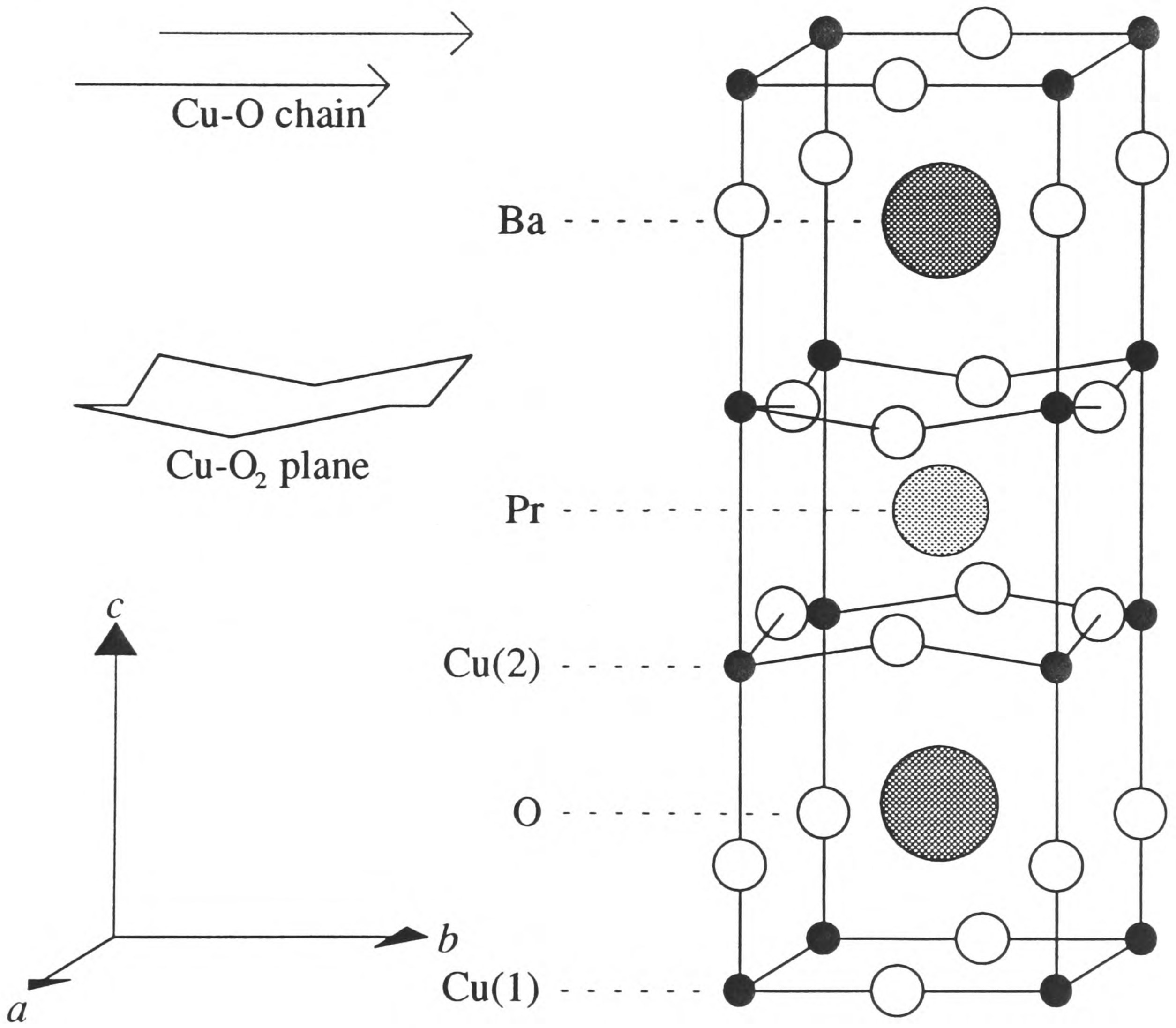

Figure 1: The chemical unit cell of $PrBa_2Cu_3O_7$.

---

[10] H.B. Radousky, *A review of the superconducting and normal state properties of* $Y_{1-x}Pr_xBa_2Cu_3O_7$, J. Mater. Res. 7, 1917-1954, (1992).

In $YBa_2Cu_3O_{6+x}$ the superconductivity is widely believed to occur on the $Cu\text{-}O_2$ planes which are situated above and below the rare-earth ion. It is the chain-layer sites that are oxygen-deficient for $x < 1$, and the remaining oxygen atoms in the chain-layer can group in different ways depending on x and the method of preparation.

A look at the formal valence states of the ions in $YBa_2Cu_3O_7$ is instructive. For yttrium, barium, copper and oxygen we have Y^{3+}, Ba^{2+}, Cu^{2+} and O^{2-}. This gives a net valence of $(+3) + 2(+2) + 3(+2) + 7(-2) = -1$. Not enough electrons have been given up by the positive ions to satisfy the demands of the O^{2-} ions. This imbalance must be redressed; copper can also exist in a trivalent state, and so it is thought that the copper ions give up an extra electron per chemical unit cell. Hence their is a 'spare' valence of +1 (a hole), which is thought to reside on the $Cu\text{-}O_2$ plane layers. It is the coupling of these holes which form the Cooper pairs and so $YBa_2Cu_3O_{6+x}$ is a p-type superconductor.

As oxygen is removed from the chain-layer sites (x decreases from one), the imbalance that needs to be redressed decreases, less holes exist on the $Cu\text{-}O_2$ plane layers, and so the number of Cooper pairs decreases. At $x = 0.5$, the charge balance can be achieved by a formal copper valence of 2+, and you would predict no holes. In fact, superconductivity is destroyed at about $x \sim 0.3$ (see Figure 2), although this may be due to inhomogenities in the oxygen content of the sample.

As yttrium is replaced by praseodymium, the critical temperature T_c falls until the substance is no longer superconducting at $z \sim 0.55$[11] (see Figure 2). This is unique: all other rare-earth substitutions that can be made (Nd, Sm, Eu, Gd, Dy, Ho, Er, Tm, Yb, and Lu) have little effect on T_c, which remains at around 90 K. It was this unique property which initially sparked off so much interest in $Y_{1-z}Pr_zBa_2Cu_3O_{6+x}$.

---

[11] L. Soderholm, K. Zhang, D.G. Hinks, M.A. Beno, J.D. Jorgenson, C.U. Segre, and I.K. Schuller, *Incorporation of Pr in $YBa_2Cu_3O_{7-\delta}$:electronic effects on superconductivity*, Nature **328**, 604-605, (1987); J.K. Liang, X.T. Xu, S.S. Xie, G.H. Rao, X.Y. Shao, and Z.G. Duan, *The superconductive properties and crystal structure of $Ba_2(Y_{1-x}Pr_x)Cu_3O_{9-y}$ solid solutions*, Z. Phys. B 69, 137-140, (1987).

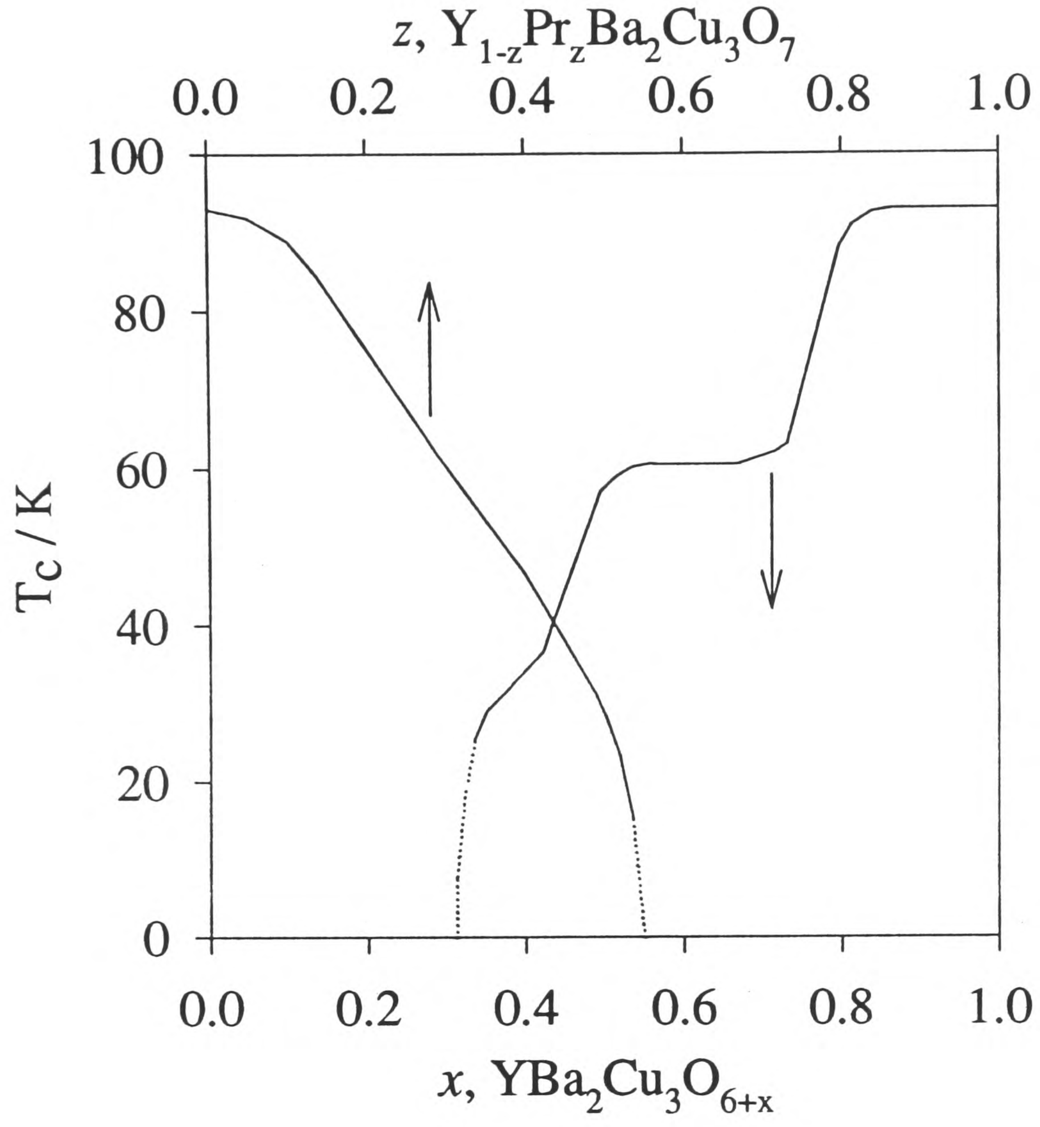

Figure 2: Schematic representation of the variation of T_c with oxygen (x) and praseodymium content (z) in $Y_{1-z}Pr_zBa_2Cu_3O_{6+x}$: the variation with x, denoted by the downwards arrow, is for $z = 0$, whereas the variation with z, denoted by the upwards arrow, is for $x = 1$.

Structural studies agree that the c-parameter of the unit cell is anomalously short[12, 13], though they disagree on which bond length is responsible. Some claim that

---

[12] C.K. Lowe-Ma and T.A. Vanderah, *In search of chemical clues: single-crystal structural studies of* $PrBa_2Cu_3O_6$ *and* $PrBa_2Cu_3O_7$, Physica C **201**, 233-248, (1992); T.A. Vanderah and C.K. Lowe-Ma, *Crystal-chemical anomalies in nonsuperconducting* $PrBa_2Cu_3O_7$, J. Superconductivity **7**, 107-111, (1994).

[13] M.E. López-Morales, D. Ríos-Jara, J. Tagüeña, R. Escudero, S. La Placa, A. Bezinge, V.Y. Lee, E.M. Engler, and P.M. Grant, *Role of oxygen in* $PrBa_2Cu_3O_{7-y}$*: Effect on structural and physical properties*, Phys. Rev. B **41**, 6655-6667, (1990); M. Guillaume, P. Allenspach, W. Henggeler, J.

the Pr-O distance is as expected for trivalent praseodymium[12], whilst others claim that it is shorter: this was initially interpreted as evidence for the existence of praseodymium in the tetravalent state[11]. This seemed to be the most logical interpretation, since it could explain the disappearance of superconductivity with praseodymium doping. Suppose that all the praseodymium ions were tetravalent - the valence balance of $PrBa_2Cu_3O_7$ would then be (4) + 2(2) + 3(2) + 7(−2) = 0. Hence their is no necessity for extra holes, and so no superconductivity in $PrBa_2Cu_3O_7$.

With hindsight, however, it is now thought that the shorter Pr-O bond distance indicates the hybridisation of praseodymium with its surrounding oxygen ions[13]; the valence of praseodymium is 3+, just as in yttrium, and a subtler reason for the disappearance of superconductivity must be found.

4.2 Inelastic neutron scattering

The controversy concerning the valence of praseodymium first arose from early measurements of magnetic susceptibility. The free-ion magnetic moments, given by

$$\mu = g_J \mu_B \sqrt{J(J+1)} \tag{3}$$

are $3.58\mu_B$ and $2.54\mu_B$, for Pr^{3+} and Pr^{4+} respectively (g_J is the Landé factor). Fitting the susceptibility data to a simple Curie-Weiss law

$$\begin{aligned} \chi(T) &= \chi_0 + \frac{C}{T-\theta}, \\ C &= \frac{N\mu^2}{3k_B} \end{aligned} \tag{4}$$

results in a measured moment of about $2.8\mu_B$[14], which was initially taken as evidence for a Pr valence intermediate between three and four[15].

Mesot, B. Roessli, U. Stuab, P. Fischer, A. Furrer, V. Trounov, *A systematic low-temperature neutron diffraction study of the* $RBa_2Cu_3O_x$ *(R = yttrium and rare earths; x = 6 and 7) compounds*, J. Phys.: Condensed Matter **6**, 7963-7976, (1994).

[14] J.L. Peng, P. Klavins, R.N. Shelton, H.B. Radousky, P.A. Hahn, and L. Bernardez, *Upper critical field and normal-state properties of single-phase* $Y_{1-x}Pr_xBa_2Cu_3O_{7-\delta}$ *compounds*, Phys. Rev. B **40**, 4517-4526, (1989).

However, the simplistic use of the Curie-Weiss law in Equation (4) neglects crystal field effects, since the splitting of the ground-state J-multiplet by the crystal field changes the paramagnetic moment. Combined crystal field and susceptibility studies have generally concluded that the praseodymium is at least 90% trivalent[16], and this is supported by photoemission spectroscopy[17]. Although the study of the crystal field levels helped to clear up the nature of the valence, they also introduced a new problem: the crystal field lines are unusually broad, and it is not yet known what microscopic process is causing this broadening. This is discussed further in Section *III*.

4.3 Elastic magnetic scattering

The Pr ions order magnetically; however, this does not necessarily imply that it is the magnetic nature of the Pr ions which destroys the superconductivity, as some of the superconducting members of the $R\mathrm{Ba_2Cu_3O_{6+x}}$ series also have magnetic rare-earth ions. What is unusual is the magnitude of the Pr ordering temperature: about 17 K for oxygenated samples ($x \sim 1$), and about 11 K for reduced samples ($x \sim 0$)[18]. This is a factor of at least 10 higher than expected, based on the scaling of T_N from the other $R\mathrm{Ba_2Cu_3O_{6+x}}$ compounds as predicted by, for example, RKKY theory (see Table 2).

---

[15] Y. Dalichaouch, M.S. Torikachvili, E.A. Early, B.W. Lee, C.L. Seaman, K.N. Yang, H. Zhou, and M.B. Maple, *Superconducting and normal state properties of* $Y_{1-x}Pr_xBa_2Cu_3O_{7-\delta}$ *(M = Pr, Na)*, Solid State Commun. **65**, 1001-1006, (1988).

[16] A.T. Boothroyd, S.M. Doyle, and R. Osborn, *The magnetic state of Pr in* $PrBa_2Cu_3O_7$, Physica C **217**, 425-438, (1993); L.S. Vaidhyanathan and G. Rangarajan, *A magnetic study of the oxide superconductors of the type* $(Pr_xY_{1-x})Ba_2Cu_3O_{7-y}$, $0 < x \leq 1$, Solid State Commun. **79**, 495-500, (1991).

[17] O. Cohen, F.H. Potter, C.S. Ratomjee, and R.G. Egdell, *A core and valence level photoemission study of* $Y_{1-x}Pr_xBa_2Cu_3O_7$, Physica C **201**, 58-68, (1992).

[18] See Section *II-2.2* for references.

Table 2: Table showing the scaling of the magnetic ordering temperature T_N with $(g_J-1)^2J(J+1)$ for $R\mathrm{Ba_2Cu_3O_7}$. The effect of crystal field levels has not been taken into account.

ion	g	J	T_N (K^{-1})	$T_N / (g_J-1)^2J(J+1)$ (K^{-1})
$\mathrm{Pr^{3+}}$	$^4/_5$	4	17[18]	20
$\mathrm{Nd^{3+}}$	$^8/_{11}$	$^9/_2$	0.5[19]	0.3
$\mathrm{Gd^{3+}}$	2	$^7/_2$	2.2[20]	0.14
$\mathrm{Dy^{3+}}$	$^4/_3$	$^{15}/_2$	0.9[21]	0.13
$\mathrm{Ho^{3+}}$	$^5/_4$	8	0.2[22]	0.04
$\mathrm{Er^{3+}}$	$^6/_5$	$^{15}/_2$	0.5[23]	0.2

In rare-earth ions, the wave function of the magnetic electrons are normally screened from their neighbours, in which case an indirect exchange interaction must occur to cause any magnetic ordering. The RKKY model calculates the exchange interaction when mediated through nearly-free electrons by second order perturbation theory. Ruderman and Kittel developed the theory for the coupling of nuclear magnetic moments[24], Kasuya performed a similar calculation for the coupling of

---

[19] K.N. Yang, J.M. Ferrieira, B.W. Lee, M.B. Maple, W.-H. Li, J.W. Lynn, R.W. Erwin, *Antiferromagnetic order in superconducting and oxygen-deficient nonsuperconducting* $\mathrm{R}Ba_2Cu_3O_{7-\delta}$ *compounds (*R = *Nd and Sm)*, Phys. Rev. B **40**, 10963-10972, (1989).

[20] D. McK. Paul, H.A. Mook, A.W. Hewat, B.C. Sales, L.A. Boatner, J.R. Thompson, and M. Mostoller, *Magnetic ordering in the high-temperature superconductor* $GdBa_2Cu_3O_7$, Phys. Rev. B **37**, 2341-2344, (1988).

[21] T.W. Clinton, J.W. Lynn, J.Z. Liu, Y.X. Jia, and R.N. Shelton, *Magnetic order of Dy in* $DyBa_2Cu_3O_7$, J. Appl. Phys. **70**, 5751-5753, (1991).

[22] B. Roessli, P. Fischer, U. Staub, M. Zolliker, and A. Furrer, *Combined electronic-nuclear magnetic ordering of the* Ho^{3+} *ions and magnetic stacking faults in the high-*$\mathrm{T_c}$ *superconductor* $HoBa_2Cu_3O_7$, Europhys. Lett. **23**, 511-515, (1993).

[23] J.W. Lynn, W-H. Li., Q. Li, H.C. Ku, H.D. Yang, and R.N. Shelton, *Magnetic fluctuations and two-dimensional ordering in* $ErBa_2Cu_3O_7$, Phys. Rev. B **36**, 2374-2377, (1987).

[24] M.A. Ruderman and C. Kittel, *Indirect exchange coupling of nuclear magnetic moments by conduction electrons*, Phys. Rev. **96**, 99-102, (1954).

unfilled inner shell electrons[25], and Yosida compared the second order contribution to the hyperfine interaction with the first order[26]. As far as the rare-earth ions are concerned, the theory predicts a scaling of the coupling constant (and hence the magnetic ordering temperature) with the de Gennes factor $(g_J-1)^2J(J+1)$. In fact, this scaling factor should occur whatever the nature of the exchange mechanism, provided that we have the same interaction strength for the compounds we are comparing.

The fact that the ordering temperature of praseodymium is so much higher than you would predict by a simple scaling implies that the Pr^{3+} ions are much more strongly coupled together than they would be if the wave function of the magnetic electrons were truly isolated. This is now interpreted as being due to their extensive hybridisation with respect to their adjacent oxygen ions, and this is supported by EELS (electron energy loss spectroscopy)[27], PES (photoemission spectroscopy)[17] and some structural studies[13]. It seems probable that this hybridisation may in some way be connected to the suppression of superconductivity.

4.4 The effects of hybridisation

There are two main conjectures as to how this suppression could be happening. The first is that because of the hybridisation, the magnetic interaction of the Pr ions can now prevent the pairing in a way which the other magnetic rare-earth ions could not. This would imply some form of pair-breaking mechanism, just as magnetic impurities destroy superconductivity in conventional BCS superconductors. The second is that the holes are simply localised, and so can no longer form dynamic Cooper pairs; this could be a result of the change in the electronic balance caused by the hybridisation.

Hence, given that the Pr ions in $PrBa_2Cu_3O_{6+x}$ have been established to be trivalent, the fundamental question now is: How do the Pr ions and their surroundings interact with each other? To investigate how the Pr ions affect their surrounding

---

[25] T. Kasuya, *A theory of metallic ferro- and antiferromagnetism on Zener's model*, Prog. Theor. Phys. **16**, 45-57, (1956).

[26] K. Yosida, *Magnetic properties of Cu-Mn alloys*, Phys. Rev. **106**, 893-898, (1957).

[27] A. Hartmann, G.J. Russel, W. Frentrup, and K.N.R. Taylor, *Electronic structural changes in $Y_{1-x}Pr_xBa_2Cu_3O_{7-\delta}$ single crystals due to Pr 4f states*, Solid State Commun. **89**, 77-80, (1994).

atoms, we have studied the magnetic phases of $PrBa_2Cu_3O_{6+x}$, involving the ordering of both the Pr and the Cu ions, and compared them to other members of the $RBa_2Cu_3O_{6+x}$ series; and to examine how the surrounding oxygen atoms affects praseodymium's ground state and the low-lying energy levels, we have studied the crystal field levels of PrO_2 and $Y_{0.3}Pr_{0.7}Ba_2Cu_4O_8$, which contain praseodymium in a similar environment to $PrBa_2Cu_3O_{6+x}$.

II - Elastic magnetic scattering

1. Theory

1.1 The neutron interaction

1.1a The intensity

The simplest way to discover the magnetic structure of a substance is to study the elastic scattering of neutrons from the ordered components of the magnetic moments. Because a magnetic structure exists, the ordered moments are arranged periodically. The neutron interacts with these moments via its own magnetic moment, and Bragg reflections are observed where scattered waves combine constructively. This is therefore a similar phenomenon to X-ray scattering, and to neutron scattering from nuclei.

However, since the interaction involved is a vector field (i.e. the magnetic moments are defined by vectors, rather than scalars) the equations involved are slightly more complicated. It can be shown[28] that the intensity of diffraction from a non-collinear magnetic structure at a scattering vector κ is proportional to

$$I(\kappa) = \sum_{\alpha,\beta} \left\langle (\delta_{\alpha\beta} - \hat{\kappa}_\alpha \hat{\kappa}_\beta) F^\alpha(\kappa) F^{\beta *}(\kappa) \right\rangle \qquad (5)$$

where:

α, β	index the Cartesian axes x, y, z
$\langle\ \rangle$	denotes a domain average
$\delta_{\alpha\beta}$	is the Kronecker delta
$\hat{\kappa}_\alpha$	is the α-component of the unit scattering vector, and
$F^\alpha(\kappa)$	is the magnetic structure factor given by

---

[28] G.L. Squires, *Introduction to the theory of thermal neutron scattering*, p146-147, Cambridge University Press (1978).

$$F^{\alpha}(\kappa)=\sum_j \mu_j^{\alpha} f_j(\kappa)\exp(i\kappa.\mathbf{r}_j) \tag{6}$$

where		
	j	labels the magnetic moments in the unit cell
	μ_j^{α}	is the α-component of the jth moment
	$f_j(\kappa)$	is the form factor of that moment, and
	$\mathbf{r}_j$	is its position.

Although in my analysis I frequently have to use these equations in their present form, they are simplified in the case of a collinear arrangement of magnetic moments. If each of the magnetic moments has the same magnitude μ, and lies either parallel or antiparallel to a particular direction, then we can write

$$\mu_j^{\alpha}=\sigma_j\mu^{\alpha} \tag{7}$$

where $\sigma_j = \pm 1$, so that

$$I(\kappa)=\mu^2\left(1-(\hat{\kappa}.\hat{\mu})^2\right)\left|\sum_j \sigma_j f_j(\kappa)\exp(i\kappa.\mathbf{r}_j)\right|^2 \tag{8}$$

For the compounds discussed in this thesis two magnetic form factors are needed, the form factor of copper and the form factor of praseodymium.

1.1b The Cu form factor

The form factor of any magnetic ion is the Fourier transform of the normalised spin density[29]:

$$\begin{aligned} f(\kappa) &= \langle \exp(i\kappa.\mathbf{r})\rangle \\ &= \int \Psi_s{}^* \exp(i\kappa.\mathbf{r})\Psi_s d^3\mathbf{r} \end{aligned} \tag{9}$$

where Ψ_s is the amplitude of the normalised spin density of the relevant ion.

The electronic state of the Cu^{2+} ions is $(4s^0 3d^9)$; however, we can just consider the single hole in the $3d$ orbital, rather than the nine magnetic electrons. For the local environment of the Cu ions in the 123 structure, the $l = 2$ symmetry of the hole is at

---

[29] S.W. Lovesey, *Theory of neutron scattering from condensed matter* volume 2, §7.3, Oxford Science Publications (1986).

between being parallel to *a* and being parallel to *b*. However, it became recognised[30] that this was inadequate, since the magnetic reflections in K_2CuF_4 are seen at integer miller indices (*h*, *k*, *l*), whereas in $RBa_2Cu_3O_{6+x}$ *h* and *k* are half-integer; this is clearly an important consideration when the spin density is strongly aspherical. Furthermore, covalent effects were playing an important role in K_2CuF_4; the fluorine ligands were contributing significantly at low κ, whereas because $YBa_2Cu_3O_{6+x}$ is antiferromagnetic, the spin density midway between oppositely aligned copper moments must be zero.

For the case of Cu^{2+}, however, the theory can be greatly simplified. The description here follows the procedure of Weiss and Freeman[31]. Because the orbital component of the angular momentum is quenched, only the spin component contributes. Furthermore, since there is only one magnetic hole, the spin-density must then be simply proportional to the charge density of the hole's wave function. The hole wave function can be described in terms of the spherical harmonics with the appropriate orbital angular momentum *l*:

$$\begin{aligned} \Psi &= \sum_m a_m \varphi_m, \\ \varphi_m &= \frac{R(r)}{r} \Phi_m(\phi) \Theta_l^m(\cos\theta) \end{aligned} \tag{10}$$

The angular terms $\Phi_m(\phi)$ and $\Theta_l^m(\theta)$ are defined according to the convention of Condon and Shortley[32]. The equation for the form factor can now be written in terms of form factor matrix elements $f_{mm'}(\kappa)$ as follows:

---

[30] T.A. Kaplan, S.D. Mahanti, and H. Chang, *Spin fluctuations and covalence in the half-filled narrow-band Hubbard model*, Phys. Rev. B **45**, 2565-2568, (1992).

[31] R.J. Weiss and A.J. Freeman, *X-ray and neutron scattering from electrons in a crystalline field and the determination of outer electron configurations in iron and nickel*, J. Phys. Chem. Solids **10**, 147-161, (1959).

[32] E.U. Condon and G.H. Shortley, *Theory of atomic spectra*, p52, Cambridge University Press (1953).

$$\begin{aligned} f(\kappa) &= \int \sum_{m} a_m{}^* \varphi_m{}^* \exp(i\kappa.\mathbf{r}) \sum_{m'} a_{m'} \varphi_{m'} d^3\mathbf{r} \\ &= \sum_{m,m'} a_m{}^* a_{m'} \int \varphi_m{}^* \exp(i\kappa.\mathbf{r}) \varphi_{m'} d^3\mathbf{r} \\ &= \sum_{m,m'} a_m{}^* a_{m'} f_{mm'}(\kappa) \end{aligned} \qquad (11)$$

The exponential term can be expanded in terms of any complete set, and we choose the set of Bessel functions,

$$\exp(i\kappa.\mathbf{r}) = 4\pi \sum_{n=0}^{\infty} \sum_{p=-n}^{\infty} i^n j_n(\kappa r) \Phi_p(\phi) \Theta_n^p(\cos\theta) \Phi_p(\gamma) \Theta_n^p(\cos\beta) \qquad (12)$$

where κ, γ, and β define **κ** in reciprocal space as r, ϕ, and θ define **r** in direct space (see Figure 4).

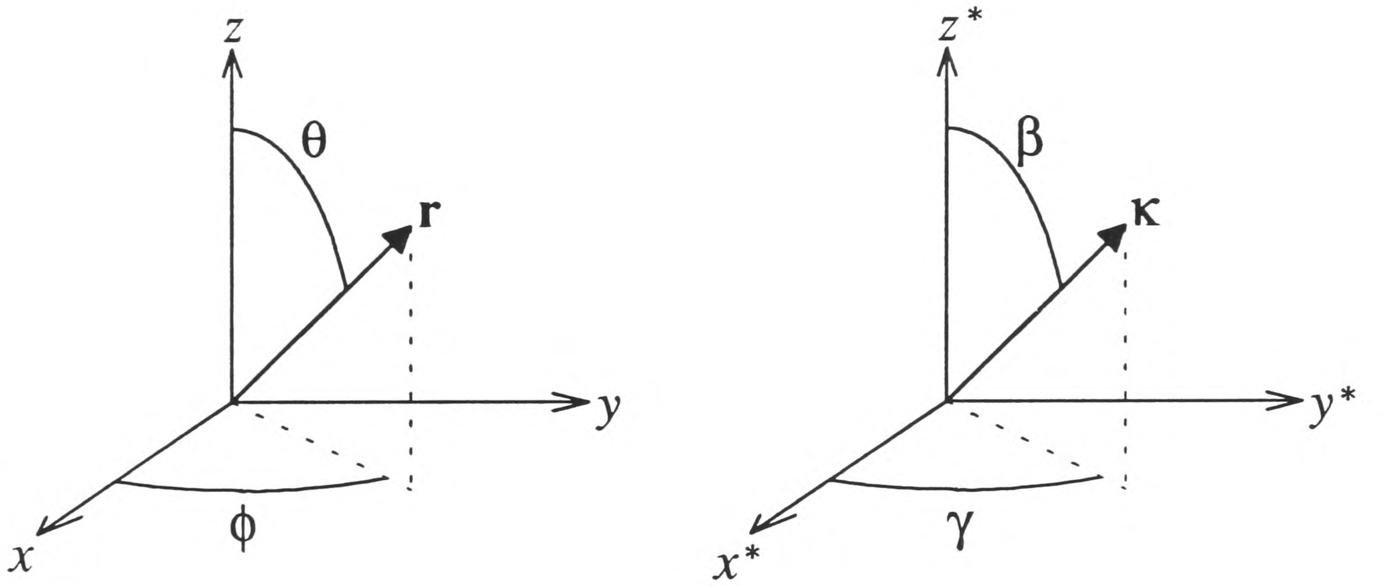

Figure 4: Definition of ϕ and θ in direct space, and γ and β in reciprocal space. z and z^* are the axes of quantisation.

The volume element $d^3\mathbf{r}$ is given by

$$d^3\mathbf{r} = r^2 dr\, d\phi\, d(\cos\theta) \qquad (13)$$

and so $f_{mm'}(\kappa)$ has integrals in r, ϕ, and cos θ. The integral in r produces the expectation value of the nth order Bessel function:

$$\int j_n(\kappa r)R(r)^* R(r)dr = \begin{cases} \langle j_n(\kappa)\rangle, & n \text{ even} \\ 0, & n \text{ odd} \end{cases} \tag{14}$$

This means that the sum over n in Equation (12) need only sum over even values of n. The integral over ϕ is

$$\begin{aligned} \int \Phi_p(\phi)\Phi_m{}^*(\phi)\Phi_{m'}(\phi)d\phi &= \frac{1}{(2\pi)^{1/2}}\int \exp\left(i(p-m+m')\phi\right)d\phi \\ &= \frac{1}{(2\pi)^{1/2}}\delta(p-m+m') \end{aligned} \tag{15}$$

the delta function again simplifying the expressions we are working with. Finally, the integral over cos θ is

$$\int \Theta_n^{m-m'}(\cos\theta)\Theta_l^{m}(\cos\theta)\Theta_l^{m'}(\cos\theta)d(\cos\theta) = \left(\frac{2n+1}{2}\right)^{1/2} C^n(lm,lm') \tag{16}$$

where the coefficients $C^n(lm,lm')$ can either be calculated by simple integration of Equation (16) or looked up[32]. Hence the expression for the matrix element $f_{mm'}(\kappa)$ reduces to

$$f_{mm'}(\kappa) = (4\pi)^{1/2} \sum_{n=0,2,4\ldots}^{\infty} (2n+1)^{1/2} i^n C^n(lm,lm')\langle j_n(\kappa)\rangle \Phi_{m-m'}(\gamma)\Theta_n^{m-m'}(\cos\beta) \tag{17}$$

The expectation values of the Bessel functions can be estimated from expressions with tabulated coefficients, calculated from suitable wave functions. These expressions are generally calculated in terms of s (Å^{-1}), rather than κ, s being defined as

$$s = \frac{\sin\theta_s}{\lambda} = \frac{\kappa}{4\pi} \tag{18}$$

where θ_s is the Bragg angle at the sample, and
λ is the wavelength of the incident radiation.

The standard expressions used to describe the expectation values of the Bessel functions are

$$\begin{aligned} \langle j_0(s)\rangle &= A\exp\left(-as^2\right) + B\exp\left(-bs^2\right) + C\exp\left(-cs^2\right) + D \\ \langle j_{n>0}(s)\rangle &= \left(A\exp\left(-as^2\right) + B\exp\left(-bs^2\right) + C\exp\left(-cs^2\right) + D\right)s^2 \end{aligned} \tag{19}$$

the relevant coefficients for copper being given in Table 4.

Table 4: Coefficients for $\langle j_n(\kappa)\rangle$, the expectation values of the nth Bessel functions, for the Cu^{2+} ion[33].

n	A	a	B	b	C	c	D
0	0.0232	34.969	0.4023	11.564	0.5882	3.843	−0.0137
2	1.5189	10.478	1.1512	3.813	0.2918	1.398	0.0017
4	−0.3914	14.740	0.1275	3.384	0.2548	1.255	0.0103

Hence, for a single magnetic electron or hole, the form factor can be calculated from a knowledge of the spherical harmonics of the wave function; conversely, if the form factor has been measured, the spherical harmonics can be deduced by fitting. The expression for a pure $(x^2 - y^2)$ orbital is[34]

$$f(\kappa) = \langle j_0(\kappa)\rangle - \frac{5}{7}\left(1 - 3\cos^2\beta\right)\langle j_2(\kappa)\rangle + \frac{9}{56}\left(1 - 10\cos^2\beta + \frac{35}{3}\cos^4\beta\right)\langle j_4(\kappa)\rangle \qquad (20)$$

whereas the expression for a spherical charge density is

$$f(\kappa) = \sum_m f_{mm}(\kappa) = \langle j_0(\kappa)\rangle \qquad (21)$$

Finally, an empirical adjustment to the form factor can be made to allow for the effects of the surrounding ions. Suppose that the wave functions of the ions in their crystalline surroundings have expanded radially by a factor of $(1+\alpha)$, in comparison to a free ion wave function. Then the resulting form factor $f'(\kappa)$ will be given by

$$\begin{aligned} f'(\kappa) &= (1+\alpha)^{-3}\int \Psi\left(\mathbf{r}(1+\alpha)^{-1}\right)^* \exp(i\kappa.\mathbf{r})\Psi\left(\mathbf{r}(1+\alpha)^{-1}\right)d^3\mathbf{r} \\ &= \int \Psi(\mathbf{r}')^* \exp\left(i\kappa.\mathbf{r}'(1+\alpha)\right)\Psi(\mathbf{r}')d^3\mathbf{r}' \\ &= f\left(\kappa(1+\alpha)\right) \end{aligned} \qquad (22)$$

where the factor of $(1+\alpha)^{-3}$ is due to the normalisation of $\Psi\left(\mathbf{r}(1+\alpha)^{-1}\right)$. Hence an

---

[33] P.J. Brown, *International tables of crystallography* vol. C, Dordecht (1993).

[34] S. Shamoto, M. Sato, J.M. Tranquada, B.J. Sternlieb, and G. Shirane, *Neutron-scattering of antiferromagnetism in $YBa_2Cu_3O_{6.15}$*, Phys. Rev. B **48** 13817-13825, (1993).

estimate can also be made of any radial expansions or contractions of the wave function, in comparison to the free ion wave function, if there are sufficient data points over which to obtain a fit to α.

1.1c The Pr form factor

The method of Weiss and Freeman[31] can not be used to calculate the form factor of praseodymium, because Pr^{3+} ($4f^2$, $^3H_4$) has two magnetic electrons with unquenched orbital angular momenta. However, you can make use of the fact that the $l = 3$ orbitals are confined to be close to the centre of the atom: this is the reason why rare-earth ions are sufficiently shielded from crystal field effects to not be orbitally quenched. If we assume that κ^{-1} is much larger than the extent of the wave function, so that the spin density can be regarded as existing at a point, then we can make use of the *dipole approximation*[35], which gives a spherically symmetric form factor

$$\begin{aligned} f(\kappa) &= \langle j_0(\kappa)\rangle + \frac{g_L}{g_J}\langle j_2(\kappa)\rangle \\ &= \langle j_0(\kappa)\rangle + \frac{2-g_J}{g_J}\langle j_2(\kappa)\rangle, \\ g_L &= \frac{J(J+1)-S(S+1)+L(L+1)}{2J(J+1)} \\ g_J &= \frac{3J(J+1)+S(S+1)-L(L+1)}{2J(J+1)} \end{aligned} \qquad (23)$$

It can be seen that the form factor for a spherically symmetric spin-only system ($g_L = 0$, $g_J = 2$) is equal to $\langle j_0(\kappa)\rangle$, in agreement with the approach by Weiss and Freeman shown above (Equation (21)). For Pr^{3+}, $g_L = {}^6/_5$ and $g_J = {}^4/_5$.

Again, $\langle j_0(\kappa)\rangle$, the expectation values of the Bessel functions, can approximately be calculated by the expressions given in Equation (19), with the coefficients appropriate to praseodymium:

---

[35] S.W. Lovesey, *Theory of neutron scattering from condensed matter* volume 2, §7.3, Oxford Science Publications (1986).

Table 5: Coefficients for $\langle j_n(\kappa)\rangle$, the expectation values of the nth Bessel functions, for the Pr^{3+} ion[36]. $C = 0$.

n	A	a	B	b	D
0	0.2277	16.11	0.7923	5.277	−0.0204
2	1.8655	8.1948	1.0779	2.6641	0.01199

---

[36] E.J. Lisher and J.B. Forsyth, *Analytic approximations to form factors*, Acta Cryst. A 27, 545-549, (1971).

1.2 The Lorentz factor

The elastic measurements which this thesis describes were not made in the conventional manner of single crystal diffraction experiments. For instance, an analyser was used - this gave a better signal to noise, and gave more clearly defined ordering temperatures, since otherwise the measurements would integrate over the critical inelastic scattering. Also, measurements were often made by taking linear scans in reciprocal space, due to the existence of intrinsic scattering functions. It was therefore necessary to develop the formalism required to extract accurate peak intensities from the measurements which were performed, and in this section I outline the theories which were developed.

1.2a The geometric Lorentz factor

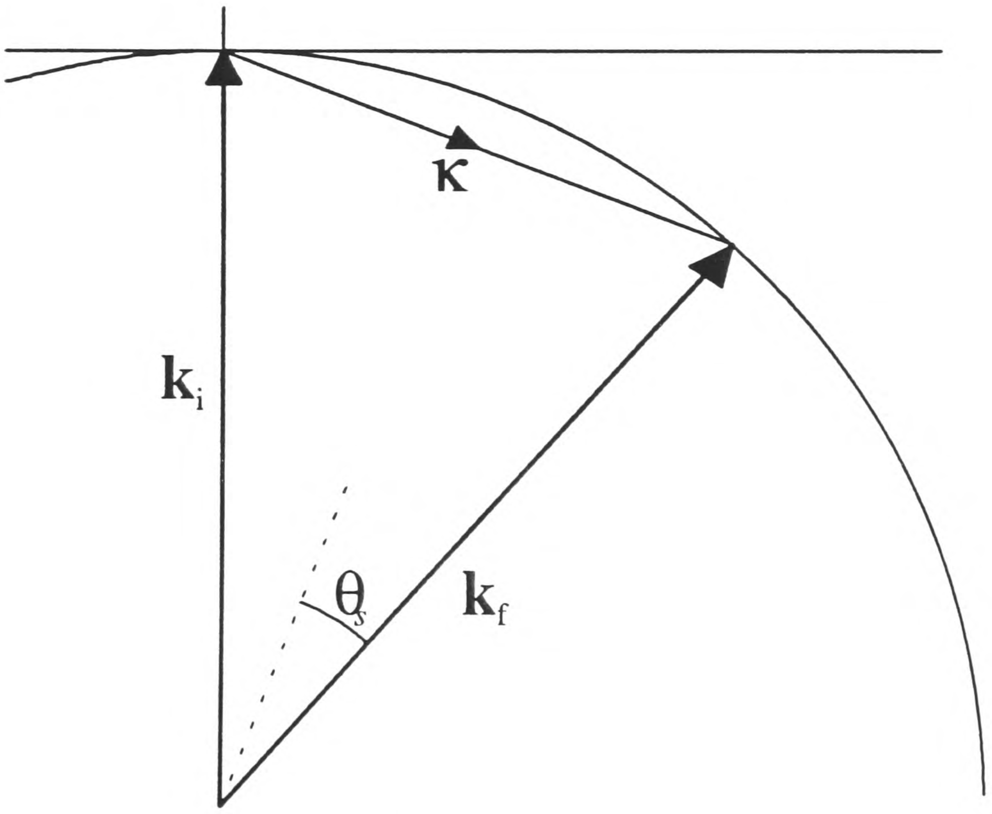

Figure 5: The Ewald sphere defined by $\kappa = k_f - k_i$. The Bragg angle at the sample, θ_s, is the half-angle between k_i and k_f.

The area of a peak (in *count rate* . $\mathring{A}^{-1}$) measured in a neutron scattering experiment doesn't just depend on the intensity of the Bragg peak; it also depends on how the scan is performed. The Lorentz factor relates the measured area *A* to the intrinsic peak intensity I, and in the simplest approximation, this factor depends solely on the geometry of the scan in reciprocal space.

The von Laue scattering law states that scattering is measured from a Bragg peak whenever the wavevector transfer, $\boldsymbol{\kappa} = \mathbf{k}_f - \mathbf{k}_i$, equals a reciprocal lattice vector τ. On a triple-axis spectrometer, $\mathbf{k}_i$ is normally fixed, though $\mathbf{k}_f$ can vary both in magnitude and direction. For elastic experiments, $|\mathbf{k}_i| = |\mathbf{k}_f| = k$ and so the locus of the possible vectors for $\boldsymbol{\kappa}$ forms a sphere of radius k. This sphere is known as the Ewald sphere (see Figure 5). In Figure 5, it is $\mathbf{k}_i$ (and therefore the Ewald sphere) that is fixed; this is the **k**-space of the spectrometer. However, in the reciprocal space of the crystal, it is the reciprocal lattice points that are fixed, and so this is the co-ordinate frame that we should now use. As we perform the scan, we trace the wavevector transfer through reciprocal space along a direction $\Delta\hat{\kappa}$ (see Figure 6).

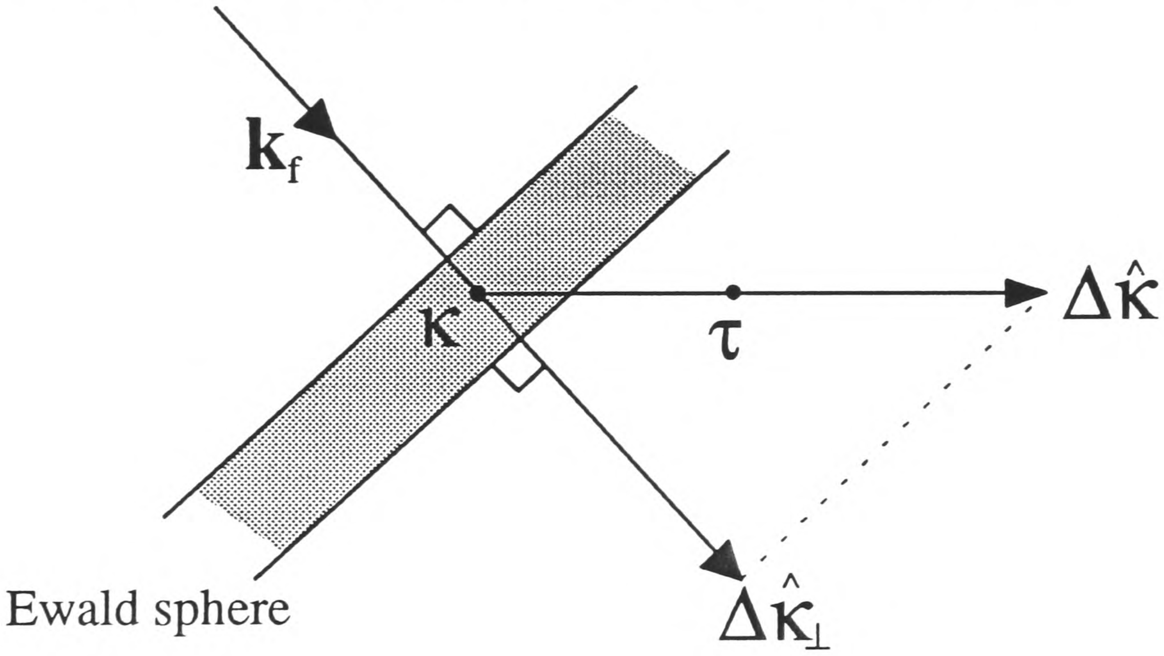

Figure 6: As the wavevector transfer $\boldsymbol{\kappa}$ moves through reciprocal space along $\Delta\hat{\kappa}$, the Ewald sphere (shaded region) passes over the Bragg point τ. The number of neutrons scattered is proportional to the time τ is coincident with the Ewald sphere, which is inversely proportional to the component of $\Delta\hat{\kappa}$ projected perpendicularly to the Ewald sphere, $\Delta\hat{\kappa}_\perp$.

First consider an open detector. By this we mean that the outgoing neutrons are not collimated at all, and so scattered neutrons will be observed whenever the

Ewald sphere lies across the Bragg point. As the Ewald sphere passes through the Bragg peak τ, scattering is measured by the detector. The rate at which neutrons are counted is clearly proportional to the time taken for the sphere to pass through the Bragg peak, and therefore inversely proportional to the velocity of κ projected perpendicularly to the Ewald sphere.

If the Ewald sphere cuts the Bragg peak obliquely, it will have more opportunity to reflect than if it were to cut the sphere perpendicularly, and so A, the measured area of the peak, will be larger. It is therefore necessary to relate the measured area A of the peak, which is a function of how the scan is performed, to the peak's intrinsic intensity I. The Lorentz factor L is proportional to the ratio of A to I, although it is often more convenient to work in terms of L^{-1}.

$$L^{-1} \propto \frac{I}{A} \tag{24}$$

As we have seen, this will in turn be proportional to $\Delta\hat{\kappa}_\perp$. We can relate this to the Bragg angle at the sample, θ_s, and the direction of the scan in reciprocal space α. We define α as being the angle between $\Delta\hat{\kappa}$ and the reciprocal lattice vector τ (see Figure 7). Then we have

$$\begin{aligned} L^{-1} &= \Delta\hat{\kappa}_\perp \\ &= \Delta\hat{\kappa}.\hat{\kappa}_f \\ &= \left|\cos\left(\pi - \left(\theta_s + \tfrac{\pi}{2} + \alpha\right)\right)\right| \\ &= \left|\sin\left(\theta_s + \alpha\right)\right| \end{aligned} \tag{25}$$

which shall henceforth be referred to as the geometric Lorentz factor.

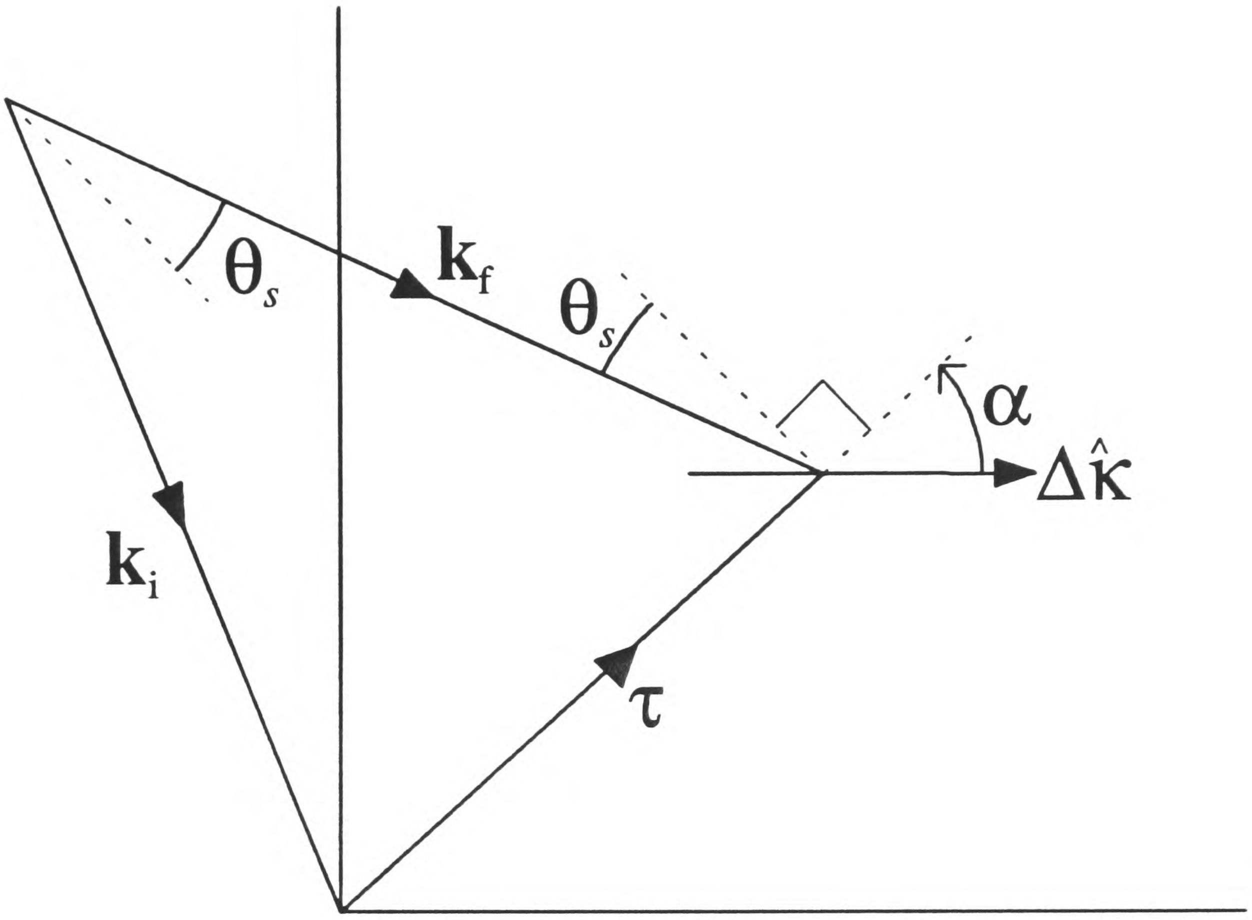

Figure 7: The point when the wavevector transfer $\boldsymbol{\kappa}$ equals the reciprocal lattice vector $\boldsymbol{\tau}$. α is defined as the angle between the scan direction $\Delta\hat{\boldsymbol{\kappa}}$ and $\boldsymbol{\tau}$.

As an example, we consider a special case which is frequently encountered: the ω-scan. In this kind of scan, the spectrometer (and so $\mathbf{k}_f$) stays fixed as the sample is rotated around its axis. Hence in Figure 7, $\Delta\hat{\boldsymbol{\kappa}}$ is perpendicular to $\boldsymbol{\tau}$, $\alpha = \frac{\pi}{2}$, and L^{-1} = cos θ_s. However, the area is normally measured in terms of the angular rotation, i.e. in units of *count rate . degrees* rather than *count rate . Å*$^{-1}$. Since $\Delta\kappa = \kappa\Delta\omega =$ $2k$ sin θ_s $\Delta\omega$, in these units the Lorentz factor is

$$\begin{aligned} L^{-1} &= \cos\theta_s \, 2k\sin\theta_s \\ &= k\sin 2\theta_s \end{aligned} \tag{26}$$

which is the well-known result for an ω-scan.

Although the geometric Lorentz factor is given by a simple expression, the resolution of a real triple-axis spectrometer and the intrinsic shape of the Bragg peak must be taken into account.

1.2b The spectrometer resolution

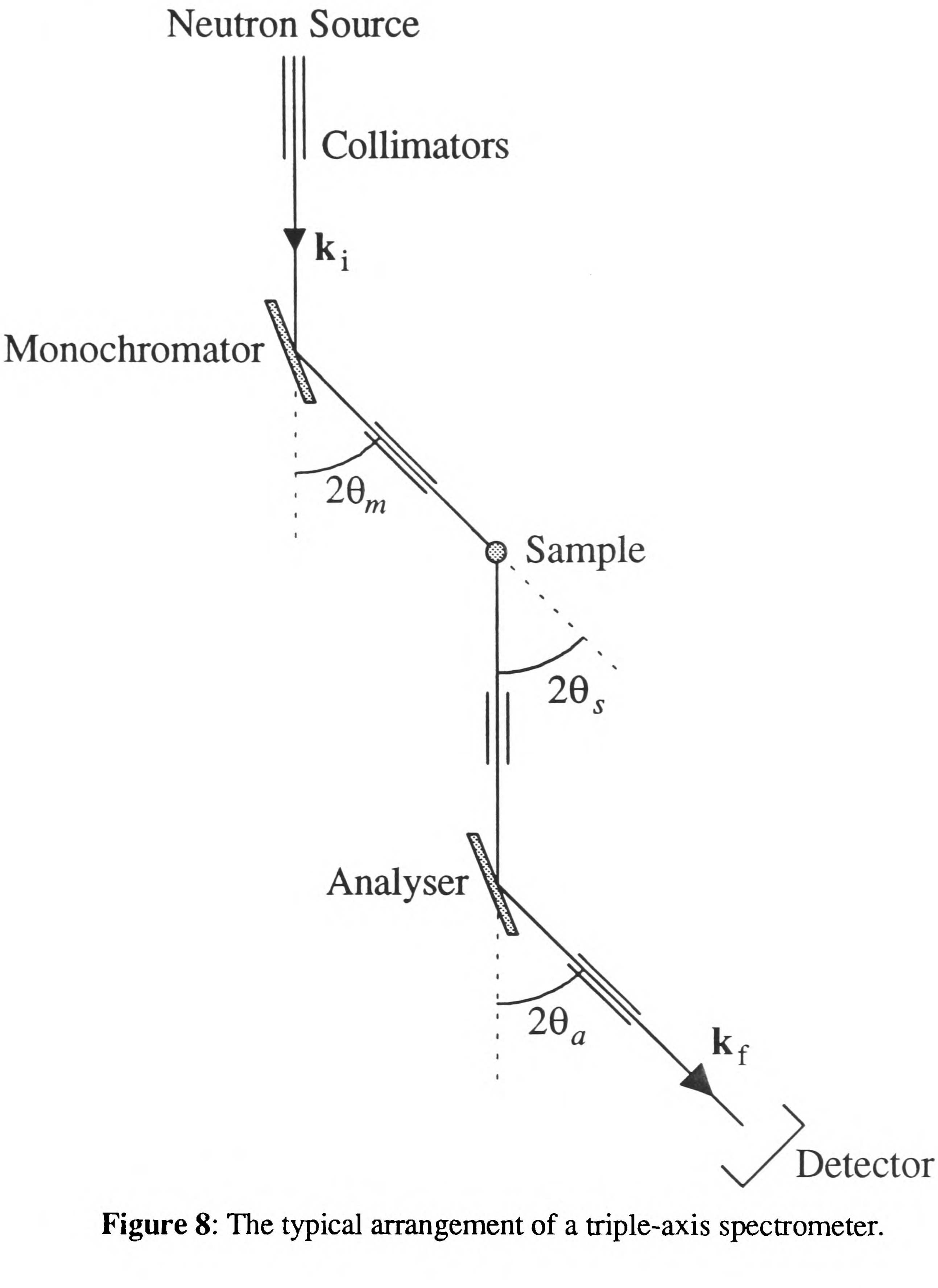

Figure 8: The typical arrangement of a triple-axis spectrometer.

A diagram of a triple-axis spectrometer, showing the Bragg angles at the monochromator, sample, and analyser (θ_m, θ_s, and θ_a), is shown in Figure 8. The resolution function of a triple-axis spectrometer was successfully described by Cooper and Nathans[37] (with some typographical errors remedied by Chesser and Axe[38]), by convoluting suitable Gaussian functions for the collimations and the mosaicity of the monochromator and detector.

The original work by Cooper and Nathans was not restricted to elastic scans, but here we can make that simplification, since we are only interested in elastic measurements. This approach was used by Cowley and Bates[39], and I am deeply indebted to Professor Cowley for explaining to me the principles behind including resolution effects in the Lorentz factor. In this thesis, however, I will go beyond just including spectrometer resolution, and consider also the effects of sample mosaicity, 2*D* ordering and 3*D* correlations.

The resolution function, or resolution ellipsoid, is the locus of $\boldsymbol{\kappa}$ positions in reciprocal space where the transmission of the spectrometer has fallen to half what it is at the nominal position of the spectrometer, $\boldsymbol{\kappa}_0$. We can ignore the out-of-plane resolution, as this is so broad that total integration will always occur. Hence we can confine our discussion to the resolution in the scattering plane. Defining $\mathbf{q}$ as the displacement in reciprocal space from the nominal spectrometer position, the resolution function can be represented mathematically as

$$R(\mathbf{q}) = N\exp\left[-\tfrac{1}{2}M_{11}q_x^{\,2} - M_{12}q_xq_y - \tfrac{1}{2}M_{22}q_y^{\,2}\right] \tag{27}$$

where N is the normalisation factor and M_{ij} define the resolution ellipsoid. Axes are chosen so that the q_x-axis is parallel to $\boldsymbol{\kappa}_0$ (see Figure 9).

Using the notation of Cooper and Nathans, and considering only the in-plane resolution, the standard deviations of the Gaussians representing the in-plane collimator transmission functions are (starting with the source-to-moderator

---

[37] M.J. Cooper and R. Nathans, *The resolution function in neutron diffractometry I. The resolution function of a neutron diffractometer and its application to phonon measurements*, Acta. Cryst. **23**, 357-267, (1967).

[38] N.J. Chesser and J.D. Axe, *Derivation and experimental verification of the normalized resolution function for inelastic neutron scattering*, Acta. Cryst. A **29**, 160-169, (1973).

[39] R.A. Cowley and S. Bates, *The magnetic structure of holmium: I*, J. Phys. C: Solid State Phys. **21**, 4113-4121, (1988).

collimation) α_0, α_1, α_2, and α_3. Similarly, the mosaicity of the monochromator and the analyser are η_m and η_a respectively. Cooper and Nathans defined some a_j parameters as

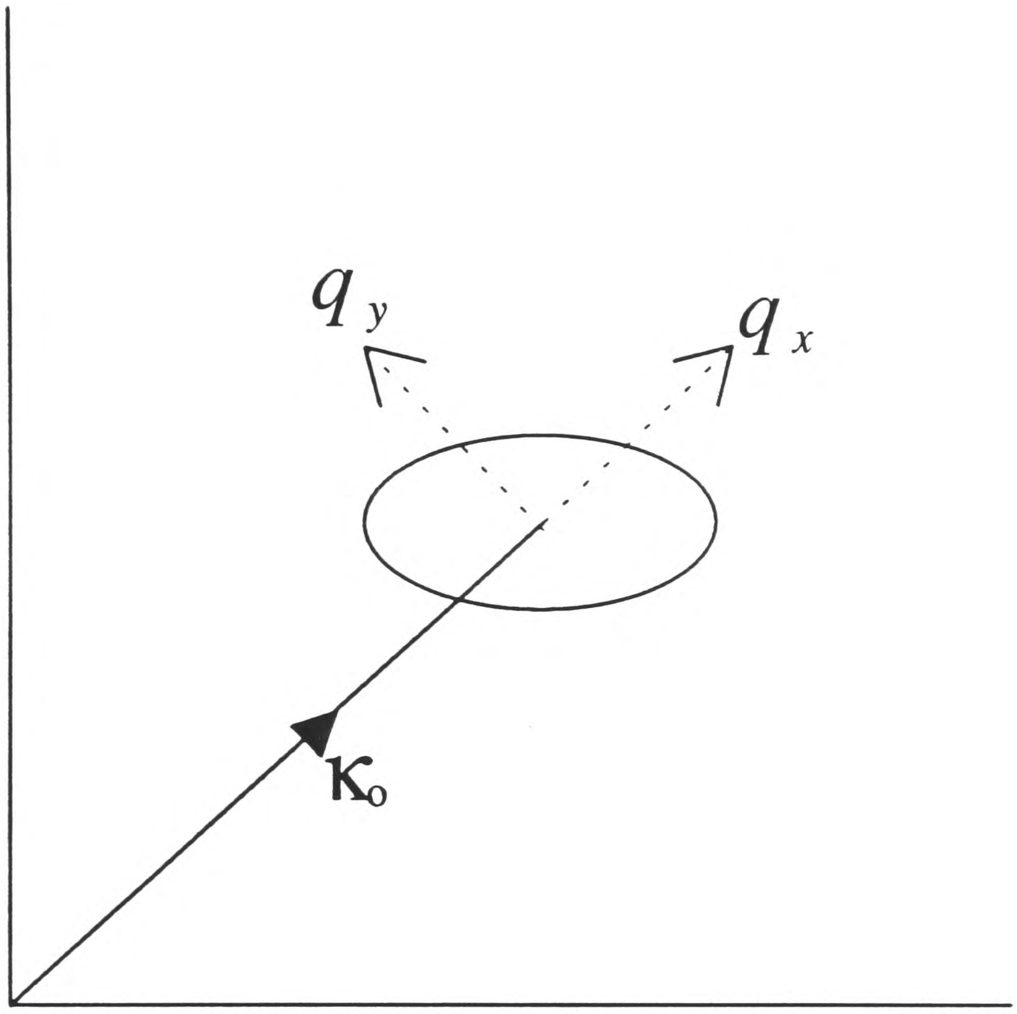

Figure 9: The resolution ellipsoid. The q_x-axis is defined to be parallel to κ_o.

$$\begin{aligned}
a_1 &= \frac{\tan\theta_m}{\eta_m k_i} & a_2 &= \frac{1}{\eta_m k_i} & a_3 &= \frac{1}{\alpha_1 k_i} \\
a_4 &= \frac{1}{\alpha_2 k_f} & a_5 &= \frac{\tan\theta_a}{\eta_a k_f} & a_6 &= \frac{-1}{\eta_a k_f} \\
a_7 &= \frac{2\tan\theta_m}{\alpha_0 k_i} & a_8 &= \frac{1}{\alpha_0 k_i} & a_9 &= \frac{2\tan\theta_a}{\alpha_3 k_f} \\
& & a_{10} &= \frac{-1}{\alpha_3 k_f}
\end{aligned} \tag{28}$$

and b_j parameters as

$$\begin{aligned}
b_0 &= a_1 a_2 + a_7 a_8 \\
b_1 &= a_2^2 + a_3^2 + a_8^2 \\
b_2 &= a_4^2 + a_6^2 + a_{10}^2 \\
b_3 &= a_5^2 + a_9^2 \\
b_4 &= a_5 a_6 + a_9 a_{10} \\
b_5 &= a_1^2 + a_7^2
\end{aligned} \tag{29}$$

Chesser and Axe[38] considered the normalisation N, and following the notation of Cowley and Bates, it can be written as

$$N = \frac{C}{\sqrt{A'}\sin 2\theta_s} \tag{30}$$

where C is a constant for fixed collimation and incident energy and A' is defined in Equation (32).

The resolution function as calculated by Cooper and Nathans was a complicated expression. However, Cowley and Bates showed that in the elastic case, the matrix elements M_{ij} could be written as

$$\begin{aligned}
M_{11} &= \frac{B_{11}}{4A'\cos^2\theta_s} \\
M_{12} &= \frac{B_{12}}{4A'\cos\theta_s\sin\theta_s} \\
M_{22} &= \frac{B_{22}}{4A'\sin^2\theta_s}
\end{aligned} \tag{31}$$

where

$$\begin{aligned}
A' &= (b_1 + b_2)\tan^2\theta_s + 2(b_4 - b_0)\tan\theta_s + b_3 + b_5 \\
B_{11} &= (b_1 + b_2)(b_3 + b_5) - (b_4 - b_0)^2 \\
B_{12} &= 2(b_1 b_4 + b_0 b_2)\tan\theta_s + b_4^2 - b_0^2 + (b_1 - b_2)(b_3 + b_5) \\
B_{22} &= 4b_1 b_2 \tan^2\theta_s + 4(b_1 b_4 - b_0 b_2)\tan\theta_s + (b_1 + b_2)(b_3 + b_5) - (b_4 + b_0)^2
\end{aligned} \tag{32}$$

In an open detector, all the scattered neutrons that leave the sample enter the detector. Hence this can be represented by $\alpha_2 = \alpha_3 = \eta_a = \infty$, so $b_2 = b_3 = b_4 = 0$ and $B_{11} = B_{12} = B_{22} = B_0$, where $B_0 = b_1 b_5 - b_0^2$.

1.2c The Lorentz factor - inclusion of spectrometer resolution

Now that we have a description of the spectrometer resolution, we can use it to create a Lorentz factor that includes this resolution. The geometric factor obtained in Section *II-1.2a* effectively assumed that the resolution function had a constant normalisation *N* throughout reciprocal space, and that the 'ellipsoid' had no ends; there will clearly be occasions when this is not a good approximation. For the moment I will represent the scattering function as a delta-function Bragg peak at τ in reciprocal space, with an intrinsic intensity *I*. Hence the scattering function is $I\,\delta(\kappa - \tau)$.

As we have seen, what you normally measure in a neutron scattering experiment is the area under a peak,

$$A = \frac{|\Delta\kappa|}{p-1}\sum_{i=1}^{p} \mathrm{C}_i \tag{33}$$

where $|\Delta\kappa|$ is the length of the scan in reciprocal space, *p* is the number of points in the scan, and C_i is the measured count rate at the *i*th point. It is easiest to proceed by defining the scan in terms of the q_x, q_y co-ordinates of the resolution ellipsoid,

$$\mathbf{t} = \boldsymbol{\tau} - \boldsymbol{\kappa}_o = t\begin{pmatrix}\cos\alpha \\ \sin\alpha\end{pmatrix} \tag{34}$$

(see Figure 10).

The count rate observed at the nominal centre of the spectrometer κ_o is the convolution of the resolution function with the scattering function,

$$\begin{aligned}\mathrm{C}(\mathbf{t}) &= \iint I\delta(\mathbf{q}-\mathbf{t})R(\mathbf{q})dq_x dq_y \\ &= NI\exp\left[-\tfrac{1}{2}M_{11}t_x{}^2 - M_{12}t_xt_y - \tfrac{1}{2}M_{22}t_y{}^2\right]\end{aligned} \tag{35}$$

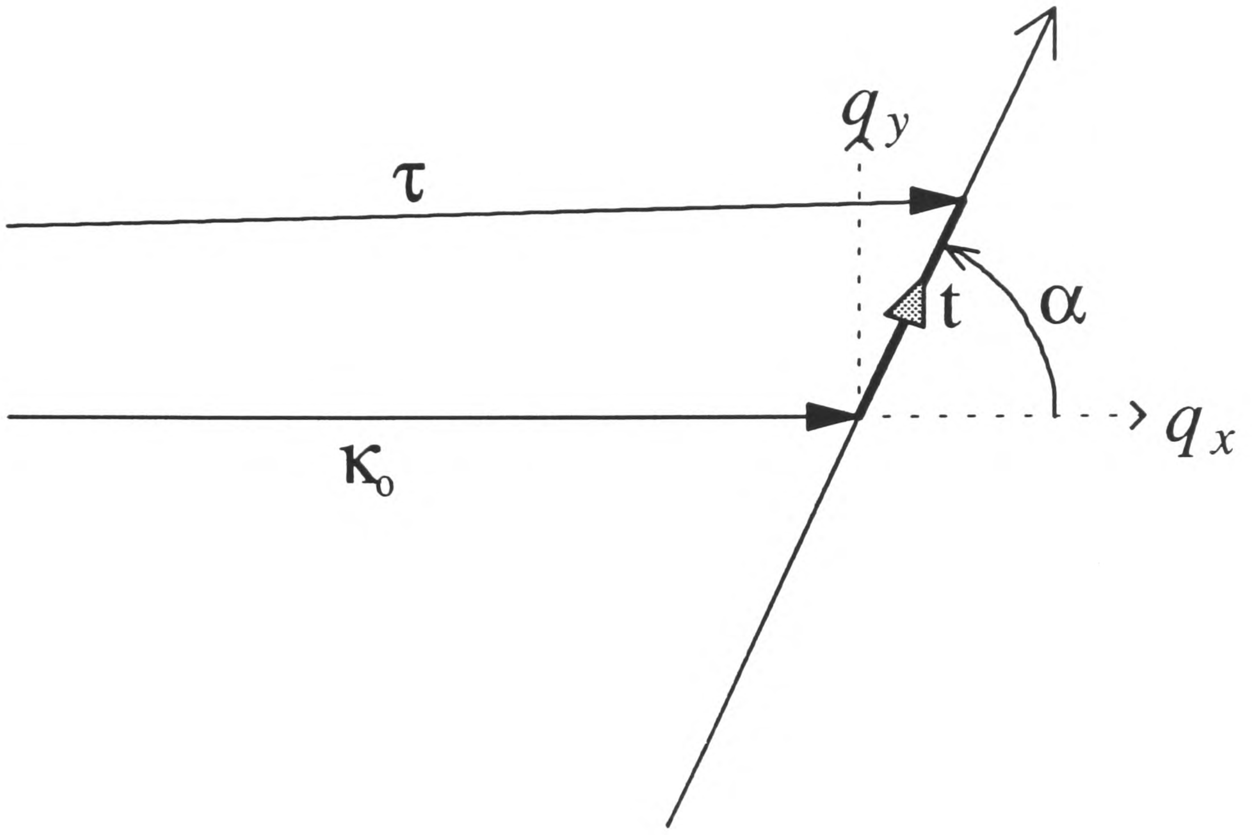

Figure 10: Diagram showing the scan in the resolution ellipsoid's co-ordinates. As the scan is performed, the nominal position of the spectrometer κ_0 passes through the Bragg peak at τ. The displacement of the Bragg peak from κ_0 is given in terms of q_x, q_y by **t**.

Hence if we do a scan which is linear in reciprocal space across a Bragg peak, the measured area is

$$A = \int C(\mathbf{t})dt$$
$$= NI\left(\frac{\pi}{\frac{1}{2}M_{11}\cos^2\alpha + M_{12}\cos\alpha\sin\alpha + \frac{1}{2}M_{22}\sin^2\alpha}\right)^{½} \quad (36)$$

where α, M_{ij} etc. are calculated at $\kappa_0 = \tau$. In analogy to the geometric Lorentz factor, we define L^{-1} as

$$L^{-1} = \frac{I}{A}\cdot C\sqrt{\frac{2\pi}{B_0}} \quad (37)$$

which gives

$$\begin{aligned} L^{-1} &= \frac{1}{N'B_0}\left(M_{11}\cos^2\alpha + 2M_{12}\cos\alpha\sin\alpha + M_{22}\sin^2\alpha\right)^{1/2} \\ &= \frac{\sin\theta_s\cos\theta_s}{B_0}\left(\frac{\cos^2\alpha}{\cos^2\theta_s}B_{11} + \frac{2\cos\alpha\sin\alpha}{\cos\theta_s\sin\theta_s}B_{12} + \frac{\sin^2\alpha}{\sin^2\theta_s}B_{22}\right)^{1/2} \end{aligned} \tag{38}$$

where N' is defined as

$$N' = \frac{N}{C} = \frac{1}{\sqrt{A'}\sin 2\theta_s} \tag{39}$$

This is essentially the result obtained by Cowley and Bates, with a slightly different normalisation. For an open detector it reduces to $L^{-1} = \sin(\theta_s + \alpha)$, which is exactly the geometric Lorentz factor obtained in Section *II-1.2a*. (This is the reason for the choice of normalisation in Equation (37)). Rearranging Equation (37), and using the experimentally measured area of Equation (33), we have

$$I \propto \frac{L^{-1}|\Delta\kappa|\sum_{i=1}^{p} C_i}{p-1} \tag{40}$$

The measurement of nuclear reflections of known intensity allows the constant of proportionally to be determined (see Appendix *II-4.5*).

Occasionally, it is only possible to measure the amplitude of a peak, C(0), rather than the whole area, for example if there are two or more peaks close together. If this is the case, then we can define a factor z, analogous to L^{-1}, to relate the intrinsic intensity of the Bragg peak I with the measured peak height C(0):

$$z = \frac{I}{C(0)} \cdot C\sqrt{\frac{2\pi}{B_0}} \tag{41}$$

this gives us

$$\begin{aligned} z &= \frac{1}{N'}\sqrt{\frac{2\pi}{B_0}} \\ I &\propto z\,C(0) \end{aligned} \tag{42}$$

The constant of proportionality is the same as that in Equation (40). However, measuring peak amplitudes is not generally as accurate as measuring their areas, and so the use of the Lorentz factor is the method of preference.

1.2d Inclusion of sample mosaicity

As well as taking into account the spectrometer resolution, it is also possible to take into account the mosaicity of the sample, especially as the two effects on peak width can often be comparable.

For example, if a transverse scan is performed, i.e. the scan direction is perpendicular to τ in reciprocal space ($\alpha = 90°$), then the measured Bragg peak will be broadened by the mosaicity, and will have a smaller amplitude than it would have had with no mosaic broadening. However, the *area* will be the same; it is just spread out across the scan. On the other hand, a longitudinal scan ($\alpha = 0°$) has the same width as it would with no mosaic broadening, but since the amplitude must be diminished by the transverse broadening, its area is *smaller*. The Lorentz factor needs to take account of this.

For most experiments, the sample mosaicity η_s is sufficiently small to allow the mosaicity to be considered as purely tangential to τ. By this I mean that I can consider the effects of the mosaicity to be linear in reciprocal space, rather than tracing an arc of radius τ (see Figure 11). Hence the scattering function of the Bragg peak can be represented by

$$\frac{I\delta(q_x - t_x)}{\eta_s \tau \sqrt{2\pi}} \exp\left[-\frac{1}{2}\left(\frac{q_y - t_y}{\eta_s \tau}\right)^2\right] \tag{43}$$

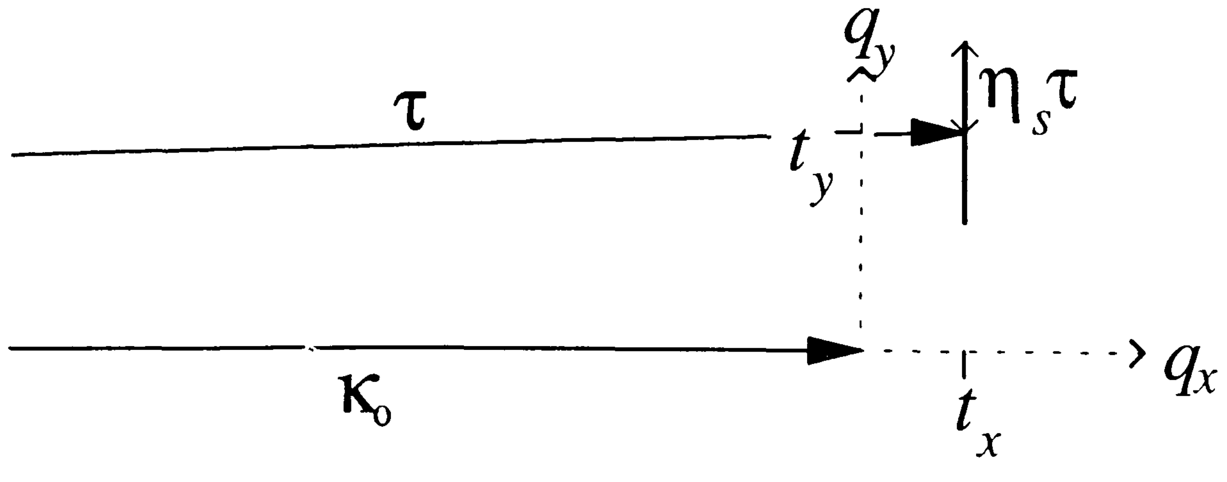

Figure 11: The sample mosaicity. If the angular standard deviation is η_s, then the standard deviation in reciprocal space is $\eta_s\tau$.

In analogy to M_{ij}, I define m as

$$m = \frac{1}{(\eta_s \tau)^2} \tag{44}$$

Following the method of Section *II-1.2c*, replacing the scattering function in Equation (35) with that corresponding to the mosaic spread, it can be shown that

$$\mathrm{C}(\mathrm{t}) = NI\sqrt{\frac{m}{M_{22}+m}}\exp\left[-\tfrac{1}{2}\left(M_{11} - \frac{M_{12}{}^2}{M_{22}+m}\right)t_x{}^2 - \frac{M_{12}m}{M_{22}+m}t_x t_y - \tfrac{1}{2}\frac{M_{22}m}{M_{22}+m}t_y{}^2\right] \tag{45}$$

Hence the effect of mosaicity is to make the following transformations:

$$\begin{aligned} N &\rightarrow \frac{N}{(1+M_{22}/m)^{1/2}} \\ M_{11} &\rightarrow M_{11} - \frac{M_{12}{}^2}{M_{22}+m} \\ M_{12} &\rightarrow \frac{M_{12}}{1+M_{22}/m} \\ M_{22} &\rightarrow \frac{M_{22}}{1+M_{22}/m} \end{aligned} \tag{46}$$

(N' follows the same transformations as N). The results of Section *II-1.2c* can therefore be made to include the sample mosaicity simply by including the above transformations, with the following results:

$$\begin{aligned} L^{-1} &= \frac{1}{N'B_0}\left(\left(M_{11} + \frac{M_{11}M_{22} - M_{12}{}^2}{m}\right)\cos^2\alpha + 2M_{12}\cos\alpha\sin\alpha + M_{22}\sin^2\alpha\right)^{1/2} \\ z &= \frac{1}{N'}\sqrt{\frac{2\pi(1+M_{22}/m)}{B_0}} \end{aligned} \tag{47}$$

where M_{ij} and N' are as initially defined in Equations (31) and (39).

Recall that introducing sample mosaicity should leave the area of transverse scans unchanged, but decrease the area of longitudinal scans. L^{-1} is unchanged for $\alpha = 90°$ (transverse scan), and increased for $\alpha = 0°$ (longitudinal scan); hence the calculation obeys the qualitative prediction.

The effect of the sample mosaicity can now be decoupled from the form of the intrinsic scattering, and included in the resolution function by the transformations of Equation (46).

1.2e The Bragg rod

If a system is magnetically ordered in two directions, but has *no* order in the third direction, then Bragg peaks are no longer observed. Instead, Bragg rods - ridges of scattering in reciprocal space - are seen. Naturally, this will affect the area measured in a scan of reciprocal space, and so it is desirable to have a suitable Lorentz factor.

First, we can see how the Bragg rods arise. The amplitude of the reflected wave is proportional to the Fourier transform of the scattering sites, and hence proportional to the Fourier transform over the unit cells at **R**. We can represent this by A,

$$\mathrm{A} = \sum_{\mathbf{R}}^{3D} \exp(i\kappa.\mathbf{R}) \tag{48}$$

where the three-dimensional sum is over all the unit cells in the crystal (of which there are n).

The intensity is then the squared-modulus of the amplitude, and we can represent this by i,

$$\begin{aligned} \mathrm{i} &= |\mathrm{A}|^2 \\ &= \sum_{\mathbf{R},\mathbf{R}'}^{3D} \exp[i\kappa.(\mathbf{R}-\mathbf{R}')] \end{aligned} \tag{49}$$

Now we can consider two cases: the case where order exists in all three directions, and the case when order only exists in two dimensions.

For three-dimensional order,

$$\begin{aligned} \mathrm{i}_3 &= n\sum_{\mathbf{R}}^{3D}\exp(i\kappa.\mathbf{R}) \\ &= n\frac{(2\pi)^3}{V_0}\delta(\kappa-\tau) \end{aligned} \tag{50}$$

The first line is obtained by saying that each sum over $\mathbf{R}'$ is equivalent, due to the three dimensional periodicity. Hence this sum can be replaced by n, the number of unit cells.

The theory is now simplified if we just consider the case of an orthorhombic crystal. Let the dimensions of the unit cell be a, b, and c, and let the number of unit cells in each direction be n_a, n_b, and n_c, so that $n = n_a\, n_b\, n_c$. Hence the intensity in the three-dimensionally ordered case is

$$\mathrm{i}_3 = n\frac{(2\pi)^3}{abc}\delta(\kappa_x-\tau_x)\delta(\kappa_y-\tau_y)\delta(\kappa_z-\tau_z) \tag{51}$$

Now consider the situation where there is the same long-range order along a and b, but no order along c. Each layer along c contributes to the intensity incoherently, and so these need to be added as intensities, not amplitudes. The intensity in the two-dimensionally ordered case is then

$$\begin{aligned} \mathrm{i}_2 &= n_c\sum_{\mathbf{R},\mathbf{R}'}^{2D}\exp[i\kappa.(\mathbf{R}-\mathbf{R}')] \\ &= n_c.n_a n_b\sum_{\mathbf{R}}^{2D}(\exp i\kappa.\mathbf{R}) \\ &= n\frac{(2\pi)^2}{ab}\delta(\kappa_x-\tau_x)\delta(\kappa_y-\tau_y) \end{aligned} \tag{52}$$

Hence it can be seen that the effect of going from three-dimensional to two-dimensional order is to make the transformation

$$\delta(\kappa_z-\tau_z)\rightarrow\frac{c}{2\pi} \tag{53}$$

This is equivalent to saying that the Bragg peak intensity has been spread evenly along the ridge over a distance of $c^* = 2\pi/c$, which is exactly the distance separating the Bragg peaks in reciprocal space.

The natural way to proceed is to rotate axes so that the Bragg rod lies parallel to an axis (see Figure 12).

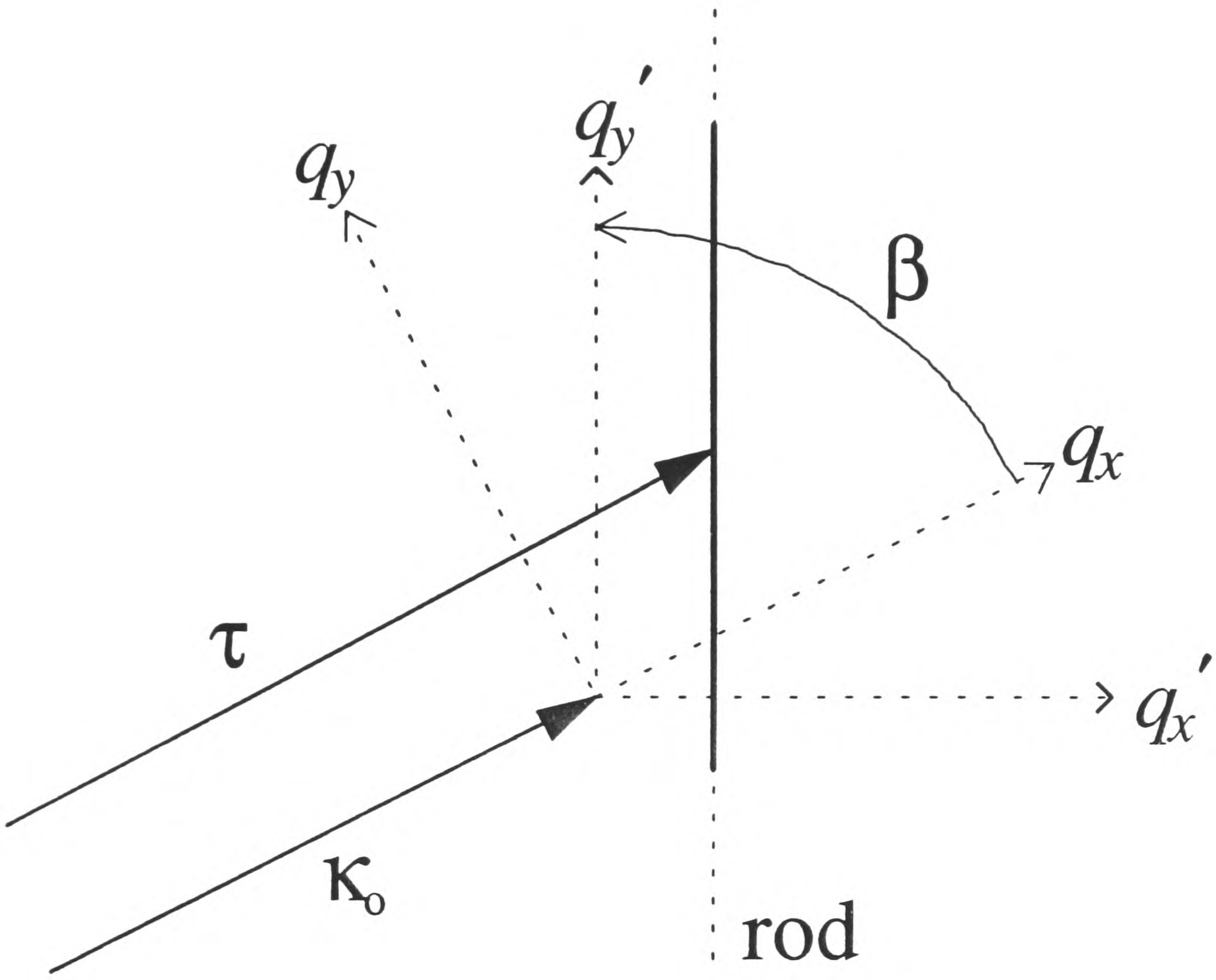

Figure 12: Definition of the q_x', q_y' axes. q_y' lies parallel to the Bragg rod, and the angle between κ_0 and the rod is β.

The rotation can be represented by

$$\begin{aligned}\begin{pmatrix} q_x \\ q_y \end{pmatrix} &= \begin{pmatrix} \sin\beta & \cos\beta \\ -\cos\beta & \sin\beta \end{pmatrix}\begin{pmatrix} q_x' \\ q_y' \end{pmatrix} \\ &= \beta\begin{pmatrix} q_x' \\ q_y' \end{pmatrix}\end{aligned} \qquad (54)$$

Applying the transformation of Equation (53), we can represent the scattering function by

$$I\delta\left(q_x' - t_x'\right)\delta\left(q_y' - t_y'\right) \rightarrow \frac{I}{c^*}\delta\left(q_x' - t_x'\right) \qquad (55)$$

where the layers have no order perpendicular to the *ab*-plane.

The resolution function, defined in Equation (27), can be rewritten in matrix form as

$$R(\mathbf{q}) = N\exp\left(-\tfrac{1}{2}\mathbf{q}^T\mathbf{M}\mathbf{q}\right) \tag{56}$$

where

$$\mathbf{M} = \begin{pmatrix} M_{11} & M_{12} \\ M_{12} & M_{22} \end{pmatrix} \tag{57}$$

Hence the resolution function in the rotated co-ordinates is

$$\begin{aligned} R(\mathbf{q}') &= N\exp\left(-\tfrac{1}{2}\mathbf{q}'^T\boldsymbol{\beta}^T\mathbf{M}\boldsymbol{\beta}\mathbf{q}'\right) \\ &= N\exp\left(-\tfrac{1}{2}\mathbf{q}'^T\mathbf{M}'\mathbf{q}'\right) \end{aligned} \tag{58}$$

where

$$\begin{aligned} \mathbf{M}' = \boldsymbol{\beta}^T\mathbf{M}\boldsymbol{\beta} &= \begin{pmatrix} M_{11}' & M_{12}' \\ M_{21}' & M_{22}' \end{pmatrix}, \\ M_{11}' &= M_{11}\sin^2\beta + M_{22}\cos^2\beta - 2M_{12}\sin\beta\cos\beta \\ M_{12}' = M_{21}' &= \left(M_{11} - M_{22}\right)\cos\beta\sin\beta + M_{12}\left(\sin^2\beta - \cos^2\beta\right) \\ M_{22}' &= M_{11}\cos^2\beta + M_{22}\sin^2\beta + 2M_{12}\sin\beta\cos\beta \end{aligned} \tag{59}$$

Applying the rotation to **t**,

$$\begin{aligned} \mathbf{t} &= \boldsymbol{\beta}\mathbf{t}' \\ &= t\begin{pmatrix} \cos\alpha' \\ \sin\alpha' \end{pmatrix} \end{aligned} \tag{60}$$

where

$$\alpha' = \left(\frac{\pi}{2} - \beta\right) + \alpha \tag{61}$$

It is now possible to follow the formalism of Section *II-1.2c*:

$$\begin{aligned} \mathrm{C}(\mathbf{t}') &= \iint \frac{I}{c^*}\delta\left(q_x' - t_x'\right)R(\mathbf{q}')dq_x'dq_y' \\ &= \frac{NI}{c^*}\sqrt{\frac{2\pi}{M_{22}'}}\exp\left[-\tfrac{1}{2}\left(M_{11}' - \frac{M_{12}'^2}{M_{22}'}\right)t^2\cos^2\alpha'\right] \end{aligned} \tag{62}$$

By noting that, for an ellipse,

$$\begin{aligned} M_{11}{}' M_{22}{}' - M_{12}{}'^{2} &= M_{11}M_{22} - M_{12}{}^{2} \\ &= \left(\frac{\pi}{area}\right)^{2} \end{aligned} \tag{63}$$

it can be shown that

$$\begin{aligned} L^{-1} &= \frac{c^{*}\cos\alpha'}{N'}\sqrt{\frac{M_{11}M_{22} - M_{12}{}^{2}}{2\pi B_0}} \\ z &= \frac{c^{*}}{N'}\sqrt{\frac{M_{22}{}'}{B_0}} \end{aligned} \tag{64}$$

Hence the intensity of a Bragg rod can also be measured. Note that $L^{-1} = 0$ for $\alpha' = \pi/2$; this is the case when the scan runs along the top of the rod, in which case an infinite area is measured.

1.2f The Lorentzian

The final situation that needs investigating is the case when the intrinsic peak shape is a Lorentzian along one direction. This is caused when the coherence between layers along a particular direction decays exponentially. Suppose that the Lorentzian lies at an angle β to the nominal spectrometer position κ_o. Making the same transformations as in Section *II-1.2e*, we can write the Lorentzian as

$$\frac{\Gamma I}{\pi}\frac{\delta\left(q_x{}' - t_x{}'\right)}{\Gamma^{2} + \left(q_y{}' - t_y{}'\right)^{2}} \tag{65}$$

where Γ is the half-width at half-maximum of the Lorentzian. Following the usual method, this gives

$$\mathrm{C}(\mathrm{t}') = \frac{NI}{\pi}\exp\left[-\tfrac{1}{2}M_{11}{}' t^{2}\cos^{2}\alpha'\right]\mathrm{u}(\mathrm{t}') \tag{66}$$

for the count rate, where

$$\mathrm{u}(\mathrm{t}') = \int \frac{\Gamma}{\Gamma^2 + {q_y}'^2} \exp\left[-{M_{12}}' t \cos\alpha' \left({q_y}' + t\sin\alpha'\right) - \tfrac{1}{2}{M_{22}}'\left({q_y}' + t\sin\alpha'\right)^2\right] d{q_y}' \tag{67}$$

It can be shown that

$$\begin{aligned} L^{-1} &= \frac{\pi}{N'}\sqrt{\frac{a(\alpha)}{B_0}}\frac{1}{U(\alpha)} \\ z &= \frac{\pi}{N'}\sqrt{\frac{2\pi}{B_0}}\frac{1}{u(\mathbf{0})} \end{aligned} \tag{68}$$

where

$$\begin{aligned} U(\alpha) &= \int \frac{\Gamma}{\Gamma^2 + {q_y}'^2} \exp\left\{-\frac{M_{11}M_{22} - {M_{12}}^2}{2a(\alpha)}{q_y}'^2\right\} d{q_y}' \\ a(\alpha) &= M_{11}\cos^2\alpha + 2M_{12}\cos\alpha\sin\alpha + M_{22}\sin^2\alpha \end{aligned} \tag{69}$$

The two dimensionless integrals u(t) and U(α) can not be solved analytically, but contain smooth integrands and are easily solved by numerical methods.

It can be seen that the cases for a delta-function Bragg peak, Section *II-1.2c*, and the Bragg rod, Section *II-1.2e*, are the limiting forms of Equation (69) when $\Gamma \rightarrow 0$ and $\Gamma \rightarrow \infty$, respectively.

2. Literature review

In Section *I-4*, I gave a brief overview of the various experimental techniques that have been used to investigate $PrBa_2Cu_3O_{6+x}$. Here I shall give a more detailed account of previous studies of the magnetic ordering, explaining how the measurements I present here complement or supersede them.

2.1 Copper magnetic ordering

Quite soon after the discovery of superconducting $YBa_2Cu_3O_{6+x}$, it became apparent that the Cu-O_2 planes, when not superconducting, contained anti-ferromagnetically ordered Cu moments. Those early studies[40] established several details of the Cu(2) moment ordering which were to become almost universal features of the non-superconducting Cu-O_2 planes of $RBa_2Cu_3O_{6+x}$ samples.

Firstly, the Néel temperatures for the antiferromagnetic ordering were very high, generally around room temperature. Secondly, the reflections were measured at $(h + {}^1/_2, k + {}^1/_2, l)$, h, k, l being integers, and $l \neq 0$. Thirdly, the ordered Cu(2) moment was found to be ~ 0.5 μ_B, whereas the predicted magnetic moment for orbitally quenched Cu^{2+} ions is 1 μ_B. Similar effects had previously been observed in the La_2CuO_{4-y}[41], and fuelled speculation that cuprate superconductivity and magnetic interactions were inextricably linked.

Different copper magnetic structures (giving different reflections) occur under different circumstances, and it will be necessary for me to differentiate between them. I have decided that the best way to characterise the different measurements, and so the

---

[40] J.M. Tranquada, D.E. Cox, W. Kunnmann, H. Moudden, G. Shirane, M. Suenaga, P. Zolliker, D. Vaknin, S.K. Sinha, M.S. Alvarez, A.J. Jacobson, and D.C. Johnston, *Neutron-diffraction determination of antiferromagnetic structure of Cu ions in* $YBa_2Cu_3O_{6+x}$ *with* $x = 0.0$ *and* 0.15, Phys. Rev. Lett. **60**, 156-159, (1988); W-H. Li, J.W. Lynn, H.A. Mook, B.C. Sales, and Z. Fisk, *Long-range antiferromagnetic order of the Cu in oxygen-deficient* $RBa_2Cu_3O_{6+x}$, Phys. Rev. B **37**, 9844-9847, (1988).

[41] D. Vaknin, S.K. Sinha, D.E. Moncton, D.C. Johnston, J.M. Newsam, C.R. Safinya, and H.E. King, Jr., *Antiferromagnetism in* La_2CuO_{4-y}, Phys. Rev. Lett. **58**, 2802-2805, (1987).

different structures, is by what is actually observed, rather than the interpretation that is put upon them; this is important for some results, where controversy exists over which magnetic ions are actually ordering. Hence the copper ordering described above, as observed, for instance, by Tranquada *et al*[40], shall be referred to as 'type-I', where type-I is defined as a magnetic structure which gives reflections at $(h + {}^1/_2, k + {}^1/_2, l)$, h, k, l being integers, and $l \neq 0$.

The measured intensities were successfully explained by a model in which the Cu(2) moments are ordered antiferromagnetically with respect to their nearest neighbours along all three crystallographic axes (see Figure 13). Because there are two antiferromagnetically coupled planes per chemical unit cell, the magnetic structure has period c along the c-axis, giving reflections at $(h + {}^1/_2, k + {}^1/_2, l)$, h, k, l being integers.

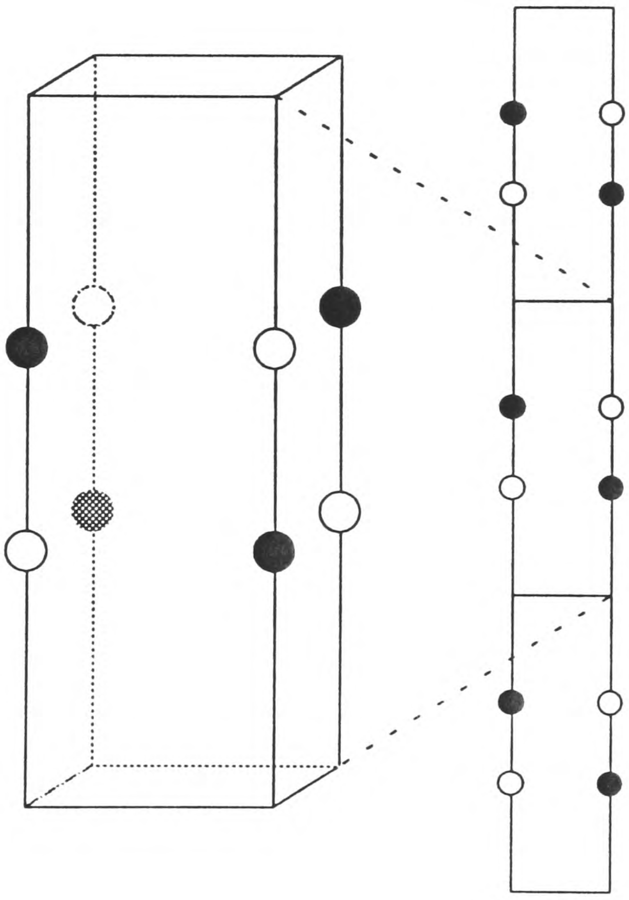

Figure 13: The antiferromagnetic structure of the Cu(2) ions, causing type-I reflections. The moments lie parallel to the *ab*-plane.

Some of the other magnetic structures have period $2c$ along the c-axis, and so it is useful at this point to define a magnetic unit cell which is 2 x 2 x 2 chemical unit cells. Magnetic structure factors and intensities will be calculated with respect to the magnetic unit cell and will therefore be directly comparable, although reflections will always be indexed with respect to the chemical unit cell of Figure 1.

Applying Equation (6) from Section *II-1.1a*, it can be seen that the magnetic structure factor for the structure shown in Figure 13 is

$$F^{\alpha}(\kappa) = 16i\mu^{\alpha}_{Cu(2)} f_{Cu(2)}(\kappa)\sin(2\pi l z) \tag{70}$$

where z is the fractional height of the Cu(2) ion from the basal plane (typically $z \sim 0.35$). From this it can be seen that no reflection is expected for $l = 0$, as experimentally observed.

Soon after these initial findings, further magnetic phases were reported in oxygen deficient RBa$_2$Cu$_3$O$_{6+x}$[42, 43]. As temperature was decreased, the initial type-I ordering occurred at $T_N \sim 400$ K; then, at about 50 K, peaks would start to develop at $(h + {}^1/_2, k + {}^1/_2, l + {}^1/_2)$, h, k, l being integers. As these peaks grew in intensity, so the integer-l peaks fell in intensity and, in some cases, by the lowest temperatures attainable the integer-l peaks would disappear completely.

Similarly to my definition of the type-I phase, I shall define type-II phases as those which have reflections at $(h + {}^1/_2, k + {}^1/_2, l + {}^1/_2)$, h, k, l being integers. Furthermore, 'type-II intermediate' means that the integer-l peaks are still present, whereas 'type-II ground-state' means that the integer-l peaks are absent.

The type-II reflections can be understood in terms of the rotation of alternating pairs of Cu(2) moments in opposite directions (see Figure 14). Each Cu(2) moment has, along the c-direction, two neighbours - one in the same chemical unit cell, which is near, and one in the next chemical unit cell, which is far. Within a chemical unit cell, the coupling of the 'near' pair always remains antiferromagnetic. In the type-I phase, the coupling of the 'far' pair (coupled across two chemical unit cells) is also antiferromagnetic. However, as temperature is decreased, the moments of the 'far'

---

[42] H. Kadowaki, M. Nishi, Y. Yamada, H. Takeya, H. Takei, S.M. Shapiro, and G. Shirane, *Successive magnetic phase transitions in tetragonal YBa$_2$Cu$_3$O$_{6+x}$*, Phys. Rev. B **37**, 7932-7935, (1988).

[43] J.W. Lynn, W.-H. Li, H.A. Mook, B.C. Sales, and Z. Fisk, *Nature of the magnetic order of Cu in oxygen-deficient NdBa$_2$Cu$_3$O$_{6+x}$*, Phys. Rev. Lett. **60**, 2781-2784, (1988).

pair gradually rotate an amount ϕ in opposite directions - this produces the non-collinear ordering responsible for the reflections seen in the type-II intermediate phase. When their rotation is complete, at ϕ = 90°, the 'far' pair is ferromagnetically coupled, and the type-II ground-state has been reached.

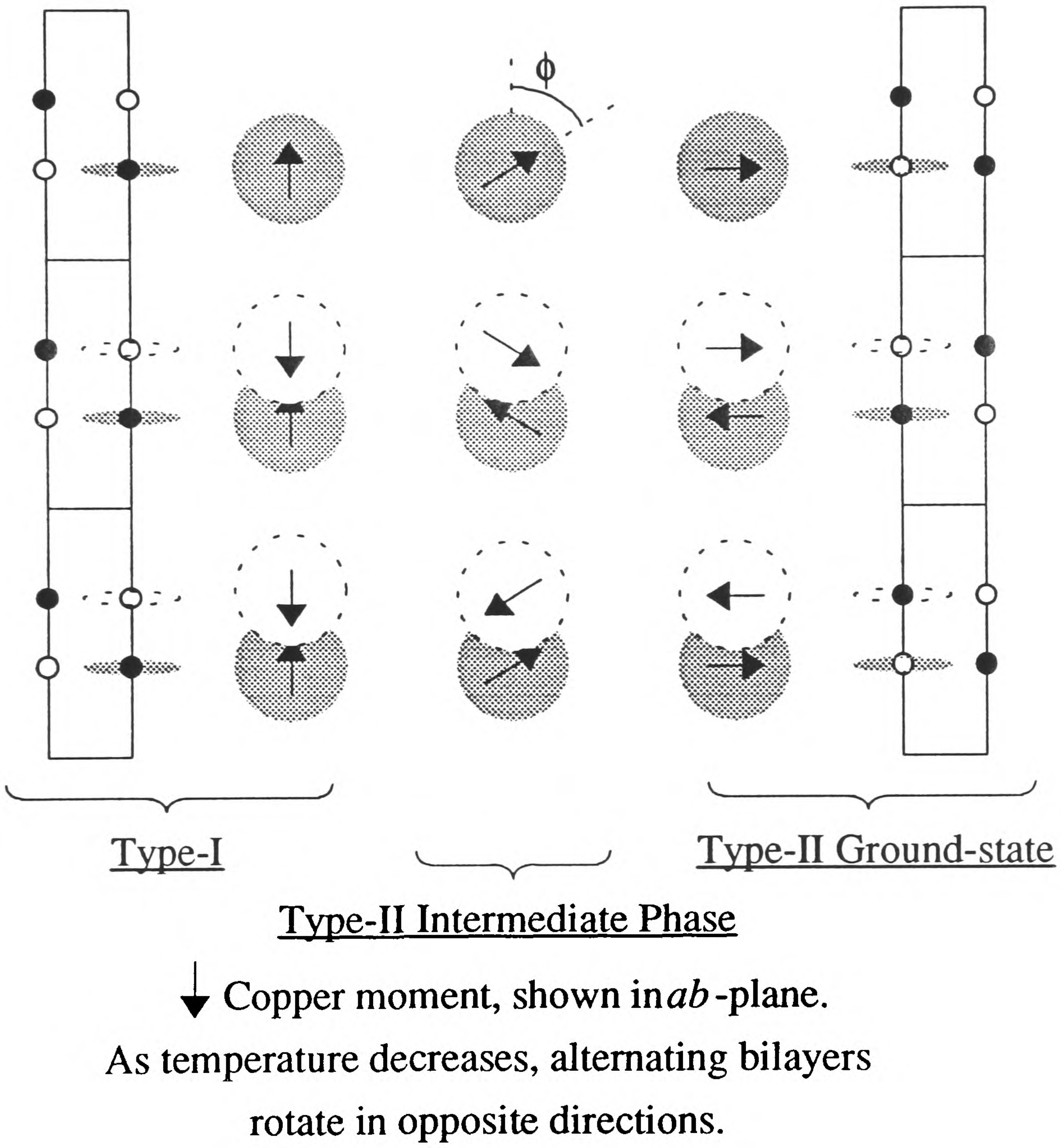

Figure 14: The transition from Cu type-I ordering to the type-II ground-state, via the type-II intermediate phase. The rotation of the moments shows the change in the coupling along *c* across two chemical unit cells. The coupling within a Cu-O_2 plane is always antiferromagnetic. The moments lie parallel to the *ab*-plane.

Both Kadowaki *et al*[42] and Lynn *et al*[43] independently concluded that this rotation was the cause of the type-II reflections they observed. From this, they also both deduced that the cause of the change in the coupling of the 'far' pair was the presence of an ordered copper moment on the Cu(1) site (see Figure 15).

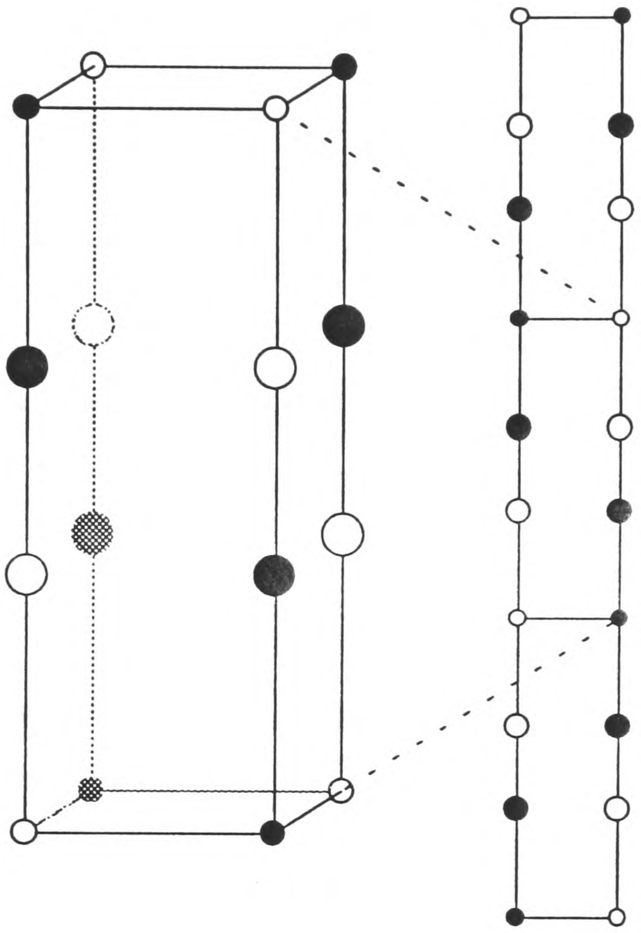

Figure 15: The Cu type-II ground state, showing the case when the Cu(1) moments are ordered and coupled ferromagnetically to their adjacent Cu(2) moments.

It is the presence and coupling of a Cu(1) moment which has caused the controversy to which I referred earlier. Kadowaki *et al* measured magnetic moments in their $YBa_2Cu_3O_{6+x}$ sample of $\mu_{Cu(2)} = (0.50\pm0.07)\mu_B$ and $\mu_{Cu(1)} = (0.012\pm0.007)\mu_B$, with the Cu(1) moments favouring *ferromagnetic* coupling along *c*. Lynn *et al*, on the other hand, measured moments of $\mu_{Cu(2)} = (0.81\pm0.08)\mu_B$ and $\mu_{Cu(1)} = (0.35\pm0.06)\mu_B$ in their $NdBa_2Cu_3O_{6+x}$ samples, with the Cu(1) moments favouring *antiferromagnetic* coupling along *c*. This was a higher moment than had ever been seen before on the Cu(2) ions.

To make matters worse, NMR and NQR measurements by Lütgemeier[44] showed that, in his samples of $YBa_2Cu_3O_{6+x}$ and $PrBa_2Cu_3O_{6+x}$, *no* ordered magnetic moment occurred at the Cu(1) site, at least down to 1.2 K.

It is important at this point to note that the existence of type-II ordering does not necessarily indicate the presence of a Cu(1) moment. The same types of reflections will be caused by the rotations of Figure 14 whether or not the Cu(1) moment is ordered. Traditionally, the occurrence of $(h + {}^1/_2, k + {}^1/_2, l + {}^1/_2)$ reflections has been called 'chain ordering' - I feel that this is a mistake, since it implies that the Cu(1) moment must be ordered. It is for this reason that I have named the different phases according to what is observed, rather than on a particular interpretation of the observations.

I shall now discuss measurements made specifically on the $PrBa_2Cu_3O_{6+x}$ compounds. Table 6 shows the observed ordering temperatures for the different magnetic phases of $PrBa_2Cu_3O_{6+x}$, for different values of x. These are shown graphically in Figure 16.

A number of things should be noted. First, although there is perhaps a slight drop in T_N for the type-I phase with x, there is a spread of about 50 K for the same x. This could indicate differences in sample purity. Second, the oxygen contents determined by Rosov *et al*[49] seem questionable, being estimated by susceptibility measurements ($x_1 = 0.2$), the amount of twinning ($x_2 = 0.65$), the mass-change on a further annealing ($x_3 = 0.65+0.02$), and the ordering temperatures themselves ($x_1 < x_4 < x_2$, i.e. $0.2 < x_4 < 0.65$). Such tortuous and unreliable deductions are curious, given that a four-circle neutron diffraction experiment can determine unambiguously the oxygen content.

---

[44] H. Lutgemeier, *NMR and NQR investigation of the magnetic order of Cu in the 123 compounds $REBa_2Cu_3O_y$*, JMMM **90**, 633-634, (1990).

Table 6: Reported Néel temperatures (K) of the type-I, type-II intermediate, and type-II ground-state phases for $PrBa_2Cu_3O_{6+x}$.

Year	x	Type-I	Type-II int.	Type-II g.s.	Method
1988	0.9	325			1% and 10% Fe Mössbauer[45]
1989	0	350			10% Fe
	1	325			Mössbauer[46]
1990	0	325			powder μSR[47]
	1	285			
1990	1	280			powder Cu NMR[48]
1992	0.2?			370	single-crystal
	0.65?	370	160		neutron diffraction[49]
	0.65? + 0.02	404	180		
	0.2?<x<0.65?	370	278		

---

[45] I. Nowik, M. Kowitt, I. Felner, and E.R. Bauminger, *Magnetic order and superconductivity in* $RBa_2Cu_3O_z$, Phys. Rev. B **38**, 6677-6682, (1988).

[46] I. Felner, U. Yaron, I. Nowik, E.R. Bauminger, Y. Wolfus, E.R. Yacoby, G. Hilscher, and N. Pillmayr, *Magnetic order and superconductivity in* $Y_{1-x}Pr_xBa_2Cu_3O_7$, Phys. Rev. B **40**, 6739-6744, (1989).

[47] D.W. Cooke, R.S. Kwok, M.S. Jahan, R.L. Lichti, T.R. Adams, C. Boekama, W.K. Dawson, A. Kebede, J. Schwegler, J.E. Crow, and T. Mihalisin, *Magnetic ordering in* $(Y_{1-x}Pr_x)Ba_2Cu_3O_7$ *as evidenced by muon spin relaxation*, J. Appl. Phys. **67**, 5061-5063, (1990).

[48] A.P. Reyes, D.E. MacLaughlin, M. Takigawa, P.C. Hammel, R.H. Heffner, J.D. Thompson, J.E. Crow, A. Kebede, T. Mihalisin, and J. Schwegler, *Observation of Cu NMR in antiferromagnetic* $PrBa_2Cu_3O_7$*: evidence for hole-band filling*, Phys. Rev. B **42**, 2688-2691, (1990).

[49] N. Rosov, J.W. Lynn, G. Cao, J.W. O'Reilly, P. Pernambuco-Wise, J.E. Crow, *Magnetic ordering of the Cu spins in* $PrBa_2Cu_3O_{6+x}$, Physica C **204**, 171-178, (1992).

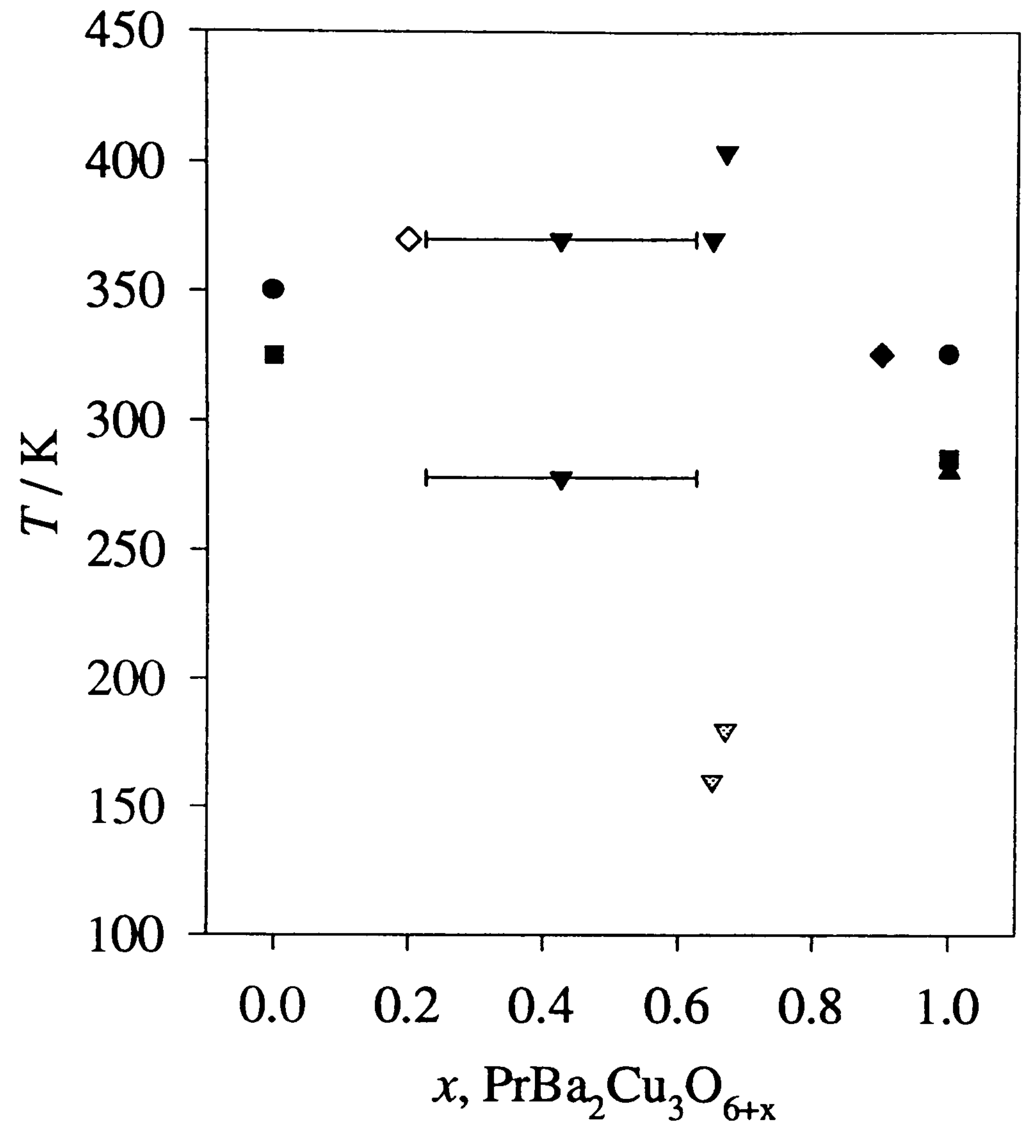

Figure 16: Ordering temperatures for type-I (filled symbols), type-II intermediate (grey symbols) and type-II ground-state (open symbols).

Third, in almost all experiments on RBa$_2$Cu$_3$O$_{6+x}$ compounds, when the copper magnetism changes it does so in the sequence *paramagnetic → type-I → type-II intermediate → type-II ground-state* as temperature decreases. The $x_l = 0.2$ crystal of Rosov *et al*[49] is unique in that they observe the direct transition *paramagnetic → type-II ground-state.* Given that this paper is the only previous neutron-diffraction determination of the copper magnetic ordering in PrBa$_2$Cu$_3$O$_{6+x}$, and that it has curious observations, the work presented in this thesis is clearly important.

Interesting features also exist concerning the sizes of the Cu moments present; here, though, there is even less previous data, since some methods can say whether or not a moment is ordered, but can give no accurate details of its size.

Table 7: Reported ordered moments, and sizes (μ_B) where available, of the Cu(2) and Cu(1) ions for $PrBa_2Cu_3O_{6+x}$.

Year	x	Cu(2)	Cu(1)	Method
1988	0.9	√	-	1% & 10% Fe Mössbauer[45]
1989	0, 1	√	-	10% Fe Mössbauer[46]
1990	0.3, 1	√	0	powder Cu NMR, NQR[44]
1990	0	√	√	powder μSR[47]
	1	√	0	
1990	1	~ 0.5	0	powder Cu NMR[48]
1992	0.2?	?	?	single-crystal neutron diffraction[49]
	0.65?	0.55(10), 300 K		
		0.7, 20 K	0.10, 20 K	
	0.65? + 0.02	0.55(10), 300 K		
		?, low T	?, low T	
	$0.2<x<0.65$?	?	?	

The work of Rosov *et al*[49] is the only paper that attempts a thorough investigation of moment size. However, it again has some curious points: no tables, or details of χ^2, are given to allow the reader to compare experiment with model - this is most unusual for a magnetic diffraction experiment. For some oxygen contents, no details of the magnetic moments are given at all. No details are given as to how the magnetic form-factors were calculated - this was demonstrated to be very important in Section *II-1.1b*; however, J.W. Lynn, the paper's second author, generally used the now discredited method of extracting form-factors measured in K_2CuO_4[50]. Finally, until then, all the Cu moments had been universally found to lie parallel to the *ab*-plane. However, in the $x_2 = 0.65$ crystal at 20 K, the Cu(1) moment is found to have

---

[50] See, for example, W-H. Li, J.W. Lynn, Z. Fisk, *Magnetic order of the Cu planes and chains in* $RBa_2Cu_3O_{6+x}$, Phys. Rev. B **41**, 4098-4111, (1990).

components $0.05\mu_B$ parallel to the *ab*-plane and $0.09\mu_B$ parallel to the *c*-axis. Clearly a careful study is required.

Hence there is no consensus on the ordering temperatures and the sizes and coupling of the magnetic moments. It is perhaps worth mentioning at this point that, until recently, it has been quite difficult to grow high-purity single crystals of a sufficient size to allow magnetic neutron diffraction measurements. The standard method was to grow the crystals in crucibles made of alumina, which aided the growth of large crystals; it was not clear whether the alumina was acting as a catalyst, or whether it was chemically changing the crystals produced. Our samples grown in such a way have been investigated for sample impurity, with the result that we can definitively say that Al ions do dope into the crystals produced; obviously this will affect the results measured, potentially in terms of the ordering temperatures and the coupling and the magnitudes of the magnetic moments.

This effect has already been investigated in $YBa_2Cu_3O_{6+x}$, where it has been discovered that pure (i.e. aluminium-free) crystals do not exhibit the type-II phases[51]. The measurements presented here are the first on demonstrably pure $PrBa_2Cu_3O_{6+x}$ crystals, and also the first on properly characterised Al-doped crystals.

---

[51] H. Casalta, P. Schleger, E. Brecht, W. Montfrooij, N.H. Andersen, B. Lebech, W.W. Schmahl, H. Fuess, Ruixing Liang, W.N. Hardy, and Th. Wolf, *Absence of a second antiferromagnetic transtition in pure $YBa_2Cu_3O_{6+x}$*, Phys. Rev. B **50**, 9688-9691, (1994).

2.2 Praseodymium magnetic ordering

The Néel temperatures for the Pr ordering are much more well-defined experimentally than for its counterpart in Cu ordering: reported values are $T_N = 17$ K for oxygenated samples ($x = 1$)[52,53,46], and $T_N = 10.5$ K for reduced samples ($x = 0$)[54]. The reason for this better agreement between different authors is probably that, at the Pr ordering temperatures, methods measuring the specific heat and magnetic susceptibility can be performed using powders; and powders can be made to high purity and easily oxygenated or reduced. At the much higher Cu ordering temperatures, on the other hand, these experiments become more difficult, and methods such as neutron diffraction and Mössbauer spectroscopy become necessary, with more stringent demands on their samples.

However, when it comes to measuring the ordered moment, elastic neutron scattering, preferably on a single-crystal, is always the method of choice. Very little work has previously been performed on measuring the Pr moment and determining its direction. For the case of $x = 1$, powder neutron-diffraction[53] has shown that the Pr moments order antiferromagnetically along all three crystallographic directions, giving reflections at $(h + {}^1/_2, k + {}^1/_2, l + {}^1/_2)$, h, k, l being integers. The size of the Pr moment is (0.74 ± 0.08) μ_B, with the moment direction 'tentatively' assigned to the c-axis (see Figure 17). However, it must be pointed out that this result is based on just two reflections, the $({}^1/_2, {}^1/_2, {}^1/_2)$ and the $({}^1/_2, {}^1/_2, {}^3/_2)$.

---

[52] A. Kebede, C.S. Jee, J. Schwegler, J.E. Crow, T. Mihalisin, G.H. Myer, R.E. Salomon, P. Schlottmann, M.V. Kuric, S.H. Bloom, and R.P. Guertin, *Magnetic ordering and superconductivity in* $Y_{1-x}Pr_xBa_2Cu_3O_{7-y}$, Phys. Rev. B **40**, 4453-4462, (1989).

[53] W-H. Li, J.W. Lynn, S. Skanthakumar, T.W. Clinton, A. Kebede, C.-S. Jee, J.E. Crow, and T. Mihalisin, Phys. Rev. B **40**, 5300-5303, (1989).

[54] A. Kebede, J.P. Rodriquez, I. Perez, T. Mihalisin, G. Myer, J.E. Crow, P.P. Wise, and P. Schlottmann, *Magnetic and thermodynamic properties of nonsuperconducting* $(Y,Pr)Ba_2Cu_3O_6$, J. Appl. Phys. **69**, 5376-5378, (1991).

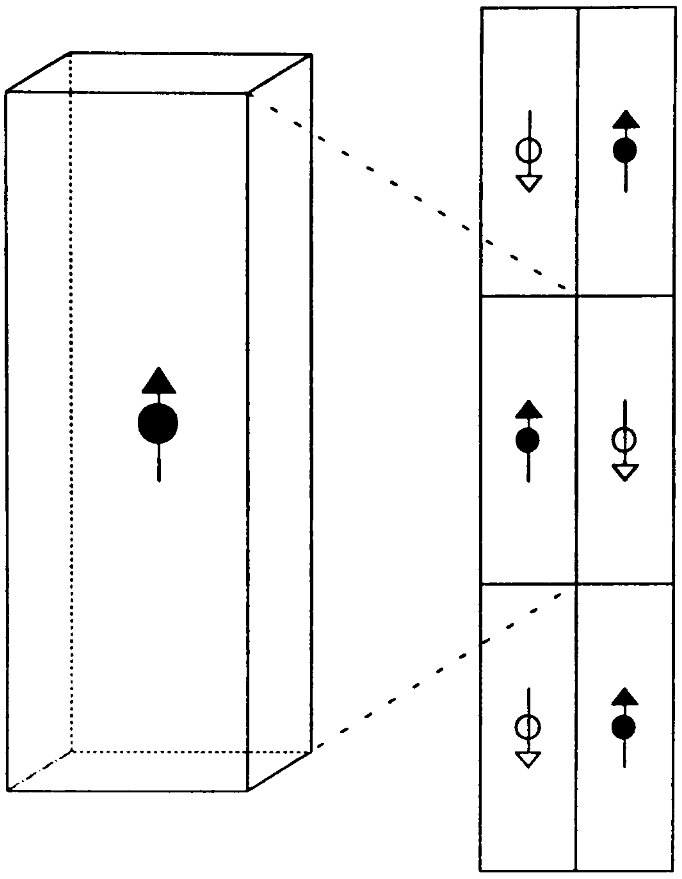

Figure 17: Pr ordering, with the coupling antiferromagnetic along all three axes and moment direction parallel to the *c*-axis, as reported by Li *et al*[53] for $x = 1$.

A similar result has been observed for the case of $x = 0$, again using powder neutron-scattering[55]. The Pr moments order antiferromagnetically along all three crystallographic directions, and the size of the Pr moment is reported to be (1.9 ± 0.2) μ_B. However, the fit is not able to distinguish between moments parallel to the *c*-axis and moments perpendicular to the *c*-axis, again due to the relatively few peaks that were measurable. The peaks were observed to be broadened, indicating a correlation length along the *c*-axis of (10 ± 1) Å.

No single crystal elastic scattering measurements have been performed, and hence the moment direction has not been properly determined by neutron scattering. The result of Li *et al*[53] must be viewed cautiously, as any deviation of the Pr magnetic form factor from that predicted by the dipole approximation may not be recognised with just two magnetic reflections. Our data, using 11 different reflections from a

---

[55] M. Guillaume, P. Fischer, B. Roessli, A. Podlesnyak, J. Schefer, and A. Furrer, *Magnetic order of Pr ions in related perovskite-type Pr123 compounds*, J. Appl. Phys. **75**, 6331-6333, (1994).

single crystal, show unambiguously that the Pr moment is orientated significantly away from the *c*-axis, and that the Pr form factor is distorted from the dipole approximation.

Although a Pr moment direction away from the *c*-axis has not been seen previously in the literature of neutron diffraction, which is where you might expect such a discovery, it has been observed by Mössbauer spectroscopy[56]. Here, in polycrystalline samples, the moment was observed to be at an angle of $\theta \sim 65°$.

In view of the many ambiguities and discrepancies found in earlier investigations of $PrBa_2Cu_3O_{6+x}$, the present work on single crystals, with its emphasis on detailed sample characterisation and thorough data analysis procedures, must be regarded as providing the most reliable account of magnetic ordering phenomena in $PrBa_2Cu_3O_{6+x}$ to date.

---

[56] J.A. Hodges, G. le Bras, P. Bonville, P. Imbert, G. Jéhanno, *Magnetic correlations in* $Pr_{1-x}Y_xBa_2Cu_3O_7$ *studied by Mössbauer spectroscopy on substituted* $^{170}Y^{3+}$, Physica C **218**, 283-294, (1993).

3. Measurements

In this section I present the results of neutron scattering experiments on both pure (i.e. aluminium-free) single-crystals of $PrBa_2Cu_3O_{6+x}$, and properly characterised Al-contaminated crystals. No such measurements have ever been previously published[57]. The pure crystals were grown by Dr. T. Wolf (University of Karlsruhe), and the Al-contaminated crystals were grown by Chen Changkang and Hu Yongle (Clarendon Laboratory).

Historically, our Al-doped crystals were measured before the pure crystals. However, the magnetic features of the pure crystals are less complicated, and so it will be simpler if I present these results first. In all, we measured four crystals: two pure crystals (one oxygenated, one reduced), and two Al-contaminated crystals (one oxygenated, one reduced). The results are discussed in Section *II-3.6*.

3.1 Crystal composition

Two tests were performed to determine the composition of the crystals. Each of the crystals was examined by four-circle neutron diffraction - this was primarily to determine the oxygen content, rather than to perform a precise structural refinement. (X-rays are normally better for the latter, but are relatively insensitive to the light oxygen ions). However, the neutron diffraction could not determine the amount of Al contamination of the Cu(1) site, or any Pr substitution onto the Ba site. This is due to the fact that you can not assume that these sites are fully occupied - hence the diffraction can tell you the mean scattering length of the site, but with two unknowns (the occupancies of both ions) it is not possible to determine both uniquely.

This was overcome by measuring the ratios of the cation constituents by plasma mass spectrometry. Unlike neutron diffraction, this is a destructive technique, and so was not used on all the crystals. Measurements were made on a pure crystal from the

---

[57] A. Longmore, A.T. Boothroyd, Chen Changkang, Hu Yongle, M.P. Nutley, N.H. Andersen, H. Casalta, P. Schleger, and A.N. Christensen, *Magnetic Ordering in* $PrBa_2Cu_{3-y}Al_yO6_{+x}$, submitted to Phys. Rev. B (1995). Measurements on the pure crystals will be submitted at a future date.

same batch as our pure crystals, and also on a fragment (~10 mg) of the Al-contaminated oxygenated crystal.

3.1a Four-circle neutron diffraction

Table 8: Four-circle neutron diffraction results for the oxygenated crystals. For the refinement the lattice parameters 3.873 Å, 3.928 Å, 11.710 Å obtained by H.-D. Jorstarndt *et al*[58] for $PrBa_2Cu_3O_7$ were used. The 'occupancy' of the Cu(1) sites is a weighted average of Cu and any Al contribution. The presence of vacancies on the Cu(1) site has previously been observed[59]. The structure was refined with space group symmetry *Pmmm*.

			z		'Occupancy'	
	x	*y*	Pure	Impure	Pure	Impure
Pr	0.5	0.5	0.5		1	
Ba	0.5	0.5	0.1815(2)	0.1847(2)	1	
Cu(1)	0	0	0		1.04(2)	0.75(1)
Cu(2)	0	0	0.3496(2)	0.3509(1)	1	
O(1)	0	0.5	0		0.89(3)	0.92(1)
O(5)	0.5	0	0			
O(2)	0.5	0	0.3762(6)	0.3702(1)	1	
O(3)	0	0.5	0.3606(1)	0.3689(1)	1	
O(4)	0	0	0.1583(2)	0.1537(2)	1.02(2)	0.91(1)
Total oxygen content					6.92(4)	6.73(1)
$R_w(F)$					5.9%	6.2%

I first discuss the four-circle diffraction results. Although the basal plane of the unit cell in $PrBa_2Cu_3O_7$ is often considered as containing Cu-O chains, i.e. one fully occupied oxygen site (O1) and one totally vacant oxygen site (O5) (see Figure 1), it is

---

[58] H.-D Jorstarndt, U. Walter, J. Harnischmacher, J. Kalenborn, A. Severing, and E. Holland-Moritz, Phys. Rev. B **46**, 14872 (1992).

[59] C.L. Lowe-Ma and T.A. Vanderah, Physica C **201**, 233 (1992).

necessary for imperfect oxidation to allow for different occupancies. Distinguishing between these sites in an untwinned crystal is very difficult, and so for the (orthorhombic) oxygenated crystals I have combined the results of these sites, giving the sum of their occupancies (a number which is therefore expected to be between 0 and 1). Table 8 gives the results for the oxygenated crystals, and Table 9 the results for the reduced crystals.

Table 9: Four-circle neutron diffraction results for the reduced crystals. For the refinement the lattice parameters 3.908 Å, 3.908 Å, 11.844 Å obtained by M.E. López-Morales *et al*[60] for $PrBa_2Cu_3O_6$ were used. The structure was refined with space group symmetry *P4/mmm*.

			z		'Occupancy'	
	x	*y*	Pure	Impure	Pure	Impure
Pr	0.5	0.5	0.5		1	
Ba	0.5	0.5	0.1909(4)	0.1884(3)	1	
Cu(1)	0	0	0		1.04(4)	0.80(3)
Cu(2)	0	0	0.3519(2)	0.3511(2)	1	
O(1)/O(5)	0.5	0	0		0.19(3)	0.28(3)
O(2)/O(3)	0.5	0	0.3696(2)	0.3694(2)	1	
O(4)	0	0	0.1525(4)	0.1520(4)	0.99(4)	0.92(3)
Total oxygen content					6.35(7)	6.40(6)
R_w(F)					6.2%	6.0%

It can be seen that the Al contamination increases the number of vacancies found on the apical oxygen site 0(4). It probably also hinders the removal of oxygen from the crystals.

---

[60] M.E. López-Morales, D. Ríos-Jara, J. Tagüeña, R. Esudero, S. La Placa, A. Bezinge, V.Y. Lee, E.M. Engler, and P.M. Grant, Phys. Rev. B **41**, 6655 (1990).

3.1b Plasma mass spectrometry

The plasma mass spectrometry measurements were performed and analysed in Risø by Dr. Per Solgaard. The results are shown in Table 10. As well as there being Al-contamination on the Cu(1) site in the impure crystal, there is also Pr substitution onto the Ba site and a significant number of Cu-site vacancies. Even the 'pure' crystal has some contamination: Mg, from the Mg crucible, which contaminates the Cu(1) site; and Sr, from the starting material of BaO, which contaminates the Ba site. The Al-contaminated crystals were made with the purer $BaCO_3$.

Table 10: Results of the plasma mass spectrometry on a pure (Al-free) sample from the same batch as our pure oxygenated and reduced crystals, and for a fragment of our contaminated, oxygenated crystal. The data has been normalised so that the total occupation of the Pr and Ba sites is 3; the error in the values is about 1%.

	Pr	Ba	Sr	Cu	Al	Mg
Pure	0.95	1.96	0.09	2.85		0.014
Al-contaminated	1.05	1.95		2.58	0.12	

Hence, ignoring the trace amount of Mg and the contamination of the Ba site, the chemical composition can be written as

$$PrBa_2(Cu_{3-z-v}Al_z)O_{6+x}$$

where v is the number of Cu(1) vacancies, x is the number of O atoms above 6, and z is the Al contamination of the Cu(1) site. Estimates for the values of v, x, and z for the different crystals are given in Table 11. For reasons of readability, in the rest of the thesis the formula will generally be abbreviated to $PrBa_2Cu_3O_{6+x}$.

Table 11: Estimated coefficients for the composition of the $PrBa_2(Cu_{3-z-v}Al_z)O_{6+x}$ crystals studied, compared with the ideal oxygenated and reduced crystals $PrBa_2Cu_3O_7$ and $PrBa_2Cu_3O_6$.

			x	
	v	*z*	oxygenated	reduced
Ideal	0	0	1	0
Pure	0.14	0	0.92	0.35
Contaminated	0.30	0.12	0.73	0.40

I now move on to the results of the neutron diffraction experiments.

3.2 Pure, oxygenated crystal

3.2a The temperature dependence of the different magnetic phases

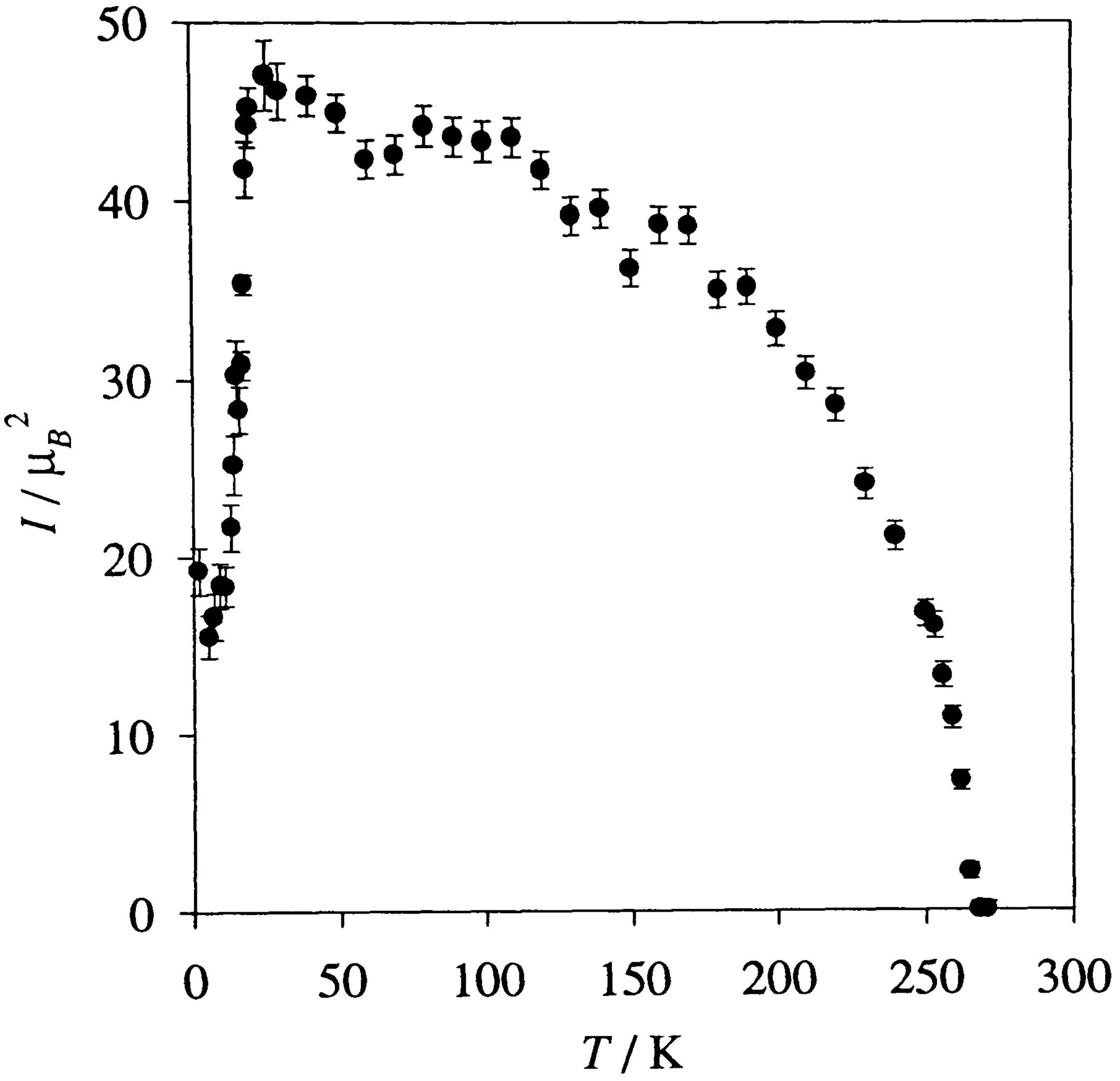

Figure 18: The variation with temperature of the Cu intensity of the ($^1/_2$, $^1/_2$, 2) reflection. The systematic error in the absolute intensity is 20%. (Pure, oxygenated crystal).

This crystal (27 mg) was grown in a magnesium oxide crucible and annealed in oxygen. As temperature is lowered, the first magnetic structure encountered is the Cu type-I phase (see Section *II-2.1* for an explanation of the different types of Cu ordering). The Néel temperature for the type-I phase is $T_{Cu,I}$ = (266 ± 1) K; Figure 18 shows the variation of the Cu contribution to the intensity of the ($^1/_2$, $^1/_2$, 2) peak with temperature. As in all figures and tables, the intensities correspond with calculated intensities as described in Appendix *II-4.5*. Equation (5) defines the calculated intensities, with the magnetic unit cell being 2 x 2 x 2 chemical unit cells. (To give an idea of the scale, for a magnetic moment of one Bohr magneton (perpendicular to κ) per chemical unit cell, with unity form-factor, the structure factor would be 8 μ_B and the intensity 64 μ_B^2).

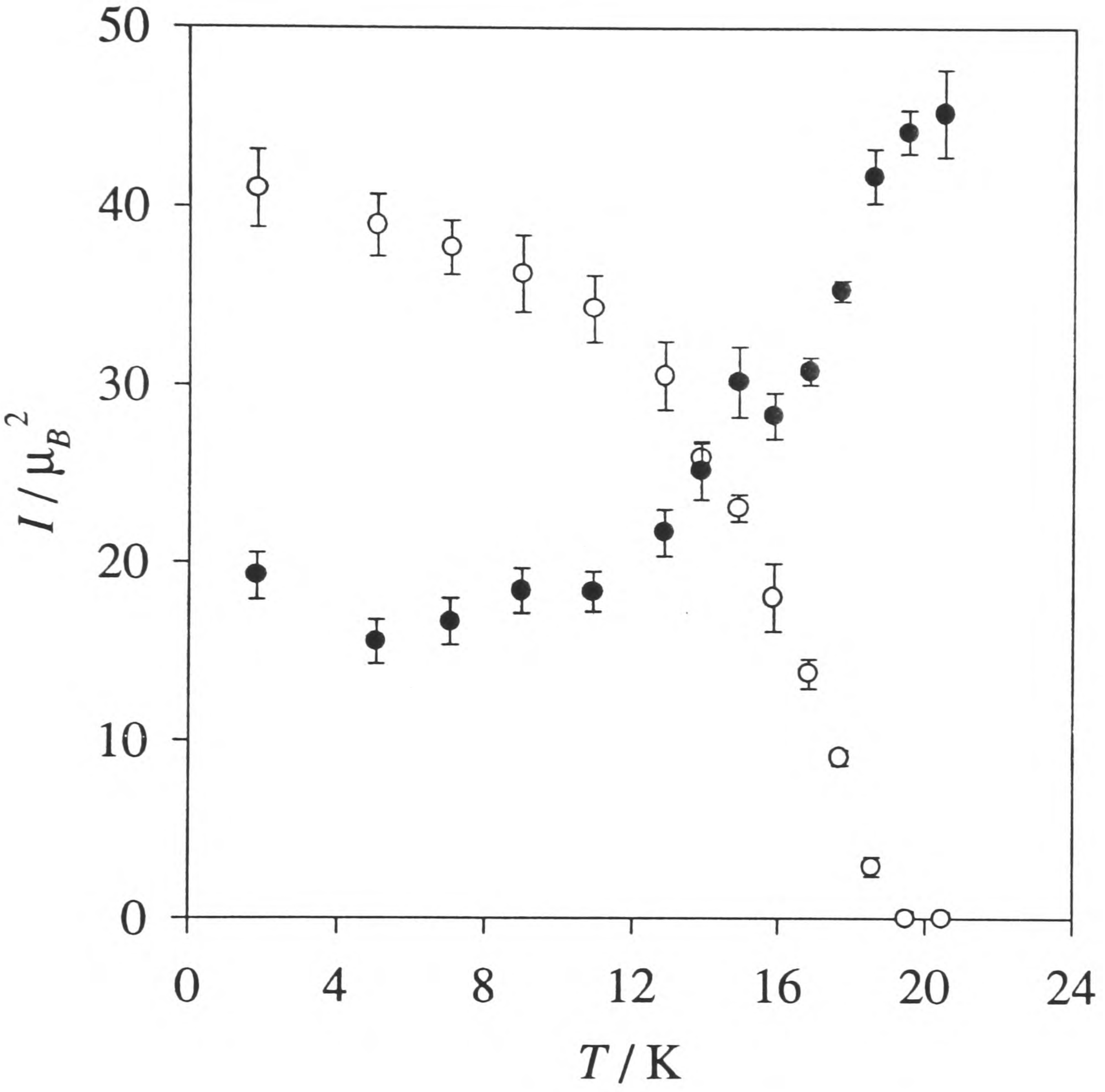

Figure 19: The variation with temperature of the Pr intensity of the ($^1/_2$, $^1/_2$, 0) reflection (open circles) and the Cu intensity of the ($^1/_2$, $^1/_2$, 2) reflection (closed circles). The systematic error in the absolute intensity is 20%. (Pure, oxygenated crystal).

By about 20 K, the Cu(2) moment causing the type-I reflections has become fully ordered. As temperature decreases, these reflections suddenly decrease in intensity. This has not been caused by the onset of a type-II magnetic structure as described in Section *II-2.1*, since there are no reflections at ($h+^1/_2$, $k+^1/_2$, $l+^1/_2$); it has instead been caused by a decrease in the ordered component of the Cu(2) moment, and this coincides with the onset of the Pr ordering. The Néel temperature for the Pr ordering is $T_{Pr} = (19.0 \pm 0.2)$ K (see Figure 19).

The Pr ordering is ferromagnetically coupled along the *c*-axis, and so peaks will occur at $(h+{}^1/_2, k+{}^1/_2, l)$, *h*, *k*, *l* being integers. This means that the reflection at $({}^1/_2, {}^1/_2, 2)$ contains both a Cu contribution and a Pr contribution to the intensity (there is no cross-term in the intensity - see Appendix *II-4.6*); however, because of their different peak shapes, it is possible to separate their individual contributions (as is described in Section *II-3.2d*), and all intensities quoted are for the separated contributions.

3.2b The intrinsic width of the Pr reflections

Figure 20 shows the Pr reflection at $({}^1/_2, {}^1/_2, 0)$, at 1.8 K. The shape is Lorentzian in character, with an intrinsic Lorentzian half-width of $\Gamma = (0.0063 \pm 0.0003)$ Å^{-1} parallel to the $(00l)$-axis (see Section *II-1.2f* for the necessary theory). This corresponds to a correlation length in the Pr ordering of (160 ± 6) Å along the *c*-axis, equivalent to (13.8 ± 0.5) unit cells. For comparison, the resolution is also shown ('resolution' here includes the mosaicity of the sample, as discussed in Section *II-1.2d*).

An interesting feature of the Pr ordering is the variation of Γ with temperature. You might expect that, if it varies at all, Γ would decrease as temperature decreased, since the reduction in thermal disorder would allow a longer correlation length. However, in this crystal we observed the opposite - Γ *increased* (indicating shorter correlation lengths) with decreasing temperature (Figure 21). The intrinsic widths only stop increasing at about 12 K, which is the temperature at which the ordered component of the Pr moment starts to level off (see Figure 19).

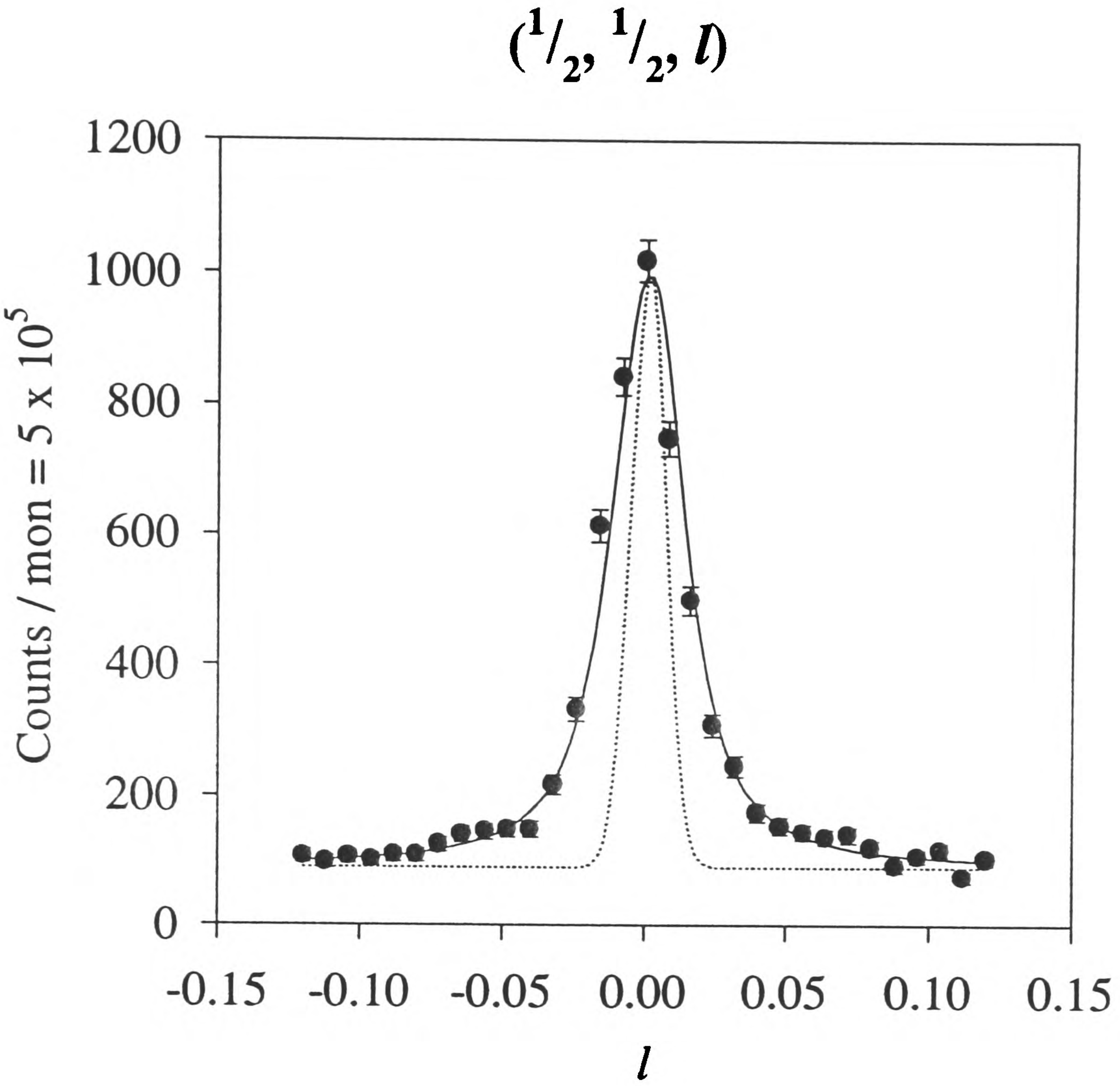

Figure 20: l-scan through the ($^1/_2$, $^1/_2$, 0) peak at 1.8 K. The solid line is the calculation for an intrinsic Lorentzian convoluted with the Gaussian resolution; the intrinsic Lorentzian half-width is $\Gamma = (0.0063 \pm 0.0003)$ Å^{-1}, and the FWHM of the resolution (dotted line) is 0.0144 (0,0,1). A monitor count of 5 x 10^5 takes about 114s. (Pure, oxygenated crystal).

There is also some hysteresis in the value of Γ, since warming the sample to above the Pr ordering temperature and then recooling gave slightly smaller values. The measurement of the intrinsic width becomes more difficult as T_{Pr} is approached, since the observed peaks are smaller and, with Γ decreasing, the resolution increasingly dominates the peak shape.

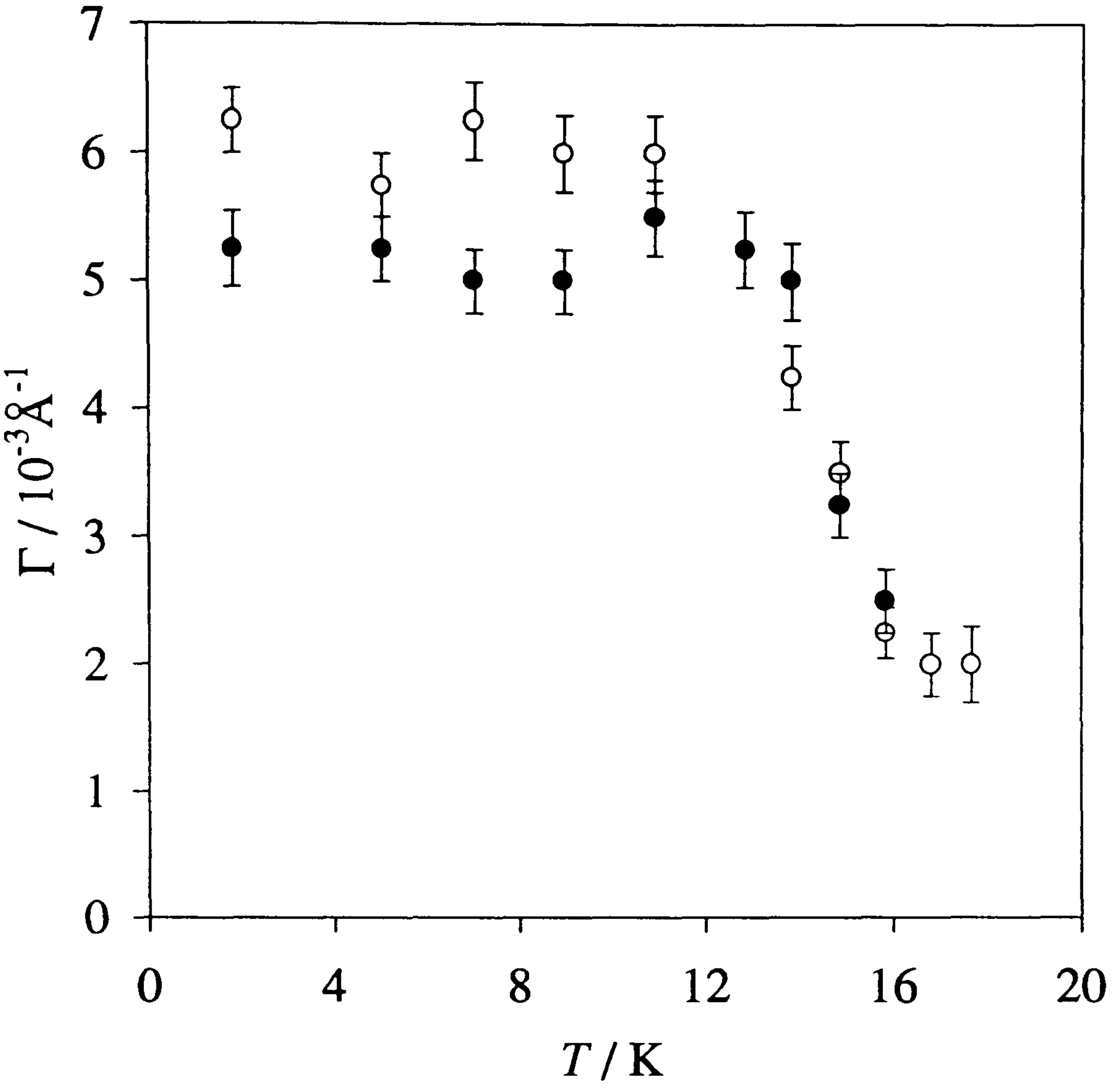

Figure 21: The variation with temperature of the intrinsic Lorentzian half-width Γ. The sample was cooled, and the first set of measurements taken (open circles). After being heated above T_{Pr}, the sample was again cooled and a second set of measurements taken (closed circles). (Pure, oxygenated crystal).

3.2c The Cu type-I phase

Reflections measured above 20 K can be analysed without having to consider the effects of Pr ordering. Table 12 shows the intensities for the Cu ordering measured at 30 K.

Table 12: Observed and fitted intensities for the Cu type-I ordering at 30 K. (Pure, oxygenated crystal).

(h, k, l)	I_{obs} / μ_B^2	I_{fit} / μ_B^2
$^1/_2, ^1/_2, 1$	30.1 ± 1.7	29.0
$^1/_2, ^1/_2, 2$	46.0 ± 1.7	48.3
$^1/_2, ^1/_2, 3$	5.2 ± 0.3	5.3
$^1/_2, ^1/_2, 4$	21.7 ± 1.1	20.8
$^1/_2, ^1/_2, 5$	59 ± 2	56.7
$^1/_2, ^1/_2, 6$	17.6 ± 1.3	17.7
$^1/_2, ^1/_2, 7$	4.5 ± 0.7	5.2
$^3/_2, ^3/_2, 1$	9.3 ± 0.6	9.6
$^3/_2, ^3/_2, 2$	16 ± 2	13.8
$^3/_2, ^3/_2, 3$	1.2 ± 0.7	1.5
		$\chi^2 = 0.8$

The fitting routine worked by minimising χ^2, since this method is best suited for data with different proportional statistical errors. The Cu form factor used in the fit was that calculated assuming a $3d(x^2\text{-}y^2)$ hole wave-function, as discussed in Section *II-1.1b*. The form factor showed a contraction of $\beta = (13 \pm 3)$ %. The Cu(2) moment, after normalising with the observed nuclear reflections, was $\mu_{Cu(2)} = (0.58 \pm 0.08)\ \mu_B$. The Cu(2) moment lies parallel to the *ab*-plane; however, the absolute ϕ-orientation can not be determined by neutron scattering in a twinned crystal. (A measurement of magnetic anisotropy could give some indication, but previous attempts at Risø on $YBa_2Cu_3O_{6+x}$ (unpublished) have failed, presumably because the anisotropy was too strong).

3.2d The separation of the Cu and Pr contributions

Below 20 K, account needs to be taken of the presence of both Cu and Pr contributions to the intensity. The Cu and Pr contributions can be distinguished by their peak shapes: the Cu intensity is a resolution-limited Gaussian, whilst the Pr intensity is a convolution of the Gaussian resolution with an intrinsic Lorentzian along (00*l*), the intrinsic widths of all Pr peaks being the same as that deduced from the ($^1/_2$, $^1/_2$, 0) reflection. The resolution is most favourable for this distinction at the ($^1/_2$, $^1/_2$, 1) and ($^1/_2$, $^1/_2$, 2) reflections.

Because there is a danger that one (or both) of the magnetic structures could be changing below T_{Pr}, I did not initially make assumptions such as keeping the Cu contributions to the intensities of different peaks in the same ratio; rather, I sought to extract as much data as possible just by using the different intrinsic peak shapes for the Cu and Pr contributions. Figure 22 shows the fitted peak shapes for the ($^1/_2$, $^1/_2$, 1) reflection. This procedure demonstrated that the Cu intensities of the ($^1/_2$, $^1/_2$, 1) reflection and the ($^1/_2$, $^1/_2$, 2) reflection stayed in the same ratio as temperature was changed (see Figure 23), which suggests that the ordered Cu(2) moment decreases, but that the structure is independent of temperature.

The same scans also gave me the Pr intensities to the reflections at ($^1/_2$, $^1/_2$, 1) and ($^1/_2$, $^1/_2$, 2). The ($^1/_2$, $^1/_2$, 7) reflection was also followed with temperature - this peak was chosen because the Cu contribution to it was very small, due to the bilayer structure factor (see Appendix *II-4.7*). The small Cu contribution was estimated, since it was then safe to assume that the Cu intensities would stay in the same ratio as temperature was changed. All of the Pr intensities thus extracted are shown in Figure 24.

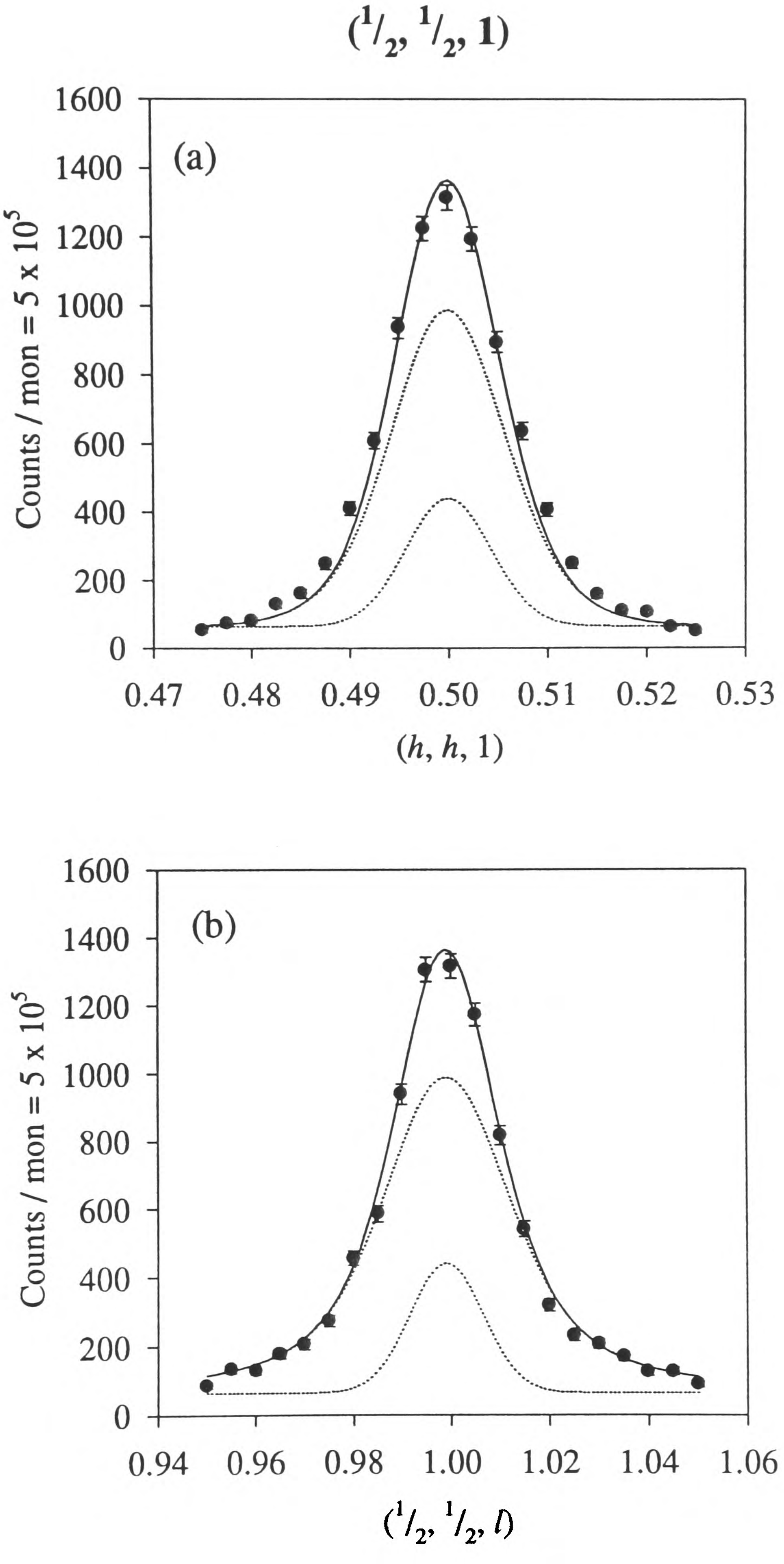

Figure 22: (a) *hh*- and (b) *l*-scan of the ($^1/_2$, $^1/_2$, 1) reflection at 4.2 K. The dotted lines are the contributions from the Cu ordering (amplitude = 380) and the Pr ordering (amplitude = 920); the solid line is the sum of their contributions. A monitor count of 5 x 10^5 takes about 105s. (Pure, oxygenated crystal).

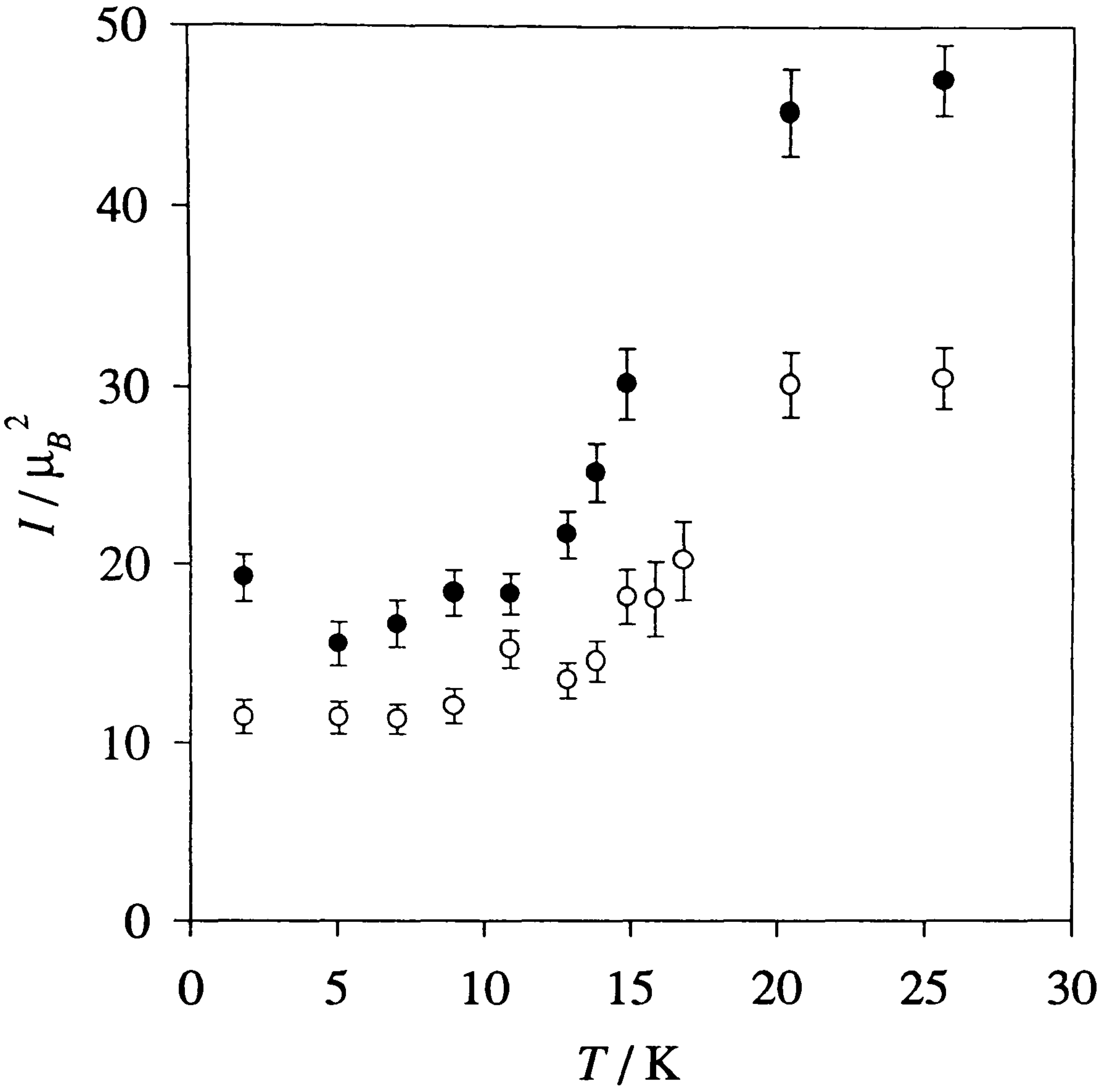

Figure 23: The variation with temperature of the Cu intensities of the ($^1/_2$, $^1/_2$, 1) reflection (open circles) and the ($^1/_2$, $^1/_2$, 2) reflection (closed circles). The systematic error in the absolute intensity is 20%. (Pure, oxygenated crystal).

It is clear that the Pr intensities also remain in the same ratio as temperature is varied, and so the Pr structure is not changing in any way as temperature changes. This then allowed me to calculate the data points which are seen in Figure 19, but not in Figure 23, by using the observed ($^1/_2$, $^1/_2$, 0) Pr intensity to predict the Pr contribution to the ($^1/_2$, $^1/_2$, 2) intensity.

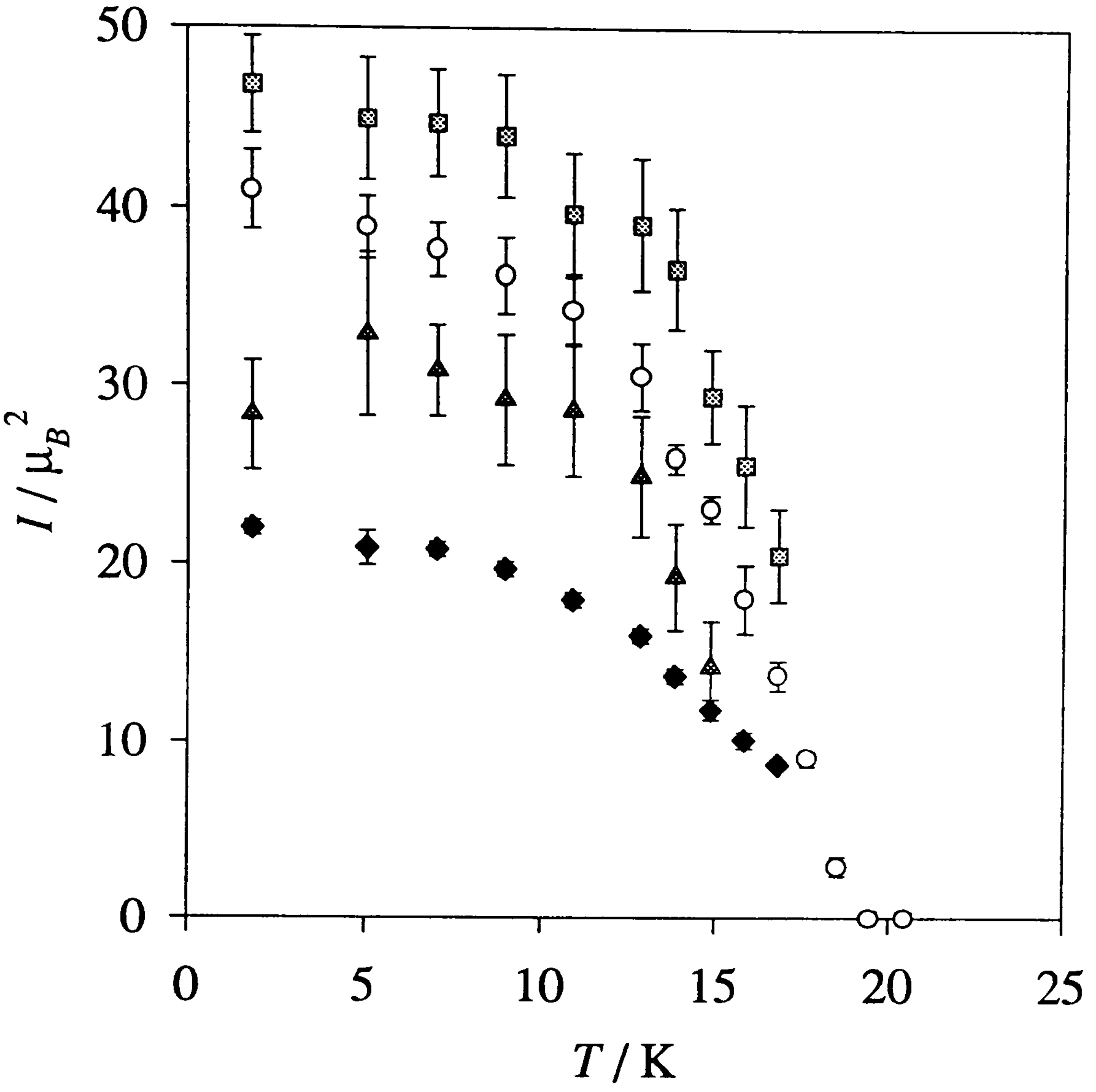

Figure 24: The variation with temperature of the Pr intensities of the ($^1/_2$, $^1/_2$, 0) reflection (open circles), the ($^1/_2$, $^1/_2$, 1) reflection (light grey squares), the ($^1/_2$, $^1/_2$, 2) reflection (dark grey triangles), and the ($^1/_2$, $^1/_2$, 7) reflection (black diamonds). The systematic error in the absolute intensity is 20%. (Pure, oxygenated crystal).

The fact that the Cu intensities at 4.2 K are reduced to a fraction 0.38 ± 0.04 of their intensity at 30 K (see Figure 18) implies that the ordered component of the Cu(2) moment has been reduced from (0.58 ± 0.08) μ_B at 30 K to (0.36 ± 0.05) μ_B at 4.2 K. This figure changes slightly each time the crystal is warmed above T_{Pr} and recooled; in a separate experiment we measured a reduction factor of 0.30 ± 0.05, giving a Cu(2) moment of (0.32 ± 0.05) μ_B at 4.2 K.

3.2e The Pr intensities

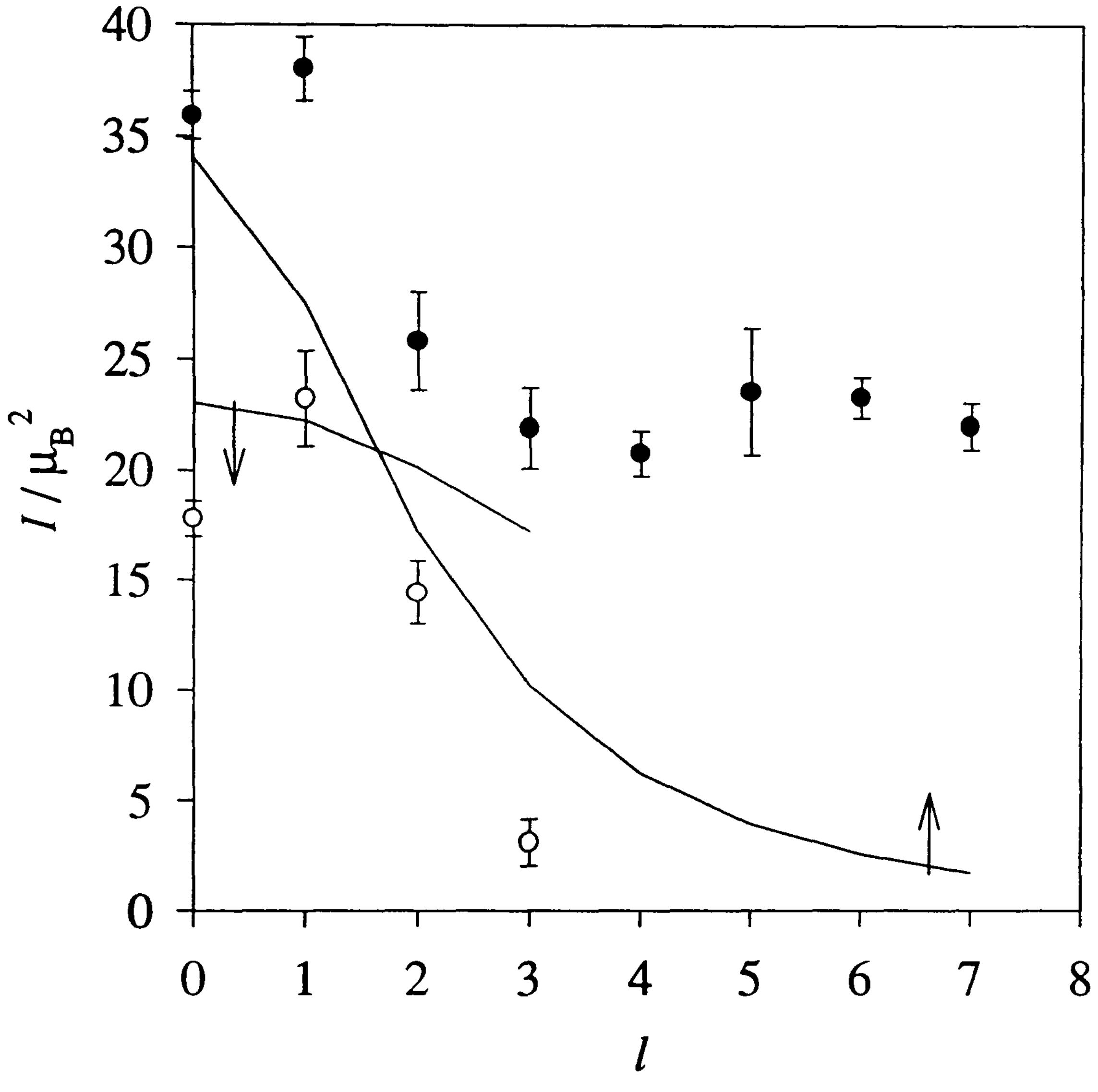

Figure 25: Pr contributions to intensities at 4.2 K. Solid circles correspond to the ($^1/_2$, $^1/_2$, l) series, $l = 0, 1, \ldots, 7$, whilst open circles correspond to the ($^3/_2$, $^3/_2$, l) series, $l = 0, 1, 2, 3$. The lines show the calculated intensities using the dipole approximation for the Pr form factor, with the moments lying parallel to the c-axis: up-arrow for the ($^1/_2$, $^1/_2$, l) series; down-arrow for the ($^3/_2$, $^3/_2$, l) series. The systematic error in the absolute intensity is 20%. (Pure, oxygenated crystal).

It is now possible to determine both the amplitude and the width of the Gaussians of the Cu contributions to all the reflections, by comparing with the measurements made at 30 K and using the extracted ($^1/_2$, $^1/_2$, 1) Cu intensity to determine the drops in intensities. This allows the determination of the intensities of the Pr contributions at all the reflections. These intensities are shown in Figure 25.

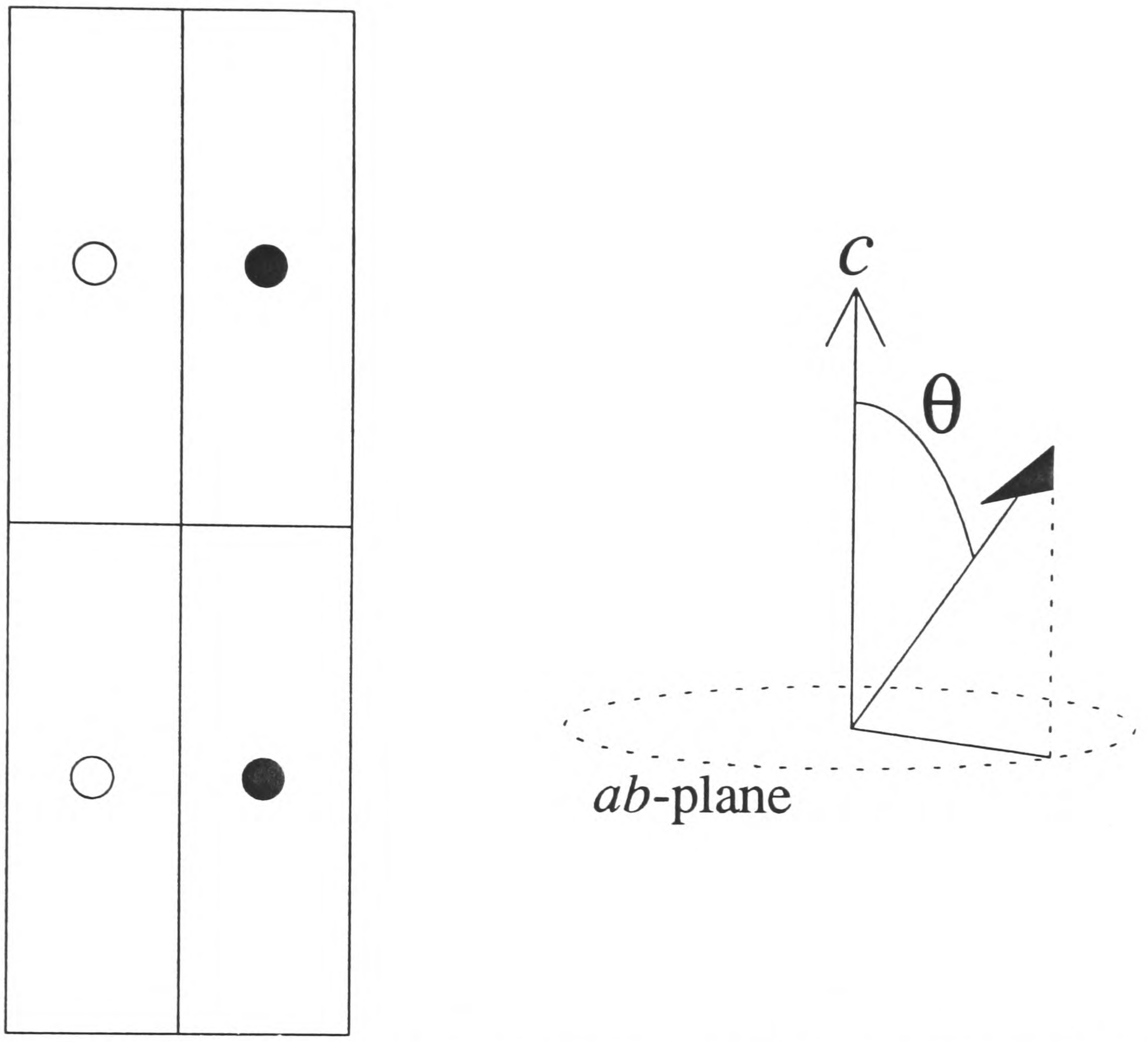

Figure 26: The Pr ordering (pure, oxygenated crystal). The moments exist in a $(^1/_2, ^1/_2, 0)$ magnetic structure, i.e. coupled antiferromagnetically perpendicular to the *c*-axis and ferromagnetically along the *c*-axis, and pointing at an angle θ away from the *c*-axis.

As can be seen, the observed intensities do not follow the calculation very well. The calculation makes two assumptions: that the Pr form factor can be represented by the dipole approximation, and that the Pr moments lie parallel to the *c*-axis. The latter assumption is clearly wrong. The measured Pr intensities are quite high at high values of l; it is the orientation factor which is responsible for the low values of the calculated intensities (the first parentheses in Equation (8)), as the scattering vector κ approaches being parallel to μ_{Pr}. No adjustment to the form factor can be made which would boost the calculated intensities to match the measured ones, and so the Pr moments must be aligned away from the *c*-axis (see Figure 26). Again, the absolute ϕ-

orientation within the *ab*-plane can not be determined; however, the structure must be collinear, since reflections are only observed at integer values of *l*.

Table 13 shows the results of attempting to refine the Pr structure constraining the moments to lie parallel to the *c*-axis, and also allowing the moments to be aligned at an angle θ away from the *c*-axis. The refined parameters for the latter fit are a Pr moment of (0.85 ± 0.12) μ_B, aligned at an angle of θ = (55.9 ± 1.2)°. However, the fit is still not very good, implying that the dipole approximation for the Pr form factor may not be very accurate.

Table 13: Observed and fitted intensities for the Pr ordering at 4.2 K. (Pure, oxygenated crystal).

(h, k, l)	I_{obs} / μ_B^2	$I_{\theta=0°} / \mu_B^2$	$I_{\theta=56°} / \mu_B^2$
½, ½, 0	35.9 ± 1.1	34.1	28.8
½, ½, 1	38.0 ± 1.4	27.5	28.7
½, ½, 2	26 ± 2	17.2	28.0
½, ½, 3	22 ± 2	10.2	26.7
½, ½, 4	20.8 ± 1.0	6.2	24.8
½, ½, 5	24 ± 3	3.9	22.6
½, ½, 6	23.3 ± 0.9	2.6	20.2
½, ½, 7	22.0 ± 1.1	1.7	17.8
3/2, 3/2, 0	17.8 ± 0.8	23.0	19.5
3/2, 3/2, 1	23 ± 2	22.3	19.3
3/2, 3/2, 2	14.4 ± 1.4	20.1	18.8
3/2, 3/2, 3	3.1 ± 1.1	17.2	17.9
		$\chi^2 = 134$	$\chi^2 = 35$

3.2f The effect of a magnetic field

If the Pr form factor is inaccurate, then the refined parameters may be incorrect. One possible way to investigate this is to apply a magnetic field. Since the

Pr moment was supposed to point along the *c*-axis, we applied a B-field perpendicular to this, parallel to the (110)-direction. We then observed the change in the intensity contributions to the ($^1/_2$, $^1/_2$, 0) and ($^1/_2$, $^1/_2$, 1) reflections with magnetic field. A change in the ratio of Pr intensities would indicate a rotation of the Pr moment in θ (as usual, the measurement is insensitive to ϕ due to the domain averaging).

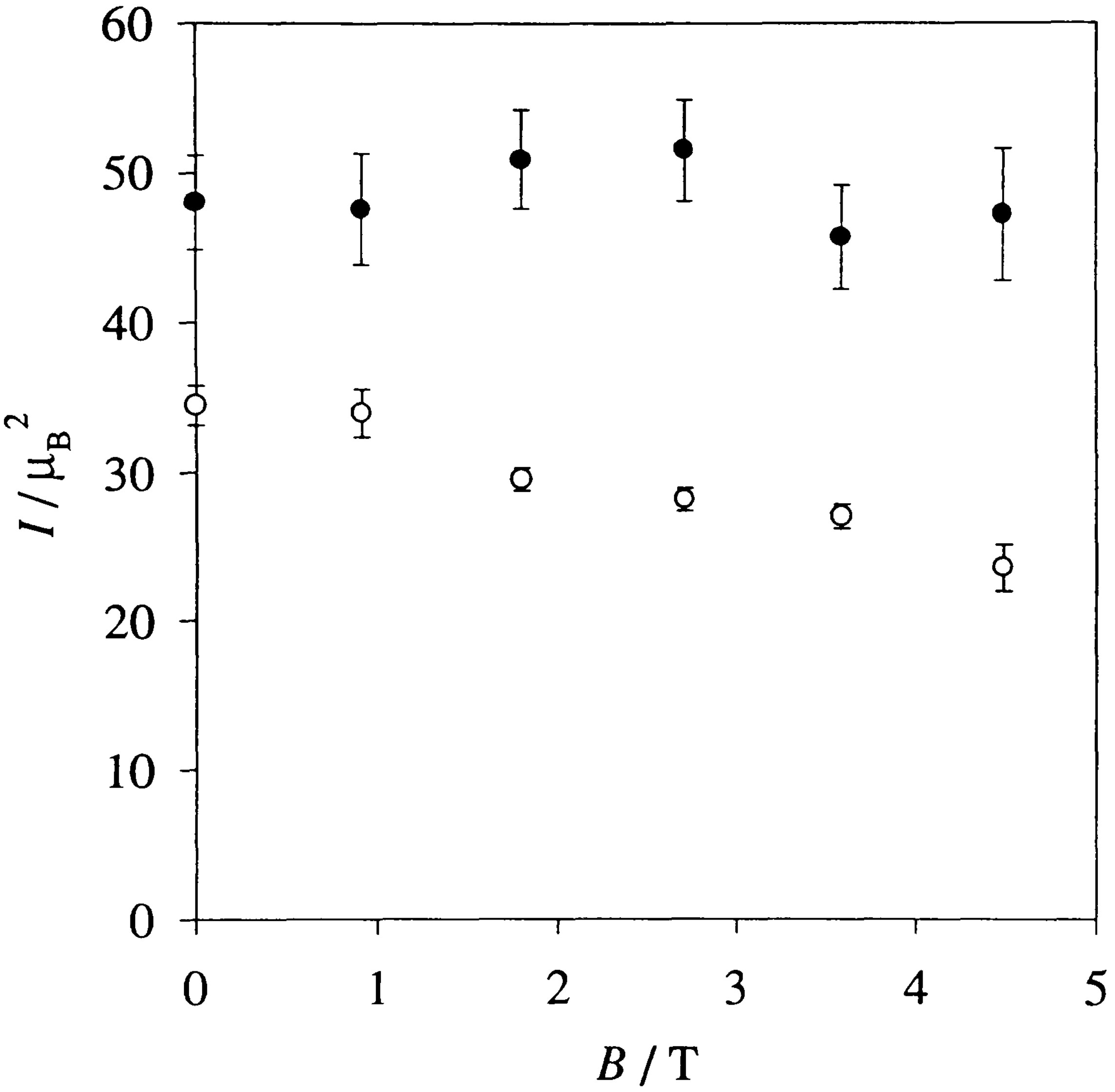

Figure 27: The variation with magnetic field of the Pr intensities of the ($^1/_2$, $^1/_2$, 0) reflection (open circles) and of the ($^1/_2$, $^1/_2$, 1) reflection (closed circles). The systematic error in the absolute intensity is 20%. (Pure, oxygenated crystal).

Figure 27 shows how the measured intensities varied with magnetic field. As can be seen, the ratio of the Pr contributions is clearly changing. The intensity of a collinear ordering is proportional to the 'orientation factor' (see Section *II-1.1a* and Equation (8)). Defining R as the ratio of the relevant orientation factors,

$$\begin{aligned} R &= \frac{1-(\hat{\kappa}.\hat{\mu})^2\Big|^{Pr}_{(\frac{1}{2},\frac{1}{2},1)}}{1-(\hat{\kappa}.\hat{\mu})^2\Big|^{Pr}_{(\frac{1}{2},\frac{1}{2},0)}} \\ &= \frac{\left(I/f^2\right)^{Pr}_{(\frac{1}{2},\frac{1}{2},1)}}{\left(I/f^2\right)^{Pr}_{(\frac{1}{2},\frac{1}{2},0)}} \end{aligned} \qquad (71)$$

it is possible to get an indication of how θ has changed. (This assumes that the Pr moment is relatively free to move in ϕ, and ignores the effects of twinning).

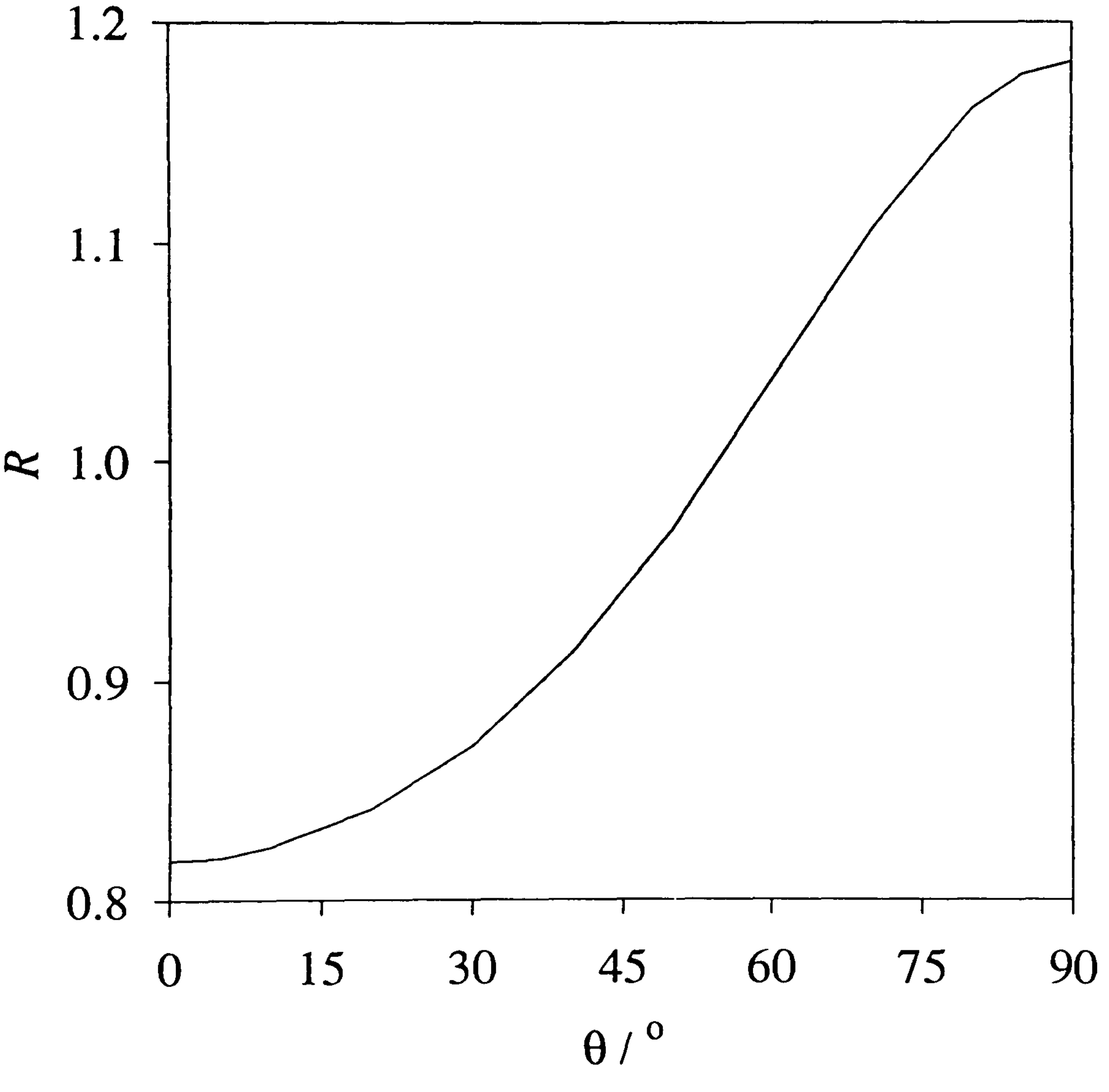

Figure 28: The variation with Pr moment direction, θ, of R, the ratio of the orientation factors of the ($^1/_2$, $^1/_2$, 1) reflection to the ($^1/_2$, $^1/_2$, 0) reflection.

Figure 28 shows how R varies with θ. As θ increases, so does R; this is in agreement with our observations, where the intensity ratio increases with magnetic field as the Pr moment is tilted further away from the c-axis. It is also possible to make a quantitative calculation: the observed proportional increase in R, as magnetic field increases from 0 to 4.5 T, is (45 ± 20)% (the unknown form factors cancel by taking the ratio of Rs). This implies, from Figure 28, that the upper limit for θ is around 46°. This is smaller than the value refined above, again implying that the Pr form factor has deviated from the dipole approximation.

3.2g The Pr form factor

Table 14: Observed values for the Pr moment multiplied by its form factor at 4.2 K, assuming a Pr moment tilt of $\theta = (45 \pm 5)°$, and the fitted values for $\theta = 45°$ using the dipole approximation. (Pure, oxygenated crystal).

(h, k, l)	$\mu_{Pr} f_{Pr}(\kappa)_{obs}$ / μ_B	$\mu_{Pr} f_{Pr}(\kappa)_{fit}$ / μ_B
$^1/_2, {}^1/_2, 0$	0.87 ± 0.03	0.83
$^1/_2, {}^1/_2, 1$	0.92 ± 0.02	0.82
$^1/_2, {}^1/_2, 2$	0.80 ± 0.04	0.81
$^1/_2, {}^1/_2, 3$	0.77 ± 0.03	0.78
$^1/_2, {}^1/_2, 4$	0.77 ± 0.04	0.75
$^1/_2, {}^1/_2, 5$	0.83 ± 0.05	0.72
$^1/_2, {}^1/_2, 6$	0.83 ± 0.06	0.68
$^1/_2, {}^1/_2, 7$	0.82 ± 0.06	0.64
$^3/_2, {}^3/_2, 0$	0.61 ± 0.02	0.679
$^3/_2, {}^3/_2, 1$	0.70 ± 0.03	0.676
$^3/_2, {}^3/_2, 2$	0.56 ± 0.03	0.666
$^3/_2, {}^3/_2, 3$	0.26 ± 0.05	0.649
		$\chi^2 = 41$

So on the one hand, θ should be less than 46°, and on the other hand, θ can not be too much smaller than the refined parameter, since otherwise the orientation factor will curtail the calculated intensities for high values of l. Hence we can probably reasonably estimate that the Pr moments are tilted away from the c-axis by an amount $\theta = (45 \pm 5)°$.

Table 14 shows the result of analysing the observed data, assuming that the Pr moment is tilted at (45 ± 5)° and using the dipole approximation for the Pr form factor. The refined Pr moment is $\mu_{Pr} = (0.85 \pm 0.12)\ \mu_B$. An idea of the deviation of the Pr form factor from the dipole approximation can be gained by plotting measured and calculated values of $\mu_{Pr}f_{Pr}(\kappa)$; this is done in Figure 29. Obviously, a change in θ will affect the measured values by altering the orientation factor; however, the general trends can be seen.

The observed form factor is not spherically symmetric, since the values for the $(^3/_2, {}^3/_2, l)$ series lie below those for the $(^1/_2, {}^1/_2, l)$ series. This implies that the spin density is less concentrated directly above and below the Pr atom than around the Pr atom. Two possible explanations for this are that the Pr wave-function is hybridised with the wave-functions of the surrounding O ions, or that the crystal field effect has removed the spherical symmetry of the atom.

The dotted line in Figure 29 is an attempt to extract a functional form to the observed form factor, for use in future analysis. A straight line of the form

$$f_{Pr}(\kappa) = a_h + bs \tag{72}$$

was fitted to both the $(^1/_2, {}^1/_2, l)$ series and the $(^3/_2, {}^3/_2, l)$ series, with the gradient constrained to be the same in each case, which my experience with the Cu form factor suggested would be a good approximation. The results, assuming that $\mu_{Pr} = (0.85 \pm 0.12)\ \mu_B$, are $a_{1/2} = (1.12 \pm 0.10)$, $a_{3/2} = (0.9 \pm 0.2)$, and $b = (-0.9 \pm 0.7)$ Å, with a systematic error of 15%. Applying this extracted form factor to the original intensity data (Table 13) gives a Pr moment of $(0.84 \pm 0.12)\ \mu_B$ aligned at an angle of $\theta = (48 \pm 1)°$, with a χ^2 of 18, consistent with the values we assumed in attempting to extract the form factor.

In summary, from a combination of measurements made both with and without an applied magnetic field, I estimate that the Pr moment is $(0.85 \pm 0.12)\ \mu_B$ aligned at an angle of $\theta = (45 \pm 5)°$. I have also extracted a semi-empirical form factor for praseodymium in this region of reciprocal space, for use with other measurements. (An attempt has been made to measure the form factor directly by using polarised neutrons, though this was severely hindered by the lack of an available crystal of suitable size[61]). This could also potentially show if there were a distribution in Pr moment direction as a funtion of θ.

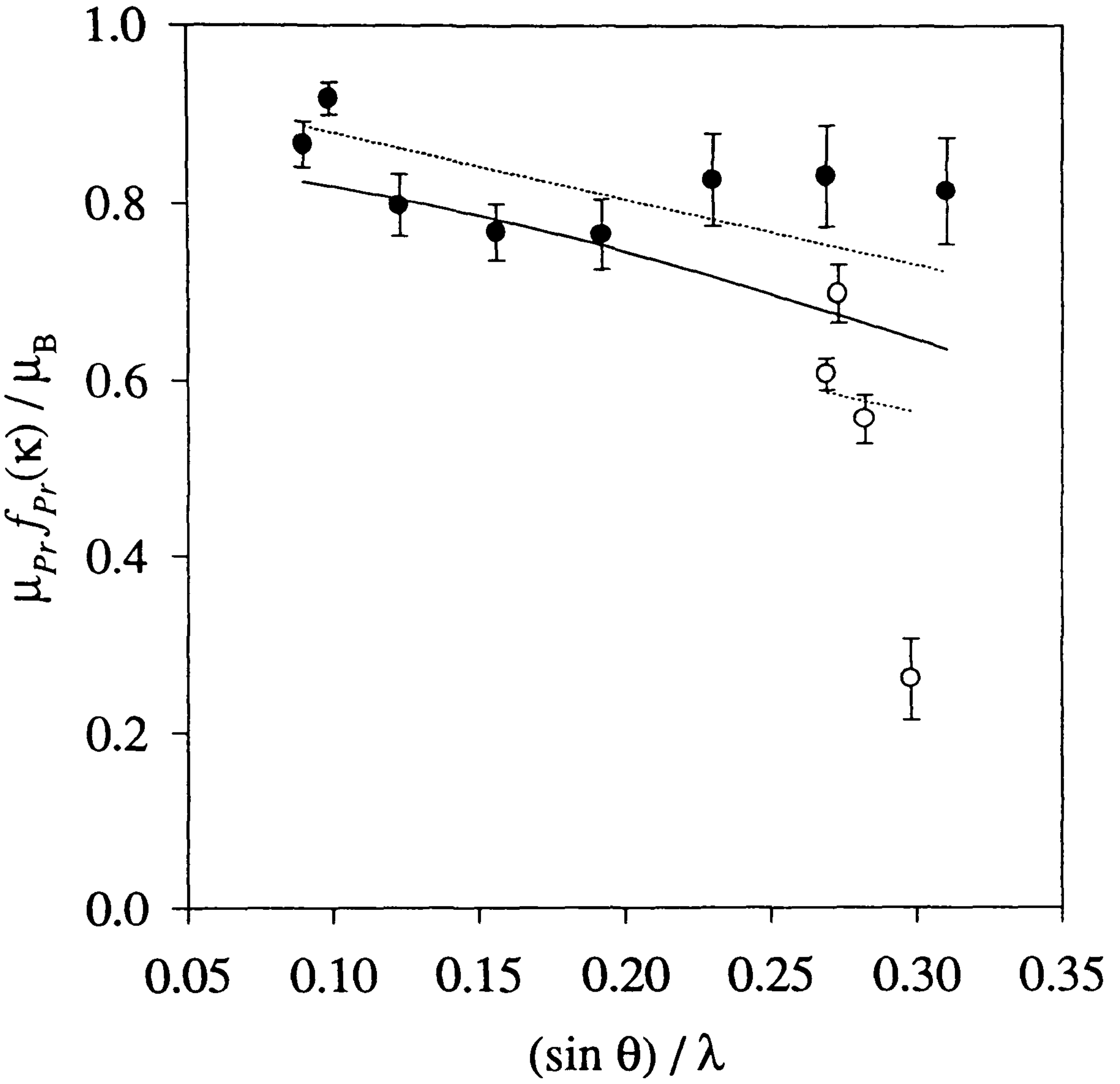

Figure 29: Measured Pr form factors (for moments aligned at an angle of θ = 45°) at 4.2 K. Solid circles correspond to the ($^1/_2$, $^1/_2$, l) series, $l = 0, 1, \ldots, 7$, whilst open circles correspond to the ($^3/_2$, $^3/_2$, l) series, $l = 0, 1, 2, 3$. The solid line shows the calculated form factor using the dipole approximation; the dotted line is a straight line fit to the observed data (see text). The systematic error in the quantity $\mu_{Pr} f_{Pr}(\kappa)$ is 10%. (Pure, oxygenated crystal).

---

[61] M.P. Nutley, PhD Thesis, University of Warwick (1994).

3.3 Pure, reduced crystal

3.3a The temperature dependence of the different magnetic phases

This crystal (12 mg) was grown in a magnesium oxide crucible and reduced by annealing in nitrogen. The Néel temperature for the type-I phase is (347 ± 1) K; Figure 30 shows the variation of the Cu contribution to the intensity of the ($^1/_2$, $^1/_2$, 2) peak with temperature.

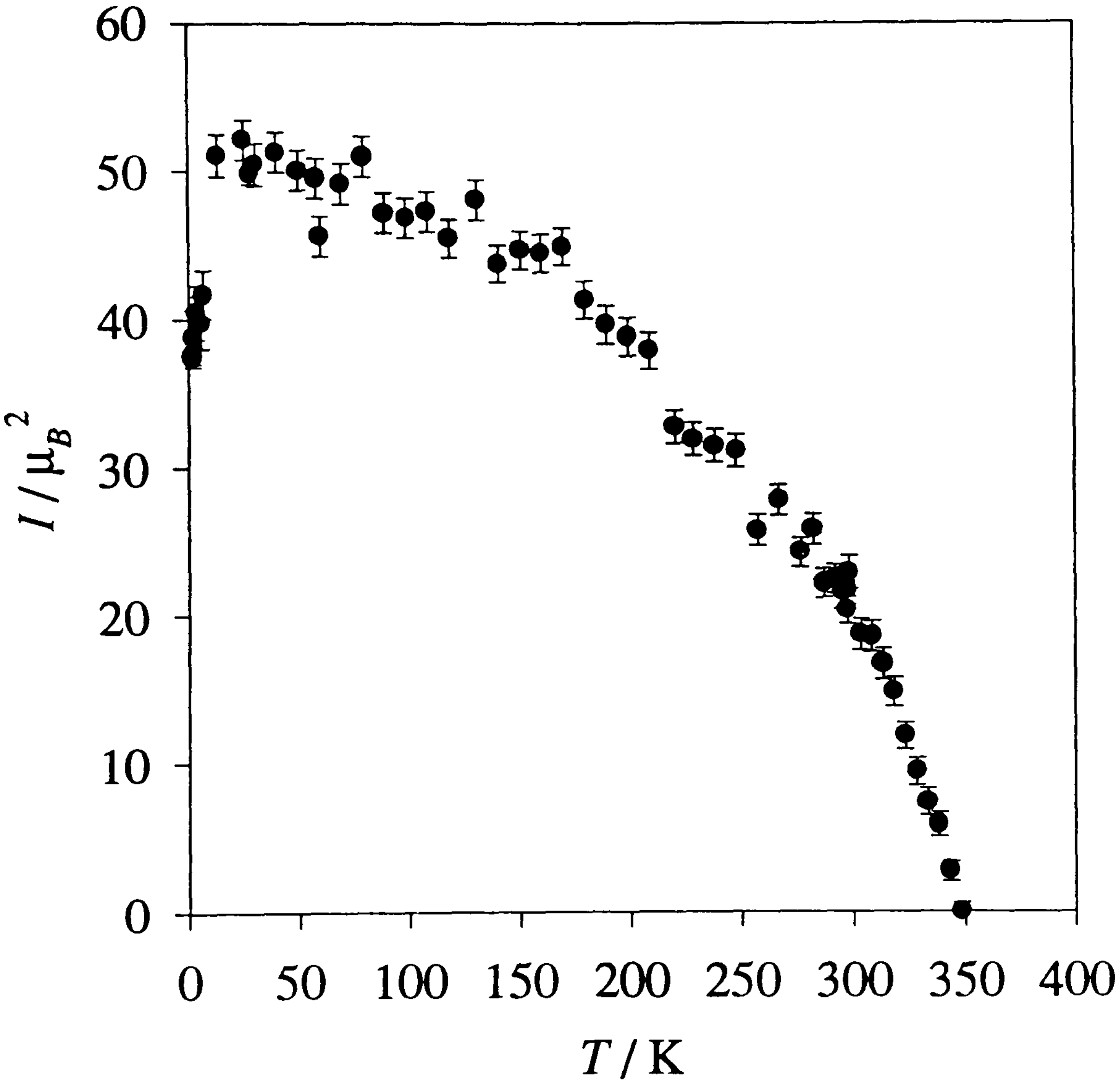

Figure 30: The variation with temperature of the Cu intensity of the ($^1/_2$, $^1/_2$, 2) reflection. The systematic error in the absolute intensity is 20%. (Pure, reduced crystal).

As was observed for the pure, oxygenated crystal, by about 20 K, the Cu(2) moment causing the type-I reflections has become fully ordered. There is then a sudden decrease in intensity, corresponding to the onset of Pr ordering. The Néel temperature for the Pr ordering is (11.0 ± 0.5) K (see Figure 31). Again, the Pr moments are ferromagnetically coupled along *c* and antiferromagnetically coupled perpendicular to *c*, so that the Pr peaks occur at $(h+{}^1/_2, k+{}^1/_2, l)$, *h*, *k*, *l* being integers.

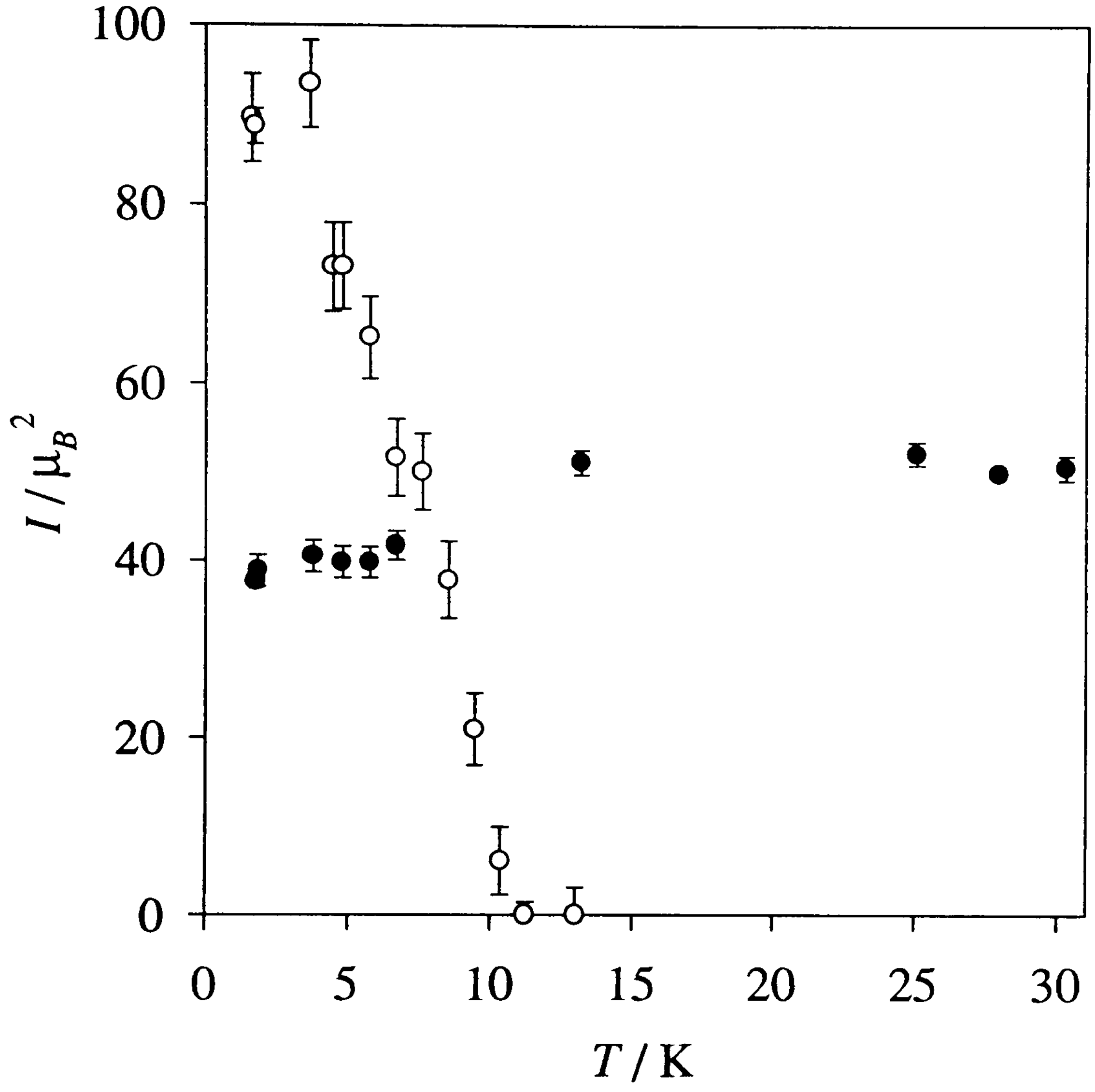

Figure 31: The variation with temperature of the Pr intensity of the $({}^1/_2, {}^1/_2, 0)$ reflection (open circles) and the Cu intensity of the $({}^1/_2, {}^1/_2, 2)$ reflection (closed circles). The systematic error in the absolute intensity is 20%. (Pure, reduced crystal).

3.3b The intrinsic width of the Pr reflections

Figure 32 shows the Pr reflection at $({}^1/_2, {}^1/_2, 0)$ at 1.7 K. The shape is Lorentzian in character, with an intrinsic Lorentzian half-width of $\Gamma = (0.090 \pm 0.004)$ Å^{-1} parallel to the (00*l*)-axis. This corresponds to a correlation length in the Pr ordering of just (11.1 ± 0.5) Å along the *c*-axis, equivalent to (0.93 ± 0.04) unit cells.

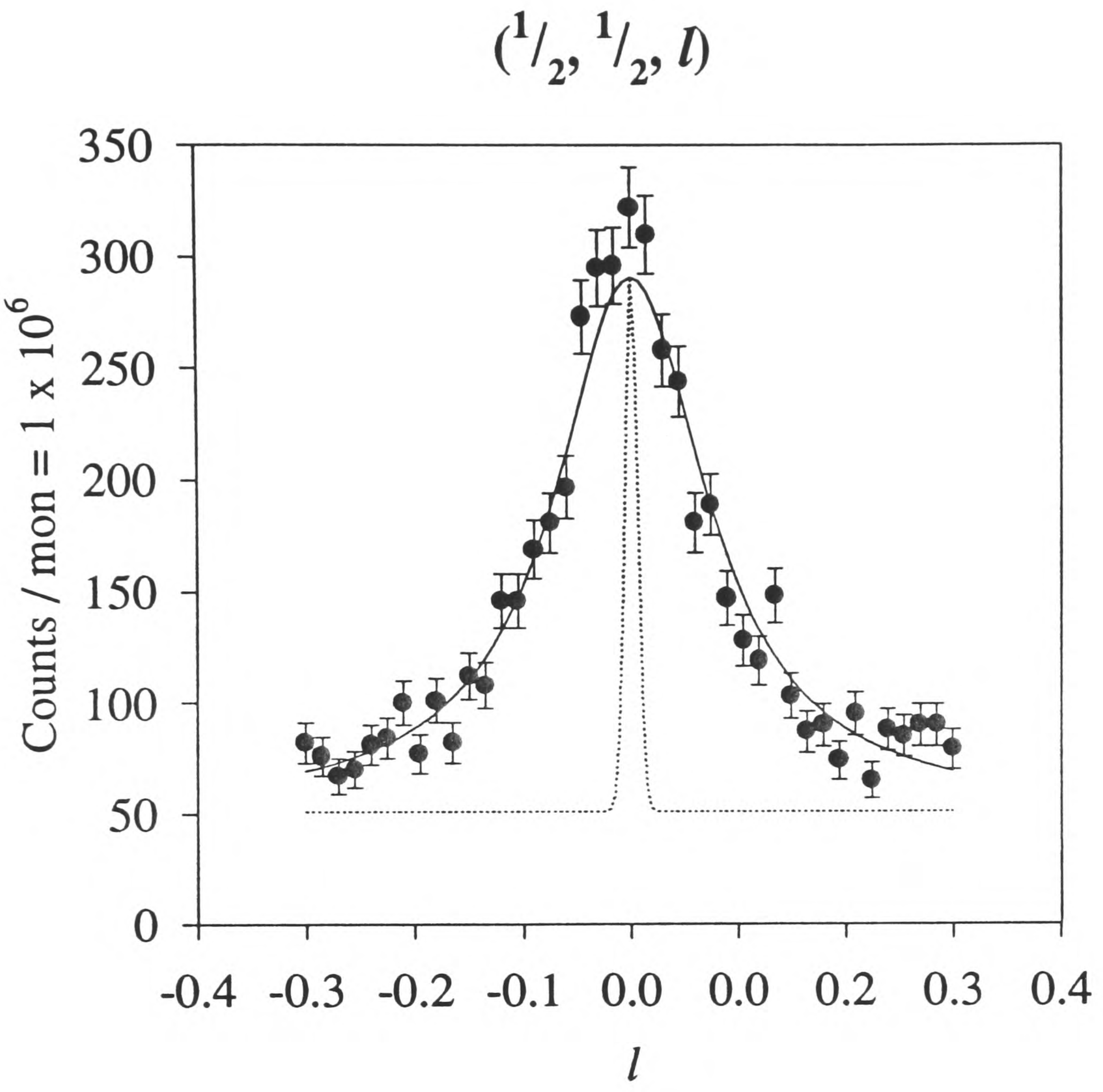

Figure 32: l-scan through the ($^1/_2$, $^1/_2$, 0) peak at 1.7 K. The solid line is the calculation for an intrinsic Lorentzian convoluted with the resolution; the Lorentzian half-width is Γ = (0.090 ± 0.004) Å^{-1}, and the FWHM of the resolution (dotted line) is 0.0138 (0,0,1). A monitor count of 1 x 10^6 takes about 220s. (Pure, reduced crystal).

3.3c The Cu type-I phase

Again, the Cu ordering can best be investigated above the Pr Néel temperature. Unfortunately, it was not possible to obtain accurate data on the Cu intensities, since the crystal had a very poor mosaicity (the crystal essentially consisted of two distinct crystallites). Figure 33 shows an ω-scan through the nuclear reflection (0, 0, 2); the presence of two distinct crystallites is apparent.

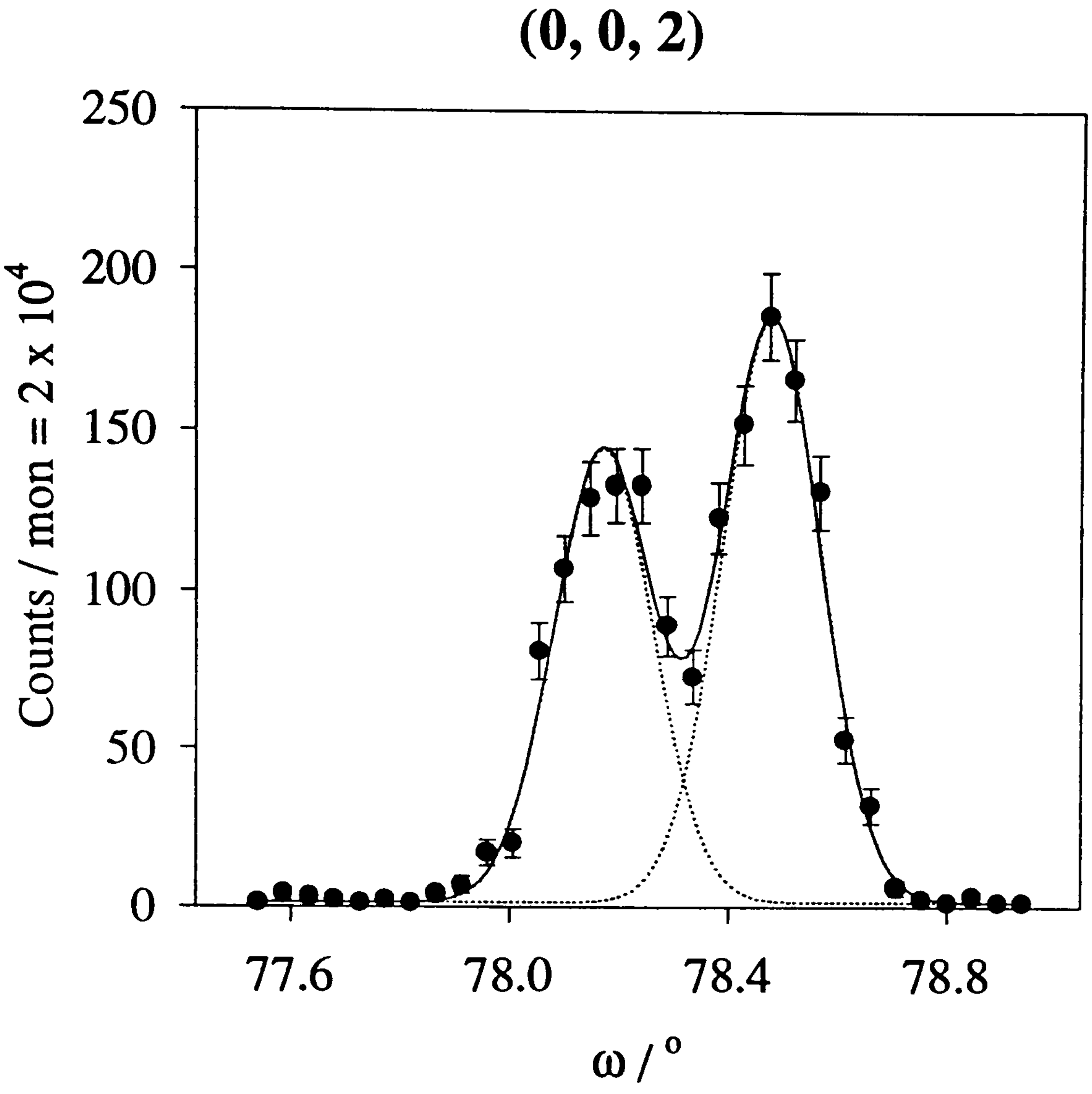

Figure 33: ω-scan of the (0, 0, 2) reflection. The crystal consists of two crystallites, hence the double-peak structure (dotted lines). A monitor count of 2 x 10^4 takes about 4s. (Pure, reduced crystal).

Measurements were performed at 30 K, and the results are presented in Table 15. Despite the poor quality of the data, it is clear that the intensities have the very strong bilayer structure factor characteristic of type-I reflections (see Appendix *II-4.7*). Following the normal fitting procedure, the Cu(2) moment is $\mu_{Cu(2)} = (0.60 \pm 0.10)\ \mu_B$, lying parallel to the *ab*-plane (the data was not good enough to also fit a radial expansion/contraction of the wave function, so β was set to 0%).

Table 15: Observed and fitted intensities for the Cu type-I ordering at 30 K. The poorness of the data is a consequence of the poor crystal mosaicity. (Pure, reduced crystal).

(h, k, l)	I_{obs} / μ_B^2	I_{fit} / μ_B^2
$^1/_2$, $^1/_2$, 1	44.5 ± 0.7	38.3
$^1/_2$, $^1/_2$, 2	66.5 ± 1.0	65.8
$^1/_2$, $^1/_2$, 3	8.5 ± 0.6	9.1
$^1/_2$, $^1/_2$, 4	22.5 ± 0.9	23.2
$^1/_2$, $^1/_2$, 5	61.1 ± 1.5	73.1
$^1/_2$, $^1/_2$, 6	20.2 ± 1.3	28.2
$^1/_2$, $^1/_2$, 7	1.5 ± 0.8	3.2
$^3/_2$, $^3/_2$, 1	12.1 ± 1.2	9.3
$^3/_2$, $^3/_2$, 2	17.2 ± 1.4	13.9
$^3/_2$, $^3/_2$, 3	2.3 ± 1.0	1.9
		$\chi^2 = 22$

3.3d The Pr ordering

The Pr peak shape, on the other hand, is not so badly affected, the splitting in the mosaicity being small compared to the width of the Lorentzian. Figure 34 shows Cu and Pr contributions to the ($^1/_2$, $^1/_2$, 1) reflection. It was possible to independently fit the Cu and Pr contributions to three other reflections, at ($^1/_2$, $^1/_2$, l), $l = 2, 3, 4$ - this is more reflections than for the pure, oxygenated crystal because here the Lorentzian half-width is much greater. The result is that the Cu intensities at 1.7 K are reduced by a factor of 0.70 ± 0.08 from their intensity at 30 K (see Figure 30). This implies that the ordered component of the Cu(2) moment has been reduced from (0.60 ± 0.10) μ_B at 30 K to (0.50 ± 0.09) μ_B at 1.7 K.

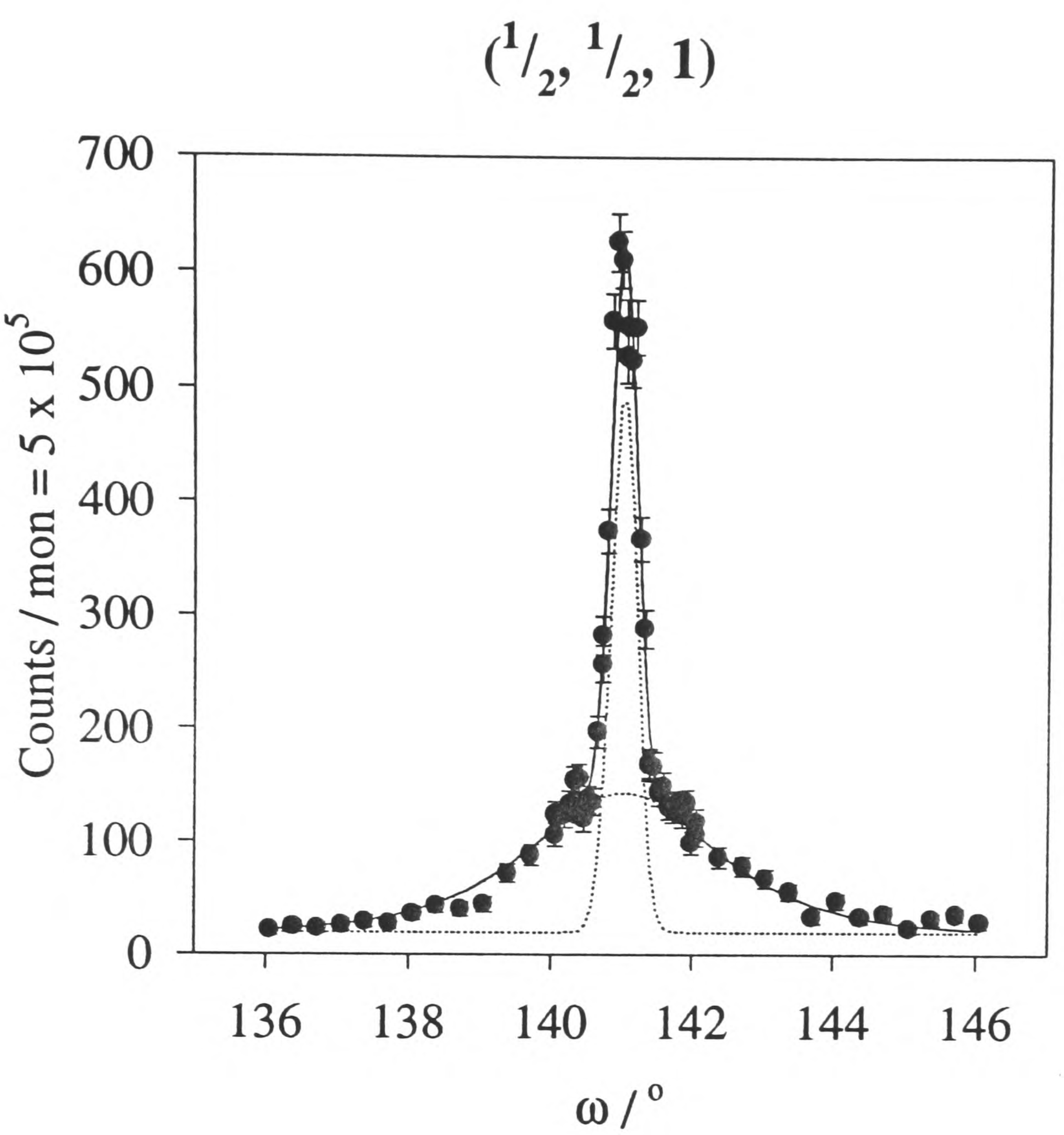

Figure 34: ω-scan of the ($^1/_2$, $^1/_2$, 1) reflection at 1.7 K. The dotted lines are the contributions from the Cu ordering (amplitude = 480) and the Pr ordering (amplitude = 120); the solid line is the sum of their contributions. A monitor count of 5 x 10^5 takes about 108s. (Pure, reduced crystal).

This allows the determination of the Pr intensities, as in the pure, oxygenated crystal. Once more it is evident that the Pr moments are aligned well away from the *c*-axis, and that the form factor is distorted from the dipole approximation. Table 16 shows the results of attempting to refine the Pr structure constraining the moments to lie parallel to the *c*-axis, and also allowing the moments to be aligned at an angle θ away from the *c*-axis (as in Figure 26), using the functional Pr form factor extracted from the data of the oxygenated crystal.

Table 16: Observed and fitted intensities for the Pr ordering at 1.7 K. (Pure, reduced crystal).

(h, k, l)	I_{obs} / μ_B^2	$I_{\theta=0^\circ} / \mu_B^2$	$I_{\theta=41^\circ} / \mu_B^2$
$(^1/_2, {}^1/_2, 0)$	89 ± 2	98	89
$(^1/_2, {}^1/_2, 1)$	78 ± 2	79	81
$(^1/_2, {}^1/_2, 2)$	66 ± 4	49	66
$(^1/_2, {}^1/_2, 3)$	61 ± 3	30	55
$(^1/_2, {}^1/_2, 4)$	56 ± 6	18	48
$(^1/_2, {}^1/_2, 5)$	55 ± 15	12	42
$(^1/_2, {}^1/_2, 6)$	45 ± 4	8	38
$(^1/_2, {}^1/_2, 7)$	32.2 ± 1.5	6	34.4
$(^3/_2, {}^3/_2, 0)$	49 ± 2	43	39
$(^3/_2, {}^3/_2, 1)$	37 ± 5	41	38
$(^3/_2, {}^3/_2, 2)$	28 ± 7	38	36
$(^3/_2, {}^3/_2, 3)$	21 ± 3	33	33
		$\chi^2 = 54$	$\chi^2 = 5$

The refinement gave values for the Pr moment of (1.3 ± 0.2) μ_B, aligned at an angle of $\theta = (40.5 \pm 1.0)^\circ$, although given the uncertainty in the Pr form factor a value of $\theta = (41 \pm 5)^\circ$ is probably a more realistic estimate.

3.4 Al-contaminated, oxygenated crystal

3.4a The type-I phase and the Cu form factor

This crystal (100 mg) was grown in an alumina crucible, accounting for its Al-contamination (see Section *II-3.1*), and was oxygenated by annealing in oxygen for six months. The Néel temperature for the type-I phase is (362 ± 2) K (see Figure 35).

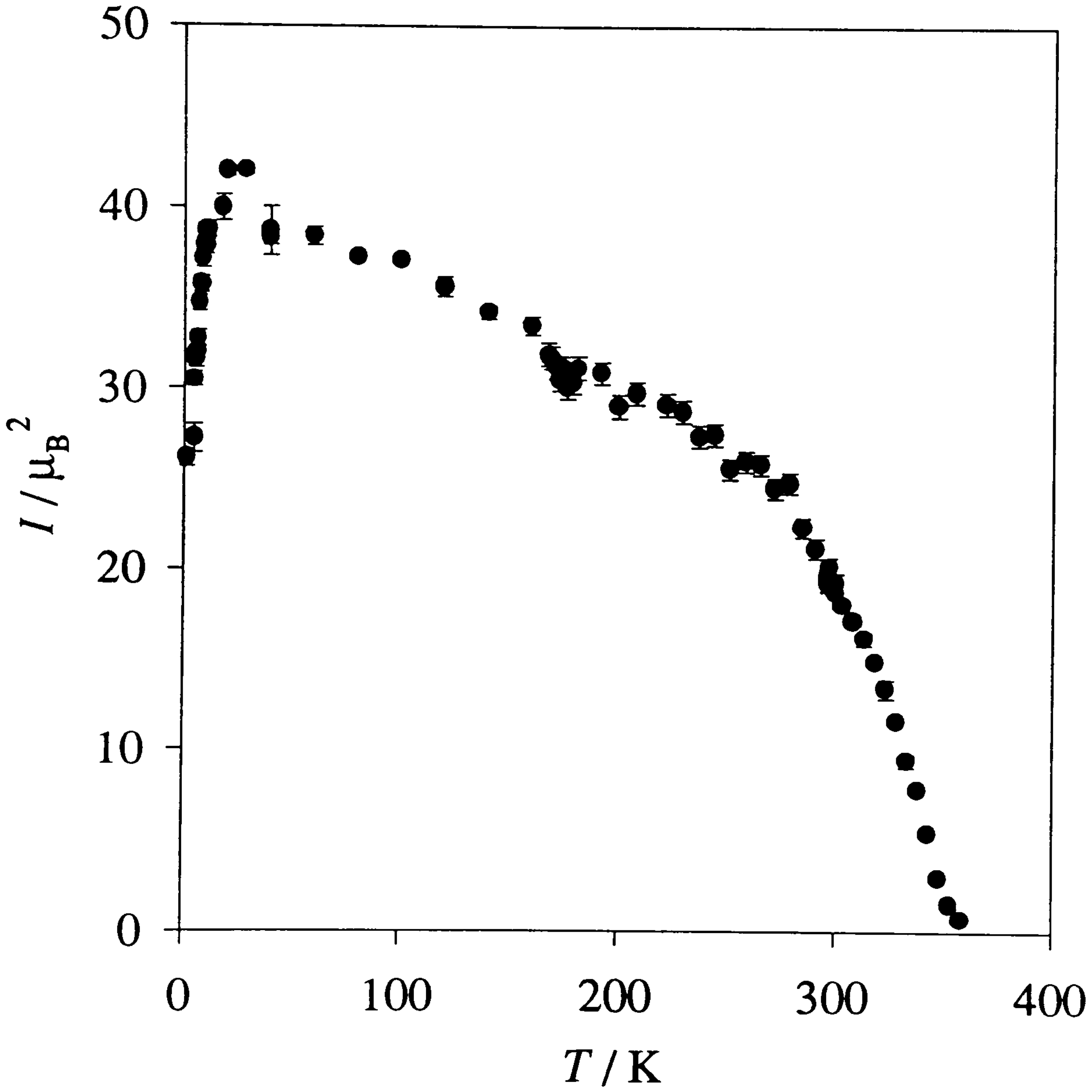

Figure 35: The variation with temperature of the Cu intensity of the ($^1/_2$, $^1/_2$, 2) reflection. The systematic error in the absolute intensity is 8%. (Contaminated, oxygenated crystal).

Historically this was the first crystal I measured, and it was on this crystal that I measured the Cu form factor and ensured that it was of the form I expected for a $3d(x^2 - y^2)$ hole orbital (see Section *II-1.1b*). To demonstrate the anisotropy of the $3d(x^2 -$

y^2) symmetry, and the necessity of using this rather than spherical symmetry, Figure 36 shows the variation of the form factor with (sin θ) / λ.

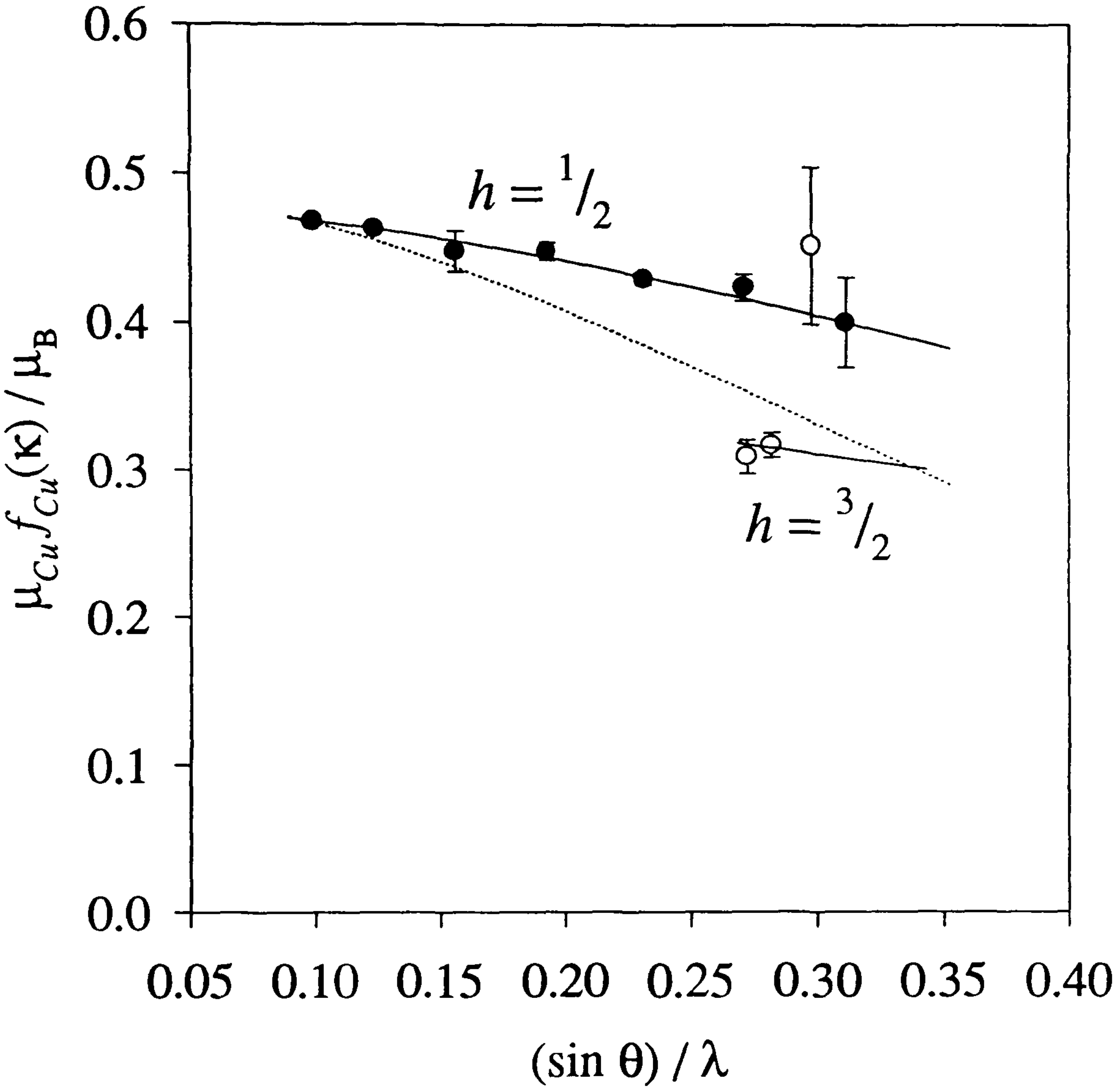

Figure 36: Measured Cu form factors at 40 K. Solid circles correspond to the ($^1/_2$, $^1/_2$, l) series, whilst open circles correspond to the ($^3/_2$, $^3/_2$, l) series. The solid line shows the calculated form factor for $3d(x^2 - y^2)$ symmetry, and the dotted line shows the spherical $3d(r^2)$ symmetry. (Contaminated, oxygenated crystal).

The intensities measured at 40 K are given in Table 17. These intensities, when analysed by a model using the $3d(x^2 - y^2)$ symmetry, correspond to a Cu(2) moment of (0.493 ± 0.010) μ_B lying parallel to the *ab*-plane (the absolute φ orientation can not be determined). The fitted form factor indicates a radial contraction (compared to the calculated free-ion wave functions) of $\beta = (22 \pm 2)$ %.

Table 17: Observed and fitted intensities for the Cu ordering at 40 K. (Contaminated, oxygenated crystal).

(h, k, l)	I_{obs} / μ_B^2	$I_{3d(x^2-y^2)} / \mu_B^2$	$I_{3d(r^2)} / \mu_B^2$
($^1/_2$, $^1/_2$, 1)	21.4 ± 0.3	21.4	21.8
($^1/_2$, $^1/_2$, 2)	36.0 ± 0.4	36.0	36.1
($^1/_2$, $^1/_2$, 3)	3.9 ± 0.2	4.0	4.0
($^1/_2$, $^1/_2$, 4)	15.8 ± 0.4	15.6	14.5
($^1/_2$, $^1/_2$, 5)	42.9 ± 0.7	43.3	38.7
($^1/_2$, $^1/_2$, 6)	14.4 ± 0.6	13.9	11.8
($^1/_2$, $^1/_2$, 7)	4.0 ± 0.6	3.9	3.0
($^3/_2$, $^3/_2$, 1)	8.1 ± 0.6	8.6	12.3
($^3/_2$, $^3/_2$, 2)	12.5 ± 0.7	12.4	17.4
($^3/_2$, $^3/_2$, 3)	2.8 ± 0.7	1.3	1.9
		$\chi^2 = 1.0$	$\chi^2 = 24$

3.4b The low-temperature phases

At a temperature of approximately 11 K there is a sudden decrease in intensity of the $(h+^1/_2, k+^1/_2, l)$ reflections (see Figure 35). As in the pure crystals, this coincides with the onset of the Pr ordering; however, the loss in Cu intensity at the ($^1/_2$, $^1/_2$, 2) reflection is not caused solely by a decrease in the ordered component of the Cu(2) moment - the occurrence of reflections at $(h+^1/_2, k+^1/_2, l+^1/_2)$, h, k, l being integers, (see Figure 37) indicates that the Cu ordering has entered the type-II intermediate phase, at a temperature of (11 ± 1) K.

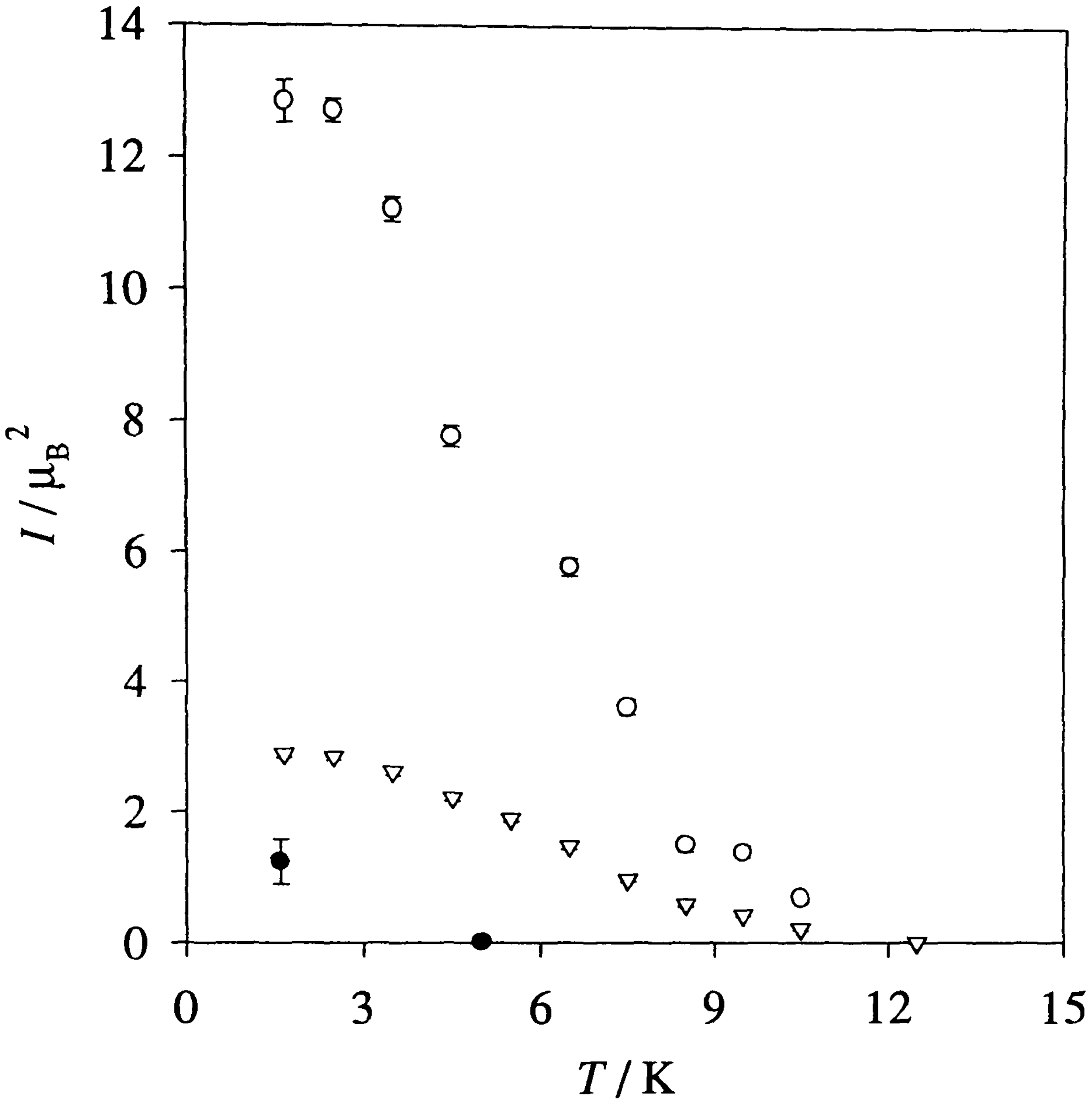

Figure 37: The variation with temperature of the Cu intensity of the ($^1/_2$, $^1/_2$, $^3/_2$) reflection (open triangles), the Pr intensity of the ($^1/_2$, $^1/_2$, 0) reflection (open circles), and the ridge intensity measured at ($^1/_2$, $^1/_2$, 0) (closed circles). (Contaminated, oxygenated crystal).

As described in Section *II-2.1*, the type-II phases are often associated with a magnetic ordering of the Cu(1) ions. However, it was not possible to determine whether or not these ions had ordered as the intermediate phase had only just developed, and so the $l + {}^1/_2$ reflections were still weak at the lowest temperatures attainable. The type-II ground state was not reached as T → 0 K.

3.4c The intrinsic width of the Pr reflections

The Néel temperature for the Pr ordering is (11 ± 1) K. A raster scan was taken of the Pr reflection ($^1/_2$, $^1/_2$, 0) at 1.6 K, and this is shown in Figure 39.

As in the pure crystals, the Pr ordering is ferromagnetically coupled along the *c*-axis. The intrinsic Lorentzian half-width is $\Gamma = (0.059 \pm 0.004)$ Å^{-1} parallel to the

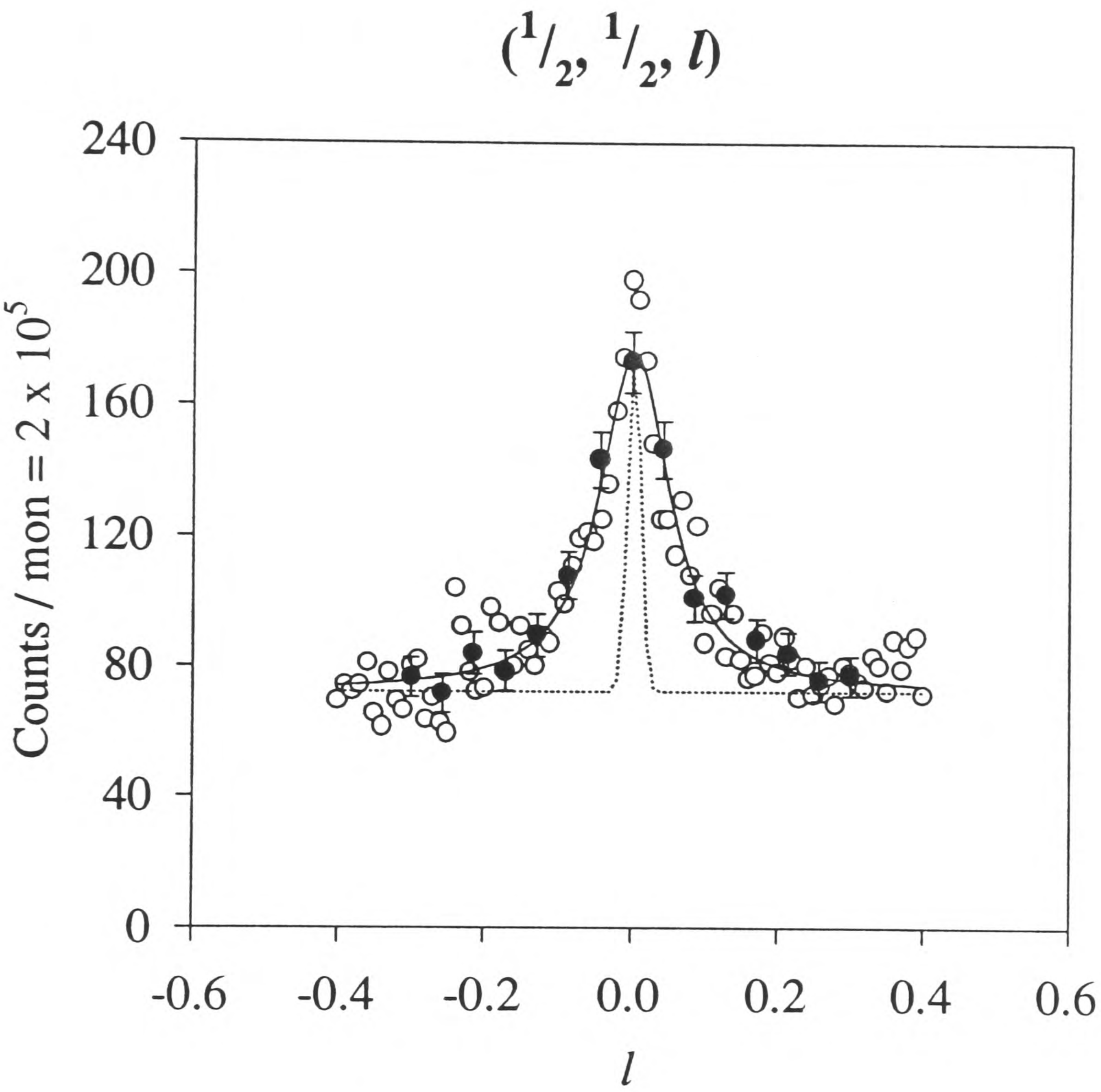

Figure 38: *l*-scan through the ($^1/_2$, $^1/_2$, 0) peak at 1.6 K. The solid line is the calculation for an intrinsic Lorentzian convoluted with the resolution; the Lorentzian half-width is $\Gamma = (0.059 \pm 0.004)$ Å^{-1}, and the FWHM of the resolution (dotted line) is 0.021 (0,0,1). A monitor count of 2 x 10^5 (open circles) takes about 50 s; the closed circles were measured for a monitor count of 4 x 10^5. (Contaminated, oxygenated crystal).

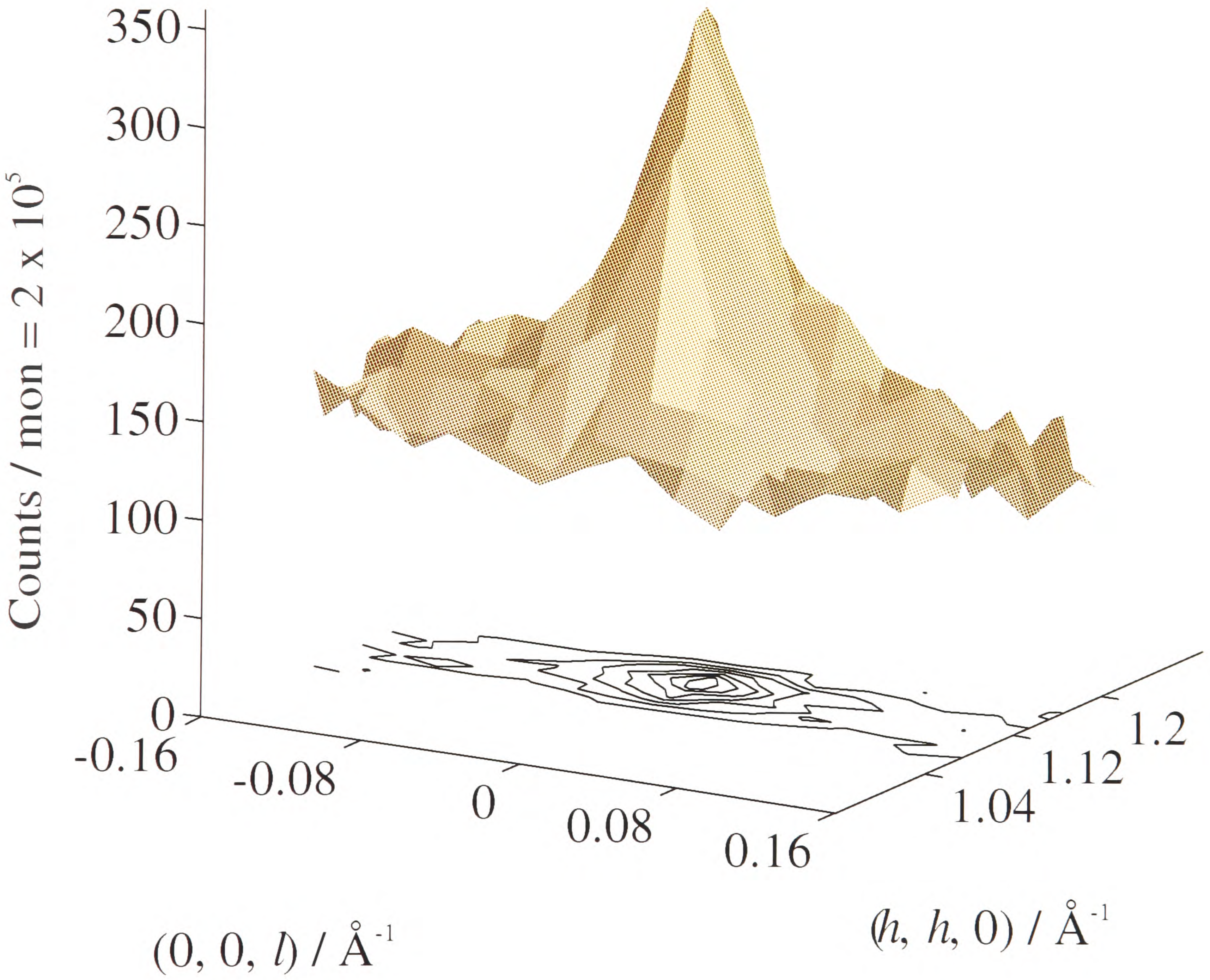

Figure 39: ($^1/_2$,$^1/_2$, 0) reflection at 1.6 K. (Contaminated, oxygenated crystal).

(00*l*)-axis (see Figure 38). This corresponds to a correlation length of (16.9 ± 1.1) Å, equivalent to (1.44 ± 0.09) unit cells.

Measurements were then taken in order to separate the Pr and Cu contributions to the peaks. These measurements included a long scan through all the reflections along the line ($^1/_2$, $^1/_2$, *l*) (see Figure 40); an inspection of the figure shows how the Cu intensity peaks with the bilayer structure factor (see Appendix *II-4.7*), at $l \approx 2$ and 5.

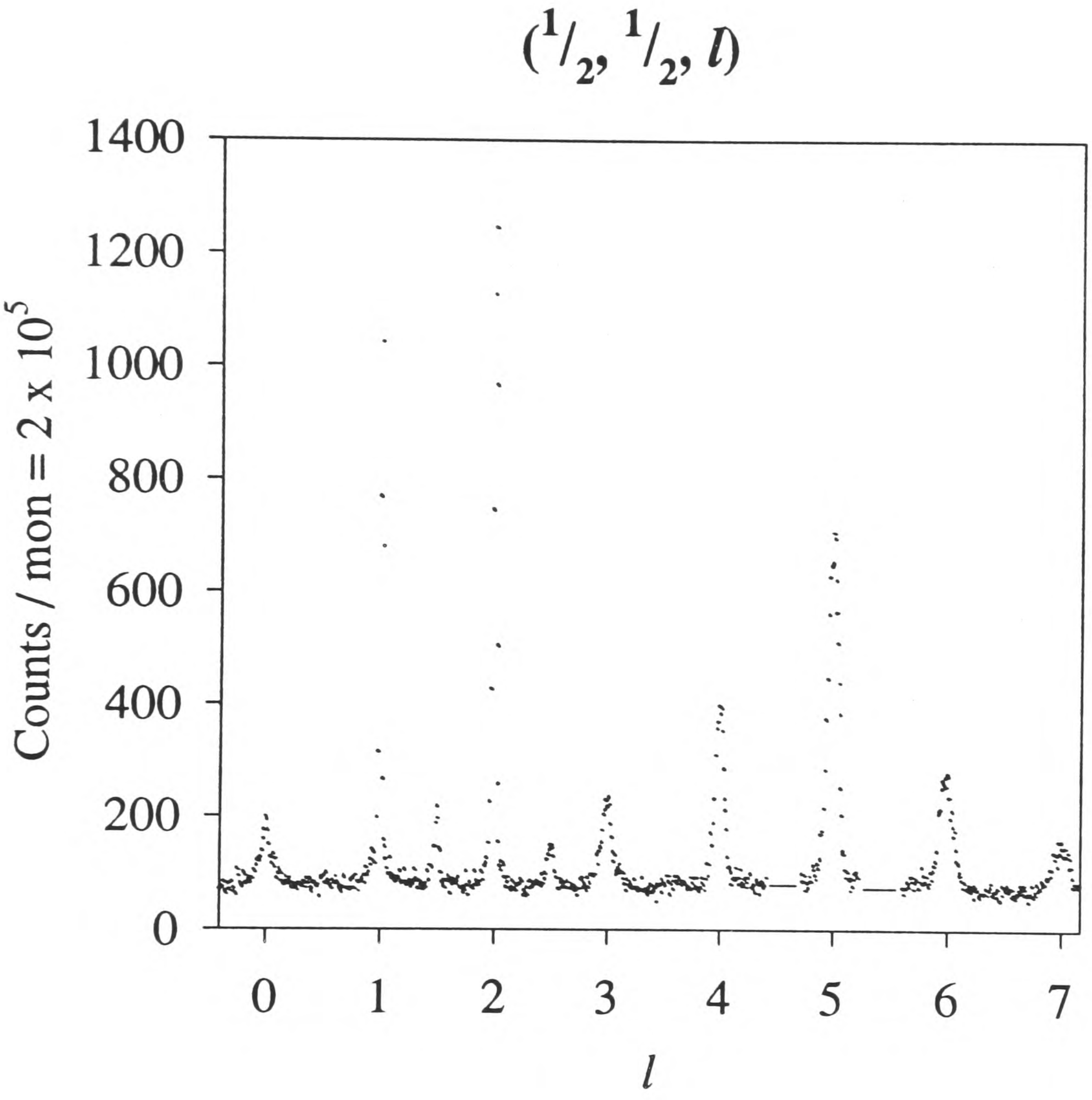

Figure 40: *l*-scan measured on the oxygenated crystal at 1.6 K, showing the Cu reflections at *l* and $l - {}^1/_2$ (l = integer > 0), and also the Pr reflections at *l* (l = integer). aluminium powder lines (from the cryostat) at $l = 4.5$ and 5.5 have been removed for clarity. A monitor count of 2 x 10^5 takes about 50 s. (Contaminated, oxygenated crystal).

However, the analysis was further complicated by a low-temperature ridge of scattering.

3.4d The ridge of scattering

During the analysis I found evidence for a continuous ridge of magnetic scattering parallel to *l* at $h = k = {}^1/_2$, which occurs at a temperature of (3 ± 1) K.

Figure 41 shows scans parallel to (*h*, *h*, 0) and (0, 0, *l*) centred on (${}^1/_2$, ${}^1/_2$, ${}^{13}/_2$) which clearly show this ridge; the type-II peak expected at this position is almost completely depressed by the bilayer structure factor, as can be seen by the absence of a peak in the *l*-scan. These ridges are only observable below about 5 K. A small fraction, (8 ± 2)%, of the ridge at this position can be attributed to the tails of the surrounding Pr Lorentzian peaks, but the rest seems to be caused by a Bragg rod of scattering (see Section *II-1.2e*). The width (FWHM) of the rod in the (*h*, *h*, 0) direction, (0.025 ± 0.006) (1, 1, 0), is comparable to the calculated width of 0.020 (1, 1, 0).

The intensities of the (${}^1/_2$, ${}^1/_2$, *l*) and (${}^3/_2$, ${}^3/_2$, *l*) ridges were determined at various points along their length from some of the *hh*- and *l*-scans (see Table 18). The scans used for this purpose were those that contained intensity from only one type of 3*D* ordering, and so were the simplest to observe the small ridges. The ridges are clearly magnetic in origin, being temperature dependent. Since the Cu(2) moments are strongly ordered three-dimensionally, there are two possible causes of the ridge: 2*D* ordering either of the Cu(1) moments or of the Pr moments.

The Cu(1) moments are generally thought to take part in the 3*D* order of the type-II phases; if this were the case, then they would not be the cause of the ridge. However, as mentioned above, there is insufficient evidence to clearly determine whether or not the Cu(1) moments are taking part in the type-II intermediate phase.

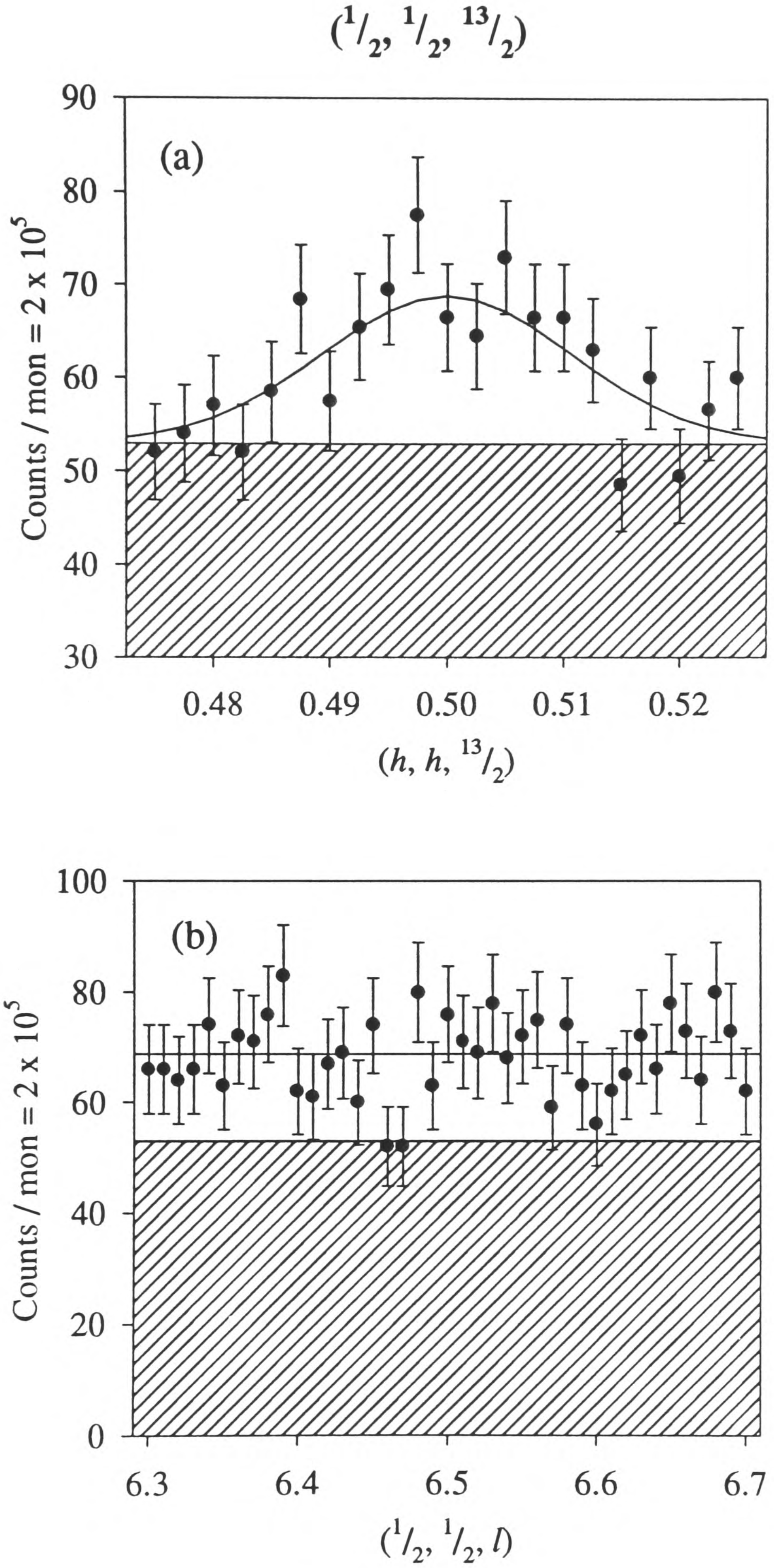

Figure 41: (a) *hh*- and (b) *l*-scan at 1.6 K through $(^1/_2, ^1/_2, ^{13}/_2)$ showing the existence of a ridge of scattering (unshaded) along *l*. A monitor count of 2 x 10^5 takes about 50 s; the *hh*-scan was actually measured for a monitor count of 4 x 10^5. (Contaminated, oxygenated crystal).

Table 18: Observed and fitted intensities for the ridge of scattering at 1.6 K. (Contaminated, oxygenated crystal).

(h, k, l)	I_{obs} / μ_B^2	$I_{Cu(1)}$ / μ_B^2	I_{Pr} / μ_B^2
($^1/_2$, $^1/_2$, 0)	1.2 ± 0.3	0.9	1.1
($^1/_2$, $^1/_2$, $^1/_2$)	1.1 ± 0.3	1.0	1.1
($^1/_2$, $^1/_2$, $^3/_2$)	1.4 ± 0.2	1.2	1.1
($^1/_2$, $^1/_2$, $^5/_2$)	0.8 ± 0.2	1.2	1.1
($^1/_2$, $^1/_2$, $^7/_2$)	1.3 ± 0.5	1.1	1.1
($^1/_2$, $^1/_2$, $^{13}/_2$)	1.2 ± 0.4	0.5	0.9
($^3/_2$, $^3/_2$, 0)	0.4 ± 0.5	0.5	0.5
($^3/_2$, $^3/_2$, $^1/_2$)	0.2 ± 0.3	0.5	0.5
($^3/_2$, $^3/_2$, $^3/_2$)	0.2 ± 0.3	0.4	0.5
		$\chi^2 = 1.5$	$\chi^2 = 1.0$

At first sight, it would seem unlikely that Pr moments are responsible for the ridge of scattering, since the Pr moments clearly order around 11 K. However, it is conceivable that there may be a region of the crystal were the Pr coupling along the *c*-axis has been disrupted, perhaps by an unusually large concentration of Al contamination. In this region it may be that the Pr moments order two-dimensionally. The refined parameters for the Pr fit has the moment aligned at an angle of $\theta = (60 \pm 12)°$ away from the *c*-axis, using the Pr form factor extracted in Section *II-3.2*, which is consistent with the previous values of θ.

The values of χ^2 show that there is not much to choose between the models. Perhaps the most important measurement is the one at ($^1/_2$, $^1/_2$, $^{13}/_2$), since this is where the models are most different. The measurement here suggests that the ridge of scattering is, in fact, being caused by Pr moments. However, given the closeness of the models, it would probably be unwise of me to choose one model over another, except for the purpose of estimating its contribution to the data.

3.4e The Cu type-II intermediate phase

Assuming for this purpose that the ridge of scattering is due to 2*D* Pr order, it is now possible to predict the size of the ridge along *l*, and from henceforth in the analysis the ridge is calculated and treated as a fixed parameter. The 3*D* Pr and Cu contributions are then separated at the ($^1/_2$, $^1/_2$, 1) and ($^1/_2$, $^1/_2$, 2) reflections, and the Cu intensity is measured at the ($^1/_2$, $^1/_2$, $^3/_2$) and ($^1/_2$, $^1/_2$, $^5/_2$) reflections. Figure 42 shows the fitted peak shapes for the ($^1/_2$, $^1/_2$, 1) reflection.

Table 19 gives the observed and fitted Cu intensities of the type-II intermediate phase at 1.6 K. The refined parameters are a Cu(2) moment of (0.46 ± 0.03) μ_B and a turn-angle of ϕ = (22.6 ± 1.0)°. The Cu form factor contraction was fixed at β = (18 ± 2) %, which was the value determined in reference measurements at 18 K. In the 18 K measurements, the moment was calculated to be (0.54 ± 0.04) μ_B. Hence the reduction in the Cu contributions to the ($h+^1/_2$, $k+^1/_2$, l) intensities is more to do with the reduction in the ordered component of the Cu(2) moment than with their rotation into the type-II intermediate structure. The Cu(1) moment is estimated to be less than 0.03 μ_B.

Table 19: Observed and fitted intensities for the Cu type-II intermediate ordering at 1.6 K. (Contaminated, oxygenated crystal).

(h, k, l)	I_{obs} / μ_B	I_{fit} / μ_B
$^1/_2$, $^1/_2$, 1	15.8 ± 0.5	15.6
$^1/_2$, $^1/_2$, $^3/_2$	3.8 ± 0.7	4.5
$^1/_2$, $^1/_2$, 2	26.2 ± 0.7	26.3
$^1/_2$, $^1/_2$, $^5/_2$	2.9 ± 0.3	2.7
		$\chi^2 = 0.7$

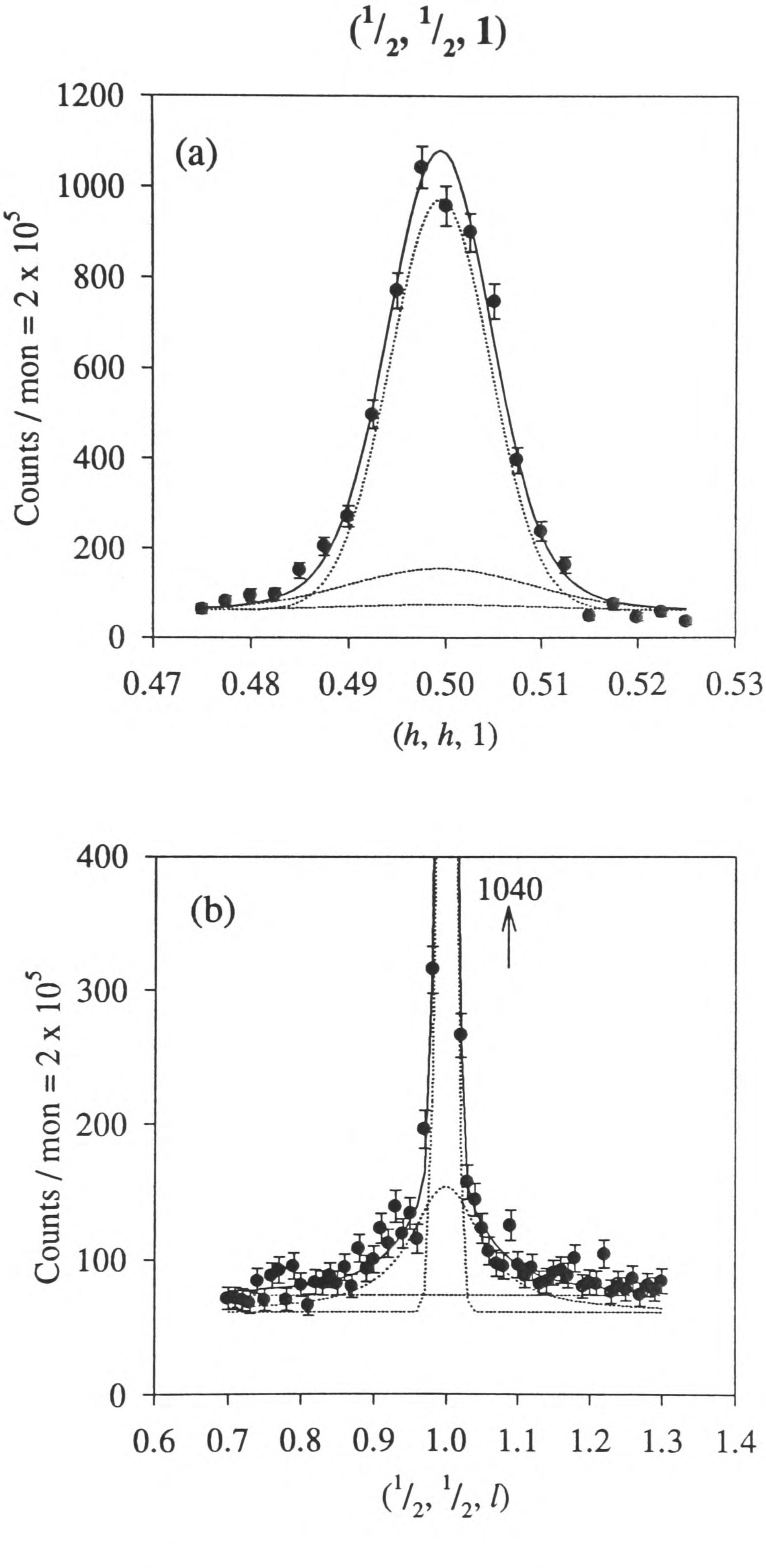

Figure 42: (a) *hh*- and (b) *l*-scan of the ($^1/_2$, $^1/_2$, 1) reflection at 1.6 K. The dotted lines are the contributions from the ridge (amplitude = 13), the Pr peak (amplitude = 95), and the Cu peak (amplitude = 910). A monitor count of 2 x 10^5 takes about 50 s; the *hh*-scan was actually measured for a monitor count of 1 x 10^5.

3.4f The Pr ordering

Knowing the Cu intensities then allows the determination of the Pr intensities, and these are given in Table 20. Once more it is evident that the Pr moments are aligned well away from the *c*-axis. The table shows the results of attempting to refine the Pr structure constraining the moments to lie parallel to the *c*-axis, and also allowing the moments to be aligned at an angle θ away from the *c*-axis (as in Figure 26), using the functional Pr form factor extracted from the data of the pure oxygenated crystal.

The refinement, assuming that all the Pr moments took part in the 3*D* ordering, gave values for the Pr moment of (0.51 ± 0.04) μ_B, aligned at an angle of θ = (49 ± 5)°. If some Pr moments are also ordering two-dimensionally then, assuming that the magnitude of the moment is the same in both cases, the Pr moment has a magnitude of (0.54 ± 0.04) μ_B, with (91 ± 4) % of the moments ordering three dimensionally and (9 ± 1) % ordering two dimensionally.

Table 20: Observed and fitted intensities for the Pr ordering at 1.6 K. (Contaminated, oxygenated crystal).

(h, k, l)	I_{obs} / μ_B^2	$I_{\theta=0°} / \mu_B^2$	$I_{\theta=49°} / \mu_B^2$
(½, ½, 0)	13.3 ± 0.7	15.6	13.1
(½, ½, 1)	11.3 ± 0.8	12.5	12.4
(½, ½, 2)	11.8 ± 1.0	7.7	11.2
(½, ½, 3)	9.0 ± 1.1	4.6	10.1
(½, ½, 4)	7.3 ± 0.9	2.8	9.2
(½, ½, 5)	11 ± 1.8	1.8	8.4
(½, ½, 6)	8.5 ± 1.1	1.2	7.7
(½, ½, 7)	7.8 ± 0.7	0.9	7.1
(3/2, 3/2, 0)	8.5 ± 1.4	6.8	5.7
(3/2, 3/2, 1)	5.4 ± 0.8	6.6	5.7
(3/2, 3/2, 2)	6.7 ± 0.9	6.0	5.5
		$\chi^2 = 25$	$\chi^2 = 1.9$

3.5 Al-contaminated, reduced crystal

3.5a The temperature dependence of the different magnetic phases

This crystal (30 mg) was grown in an alumina crucible, again accounting for its Al-contamination, and reduced under vacuum. The Néel temperature for the type-I phase is (369 ± 1) K (see Figure 43).

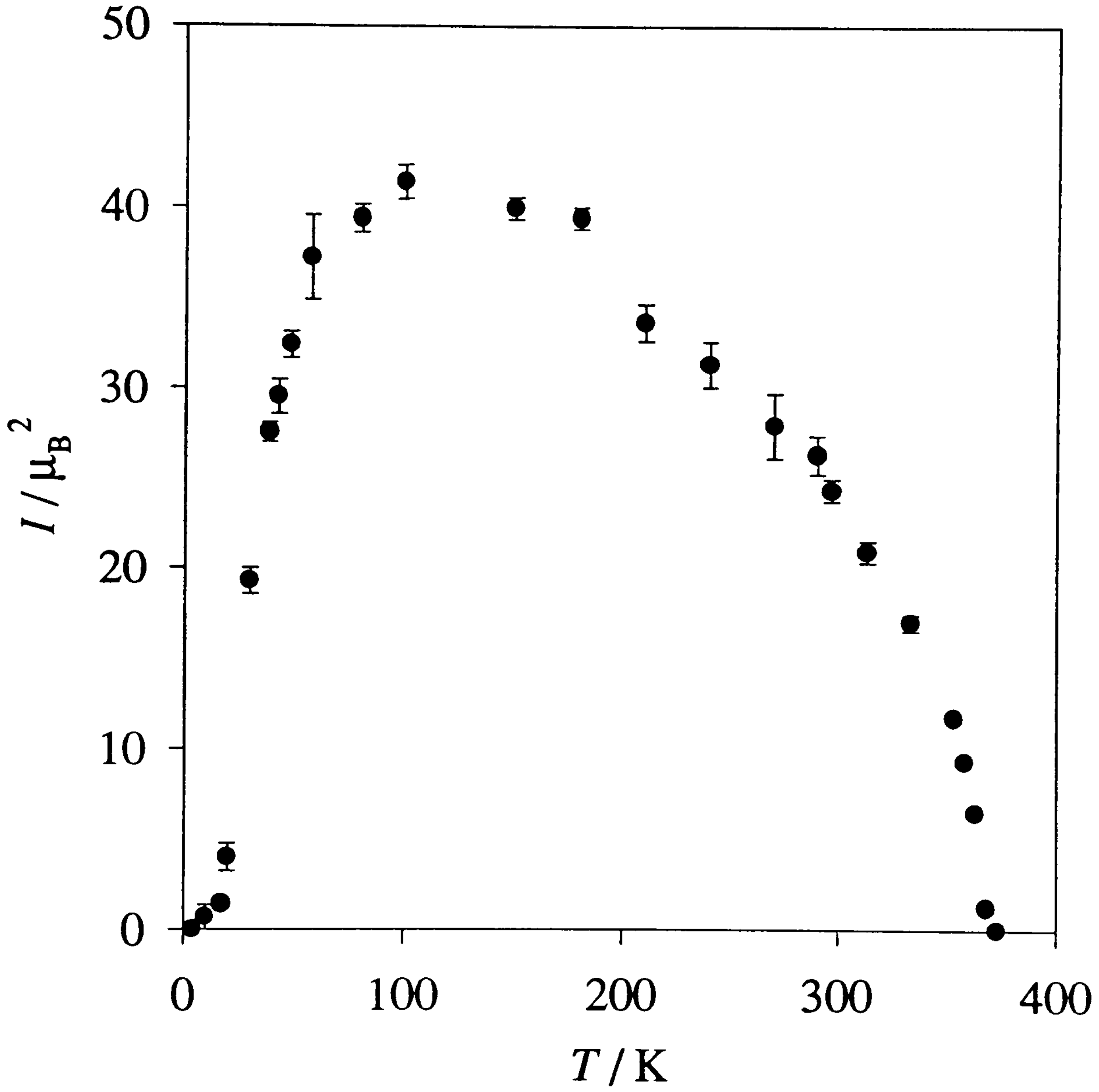

Figure 43: The variation with temperature of the Cu intensity of the ($^1/_2$, $^1/_2$, 2) reflection. The systematic error in the intensity is 12%. (Contaminated, reduced crystal).

The crystal enters the type-II intermediate phase at (100 ± 5) K, and then reaches the type-II ground state at (8 ± 2) K (Figure 44). There is no evidence of 3*D* ordering of Pr moments. This is therefore the ideal situation in which to look for the Cu(1) ordering.

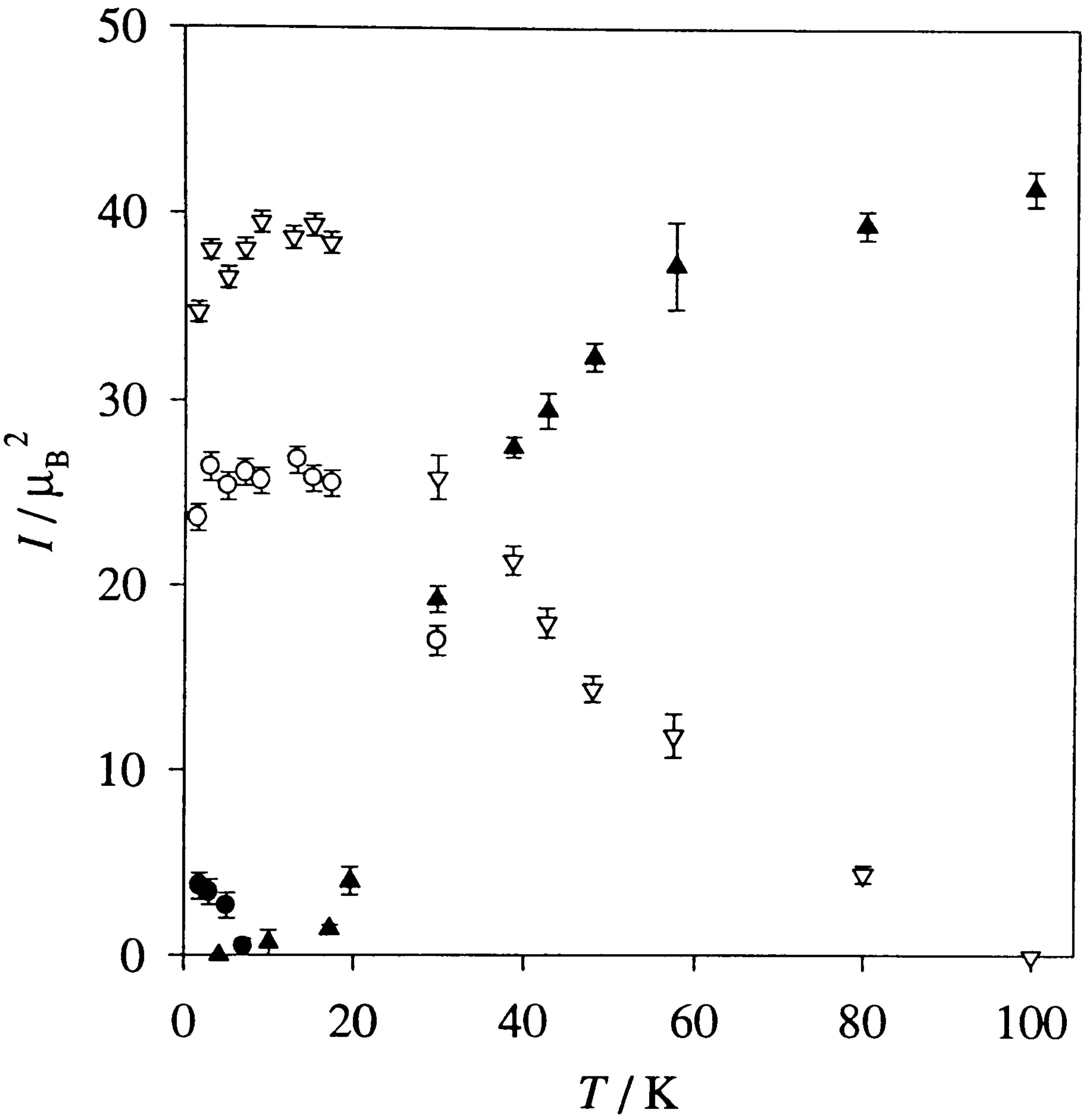

Figure 44: The variation with temperature of the Cu intensities of the ($^1/_2$, $^1/_2$, 2) reflection (closed triangles), the ($^1/_2$, $^1/_2$, $^3/_2$) reflection (open triangles), and the ($^1/_2$, $^1/_2$, $^5/_2$) reflection (open circles); and the intensity of the ridge of scattering (closed circles), measured at ($^1/_2$, $^1/_2$, 0). (Contaminated, reduced crystal).

3.5b The ridge of scattering

At a temperature of (7 ± 1) K, however, a ridge of scattering was again seen, as in the contaminated, oxygenated crystal. The ridge is shown in Figure 45. The width (FWHM) of the rod in the $(h, h, 0)$ direction, (0.024 ± 0.003) (1, 1, 0), is comparable to the calculated width of 0.026 (1, 1, 0).

Table 21 shows some measurements of the ridge intensity at different values of l at 1.6 K. Since the Pr moments do not order three-dimensionally, it is most likely that these measurements are a result of a Bragg rod arising from the *2D* ordering of Pr moments. Unfortunately, I did not make many measurements at this temperature, and so the data is inconclusive. However, I have performed a refinement, using the Pr form factor extracted from the pure, oxygenated crystal. The refinement is improved by allowing the Pr moments to be aligned away from the *c*-axis. In this model, the Pr moment is (0.25 ± 0.03) μ_B aligned at an angle $\theta = (42 \pm 13)°$.

Table 21: Observed and fitted intensities for the Pr ridge of scattering at 1.6 K. (Contaminated, reduced crystal).

(h, k, l)	I_{obs} / μ_B^2	$I_{\theta=0°} / \mu_B^2$	$I_{\theta=42°} / \mu_B^2$
$(\frac{1}{2}, \frac{1}{2}, 0)$	3.4 ± 0.3	3.5	3.4
$(\frac{1}{2}, \frac{1}{2}, \frac{3}{2})$	5.2 ± 1.3	2.2	2.8
$(\frac{1}{2}, \frac{1}{2}, 2)$	2.5 ± 0.9	1.7	2.6
$(\frac{1}{2}, \frac{1}{2}, \frac{5}{2})$	1.9 ± 0.8	1.3	2.3
		$\chi^2 = 2.2$	$\chi^2 = 1.9$

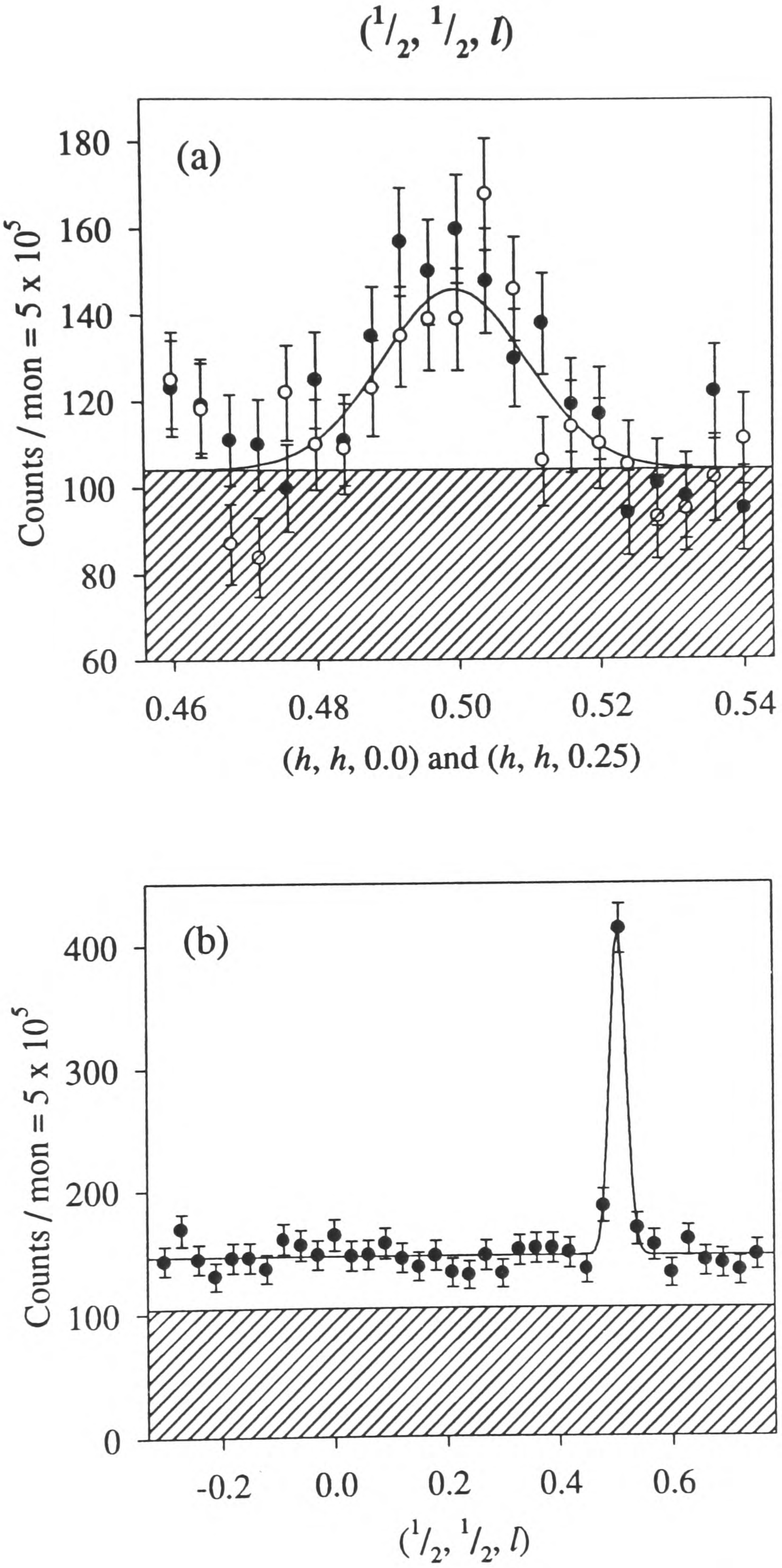

Figure 45: (a) *hh*-scans and (b) *l*-scan at 1.7 K showing the existence of a ridge along *l*. In (a) there are scans through $l = 0.0$ (closed circles) and $l = 0.25$ (open circles); in (b), the peak at $l = {}^1/_2$ is a Cu type-II ground-state reflection. A monitor count of 5 x 10^5 takes about 125 s. (Contaminated, reduced crystal).

3.5c The Cu type-II intermediate phase

To investigate the Cu type-II phases I measured sets of reflections at 57.5 K, 30 K and 4.2 K. Table 22 lists the intensities measured at 30 K, a temperature which is approximately midway between Cu type-I and type-II ground-state. The intensities were fitted both with and without an ordered moment on the Cu(1) site. A slight improvement to the fit was made by including a Cu(1) moment, and this fit is given in Table 22.

Table 22: Observed and fitted intensities for the Cu type-II intermediate phase at 30 K. (Contaminated, reduced crystal).

(h, k, l)	I_{obs} / μ_B^2	I_{fit} / μ_B^2
$^1/_2, ^1/_2, 1$	11.3 ± 0.5	12.8
$^1/_2, ^1/_2, 2$	19.3 ± 1.4	21.6
$^1/_2, ^1/_2, 3$	2.5 ± 0.5	2.6
$^1/_2, ^1/_2, 4$	9.3 ± 0.6	8.8
$^1/_2, ^1/_2, 5$	27.7 ± 0.8	25.6
$^1/_2, ^1/_2, 6$	9.7 ± 0.8	8.8
$^3/_2, ^3/_2, 1$	4.8 ± 0.7	4.7
$^3/_2, ^3/_2, 2$	5.6 ± 0.7	6.9
$^1/_2, ^1/_2, ^1/_2$	5.2 ± 0.2	5.1
$^1/_2, ^1/_2, ^3/_2$	25.9 ± 1.2	25.8
$^1/_2, ^1/_2, ^5/_2$	17.0 ± 0.8	17.4
$^1/_2, ^1/_2, ^9/_2$	27 ± 3	25
$^1/_2, ^1/_2, ^{11}/_2$	20 ± 6	27
$^3/_2, ^3/_2, ^3/_2$	8.4 ± 0.7	8.7
$^3/_2, ^3/_2, ^5/_2$	5.8 ± 0.7	5.4
		$\chi^2 = 2.7$

The results of the fit are a Cu(2) moment of (0.57 ± 0.06) μ_B, a Cu(1) moment of (0.022 ± 0.008) μ_B, a turn angle of $\phi = (48.5 \pm 0.5)°$, and a radial contraction of $\beta = (17 \pm 3)$ %. In view of the results found at lower temperatures, it is probable that the non-zero Cu(1) moment is a genuine effect. The moment is coupled ferromagnetically to the Cu(2) moments above and below it, as illustrated in Figure 15 (Section *II-2.1*).

At 57.5 K, the fit gave a Cu(2) moment of (0.57 ± 0.05) μ_B, $\phi = (29.8 \pm 1.2)°$, and a radial contraction of $\beta = (25 \pm 3)$ %. There was not enough data at 57.5 K to determine whether or not there was a small moment on the Cu(1) ions. This fit had a χ^2 of 1.2.

3.5d The Cu type-II ground-state

The data taken at lower temperatures, however, is much more conclusive. Table 23 lists the observed and fitted intensities of the type-II ground-state at 4.2 K. The refinement gave a Cu(2) moment of (0.59 ± 0.05) μ_B, a Cu(1) moment of (0.024 ± 0.006) μ_B, and a radial contraction of the Cu(2) wave function of $\beta = (14 \pm 5)$ %. If the Cu(1) moment is constrained to be zero, then a much worse χ^2 of 6.7 is obtained.

Table 23: Observed and fitted intensities for the Cu type-II ground-state at 4.2 K. (Contaminated, reduced crystal).

(h, k, l)	I_{obs} / μ_B^2	I_{fit} / μ_B^2
$\frac{1}{2}, \frac{1}{2}, \frac{1}{2}$	9.0 ± 0.3	8.9
$\frac{1}{2}, \frac{1}{2}, \frac{3}{2}$	46.7 ± 0.8	47.0
$\frac{1}{2}, \frac{1}{2}, \frac{5}{2}$	33.0 ± 0.9	33.2
$\frac{1}{2}, \frac{1}{2}, \frac{9}{2}$	42.6 ± 1.3	41.8
$\frac{1}{2}, \frac{1}{2}, \frac{13}{2}$	4.2 ± 0.9	3.4
$\frac{3}{2}, \frac{3}{2}, \frac{3}{2}$	13.5 ± 1.7	14.2
		$\chi^2 = 0.8$

Below 13 K, the Cu type-II reflections show a reduction in intensity as temperature decreases (see Figure 44). As both the ($^1/_2$, $^1/_2$, $^3/_2$) and the ($^1/_2$, $^1/_2$, $^5/_2$) reflections show this effect, the decrease can not be the result of the Cu(1) moment increasing and combining destructively with the Cu(2) moment (if this were the case, then one reflection would increase in intensity as the other decreased - see Appendix *II-4.7*). It is therefore the Cu(2) moment which is decreasing in magnitude, by a factor of 0.946 ± 0.010 between 13 K and 1.5 K.

3.6 Discussion

3.6a The measured parameters

By taking measurements on four different crystals, it is possible to examine the effects of both oxygen content and aluminium content on the different types of magnetic ordering. Table 24 lists the ordering temperatures, magnetic moments *etc.* for the different crystals.

Table 24: Parameters of the different magnetic orderings for all four crystals measured.

	Pure crystal		Al-contaminated crystal	
Parameter	Oxygenated	Reduced	Oxygenated	Reduced
$T_{Cu, I}$ / K	266 ± 1	347 ± 1	362 ± 2	369 ± 1
$T_{Cu, II}$ / K	–	–	11 ± 1	100 ± 5
$T_{Cu, II\,(g.s.)}$ / K	–	–	–	8 ± 2
$T_{Pr\,(3D)}$ / K	19.0 ± 0.2	11.0 ± 0.5	11 ± 1	–
$T_{Pr\,(2D)}$ / K	–	–	(3 ± 1) ?	7 ± 1
$\mu_{Cu(2)}$ / μ_B	0.58 ± 0.08	0.60 ± 0.10	0.54 ± 0.04	0.59 ± 0.05
$\Delta\mu_{Cu(2)}$ / μ_B	–0.22 ± 0.04	–0.10 ± 0.02	–0.081 ± 0.009	–0.025 ± 0.006
$\mu_{Cu(1)}$ / μ_B	–	–	< 0.03	0.024 ± 0.006
μ_{Pr} / μ_B	0.85 ± 0.12	1.3 ± 0.2	0.54 ± 0.04	0.25 ± 0.03
Pr (3*D* : 2*D*)	100 : 0	100 : 0	(91±4 : 9±1) ?	0 : 100
$\theta_{Pr\,(3D)}$ / °	45 ± 5	41 ± 5	49 ± 5	–
$\theta_{Pr\,(2D)}$ / °	–	–	(60 ± 12) ?	42 ± 13
Γ^{-1} / Å	160 ± 6	11.1 ± 0.5	16.9 ± 1.1	–

The names of most of the parameters are self-explanatory, for instance $T_{Cu, II\,(g.s.)}$ is the temperature at which the copper ordering reaches the type-II ground-state. The ordered component of the Cu(2) moment always decreases if the Pr moments order in three dimensions. Hence $\mu_{Cu(2)}$ is the value of the moment just above the 3*D* Pr ordering temperature, and $\Delta\mu_{Cu(2)}$ is the change in the Cu(2) moment after the Pr moments have ordered in three dimensions. Γ^{-1} is the correlation length of the 3*D* Pr ordering along the *c*-direction. Pr (3*D* : 2*D*) gives the ratio of the number of Pr moments ordering in three dimensions to the number ordering in two dimensions, assuming that the moment size is the same in both cases. μ_{Pr} is the magnitude of the Pr moment at the lowest temperatures attainable.

It is my postulate that the addition of oxygen and the removal of aluminium has similar effects on the electronic balance in $PrBa_2Cu_3O_{6+x}$, and that the trends in almost all of the measured parameters can be explained in terms of these effects.

First, it is worthwhile taking a closer look at the trends in the observed parameters (with increasing oxygen content and decreasing aluminium content) where clear trends exist, and this is done in Table 25. Parameters in which there were no clear trends were $\mu_{Cu(2)}$, $\mu_{Cu(1)}$, μ_{Pr}, $\theta_{Pr(2D)}$ and $\theta_{Pr(3D)}$, and these parameters shall be briefly discussed later.

Table 25: The clear trends in the measured parameters with increasing oxygen content and decreasing aluminium content.

	Increasing O	Decreasing Al
$T_{Cu,I}$	↓	↓
$T_{Cu,II}$	↓	↓
$T_{Cu,II(g.s.)}$	↓	↓
$T_{Pr(3D)}$	↑	↑
$T_{Pr(2D)}$	↓	↓
$\lvert\Delta\mu_{Cu(2)}\rvert$	↑	↑
Pr (3*D* : 2*D*)	↑	↑
Γ^{-1}	↑	↑

As can be seen, the trends with increasing oxygen content and decreasing aluminium content are identical, as would be expected if they were the results of similar effects on the electronic balance.

3.6b The general redistribution of charge

Figure 46 shows the postulated redistribution of electrons, as oxygen is added to the basal plane and aluminium is removed from the Cu(1) sites. As mentioned in Section *1-4.1*, the Cu(2) ions in $PrBa_2Cu_3O_7$ 'share' a spare valency per chemical unit cell. Increasing the oxygen content in the basal plane causes electronic charge to move along the directions shown by solid arrows and increases the number of holes in the $Cu\text{-}O_2$ planes. This in turn increases the tendency of the Pr ions to hybridise with their surrounding oxygen ions, which is a lesser flow of electronic charge indicated by dotted arrows. The removal of Aluminium causes a flow of charge in a similar way.

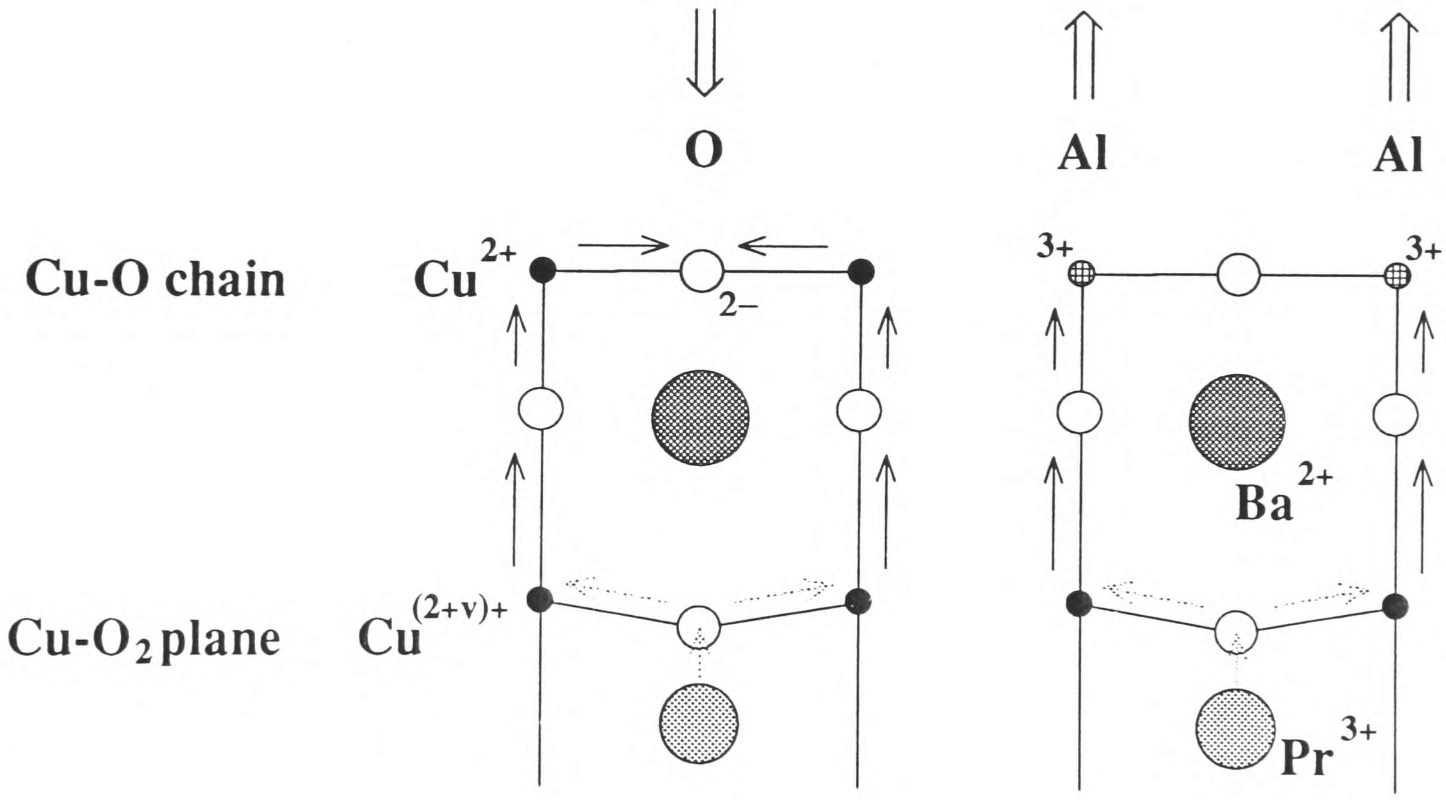

Figure 46: The flow of electrons as oxygen is added and aluminium is removed.

With this model, we are now in a position to begin to explain the trends in the measured parameters; here, 'adding oxygen' can also be read to mean 'removing aluminium'. Adding oxygen increases the number of holes in the $Cu\text{-}O_2$ planes, disrupting the Cu magnetism and so reducing $T_{Cu,I}$. On the other hand, it increases the hybridisation of the Pr atoms, strengthening the coupling between Pr atoms along the *c*-axis and so increasing $T_{Pr(3D)}$ and the correlation length Γ^{-1}. The Pr atoms only order in 2*D* when they are prevented from ordering in 3*D*, and so this correspondingly decreases $T_{Pr(2D)}$.

The Pr-Pr interaction along the *c*-axis must be an indirect exchange interaction involving the same intermediate atoms as mediate the Cu(2)-Cu(2) exchange. It would not be surprising if the precise nature of the exchange most desirable for Cu(2) ordering were not the same as that for Pr ordering, and so as the Pr coupling increases there must be a corresponding decrease in the Cu(2) coupling. This therefore explains why $|\Delta\mu_{Cu(2)}|$ should follow the same trend as $T_{Pr(3D)}$ and Γ^{-1}.

3.6c The local redistribution of charge

The only trends of Table 25 so far unexplained are the type-II phase Néel temperatures. There are two possible ways in which the type-II phases could come about, differing in what is cause and what is effect.

It should be noted that in the type-I phase, there is no 'natural' direction in which the Cu(1) moments can point, i.e. they can be neither parallel nor antiparallel to their adjacent Cu(2) moments (see Figure 13, Section *II-2.1*). Indeed, in a perfect crystal the effects of the ordering of the Cu(2) moments must cancel at the Cu(1) sites. The fact that the type-II phases only occur in the Al-contaminated samples suggests that the presence of impurities distorts the electronic balance on a local scale in some asymmetric way.

- (a) The first possibility is that the distortion produces a favourable moment direction for the Cu(1) moments, which happens to be along the line $\phi = 90°$ (Figure 14, Section *II-2.1*). As temperature decreases, the Cu(1) moments start to order, and this causes the rotation of the Cu(2) moments in the type-II intermediate phase, in a desire to produce again a collinear ordering.
- (b) The second possibility is that the distortion produces, at low temperatures, a ferromagnetic coupling of the far pair of Cu(2) moments (see Section *II-2.1*), as in

the type-II ground-state, which is more favourable than the higher-temperature antiferromagnetic coupling of the type-I phase. Hence, as temperature decreases, the Cu moments enter a noncollinear phase as the sample passes from the type-I phase to the type-II ground-state. However, the effects of the ordering of the Cu(2) moments would then no longer cancel at the Cu(1) sites, encouraging the Cu(1) moments to order.

The simple observation of the type-II ordering can not distinguish between these two possibilities. However, an attempt to explain the measured trends in the parameters is interesting. Obviously, as aluminium is removed there will be less distortion, and so you would expect $T_{Cu,II}$ and $T_{Cu,II(g.s.)}$ to decrease. But why should increasing oxygen have the same effect, when this does not produce a type-II phase in the pure crystals?

One answer would be that the removal of oxygen has disrupted the magnetism in the Cu-O_2 plane as discussed for $T_{Cu,I}$. However, the changes in $T_{Cu,II}$ with oxygen content seem strongly out of proportion with the changes in $T_{Cu,I}$ (see Table 24). A more likely scenario is that adding oxygen to the basal plane helps to 'smooth out' the distortion caused by the presence of aluminium and hence counteracts the tendency to form the type-II phases. The 'smoothing out' would be more effective the further away you are from the basal plane, which suggests that possibility (b) is more likely, i.e. the presence of aluminium changes the coupling of the far pair of the Cu(2) moments. However, this is by no means conclusive.

3.6d The Pr moment

The remaining parameters to discuss are the magnitudes of the ordered components of the magnetic moments, and the angles at which the Pr moments are aligned away from the *c*-axis. Of these, $\mu_{Cu(2)}$, $\mu_{Cu(1)}$, $\theta_{Pr(3D)}$ and $\theta_{Pr(2D)}$ are all the same within error (when they occur), suggesting that they are mostly independent of the effects of oxygenation and Al-contamination. The only anomalous parameter is the ordered component of the Pr moment, μ_{Pr}.

Decreasing the Al content does produce a trend in μ_{Pr} - as Al decreases, μ_{Pr} increases. However, it is unlikely that this is solely the result of increasing the coupling along the *c*-axis, since increasing the oxygen content does not have the same effect in the pure crystal. The size of the Pr moment will be determined by its ground-state electronic wave function. Unlike the Cu(2) ion, in which $3d(x^2{-}y^2)$ is easily the symmetry of the ground-state wave function for the magnetic hole (see Section *II-1.1b*), the crystal field eigenstates for the Pr ion are much closer together. In fact, the 'ground-state' of the Pr^{3+} ion in $PrBa_2Cu_3O_{6+x}$ is thought to consist of three closely-spaced eigenstates. The separation and order of these eigenstates could be highly sensitive to such things as the oxygen- and aluminium-content of the crystal, in which case you would not necessarily expect to find an obvious trend in the value of μ_{Pr}. Furthermore, it could well be that, because of the lower Néel temperatures of the Al-contaminated crystals, the measured moments in these crystals have not yet reached their fully ordered values.

3.6e Comparison with previous publications

As was discussed in Section *II-2.1*, these are the first measurements on crystals in which the purity has been carefully measured and characterised. It is probably reasonable to assume that, in the past, powder samples have been purer than single crystals.

Taking the previous measurements made on powder samples in Table 6, it is clear that $T_{Cu,I}$ decreases with increasing oxygen content, as I have also found. There is also an absence of any Cu type-II ordering, which was likewise observed in the pure crystals of $YBa_2Cu_3O_{6+x}$[51]. Hence, assuming that the crystal of Rosov *et al*[49] is impure, possibly through Al-contamination, our ordering temperatures are consistent with measurements in the past.

There have been no previous measurements of $\Delta\mu_{Cu(2)}$ as the Pr moments order, perhaps because people did not expect to see such an effect.

Our results concerning the Pr moment, however, are slightly at odds with what has previously been measured. In particular, our Néel temperature for the pure, oxygenated crystal, 19 K, is somewhat higher than the 17 K which is more generally measured. This implies that the Pr moments are more strongly coupled in our crystals than in powders. It is unlikely that this is because our crystals are purer, or more oxygenated, than powder samples; however, this would be as expected if there were more copper vacancies in crystals than powders (see Section *II-3.1*). This may also be responsible for the change in the Pr coupling from antiferromagnetic along the *c*-axis in the powder samples to ferromagnetic in our samples.

I measure a Pr moment aligned significantly away from the *c*-axis ($\theta \sim 45°$). This has not been previously observed in neutron scattering; however, as mentioned in Section *II-2.2*, all previous attempts at a θ-refinement were made on the basis of just two reflections and were 'tentative'. Other evidence does come from Mössbauer spectroscopy[56], with $\theta \sim 65°$.

The previous magnitudes of the Pr moments measured are $(0.74 \pm 0.08)\ \mu_B$ for an oxygenated powder sample[53], and $(1.9 \pm 0.2)\ \mu_B$ for a reduced powder sample[55]. These are in reasonable agreement with my parameters, especially considering that previous refinements may have been using the wrong geometric structure factor.

Finally, there is the correlation length of the 3*D* Pr ordering. This is harder to measure in powder neutron scattering than in single crystal neutron scattering; however, M. Guillaume *et al*[55] measured a correlation length of (10 ± 1) Å, again in agreement with my measurements.

In conclusion, the trends in all of the measured parameters relating to magnetism except μ_{Pr} can be understood in terms of a simple model describing the redistribution of electronic charge as oxygen is added or aluminium removed. The investigation of both pure and Al-contaminated samples sheds light on discrepancies in previous experimental results. Effects have been measured which have not been previously observed in neutron scattering, such as the alignment of the Pr moment away from the *c*-axis and the reduction of the ordered component of the Cu(2) moment on Pr ordering.

4. Appendix

4.1 The reactor source

All of the experiments in Section *II*, concerning elastic neutron scattering, were performed at the DR3 reactor, Risø National Laboratory, Denmark. This is a reactor source, i.e. the neutrons are produced through the same self-sustaining process of nuclear fission as is used in nuclear reactors for the production of electricity. Briefly, a thermal neutron strikes a ^{235}U nucleus; the nucleus splits into two smaller nuclei, releasing an of average 2.5 neutrons; 1.5 neutrons are needed to sustain the reaction, leaving on average 1 neutron, with an energy of ~2 MeV, to go to a neutron experiment. In a power generator, the daughter nuclei generally have a kinetic energy of ~180 MeV, and it is this energy which is used to heat the moderator, and so the coolant, and to produce electricity.

The usable neutrons do not leave the reactor core immediately - like the rest of the fission products, they will collide several times with the moderator, and so when they leave their mean energy will be characteristic of the moderator's temperature. At DR3, the moderator is cooled by liquid H_2 at 34 K and 16 atmospheres of pressure, and hence DR3 is a 'cold source'. The peak flux occurs at 13.7 meV.

The main advantage in having a cold neutron source is that you have a higher resolution in your experiments: for instance, for elastic neutron experiments using neutrons of wavevector *k*, the full range of scattering angles $0° \to 180°$ is equivalent to a wavevector transfer of $2k$. Hence, as energy (and so *k*) decreases for the same angular resolution, the resolution in reciprocal space increases. However, the price that is paid is that you access less of reciprocal space.

Our experiments were performed at an energy of 13.7 meV ($k = 2.57$ Å^{-1}), which we felt gave us the optimum conditions for our experiment. A lower energy would have given us more resolution in reciprocal space; however, this drawback was outweighed by four advantages.

First, we could access more of reciprocal space, and since we would need as many reflections as possible to determine the magnetic structures, this was clearly advantageous. (Looking much further in reciprocal space would not be as useful, however - magnetic form factors tend to drop quite quickly much after a wavevector transfer of 2π / atomic size ~ 6 Å^{-1}).

Second, it is likely that the Pr ion in $PrBa_2Cu_3O_{6+x}$ has crystal field excitations around 5 meV, and we wished to avoid such excitations as they could have affected our measurements.

Third, 13.7 meV is an energy which is compatible with a graphite filter, and as discussed in the next section, this is highly desirable in a neutron experiment.

Finally, this energy coincides with the maximum neutron flux, allowing us to gather accurate data quicker.

4.2 Filters

A triple-axis spectrometer is designed to monochromate both the beam striking the sample and that leaving it by the use of Bragg reflections at the monochromator and the analyser (see Figure 8, Section *II-1.2b*). However, if Bragg's law is satisfied for an order $n = 1$ and a wavelength λ, then it will also be satisfied by an order $n = 2$ and a wavelength $\lambda/2$,

$$\lambda = 2d\sin\theta = 2(\lambda/2) \tag{73}$$

This problem is known has 'higher order contamination', and it can be solved by the use of a filter. A filter is basically a material which allows neutrons of wavelength λ to pass, but prevents wavelengths $\lambda/2$, $\lambda/3$ *etc.* doing the same. There are two types of neutron filter in general use: the beryllium filter and the graphite filter.

The beryllium filter has a transmission which looks like a step function - below 5 meV (1.6 Å^{-1}), the transmission is very high, whilst above this the transmission is very low. The polycrystalline beryllium basically acts as a very strong powder scatterer of neutrons, by Bragg's law, with a minimum plane spacing of around $d_0 = 2$ Å. For $\lambda > 2d_0$, no diffraction is possible, and hence neutrons with $k < 2\pi/2d_0$, i.e. $k < 1.6$ Å^{-1}, pass straight through the filter. The remaining neutrons can always be scattered at some angle θ, and so very few of these make it unscattered through the filter. To make the reflections as strong as possible, beryllium filters are normally cooled by liquid nitrogen (to reduce the Debye-Waller factor).

The graphite filter works in a similar way to the Beryllium filter; however, the graphite filter is a single crystal. Hence, rather than a step function, for a given orientation there are dips in the transmission, which correspond to strong Bragg scattering of the incoming beam. The beauty of this is that if a wavelength $\lambda/2$ is reflected by the graphite filter, then $\lambda/4$, $\lambda/6$ *etc.* will be also, for exactly the same reason as the monochromator reflects them - they still fulfil the Bragg condition. The graphite filter has the advantage that it does not need to be cooled to work effectively, and hence a graphite filter was used for our experiments.

4.3 The detectors

The neutron detectors at Risø are proportional ^{3}He gas detectors. These work because thermal or cold neutrons can react with the ^{3}He particles:

$$n + {}^3\text{He} \rightarrow p + {}^3\text{T} + 0.77\ \text{MeV}.$$

(The absorption cross-section increases proportionally to the wavelength). The moving, charged reaction products then ionise their surrounding gas, and this is observed as a current pulse, since a high-voltage field of about 2 kV is applied to the gas. The size of the pulse is proportional to the reaction energy, 0.77 MeV, and so pulses caused by stray γ-rays can be distinguished and not confused with the neutron counts ('discriminated'). One of the beauties of the ^{3}He detector is that the ^{3}He never needs replacing - the tritium produced in the reaction will decay,

$${}^3\text{T} \rightarrow {}^3\text{He} + \beta^-.$$

4.4 Spectrometer geometry

In section *II-1.2*, I discussed how to calculate the Lorentzian factor under various conditions. To make use of that theory, it is necessary to be able to calculate the required angles *etc.* Here I show how to calculate the necessary quantities, using the situation which I was working on: $PrBa_2Cu_3O_{6+x}$ with the (h, h, 0) and the (0, 0, l) axes defining the scattering plane, and with the spectrometer in the right-right-right configuration. The quantities I derive are as you would observe if you were using TASCOM, the spectrometer control program used at Risø. (See Figure 47).

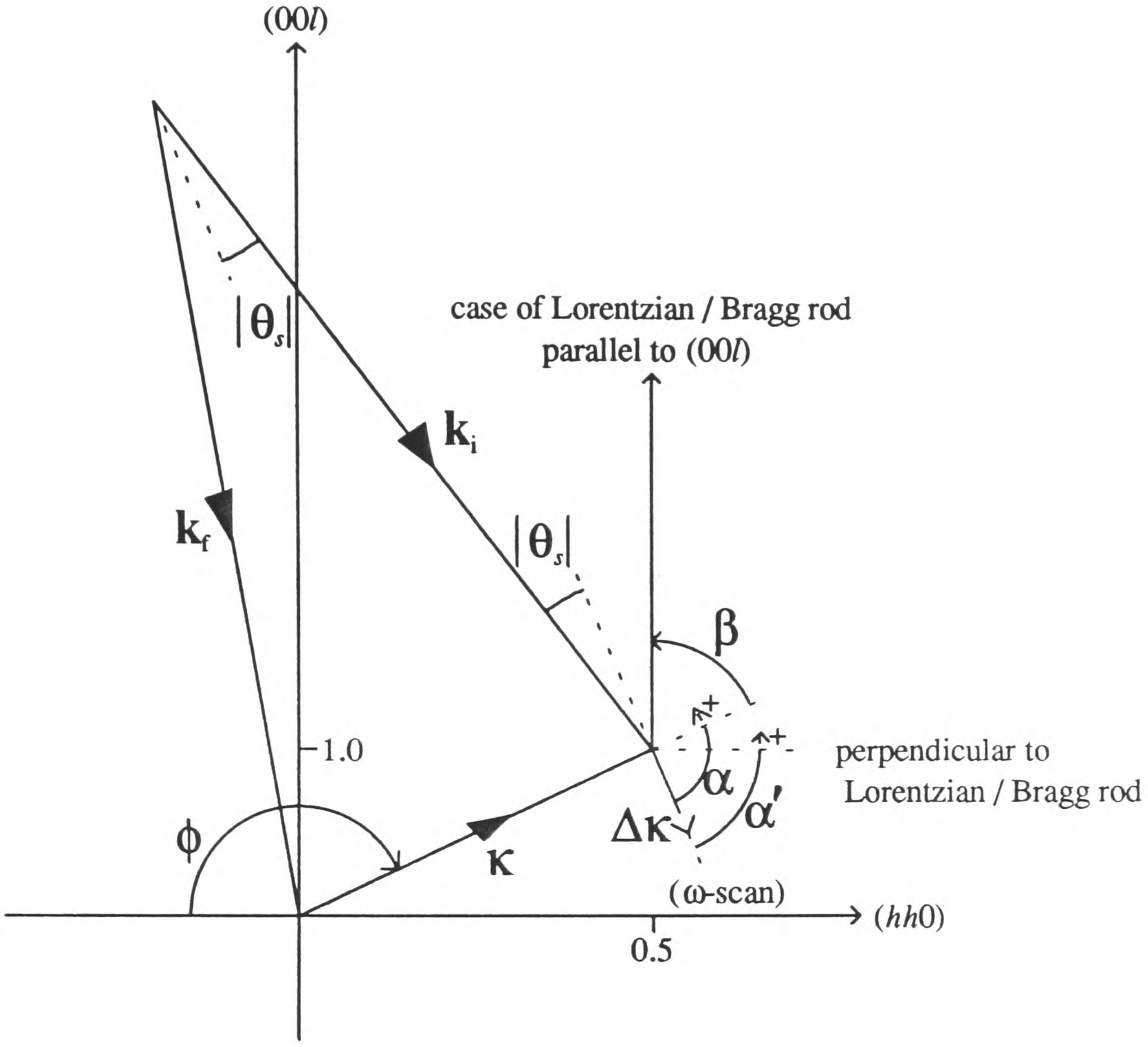

Figure 47: Various angles needed to calculate the Lorentz factors, shown for an ω-scan through the ($^1/_2$, $^1/_2$, 1).

Neutron energy:	13.7 meV
Spectrometer configuration:	right-right-right
Lattice parameters:	$a = b = 3.938$ Å
	$c = 11.809$ Å
Position in reciprocal space:	($^1/_2$, $^1/_2$, 1)
Scan:	ω-scan.

First, the position in reciprocal space must be calculated (all quantities concerning reciprocal space are in Å^{-1}, and energy is in meV):

$$\begin{aligned}\kappa_{hh0} &= 2\pi \cdot \sqrt{2}\frac{h}{a} = 1.1282 \\ \kappa_{00l} &= 2\pi \cdot \frac{l}{c} = 0.5321 \\ \kappa &= 1.2474\end{aligned} \tag{74}$$

The wavevector of the neutron is

$$k = 2\pi \cdot \sqrt{\frac{E}{81.8043}} = 2.5713 \tag{75}$$

and the Bragg angle at the sample (with 'left' being positive) is

$$\theta_s = -\sin^{-1}\left(\frac{\kappa}{2k}\right) = -14.038° \tag{76}$$

To calculate ω, the rotation of the crystal, it is necessary to relate what is happening in the reciprocal space of the crystal to the *k*-space of the spectrometer. This can be done by considering $\mathbf{k}_i$, since $\mathbf{k}_i$ is fixed in *k*-space. We know that $\mathbf{k}_i$ is at an angle of θ_s from the normal to κ; hence we should relate κ to the reciprocal axes, by using φ:

$$\begin{aligned}\phi &= -\tan^{-1}\left(\frac{\kappa_{00l}}{\kappa_{hh0}}\right);\ \text{if } \kappa_{hh0} \geq 0,\ \text{ then } \phi = \phi + \pi \\ &\rightarrow \phi = 154.751°\end{aligned} \tag{77}$$

TASCOM defines ω = 0° so that at $\mathbf{k}_f = \mathbf{k}_i$ (i.e. $\theta_s = 0°$), $\mathbf{k}_i$ is parallel to the (00*l*) axis, i.e.

$$\omega = \phi + \theta_s = 140.714° \tag{78}$$

The Bragg rods and Lorentzian broadenings we encountered were generally parallel to the (00*l*)-axis. If that is the case, then the angle which the broadening makes to κ is

$$\beta = \phi - \frac{\pi}{2} = 64.751° \tag{79}$$

That covers all the angles which can be calculated from a single position in reciprocal space; I now move onto quantities which depend on the direction of the scan. Here an important quantity is Δκ, the change in wavevector transfer over the scan. For a scan in reciprocal space, you simply calculate κ at the start- and end-points, and subtract to obtain $\Delta\kappa$. For an ω-scan around κ, the easiest thing to do is to calculate ϕ for κ and then use Equation (78) to calculate ϕ at the start- and end-points, since θ_s is fixed. The corresponding values of κ can then be calculated from ϕ; for the original value of ϕ we would get

$$\begin{aligned} \kappa_{hh0} &= -\kappa\cos\phi = 1.1282 \\ \kappa_{00l} &= \kappa\sin\phi = 0.5321 \end{aligned} \tag{80}$$

as previously determined.

The angle defining the scan direction from the wavevector transfer κ is α. Obviously the dot product rule, $\hat{\Delta\kappa}.\hat{\kappa} = \cos\alpha$, can be used to get α to within a sign; then, if the sign is wrong, κ rotated by α will not be parallel to $\Delta\kappa$, and the sign should be changed:

$$\begin{gathered} \alpha = \cos^{-1}\left(\hat{\Delta\kappa}.\hat{\kappa}\right);\ \text{if}\left(\hat{\kappa}\ \text{rotated by}\ \alpha\right) \neq \hat{\Delta\kappa},\ \ \text{then}\ \alpha = -\alpha \\ \rightarrow \alpha = -90^\circ \end{gathered} \tag{81}$$

In the case of Bragg rods and Lorentzian broadening, the co-ordinate system for the resolution function is redefined. In these new co-ordinates, the scan direction is given by

$$\alpha' = \frac{\pi}{2} + \alpha - \beta = -64.751^\circ \tag{82}$$

(see Equation (61), Section *II-1.2e*).

4.5 Normalisation of intensities

To be able to determine magnetic moments in absolute units, i.e. Bohr magnetons (μ_B), it is necessary to normalise the intensities of the magnetic reflections. In principle, it is possible to measure the mass of the crystal and so calculate the number of unit cells which are scattering; however, this is not very accurate since it does not account for absorption *etc.* A better method is to compare the magnetic reflections with the nuclear reflections - the nuclear scattering lengths are known, and so absolute magnetic moments can be calculated.

The elastic differential cross-section for nuclear reflections is[62]

$$\left(\frac{d\sigma}{d\Omega}\right)^{el}_{nuc} = N\frac{(2\pi)^3}{v_0}\left\langle\left|F_N(\kappa)\right|^2\right\rangle, \qquad (83)$$
$$F_N(\kappa) = \sum_j b_j \exp(i\kappa.\mathbf{r}_j)\exp(-W_j(\kappa))$$

where N is the number of chemical unit cells of volume v_0, b_j is the scattering length of the jth atom (in fm), W_j is the Debye-Waller factor, and the other symbols have their usual meanings.

The corresponding quantity for magnetic reflections is[28]

$$\left(\frac{d\sigma}{d\Omega}\right)^{el}_{mag} = N\frac{(2\pi)^3}{v_0}\left(\frac{\gamma r_0}{2}\right)^2\sum_{\alpha\beta}\left\langle(\delta_{\alpha\beta} - \hat{\kappa}_\alpha\hat{\kappa}_\beta)F^\alpha(\kappa)F^{\beta *}(\kappa)\right\rangle, \qquad (84)$$
$$F^\alpha(\kappa) = \sum_j \mu_j^\alpha f_j(\kappa)\exp(i\kappa.\mathbf{r}_j)$$

where γ (= 1.913) is the gyromagnetic ratio, r_0 (= 2.818 fm) is the classical electron radius, μ_j^α is the α-component of the magnetic moment of the jth atom, and the other symbols again have their usual meanings.

The nuclear intensities can then be calculated as

$$I^{el}_{nuc}(\kappa) = k_{nuc}\left\langle\left|F_N(\kappa)\right|^2\right\rangle \qquad (85)$$

where k_{nuc}, the constant of proportionality between the observed nuclear intensities (from the measured count rate) and the calculated $\left\langle\left|F_N(\kappa)\right|^2\right\rangle$, is determined by fitting. The count rates for nuclear reflections are normalised to a monitor count of 10^3.

Similarly, the magnetic intensities can be written as

$$I^{el}_{mag}(\kappa) = k_{mag}\sum_{\alpha,\beta}\left\langle(\delta_{\alpha\beta} - \hat{\kappa}_\alpha\hat{\kappa}_\beta)F^\alpha(\kappa)F^{\beta *}(\kappa)\right\rangle \qquad (86)$$

The count rates for magnetic reflections, being generally weaker, are normalised to a monitor count of 10^6; also, the magnetic unit cell is 2 x 2 x 2 chemical unit cells. The

---

[62] S.W. Lovesey, *Theory of neutron scattering from condensed matter* volume 1, §4.2, Oxford Science Publications (1986).

constant of proportionality k_{mag} can now be determined from k_{nuc}, allowing the magnetic moments to be determined absolutely, as follows.

In terms of the observed intensities, the differential nuclear cross-sections can be written as

$$\left(\frac{d\sigma}{d\Omega}\right)^{el}_{nuc} = N\frac{(2\pi)^3}{v_0} I^{el}_{nuc}(\kappa)\cdot 10^3 \tag{87}$$

where the 10^3 represents the monitor counts. Similarly,

$$\left(\frac{d\sigma}{d\Omega}\right)^{el}_{mag} = (N/8)\frac{(2\pi)^3}{(8v_0)}\left(\frac{\gamma r_0}{2}\right)^2 I^{el}_{mag}(\kappa)\cdot 10^6 \tag{88}$$

The factors of eight are due to the magnetic unit cell being 8 times greater than the chemical unit cell. Hence the relationship between the constants of proportionality is

$$\frac{k_{nuc}}{k_{mag}} = \left(\frac{\gamma r_0}{16}\right)^2 \cdot 10^3 = 113.5 \tag{89}$$

4.6 Separation of Cu and Pr intensities

There are occasions when both the Cu ordering and the Pr ordering contribute intensities to a particular reflection; in principle, their amplitudes will add, and so there could be a cross-term in the intensity of the peak. In our experiments, the Pr ordering was always ferromagnetically coupled along the *c*-axis, giving peaks at integer values of *l*. It can be shown that the Pr and Cu contributions to these peaks add as intensities with no cross-term.

In general, both the Cu(1) sites and the Cu(2) sites may be ordered, and so the Cu component of the magnetic structure factor will be

$$F^{\alpha}_{Cu} = f_{Cu(1)}(\kappa)\sum_j \mu^{\alpha}_j \exp(i\kappa.\mathbf{r}_j) + f_{Cu(2)}(\kappa)\sum_k \mu^{\alpha}_k \exp(i\kappa.\mathbf{r}_k) \tag{90}$$

The Cu(2) moments can be decomposed into two perpendicular components,

$$\mu_k = \mu_{k_I} + \mu_{k_{II}} \tag{91}$$

where μ_{k_I} is the component along the $\phi = 0$ direction (see Figure 14, Section *II-2.1*) responsible for the integer-l reflections, and $\mu_{k_{II}}$ is the component along the $\phi = 90°$ direction responsible for the half-integer-l reflections.

Now each of these components forms a collinear ordering, i.e. they can be written in the form

$$\begin{aligned} \mu_{k_I}^{\alpha} &= \sigma_{k_I}\mu_I^{\alpha} \\ \mu_{k_{II}}^{\alpha} &= \sigma_{k_{II}}\mu_{II}^{\alpha} \end{aligned} \tag{92}$$

Similarly, the Cu(1) moments are themselves collinear, i.e.

$$\mu_j^{\alpha} = \sigma_j \mu_{Cu(1)}^{\alpha} \tag{93}$$

Hence the Cu structure factor can be written as

$$\begin{aligned} F_{Cu}^{\alpha} = \mu_{Cu(1)}^{\alpha} f_{Cu(1)}(\kappa)\sum_j \sigma_j \exp(i\kappa.\mathbf{r}_j) + \mu_I^{\alpha} f_{Cu(2)}(\kappa)\sum_{k_I}\sigma_{k_I}\exp(i\kappa.\mathbf{r}_{k_I}) \\ +\mu_{II}^{\alpha} f_{Cu(2)}(\kappa)\sum_{k_{II}}\sigma_{k_{II}}\exp(i\kappa.\mathbf{r}_{k_{II}}) \end{aligned} \tag{94}$$

Both the Cu(1) moment and the $\mu_{k_{II}}$-component of the Cu(2) moment have period $2c$ along the c-axis and so do not contribute at the integer-l reflections. Hence, at integer-l reflections, the Cu structure factor can be simplified to

$$\begin{aligned} F_{Cu}^{\alpha} &= \mu_I^{\alpha} f_{Cu(2)}(\kappa)\sum_{k_I}\sigma_{k_I}\exp(i\kappa.\mathbf{r}_{k_I}) \\ &= 16 i \mu_I^{\alpha} f_{Cu(2)}(\kappa)\sin(2\pi l z) \\ &= i\Im_I^{\alpha} \end{aligned} \tag{95}$$

where z is the fractional height of the Cu(2) moments above the basal plane, and $\Im_I^{\alpha}$ is a real quantity.

Similarly, the Pr structure factor can be written as

$$\begin{aligned} F_{Pr}^{\alpha} &= f_{Pr}(\kappa)\sum_l \mu_l^{\alpha}\exp(i\kappa.\mathbf{r}_l) \\ &= \Im_{Pr}^{\alpha} \end{aligned} \tag{96}$$

where $\Im_{Pr}^{\alpha}$ is again a real quantity. Hence, at integer values of l, the Cu and Pr contributions to the intensity are 90° out of phase. The intensity is then

$$\begin{aligned} I &= \sum_{\alpha,\beta}\left\langle(\delta_{\alpha\beta} - \hat{\kappa}_\alpha\hat{\kappa}_\beta)\left(\Im^\alpha_{Pr} + i\Im^\alpha_l\right)\left(\Im^\beta_{Pr} - i\Im^\beta_l\right)\right\rangle \\ &= \sum_{\alpha,\beta}\left\langle(\delta_{\alpha\beta} - \hat{\kappa}_\alpha\hat{\kappa}_\beta)\left(\Im^\alpha_{Pr}\Im^\beta_{Pr} + \Im^\alpha_l\Im^\beta_l\right)\right\rangle \\ &= I_{Pr} + I_l \end{aligned} \tag{97}$$

and the Pr and Cu contributions add as intensities.

4.7 Geometric structure factors

In the case of a collinear ordering, it is often instructive to extract from the magnetic structure factor the term which relates solely to the arrangement of the moments (or components of the moments), excluding the size of the moments and their form factors. This is especially true for the case of the Cu(2) moments, since the fact that they are situated on planes separated by less than the unit cell's length introduces a modulation to the structure factor.

Hence, taking the μ_{k_I}-component of the Cu(2) moment (see Appendix *II-4.6*) characteristic of the type-I phase, we have

$$\begin{aligned} g_I &= \sum_{k_I}\sigma_{k_I}\exp\left(i\kappa.\mathbf{r}_{k_I}\right) \\ &= 16i\sin(2\pi lz) \end{aligned} \tag{98}$$

where z is the fractional height of the Cu(2) moments above the basal plane (the chemical unit cell is as shown in Figure 1). Similarly, the $\mu_{k_{II}}$-component of the Cu(2) moment characteristic of the type-II phases has a geometric structure factor of

$$g_{II} = 16\cos(2\pi lz) \tag{99}$$

again having a modulating factor. The Cu(1) moments (if they take part in the type-II phases) and the Pr moments have a much simpler geometric structure factor, since there is only one magnetic moment per chemical unit cell:

$$\begin{aligned} g_{Cu(1)} &= 8 \\ g_{Pr} &= 8\exp(i\pi l) \end{aligned} \tag{100}$$

Table 26 shows the values of the geometric structure factors for different values of l.

Table 26: The geometric structure factors for the four structures occurring in the measurements; $z = 0.35$.

l	g_I	g_{II}	$g_{Cu(1)}$	g_{Pr}
0	0.0			8
$^1/_2$		7.3	8	
1	12.9i			−8
$^3/_2$		−15.8	8	
2	−15.2i			8
$^5/_2$		11.3	8	
3	4.9i			−8
$^7/_2$		2.5	8	
4	9.4i			8
$^9/_2$		−14.3	8	
5	−16.0i			−8
$^{11}/_2$		14.3	8	
6	9.4i			8
$^{13}/_2$		−2.5	8	
7	4.9i			−8

III - Inelastic scattering and crystal field excitations

1. Crystal field levels

1.1 The origin of crystal field levels

Inelastic scattering occurs when the scattered neutron either loses or gains energy due to its interaction with the crystal. There are many ways in which this can happen; in some cases, the transferred energy is related to the crystal as a whole, rather than any particular ion, for example when scattering off phonons. In other cases, the energy is related to a single ion, and this therefore reveals information about that ion.

Crystal field levels are single-ion energy levels that occur because the crystalline environment has removed the spherical symmetry of the ion, making some electron orbitals energetically more favourable than others. If the ion has an incomplete shell (i.e. it is a magnetic ion), then some of these energy levels will be unoccupied. A scattering neutron can then induce transitions between the energy levels, changing its own energy as it does so.

It is the electric field of the surrounding ions which causes the electron wave functions of the magnetic ion to distort. The natural approach to solve such a problem would be to use first order perturbation theory to calculate the distorting Hamiltonian. The eigenvalues and eigenstates of the system are then the electron energy levels and wave functions. From the wave functions, the transition probabilities for neutron scattering can also be calculated, and hence it is possible to calculate the positions and intensities of the peaks in an inelastic neutron spectrum. In practice, the procedure is normally reversed - the measured positions and intensities of the peaks are used to deduce the wave functions and energy levels of the magnetic electrons.

It is therefore necessary to understand the perturbing Hamiltonian - however, this is not easy. The wave functions of the magnetic ion and the surrounding ions are spread out in space. Furthermore, the magnetic electrons themselves will be partially 'screened' from the effects of the surrounding ions, through their overlap with the magnetic ion's own closed electron shells. Hence inelastic scattering is often not calculated directly in terms of the crystalline environment, but in terms of 'crystal field parameters'. These are terms in the Hamiltonian which characterise the effective potential the magnetic ion is experiencing. They are useful in that they allow revealing comparisons to be made with other magnetic ions in similar environments, but, without further analysis, they only give qualitative details of the crystalline environment. However, quantitative information about the magnetic wave functions and their energies is still obtained.

1.2 The point charge model

One method that does follow a quantitative calculation from the crystal environment to the energy levels and wave functions of the magnetic ion is the 'point charge model'. This ignores the effects of screening, and replaces the extended charge density of the surrounding ions with point charges; the magnetic ion, however, still has an extended spatial structure. Although you can expect only limited accuracy from such a simplification, the point charge model has the advantages that it is easy to use, and it gives insight into the values of the crystal field parameters. It is often also useful in providing a first approximation for the crystal field parameters, from which more accurate parameters can be refined.

The formalism given here follows that of M.T. Hutchings[63], with the exception that the equations are now compatible with SI units. Let the origin be at the centre of the magnetic ion. The electrostatic potential at a position **r** due to the surrounding ions, each at a point $\mathbf{R}_j$ and with charge q_j, is

$$V(\mathbf{r}) = \frac{1}{4\pi\varepsilon_0} \sum_j \frac{q_j}{|\mathbf{R}_j - \mathbf{r}|} \tag{101}$$

where ε_0 is the permittivity of free-space.

Suppose the angle between **R** and **r** is ω; then the fraction $1/|\mathbf{R}-\mathbf{r}|$ can be expanded in terms of zeroth-order Legendre polynomials:

---

[63] M.T. Hutchings, *Point-charge calculations of energy levels of magnetic ions in crystalline electric fields*, Solid State Phys. **16**, 227-273, (1964).

$$\frac{1}{|\mathbf{R}-\mathbf{r}|}=\sum_{n=0}^{\infty}\frac{r^n}{R^{n+1}}P_n^0(\cos\omega) \tag{102}$$

Similarly, the Legendre polynomials can be expanded in terms of tesseral harmonics,

$$P_n^0(\cos\omega)=\frac{4\pi}{2n+1}\sum_{\alpha}Z_{n\alpha}(\hat{\mathbf{r}})Z_{n\alpha}(\hat{\mathbf{R}}) \tag{103}$$

Tesseral harmonics are simply symmetric and antisymmetric combinations of spherical harmonics, with the advantage that they are real:

$$\begin{aligned} Z_{n0} &= Y_n^0 \\ \left.\begin{aligned} Z_{nm}^c &= \tfrac{1}{\sqrt{2}}\left[Y_n^{-m}+(-1)^m Y_n^m\right] \\ Z_{nm}^s &= \tfrac{i}{\sqrt{2}}\left[Y_n^{-m}-(-1)^m Y_n^m\right] \end{aligned}\right\} &\quad 0<m\le n \end{aligned} \tag{104}$$

Each term in the α-summation implicitly sums over the tesseral harmonics of order n, i.e.

$$\sum_{\alpha}Z_{n\alpha}Z_{n\alpha}=Z_{n0}Z_{n0}+\sum_{m}Z_{nm}^cZ_{nm}^c+Z_{nm}^sZ_{nm}^s \tag{105}$$

The spherical harmonics are as defined in Hutchings, p238.

It is convenient at this stage, for reasons which will become apparent later, to separate the tesseral harmonics into a scalar factor and an angular factor:

$$Z_{n\alpha}(\hat{\mathbf{r}})=k_{n\alpha}\frac{f_{n\alpha}(\mathbf{r})}{r^n} \tag{106}$$

Some examples of $k_{n\alpha}$ and $f_{n\alpha}(\mathbf{r})/r^n$ are given in Table 27 (for $m=0$), and Table 28 (for $m\neq 0$).

Table 27: $k_{n\alpha}$ and $f_{n\alpha}(\mathbf{r})/r^n$ for $m = 0$. The $n = 0$ term is omitted, because it just offsets the energy scale, and so has no effect on the measurement of energy differences.

n	m	k_{n0}	$\frac{f_{n0}(\mathbf{r})}{r^n}$
2	0	$\frac{1}{4}\left(\frac{5}{\pi}\right)^{½}$	$3\cos^2\theta - 1$
4	0	$\frac{3}{16}\left(\frac{1}{\pi}\right)^{½}$	$35\cos^4\theta - 30\cos^2\theta + 3$
6	0	$\frac{1}{32}\left(\frac{13}{\pi}\right)^{½}$	$231\cos^6\theta - 315\cos^4\theta + 105\cos^2\theta - 5$

Table 28: $k_{n\alpha}$ and $f_{n\alpha}(\mathbf{r})/r^n$ for $m \neq 0$.

n	m	$k_{n\alpha}$	$\frac{f^c_{nm}(\mathbf{r})}{r^n}$	$\frac{f^s_{nm}(\mathbf{r})}{r^n}$
2	2	$\frac{1}{4}\left(\frac{5}{\pi}\right)^{½}$	$\sin^2\theta\cos 2\phi$	$\sin^2\theta\sin 2\phi$
4	2	$\frac{3}{8}\left(\frac{5}{\pi}\right)^{½}$	$\left(7\cos^2\theta - 1\right)\sin^2\theta\cos 2\phi$	$\left(7\cos^2\theta - 1\right)\sin^2\theta\sin 2\phi$
4	3	$\frac{3}{8}\left(\frac{70}{\pi}\right)^{½}$	$\cos\theta\sin^3\theta\cos 3\phi$	$\cos\theta\sin^3\theta\sin 3\phi$
4	4	$\frac{3}{16}\left(\frac{35}{\pi}\right)^{½}$	$\sin^4\theta\cos 4\phi$	$\sin^4\theta\sin 4\phi$
6	2	$\frac{1}{64}\left(\frac{2730}{\pi}\right)^{½}$	$\left(16\cos^4\theta - 16\sin^2\theta\cos^2\theta + \sin^4\theta\right)\sin^2\theta\cos 2\phi$	$\left(16\cos^4\theta - 16\sin^2\theta\cos^2\theta + \sin^4\theta\right)\sin^2\theta\sin 2\phi$
6	3	$\frac{1}{32}\left(\frac{2730}{\pi}\right)^{½}$	$\left(11\cos^2\theta - 3\right)\cos\theta\sin^3\theta\cos 3\phi$	$\left(11\cos^2\theta - 3\right)\cos\theta\sin^3\theta\sin 3\phi$
6	4	$\frac{21}{32}\left(\frac{13}{7\pi}\right)^{½}$	$\left(11\cos^2\theta - 1\right)\sin^4\theta\cos 4\phi$	$\left(11\cos^2\theta - 1\right)\sin^4\theta\sin 4\phi$
6	6	$\frac{231}{64}\left(\frac{26}{231\pi}\right)^{½}$	$\sin^6\theta\cos 6\phi$	$\sin^6\theta\sin 6\phi$

Hence the potential can be expressed as

$$V(\mathbf{r}) = \sum_{n=0}^{\infty} \sum_{\alpha} r^n \gamma_{n\alpha} Z_{n\alpha}(\hat{\mathbf{r}}) \tag{107}$$

where

$$\gamma_{n\alpha} = \frac{1}{(2n+1)\varepsilon_0} \sum_{j=1}^{k} \frac{q_j}{(R_j)^{n+1}} Z_{n\alpha}(\hat{\mathbf{R}}_j) \tag{108}$$

The $\gamma_{n\alpha}$ terms are not hard to calculate, just depending on the geometry of the environment, and hence the electrostatic potential is now expressed as a sum of Tesseral harmonics.

1.3 The Stevens' Operator method

We could proceed from here by integrating directly the potential $V(\mathbf{r})$ with the free-ion single-electron wave functions, following the methods of perturbation theory. This would involve us summing over all the magnetic electrons in the magnetic ion. However, the use of "Stevens' Operators" makes all this unnecessary. The theory behind this method is that the effect of the integration is to replace the sum of the angular factors over the magnetic electrons by an operator equivalent:

$$\sum f_{n\alpha}(\mathbf{r}) \Rightarrow \theta_n \langle r^n \rangle O_n^\alpha \tag{109}$$

$f_{n\alpha}(\mathbf{r})$ is proportional to r^n, and so the factor $\langle r^n \rangle$ takes care of the radial integral. (This is the reason for expressing the Tesseral harmonics in the form of Equation (106)). The Stevens' Operator O_n^α is obtained by replacing x, y, and z by the operators J_x, J_y and J_z, allowing for the non-commutation of J_x, J_y and J_z; hence the Stevens' Operator has the same transformation properties as $f_{n\alpha}(\mathbf{r})$. Finally, the factor θ_n contains the necessary numerical factor to make the angular integral work; this is a tabulated, once-for-all calculation depending on the angular momentum *etc.*

Traditionally, $\theta_2 = \alpha_J$, $\theta_4 = \beta_J$, and $\theta_6 = \gamma_J$. The method is described fully by Bleaney and Stevens[64]. For example,

---

[64] B. Bleaney and K.W.H. Stevens, *Paramagnetic resonance*, Rept. Progr. Phys. **16**, 108-159, (1953).

$$\begin{aligned}\sum f_{20}(\mathbf{r}) &= \sum 3z^2 - r^2 \Rightarrow \alpha_J\langle r^2\rangle\left[3J_z{}^2 - J(J+1)\right] = \alpha_J\langle r^2\rangle O_2^0 \\ \sum f_{22}^c(\mathbf{r}) &= \sum x^2 - y^2 \Rightarrow \alpha_J\langle r^2\rangle\left[J_+{}^2 + J_-{}^2\right]/2 = \alpha_J\langle r^2\rangle O_2^2 \\ \sum f_{22}^s(\mathbf{r}) &= \sum 2xy \Rightarrow \alpha_J\langle r^2\rangle\left[J_+{}^2 - J_-{}^2\right]/2i = \alpha_J\langle r^2\rangle O_2^2(s)\end{aligned} \tag{110}$$

where $J_\pm = J_x \pm iJ_y$. The use of operator equivalents greatly simplifies the procedure of deducing the system's eigenstates and eigenvalues; however, it is only valid between states of the same L, S, and J, i.e. within the Hund's rule ground-state multiplet. In practice there are higher J-multiplets which can mix in, but the use of Stevens' Operators is normally good to 10%. The matrix elements between the Stevens' Operators and the atomic states $|J, J_z\rangle$ are tabulated, for example in Hutchings.

The Hamiltonian can now be written as

$$\mathcal{H}_{CF} = \sum_{n\alpha} B_n^\alpha O_n^\alpha \tag{111}$$

where the crystal field parameters are

$$B_n^\alpha = -e\gamma_{n\alpha} k_{n\alpha} \theta_n \langle r^n \rangle \tag{112}$$

Hence all that remains to be done is to find the eigenvalues and eigenstates of the Hamiltonian. Crystal field parameters are generally quoted in terms of meV.

Equation (111) is the general way of expressing the Hamiltonian, even in the absence of a detailed model relating the crystal-field parameters to the magnetic ion's environment, like the point-charge model. Furthermore, which parameters are zero and which parameters are non-zero can be determined by a consideration of symmetry and the matrix elements of the Stevens' Operators, independent of the particular model which is used.

Many of the $\gamma_{n\alpha}$ terms are zero by symmetry, particularly if axes are chosen with care; others are non-zero, but their corresponding Stevens' Operators have zero matrix elements. Several general rules can show which terms are important:

- The $n = 0$ term can be ignored, since it only displaces the relative energy scale.

Results due to symmetry

- If the z-axis is an n-fold axis of symmetry, then the potential will contain $Z_{n\alpha}$ terms, since either the cos $n\phi$ or the sin $n\phi$ terms (or both) will combine constructively at every atom. Furthermore, if the distribution is even about $\phi = 0$, then only the cosine term is needed. (The $m = 0$ term is independent of ϕ, and so is not affected by axial symmetry).
- If the origin (i.e. the magnetic ion site) is a centre of inversion, then there are no odd n terms. This can be shown from examining the effects of the transformation $\theta \rightarrow \pi - \theta$, $\phi \rightarrow \pi + \phi$ on the defining equations for the spherical harmonics involved.
- If the xy-plane is a mirror plane, then there are no odd m terms for even n, and no even m terms for odd n. Again, this can be shown by examining the effects of the transformation $\theta \rightarrow \pi - \theta$, $\phi \rightarrow \phi$.

Results due to the use of Stevens' Operators

- If we are only considering the splitting of the Hund's Rule ground-state multiplet, and so are able to use Stevens' Operators, then the matrix elements of O_n^α are zero for $n \rangle 2l$, where l is the orbital angular momentum of each magnetic electron; so for $4f$ electrons it is only necessary to consider n up to 6.
- The matrix elements are also zero if $n \rangle 2J$, where J is the total angular momentum, so for Ce^{3+} ($J = {}^5/_2$) it is only necessary to consider n up to 5.
- For states of well-defined parity, the matrix elements of O_n^α, where n is odd, must be zero, since those Stevens' Operators will have odd parity.

Hence, in practice, the analysis can often be done with relatively few crystal field parameters. The application of Group Theory can also tell you which crystal field parameters are needed for a given point group (see Appendix *III-4.5*).

1.4 Inter-multiplet scattering

Besides the Hund's Rule ground-state multiplet, there are higher multiplets with different L, S and J (providing that both L and S are non-zero). The fact that states with the same L and S can have different energies, with different values of J, is a result of the spin-orbit interaction. This interaction introduces an energy term depending on the relative orientation of **L** and **S**, which also slightly mixes the previously pure LS states. This is because J is now the only good quantum number, so that states with the same J but different L and S can mix.

The presence of higher multiplets is important for two reasons. Firstly, the neutron can excite the magnetic electrons to these higher levels, giving additional information about the crystal field. Apart from transitions within the same J-multiplet, the strongest transitions are dipole transitions, with a selection rule of $\Delta J = \pm 1$. Secondly, if the low-energy wave functions have some contributions mixed in from a different level this can affect the matrix elements for the transitions.

The separation of the J-multiplets is determined by the strength of the spin-orbit interaction. In principle, the spin-orbit Hamiltonian is a sum over all of the electrons, though it can be shown that only the partially filled shells contribute. Taking **L** and **S** as good quantum numbers (a valid approximation if the spin-orbit interaction is a weak perturbation) then results in:

$$\begin{aligned} \mathcal{H}_{LS} &= \sum_i \xi(r_i)\mathbf{l}_i.\mathbf{s}_i \\ &= \zeta(L,S)\mathbf{L}.\mathbf{S} \end{aligned} \qquad (113)$$

(this is equivalent to performing a time-average in the vector model)[65]. Using the vector model, it can then be shown that

$$\begin{aligned} \mathbf{J}^2 &= (\mathbf{L}+\mathbf{S})^2 \\ &= \mathbf{L}^2 + \mathbf{S}^2 + 2\mathbf{L}.\mathbf{S} \end{aligned} \qquad (114)$$

so that, taking $\mathbf{J}^2 = J(J+1)$ *etc.*, the spin-orbit energy of a J-multiplet is

---

[65] See, for example, G.K. Woodgate, *Elementary Atomic Structure*, Clarendon Press (1989).

$$E_{LS}(J)=\tfrac{1}{2}\zeta(L,S)\{J(J+1)-L(L+1)-S(S+1)\} \tag{115}$$

This leads to the well-known 'interval rule' of *LS* coupling,

$$\begin{aligned}\Delta E_{LS}&=E(J)-E(J-1)\\&=\zeta J\end{aligned} \tag{116}$$

The value of ζ can be estimated either from a calculation, or from atomic spectra measurements on an ionised gas, or from rescaling values known for other atoms (it is predicted that ζ should be proportional to $\langle r^{-3}\rangle$).

The use of Stevens' Operators requires the initial and final states to have the same J. Hence this method can not be applied to dipole transitions ($\Delta J=\pm 1$), and a different approach must be used.

The method most commonly found in the literature is known as the Tensor Operator technique[66]. The Hamiltonian is written in terms of Tesseral harmonics (though with a slightly different normalisation to Equation (105)), and then treated as a perturbation to the case of a gaseous free-ion. The basis states to which the crystal field perturbation is applied have been calculated from the gaseous free-ion Hamiltonian (which contains, among other things, the spin-orbit interaction) by Carnall *et al*[67], and so the mixing and the inter-multiplet transition can be calculated.

1.5 Conventions

Besides B_n^α, there are also two other quantities which are frequently referred to as crystal field parameters. The first is the quantity $A_n^\alpha\langle r^n\rangle$, where A_n^α (in the point charge model) is

$$A_n^\alpha=-e\gamma_{n\alpha}k_{n\alpha} \tag{117}$$

so that

---

[66] B.G. Wyborne, *Spectroscopic Properties of Rare Earths*, Interscience Publishers (1965).

[67] W.T. Carnall, G.L. Goodman, K. Rajnak, and R.S. Rana, *A systematic analysis of the spectra of the lanthanides doped into single crystal LaF$_3$*, J. Chem. Phys. 90, 3443-3457, (1989).

$$B_n^\alpha = A_n^\alpha \theta_n \langle r^n \rangle \tag{118}$$

A_n^α can be useful because it only depends on the environment, not on the particular magnetic ion. The other quantity occurs in the tensor operator technique - these crystal field parameters are often written as B_α^n, although to avoid confusion I will write them as T_α^n, and they can be related to A_n^α and B_n^α by

$$\begin{aligned} T_0^n &= \left(\frac{2n+1}{4\pi}\right)^{\frac{1}{2}} \frac{\langle r^n \rangle}{k_{n0}} A_{n0} \\ &= \left(\frac{2n+1}{4\pi}\right)^{\frac{1}{2}} \frac{1}{k_{n0}\theta_n} B_{n0} \end{aligned} \tag{119}$$

for $m = 0$, and

$$\begin{aligned} T_\alpha^n &= \left(\frac{2n+1}{8\pi}\right)^{\frac{1}{2}} \frac{(-1)^m \langle r^n \rangle}{k_{n\alpha}} A_n^\alpha \\ &= \left(\frac{2n+1}{8\pi}\right)^{\frac{1}{2}} \frac{(-1)^m}{k_{n\alpha}\theta_n} B_n^\alpha \end{aligned} \tag{120}$$

otherwise. (For some of the more commonly occurring crystal field parameters, Kassman has tabulated the conversions between T_α^n and A_n^α [68]).

A quick mention should also be made about units. Hutchings' original paper was in cgs units, i.e. there was no factor of $4\pi\varepsilon_0$ in the potential. Furthermore, charges are often used in units of e, and distances given in units of Å. If this is the case, then the crystal field parameters and energies that result are in units of 14.400 eV. To a certain extent, this is irrelevant - the charges are screened, affecting the overall scale, and so it is the relative magnitudes of the crystal field parameters which are usually important.

---

[68] A.J. Kassman, *Relationship between the coefficients of the tensor operator and operator equivalent methods*, J. Chem. Phys. 53, 4118-4119, (1970).

1.6 An illustration - Pr_2NiO_4 and Nd_2NiO_4

As an illustration of the use of the point charge model, I here describe its application to two nickelates, Pr_2NiO_4 and Nd_2NiO_4. Although the crystalline environment in these compounds is not directly related to that of $PrBa_2Cu_3O_{6+x}$, they were being studied in my group, and it was realised that a point charge model calculation would be needed. As I was developing the relevant software anyway, I performed the calculation, and I include it here as an illustration of the effective use of the point charge model.

1.6a The undistorted and distorted structures

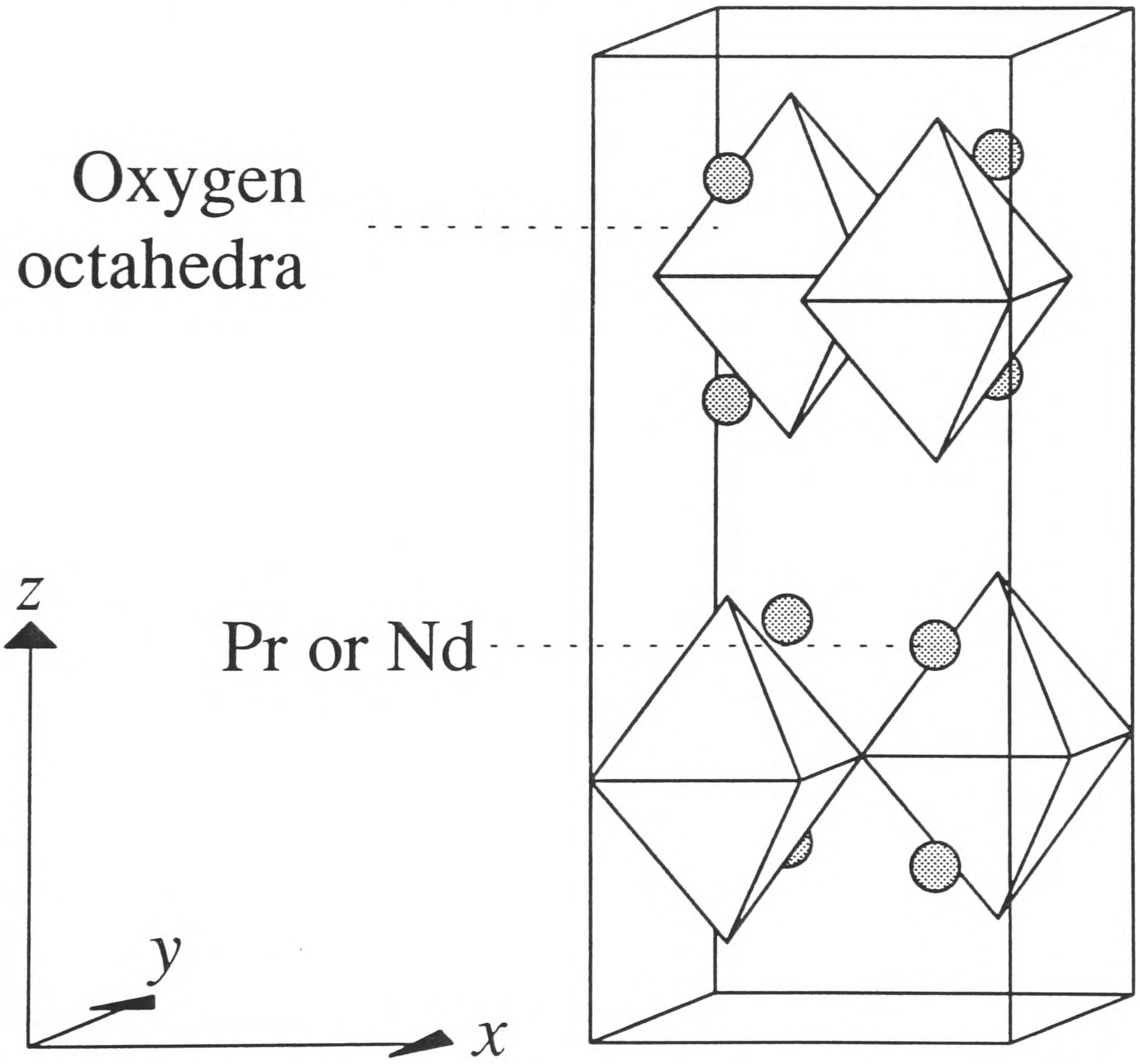

Figure 48: The 'undistorted' structure of Pr_2NiO_4 and Nd_2NiO_4. At the centre of each oxygen octahedra there is a nickel atom. This structure is the same as that of La_2CuO_4, although the unit cell shown is not the conventional one. The actual high-temperature structure is similar, but slightly orthorhombic.

At high temperatures, these nickelates have an orthorhombic structure similar to La_2CuO_4. However, at lower temperatures they undergo an orthorhombic-to-tetragonal transition involving rotations of the oxygen octahedra (see Figure 49). It is in this distorted phase that the crystal field measurements were taken. It is also possible to imagine an 'undistorted' structure, which is tetragonal but without the rotated oxygen octahedra (see Figure 48).

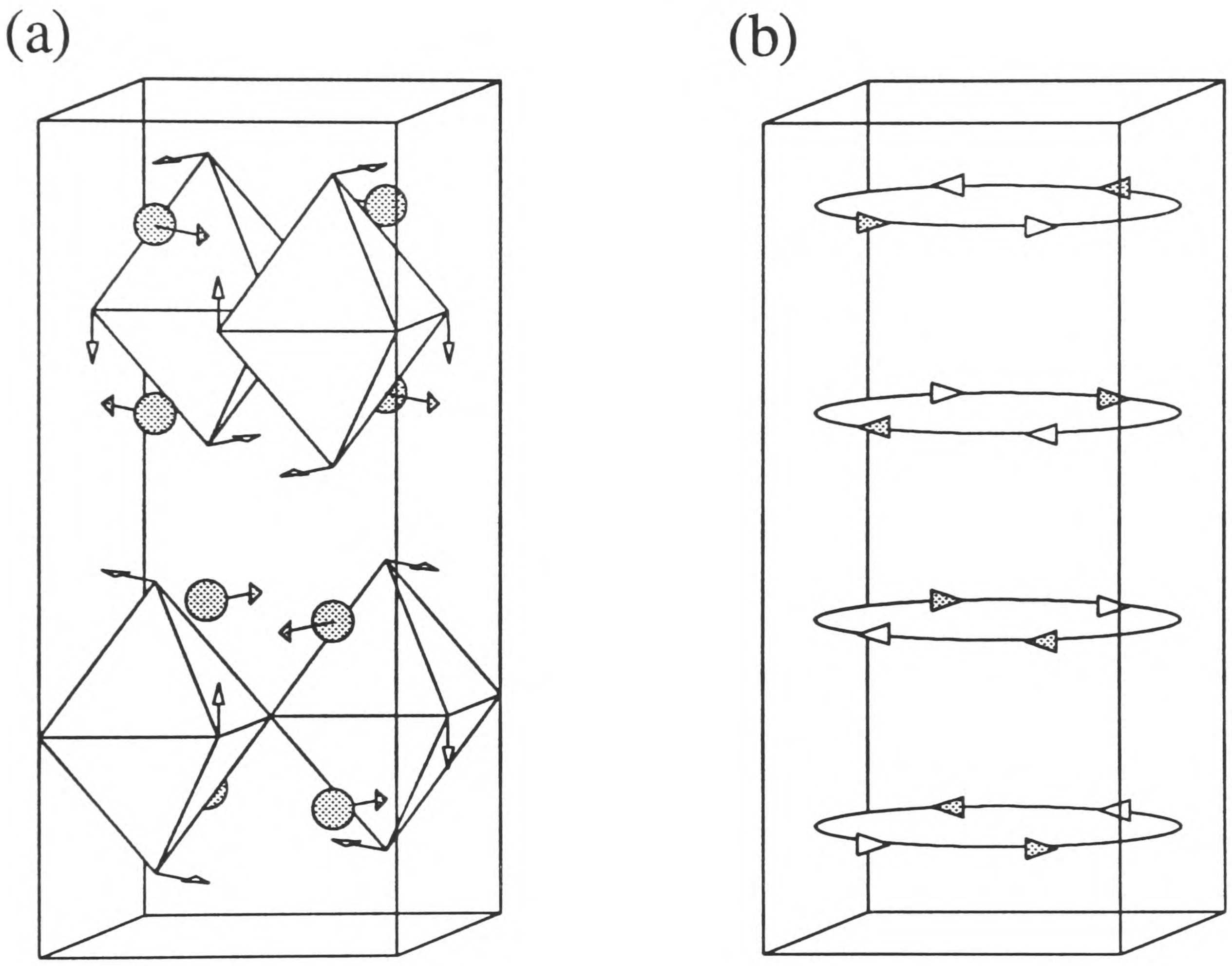

Figure 49: At lower temperatures, a distortion occurs. (a) The oxygen octahedra in the lower half of the unit cell rotate in opposite senses around the (0, 1, 1) line, whilst the octahedra in the upper half rotate in opposite senses around the $(0, 1, \bar{1})$ line. The Nd/Pr ions then move to accommodate these rotations. Perhaps the easiest way to visualise this distortion is by applying the rotations shown in (b) to the Pr/Nd ions and the apical oxygens.

Consider the Pr/Nd ion labelled in Figure 48; its surrounding oxygen ions are shown in Figure 50 (for simplicity, only the effects of the nearest oxygen ions are considered).

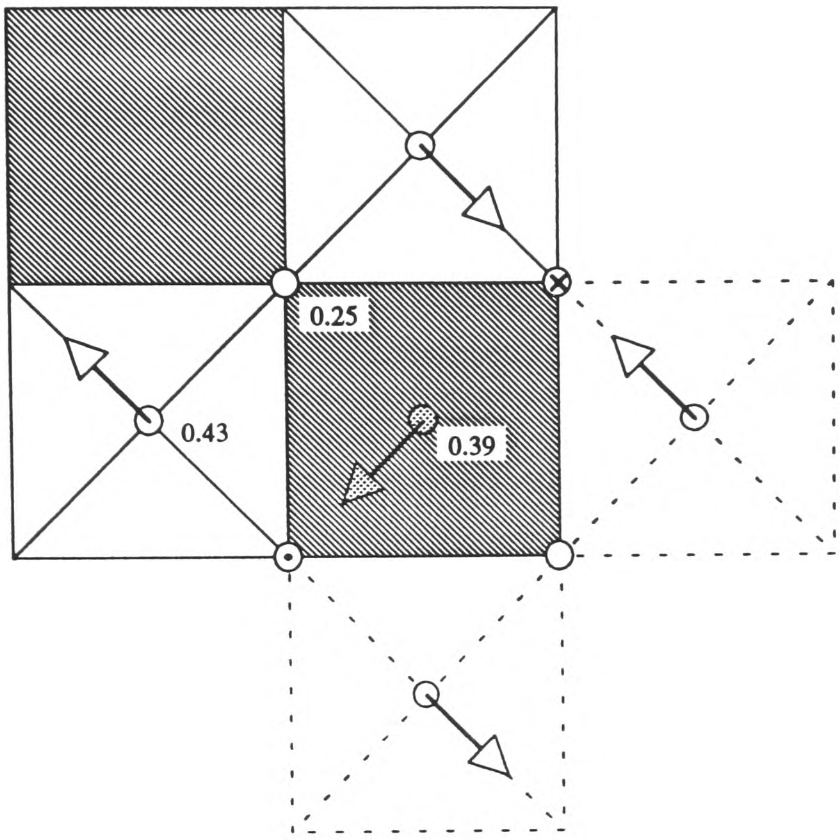

Figure 50: The oxygen environment of a Pr/Nd ion, seen from above. The heights of the ions in the undistorted cell are given as z, the fraction of the unit cell height. Surrounding the Pr/Nd ion at $z = 0.39$ (labelled in Figure 48), there are: four oxygen ions at $z = 0.25$, from the NiO_2 plane beneath Pr/Nd; four oxygen ions at $z = 0.43$, from the tops of the surrounding oxygen octahedra; and one oxygen ion at $z = 0.57$ (not shown), from the bottom of the oxygen octahedra directly above the Pr/Nd ion. The arrows give the direction the atoms move in the distortion; the dot and the cross represent upwards and downwards motions respectively.

Applying the rules given at the end of Section *III-1*, if we assume that the Pr/Nd ion is in a stable trivalent state then the wave function has a well-defined parity, and hence there is no need to consider crystal field parameters with odd n. Furthermore, if we ignore J-mixing and inter-multiplet scattering we can use Stevens' Operators, and so for the $4f$ magnetic electrons we only need to consider terms up to $n = 6$.

1.6b Predictions for the undistorted structure

The following results are derived by applying the methods described in Appendix *III-4.5*. For the undistorted structure, the point-group symmetry of the Pr/Nd site is C_{4v} (*4mm*): there is a four-fold axis (z) parallel to the crystallographic *c*-axis, and this contains four mirror planes xz, yz, $(x+y)z$, and $(x-y)z$. It is only necessary to consider the crystal field parameters $B_{20}, B_{40}, B_{44}^c, B_{60}$ and B_{64}^c.

The co-ordinates of the oxygen ions surrounding the Pr and Nd ions are given in Table 29.

Table 29: The oxygen environment of the Pr^{3+} ion in undistorted Pr_2NiO_4, and Nd^{3+} in undistorted Nd_2NiO_4. z is the fractional height of the oxygen ion, and r, θ, ϕ are its polar co-ordinates from the Pr/Nd ion ($\theta = 0$ is parallel to the crystallographic *c*-axis). In the point charge calculation each oxygen ion has a charge $-2e$, i.e. no correction is made for screening.

Pr^{3+} ($J = 4$)		Nd^{3+} ($J = {}^9/_2$)			
r / Å	θ / °	r / Å	θ / °	ϕ / °	z
2.57	130.76	2.54	130.22	45	0.25
2.57	130.76	2.54	130.22	135	0.25
2.57	130.76	2.54	130.22	225	0.25
2.57	130.76	2.54	130.22	315	0.25
2.80	79.67	2.79	79.38	0	0.43
2.80	79.67	2.79	79.38	90	0.43
2.80	79.67	2.79	79.38	180	0.43
2.80	79.67	2.79	79.38	270	0.43
2.23	0.00	2.24	0.00	0	0.57

For Pr^{3+} we expect five singlets and two doublets,

$$D^+(J=4) \to 2\Gamma_1^+ + \Gamma_2^+ + \Gamma_3^+ + \Gamma_4^+ + 2\Gamma_5^+ \tag{121}$$

with symmetry allowed transitions $\Gamma_i^+ \leftrightarrow \Gamma_5^+$ ($i = 1, 2, 3, 4, 5$), $\Gamma_1^+ \leftrightarrow \Gamma_2^+$, and $\Gamma_3^+ \leftrightarrow \Gamma_4^+$.

For Nd^{3+} we expect five doublets,

$$D^-(J=9/2) \to 3\Gamma_6^- + 2\Gamma_7^- \tag{122}$$

with all transitions symmetry-allowed.

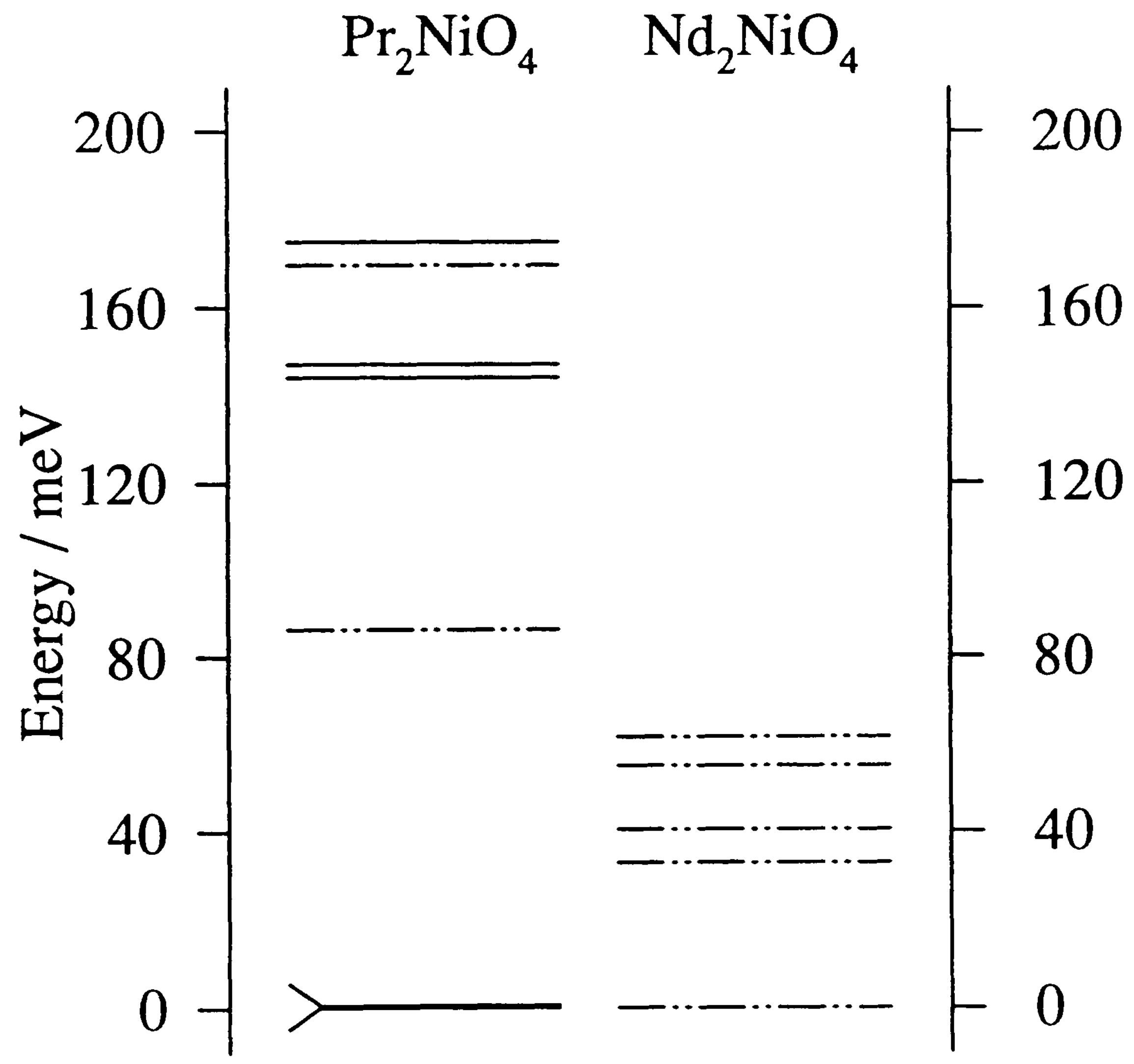

Figure 51: Crystal-field energy levels of undistorted Pr_2NiO_4 and Nd_2NiO_4 as predicted by the point charge model. Pr_2NiO_4 has energy levels at 0, 0.5, 86.3 (a doublet), 144.2, 147.2, 169.8 (a doublet), and 175.1 meV; Nd_2NiO_4 has five doublet levels at 0, 32.8, 40.5, 55.0, and 61.7 meV.

The matrix elements of the Stevens' Operators are tabulated in Hutchings[63], and the values of $\langle r^n \rangle$ can be found from Freeman and Watson[69]. Hence all that remains is to find the eigenvalues and eigenstates of the Hamiltonian. The resulting crystal field energy levels are shown in Figure 51.

1.6c Predictions for the distorted structure

For the distorted structure, the point-group symmetry of the Pr/Nd site is C_s (m): the only symmetry is a mirror plane perpendicular to the $(1\bar{1}0)$-direction (z) (see Figure 50). In the rotated co-ordinate system, where $\theta = 90°$ coincides with the mirror plane, the crystal field parameters that are needed to describe the potential for the distorted structure are $B_{20}, B^c_{22}, B^s_{22}$, $B_{40}, B^c_{42}, B^s_{42}, B^c_{44}, B^s_{44}$, $B_{60}, B^c_{62}, B^s_{62}, B^c_{64}, B^s_{64}, B^c_{66}$ and B^s_{66} (one of the crystal field parameters, normally taken to be B^s_{22}, can be made to be zero by rotating about z, leaving 14 independent parameters).

For Pr^{3+} we expect nine singlets,

$$D^+(J=4) \rightarrow 5\Gamma_1^+ + 4\Gamma_2^+ \tag{123}$$

with all transitions symmetry-allowed.

For Nd^{3+} we expect five doublets,

$$D^-(J=\tfrac{9}{2}) \rightarrow 5(\Gamma_3^- + \Gamma_4^-) \tag{124}$$

again with all transitions symmetry-allowed.

To calculate the Hamiltonian, it is necessary to know the sinusoidal Stevens' Operators. Although these are not often tabulated, they are easily deduced. Recall that we defined raising and lowering operators, $J_\pm = J_x \pm iJ_y$. The cosine-operators contain terms like $(J_+^n + J_-^n)/2$, and the sine-operators contain terms like $(J_+^n - J_-^n)/2i$. This implies that the matrix elements of the sine-operators are just antisymmetric versions of the cosine-operators (which are tabulated in Hutchings[63]):

---

[69] A.J. Freeman and R.E. Watson, *Theoretical investigation of some magnetic and spectroscopic properties of rare-earth ions*, Phys. Rev. **127**, 2058-2075, (1962).

$$
\begin{aligned}
\left\langle m_i \middle| O_n^m(s) \middle| m_j \right\rangle &= \left\langle m_i \middle| \frac{J_+^n - J_-^n}{2i} \ldots \middle| m_j \right\rangle \\
&= \begin{cases} \frac{1}{i}\left\langle m_i \middle| \frac{J_+^n}{2} \ldots \middle| m_j \right\rangle, & i = j + n \\ -\frac{1}{i}\left\langle m_i \middle| \frac{J_-^n}{2} \ldots \middle| m_j \right\rangle, & i = j - n \\ 0 \quad \text{otherwise} \end{cases} \\
&= \pm \frac{\left\langle m_i \middle| O_n^m \middle| m_j \right\rangle}{i}, \quad \begin{cases} +, & i > j \\ -, & i < j \end{cases}
\end{aligned}
\tag{125}
$$

The energy levels predicted by the point-charge model are given in Figure 52.

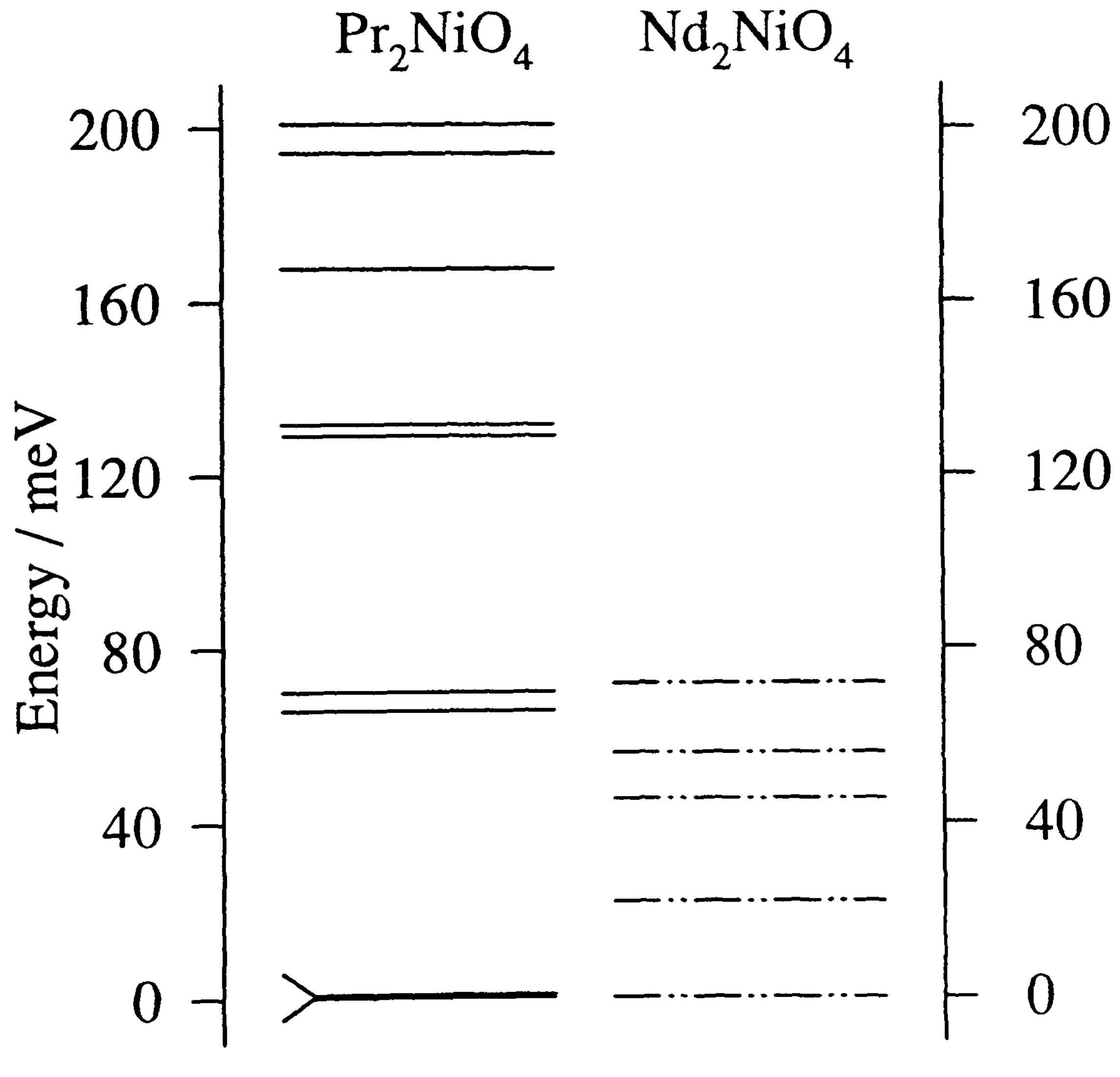

Figure 52: Crystal-field energy levels of distorted Pr_2NiO_4 and Nd_2NiO_4 as predicted by the point charge model. Pr_2NiO_4 has energy levels at 0, 0.6, 65.5, 70.0, 129.2, 131.9, 167.8, 194.3, and 201.0 meV; Nd_2NiO_4 has five doublet levels at 0, 22.1, 45.6, 55.9, and 71.9 meV.

1.6d The refinement of the crystal field parameters for the distorted structure

The purpose of the measurements taken on the distorted structures was to refine the crystal field parameters and determine the wave functions of the magnetic electrons. However, because of the low symmetry of the site, there are too many independent variables to perform a successful refinement. The point-charge calculation showed that, although the distortion introduces a large number of additional crystal field parameters (14 independent parameters rather than 5), the additional parameters have only a small effect on the crystal field levels (compare the levels of the distorted structure, Figure 52, with the undistorted structure, Figure 51).

This implies that an initial refinement, approximating the point-group symmetry to be C_{4v} (*4mm*) rather than C_s (*m*), would be useful for two reasons. First, it would produce suitable crystal field parameters to allow a full refinement to be done, using the point-charge calculation to help predict the additional parameters needed for the lower symmetry. Second, it would in itself provide simple, approximate wave functions for the distorted structure, which would be useful for future calculations.

The refinement was further aided by refining the data from both the Pr_2NiO_4 and the Nd_2NiO_4 data simultaneously to the same set of A_n^α values, since these only depend on the local environment of the magnetic ion and not on its own size or electronic configuration (see Equation (108)). The approach, combined with information from heat capacity and susceptibility measurements, was successful and is the subject of a forthcoming paper[70].

This shows that a point charge calculation can often be a valuable preliminary investigation into a crystal field problem, giving insight into the effects of symmetry, the expected magnitudes of the parameters, and their relative effects on the resulting wave functions.

---

[70] A.T. Boothroyd, A. Longmore, R. Burriel, and R. Eccleston, *The magnetic states of R^{3+} in R_2NiO_4 ($R = Pr, Nd$)*, to be published.

2. Literature review

2.1 $PrBa_2Cu_3O_7$

Since 1988, at least ten papers have been published concerning the crystal field levels in $PrBa_2Cu_3O_7$. On some points, at least, there is universal agreement: the peaks show severe intrinsic broadening, probably as a result of Pr^{3+} hybridisation with their surrounding oxygen ions. Indeed, inelastic neutron scattering was instrumental in proving that the Pr ions were (at least predominantly) trivalent rather than tetravalent, and for explaining the previously misunderstood magnetic susceptibility data (see Section *I-4.2*). However, beyond this there is less quantitative agreement. This is understandable - spectra are broadened, 'peaks' run together to form featureless regions of magnetic intensity, and interpretation is difficult.

Symmetry predicts that the crystal field should decompose the $(2J + 1)$-degenerate multiplet into nine singlets, and that either six or seven transitions are symmetry-allowed from the ground-state (the exact number depending on the nature of the ground state) - see Appendix *II-4.5a*.

Table 30 shows the magnetic transitions observed for $PrBa_2Cu_3O_7$, i.e. the energy losses (or gains) of the scattered neutrons which have been attributed to magnetic interactions (not all of the papers were an attempt to record all of the multiplet transitions). Some of the peaks attributed to magnetic scattering in the earlier papers are now thought to be due to phonons; other peaks are still of disputed origin.

Why is it so important to be worried about every single transition? The answer lies in the number of crystal-field parameters that need to be refined. For $PrBa_2Cu_3O_7$, there are nine such parameters, so there is clearly a great need to gather as much accurate information as possible. To help solve this problem, authors generally use crystal-field parameters uniquely determined from $HoBa_2Cu_3O_7$ as a starting point; in this compound the peaks show no broadening, and for Ho^{3+} ($J = 8$) there are 17 energy levels to observe. Despite this common approach, the lack of agreement in transition assignments translates into a lack of agreement in crystal-field parameters (see Table 31).

Table 30: Magnetic transitions observed in inelastic neutron scattering on $PrBa_2Cu_3O_7$. '132?' indicates magnetic scattering of unexplained origin; '15-30' indicates the range of a broad region of scattering; '1, 1.5' indicates a temperature-dependant transition energy; '113*' indicates a transition which may be due to Pr contamination of the Ba site.

	Transition energies / meV								
Walter *et al*[71]	1, 1.5		3.3	4.3	7.5	15 - 30			
Gering *et al*[72]	0 - 6								
Skanthakumar *et al*[73]	0 - 6								
Soderholm *et al*[74]	0 - 15								
	35		65	80					
Soderholm *et al*[75]	2 - 15								
	45	50	65	80	85	105			
Boothroyd *et al*[76]			65		85	105	113	123	132?
Goodman *et al*[77]	1.4	2.5	3.9						
	45	50	65	80	85	105	113?	123?	132?

---

[71] U. Walter, E. Holland-Moritz, A. Severing, A. Erle, H. Schmidt, and E. Zirngiebl, *Comparison of inelastic magnetic neutron scattering on $PrBa_2Cu_3O_7$ and $NdBa_2Cu_3O_7$*, Physica C **153-155**, 170-171, (1988).

[72] E. Gering, B. Renker, F. Gompf, D. Ewert, H. Schmidt, R. Ahrens, M. Bonnet, and A. Dianoux, *Crystal electric field excitations in $REBa_2Cu_3O_{7-x}$ compounds*, Physica C **153-155**, 184-185, (1988).

[73] S. Skanthakumar, W-H. Li, J.W. Lynn, A. Kebede, J.E. Crow, and T. Mihalisin, *Magnetic properties of Pr in non-superconducting $PrBa_2Cu_3O_7$*, Physica B **163**, 239-241, (1990).

[74] L. Soderholm, C.-K. Loong, G.L. Goodman, U. Welp, J. Bolender, and C.W. Williams, *f-electron localization/delocalization phenomena in $PrBa_2Cu_3O_7$ and $CmBa_2Cu_3O_7$*, Physica B **163**, 655-658, (1990).

[75] L. Soderholm, C.-K. Loong, G.L. Goodman, and B.D. Dabrowski, *Crystal-field splittings and magnetic properties of Pr^{3+} and Nd^{3+} in $RBa_2Cu_3O_7$*, Phys. Rev. B **43**, 7923-7935, (1991).

[76] A.T. Boothroyd, L.W. Caves, D. McK Paul, and R. Osborn, *High energy crystal field excitations in $Pr_xY_{1-x}Ba_2Cu_3O_{7-\delta}$*, Bull. Mater. Sci. **14**, 613-617, (1991).

[77] G.L. Goodman, C.-K. Loong, and L. Soderholm, *Crystal-field properties of f-electron states in $RBa_2Cu_3O_7$ for R = Ho, Nd and Pr*, J. Phys. C. **3**, 49-67, (1991). Data is from ref. 75 and ref. 76.

Jostarndt *et al*[78]	1.5	3.3	4.8					
Nekvasil *et al*[79]		63 / 68		83	97			
Boothroyd *et al*[80]	1.5?	3.3	4.8					
		65		83	103	113^*	123^*	132?
Hilscher *et al*[81]	1.1, 1.5	3.3	4.8?					
		63 / 68		83	97			

Ultimately, the magnetic properties of the Pr^{3+} ion will be determined by the wave functions and the energies of the lowest lying states. It is widely thought that the lowest states for $PrBa_2Cu_3O_7$ are a nearly degenerate quasi-triplet of states. Because of the observed broadening, it has not been possible for authors to simply observe the transitions - assignments are often made on the basis of the crystal-field parameters. Hence there is also disagreement about the ground-state energy levels (see Table 32); the symmetries Γ_i are as discussed in Appendix *III-4.5*.

There are some other interesting features in the previously published work. Boothroyd *et al*[80] mention that the peaks are sharper for their off-stoichiometric sample, $Pr_{1.06}Ba_{1.94}Cu_3O_7$, (measured in ref. 76), than for their stoichiometric sample. This can be interpreted in terms of the charge transfer model of Section *II-3.6b*: the presence of Pr^{3+} on the Ba^{2+} site may make it less likely for the Pr-site ions to hybridise with their surrounding oxygen ions. By the same reasoning, a deliberately Al-contaminated powder sample of $PrBa_2Cu_3O_7$ may also show sharper peaks, and may be the subject of a future experiment.

---

[78] H.-D. Jostarndt, U. Walter, J. Harnischmacher, J. Kalenborn, A. Severing, and E. Holland-Moritz, Phys. Rev. B **46**, 14872-14882, (1992).

[79] V. Nekvasil, E. Holland-Moritz, H.-D. Jostarndt, U. Walter, and G. Hilscher, *Crystal-field phenomena in* $PrBa_2Cu_3O_6/O_7$ *compounds*, JMMM **117**, 11-13, (1992).

[80] A.T. Boothroyd, S.M. Doyle, and R. Osborn, *The magnetic state of Pr in* $PrBa_2Cu_3O_7$, Physica C **217**, 425-438, (1993). Data from ref. 76 and ref. 78.

[81] G. Hilscher, E. Holland-Moritz, T. Holubar, H.-D. Jostarndt, V. Nekvasil, G. Schaudy, U. Walter, G. Fillion, *Valence of praseodymium in* $Pr_xY_{1-x}Ba_2Cu_3O_{7-\delta}$*: inelastic-neutron-scattering, specific-heat, and susceptibility study*, Phys. Rev. B **49**, 535-550, (1994). Data based on ref. 79 and ref. 78. Crystal field parameters are as in ref. 79.

Table 31: The point-charge calculation and reported crystal-field parameters B_{n0}, B^c_{nm} (10^{-5} eV) for $PrBa_2Cu_3O_7$.

n m	Point charge calculation	Soderholm *et al*[75]	Goodman *et al*[77]	Nekvasil *et al*[79]	Boothroyd *et al*[80]
2 0	–340	–59	–59	30	–42 ± 6
2 2	7.8	–68	–51	–18	–40 ± 20
4 0	2.1	3.2	2.3	3.9	3.40 ± 0.10
4 2	–0.35	–0.11	–0.10	–1.2	3.8 ± 0.6
4 4	–8.4	–14	–14	–9.7	–13.1 ± 0.7
6 0	0.0069	0.038	0.037	0.034	0.051 ± 0.005
6 2	0.0034	–0.16	–0.17	–	0.05 ± 0.10
6 4	0.26	1.4	1.4	0.85	1.25 ± 0.05
6 6	–0.00092	–0.0034	0.075	–	0.17 ± 0.11

Table 32: The crystal-field energies (meV) and symmetries of the 'ground-state' quasi-triplet of $PrBa_2Cu_3O_7$.

Soderholm *et al*[75]	0, Γ_1	1.5, Γ_4	4.1, Γ_2
Goodman *et al*[77]	0, Γ_1	1.4, Γ_2	3.9, Γ_4
Nekvasil *et al*[79]	0, Γ_4	1.5, Γ_2	3.3, Γ_1
Boothroyd *et al*[80]	0, Γ_2	3.5, Γ_4	5.0, Γ_1

Jostarndt *et al*[78] have measured the $|\kappa|$-dependence of the low-energy excitations, which seems to show evidence of spatial magnetic correlations between the Pr^{3+} ions. If this is the case, it is again presumably the result of Pr-O hybridisation.

Finally, it should be noted that, to aid the assignment of symmetries to the ground-state quasi-triplet, it has often been assumed that the easy axis for the Pr moment is along the *c*-axis. The results of my elastic magnetic scattering (see Section *II-3*) now throw that assumption into question.

2.2 Two alternatives: PrO_2 and $Y_{1-z}Pr_zBa_2Cu_4O_8$

Because $PrBa_2Cu_3O_7$ has already been extensively studied, a further experiment did not seem worthwhile, despite the clear discrepancies that presently exist. The question that needs answering is this: what are the magnetic energy levels of Pr^{3+}, especially around the ground-state, in $PrBa_2Cu_3O_7$? As mentioned, this is very difficult to determine because of the intrinsic broadening of the transitions. Hence we decided to investigate two similar 'model' systems, both of which contain a PrO_8 octahedra similar to that of $PrBa_2Cu_3O_7$. By approximately reproducing the electrical surroundings of the Pr ion, though possibly without such extensive hybridisation, it seemed possible to shed more light onto previous crystal-field work. The two model systems chosen were PrO_2 and $Y_{1-z}Pr_zBa_2Cu_4O_8$, with both crystals grown by David Curry (University of Southampton).

There are no published inelastic spectra for $Y_{1-z}Pr_zBa_2Cu_4O_8$, perhaps because this has only recently been synthesised as a single-phase for $z = 1$[82]. The structure of $PrBa_2Cu_4O_8$ is essentially the same as $PrBa_2Cu_3O_7$, except for an additional Cu-O chain-layer. The double chain-layer produced is found to be much more likely to have full occupation, and has the effect of shifting what were the $PrBa_2Cu_3O_7$ chemical unit cells of every other layer by half a unit cell along *b*. The chemical structure of $PrBa_2Cu_4O_8$ is shown in Figure 53, drawn in such a way as to emphasise its similarity to $PrBa_2Cu_3O_7$. As can be seen, the Pr environment is unchanged, compared to its situation in $PrBa_2Cu_3O_7$ (see Figure 1, Section *I-4.1*).

PrO_2, on the other hand, has previously been studied by inelastic neutron scattering[83]. Just one transition was observed, at 130 meV, and symmetries of Γ_8 and Γ_7 were assigned to the ground-state and the excited state respectively. Interestingly, the authors record a broadening of the transition, attributing this to a Jahn-Teller distortion which breaks the symmetry at the Pr site and splits the ground-state quartet.

---

[82] N. Seiji, S. Adachi, H. Yamauchi, *Synthesis of a new "124" compound, $PrBa_2Cu_4O_8$*, Physica C 227, 377-380, (1994).

[83] S. Kern, C.-K. Loong, J. Faber, Jr. and G.H. Lander, *Neutron scattering investigation of the magnetic ground state of PrO_2*, Sol. Stat. Comm. **49**, 295-298, (1984).

However, it is possible that this could be a hybridisation effect. The crystal structure of PrO_2 is shown in Figure 54, and the local environment of the Pr ion is shown in Figure 55.

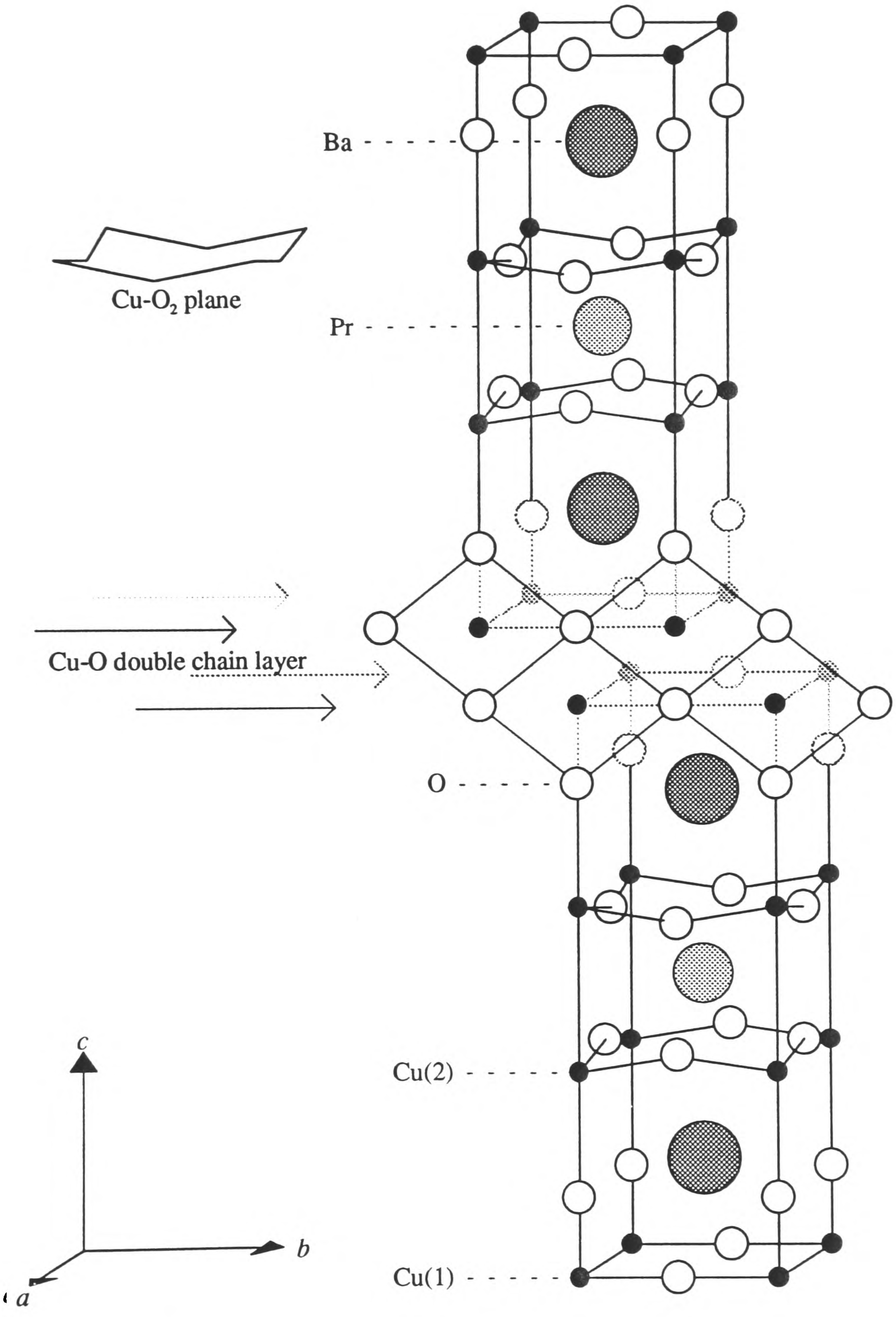

Figure 53: The chemical structure of $PrBa_2Cu_4O_8$.

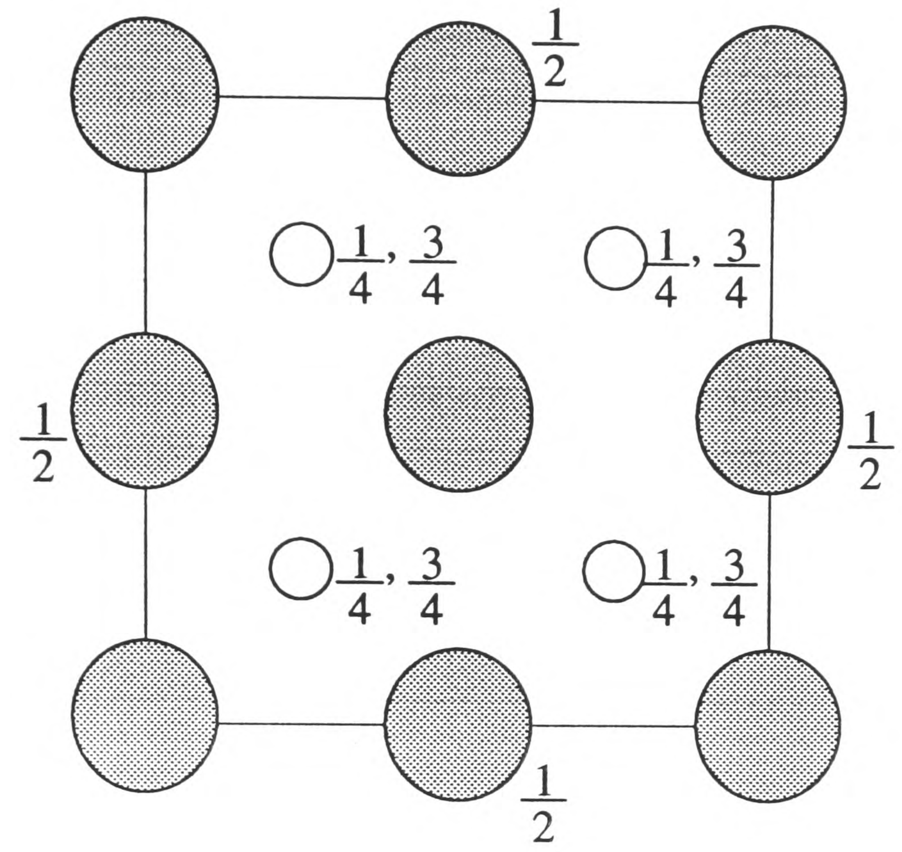

Figure 54: The crystal structure of PrO_2, shown in plan view.

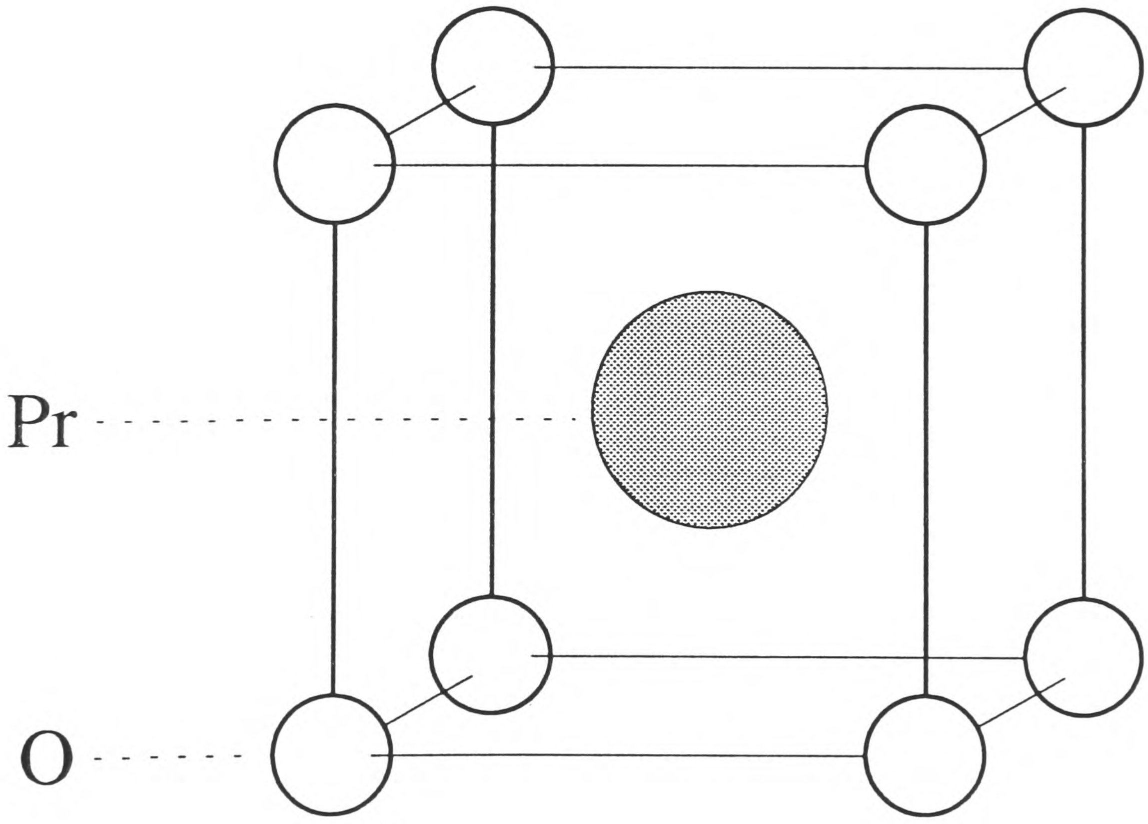

Figure 55: The local environment of the Pr ion in PrO_2.

3. Measurements

3.1 The different components of time-of-flight spectra

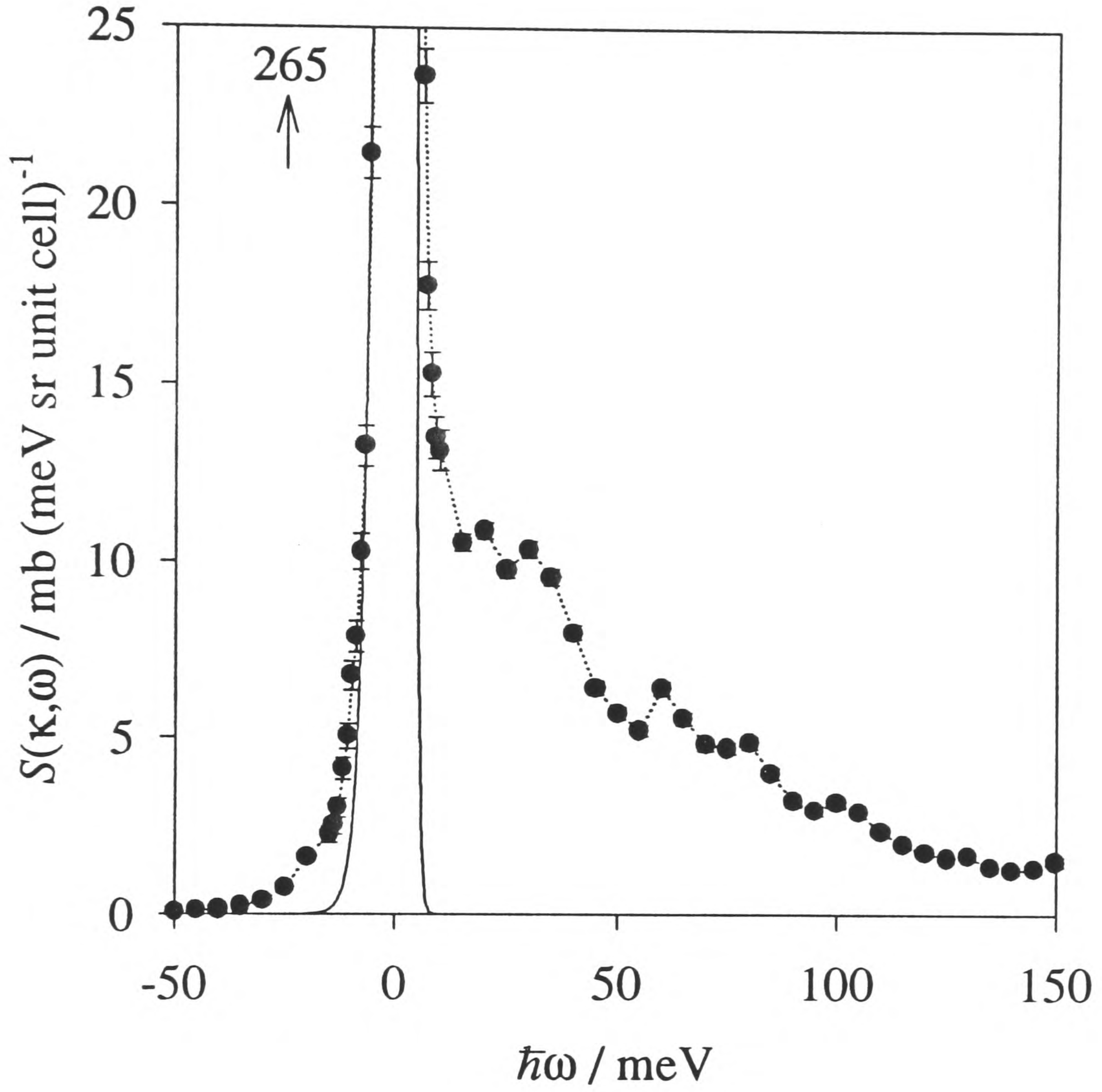

Figure 56: One of the spectra observed for $Y_{0.3}Pr_{0.7}Ba_2Cu_4O_8$, measured at 4.2 K with an incident energy of 180 meV by the detector bank at a scattering angle of $\phi = 5°$. The solid line shows the fit to the elastic peak.

Figure 56 shows a typical time-of-flight spectrum. Before the scattering from crystal field excitations can be deduced, the other components must first be accounted for. These other components are generally the elastic peak, single-phonon scattering, single-phonon/elastic multiple scattering, and multi-phonon scattering.

The elastic peak, centred at 0 meV, is the most noticeable feature of an inelastic spectrum. It consists of both incoherent scattering, where the neutrons just scatter off single atoms in all directions, and coherent scattering, which is Bragg scattering and so will only be in certain directions. It may be that a significant proportion of the elastic line is due to Bragg scattering at a particular angle, and so 'masking' the corresponding detectors can reduce the elastic line and make it easier to detect excitations at lower energies.

The shape of the purely elastic peak can be very accurately measured from a measurement on vanadium (see Appendix *III-4.2*), again making it easier to detect excitations at lower energies.

Single-phonon scattering can sometimes be observed as a single inelastic peak, and so can occasionally be confused as being a crystal-field excitation. In the creation of a phonon (when the neutron loses energy, i.e. $\hbar\omega > 0$), both energy and momentum must be conserved. The wavevector transferred from the neutron $|\kappa|$ is related to $\hbar\omega$ by Equation (136) (see Appendix *III-4.1*), and the energy of the phonon will be related to its momentum by some phonon dispersion relation $\Omega(\kappa)$. If $\omega = \Omega$ at some particular κ then a phonon can be created. The phonon will have a range of energies for a given value of $|\kappa|$, depending on the direction of κ. This is shown graphically in Figure 57, where the phonon can be created with an energy around 80 meV.

Hence a range of neutron energy losses is possible for the creation of the same phonon, and the sharpness of the peak will depend on how exactly the phonon dispersion relation changes with the direction of κ, and how they coincide with the neutron dispersion relation. Occasionally conditions can be such that the width of the single-phonon peak is the same as that of the crystal-field excitations you are looking for. On the other hand, the single-phonon process may just contribute to the continuous background, which is generally the case for acoustic phonons.

There are two ways of deciding if a peak is due to a phonon or if it is magnetic in origin. The first is from the variation of the integral $\int S(\kappa,\omega)d\hbar\omega$ with κ. If the peak is magnetic in origin, than the integral will follow the square of the form factor (see Equation (139)). If, on the other hand, the peak is due to a phonon, then the integral will have a κ^2-dependence[84]. (I have ignored the effect of the Debye-Waller factor, which is unity at sufficiently low temperatures and wavevector transfers and comes into both expressions).

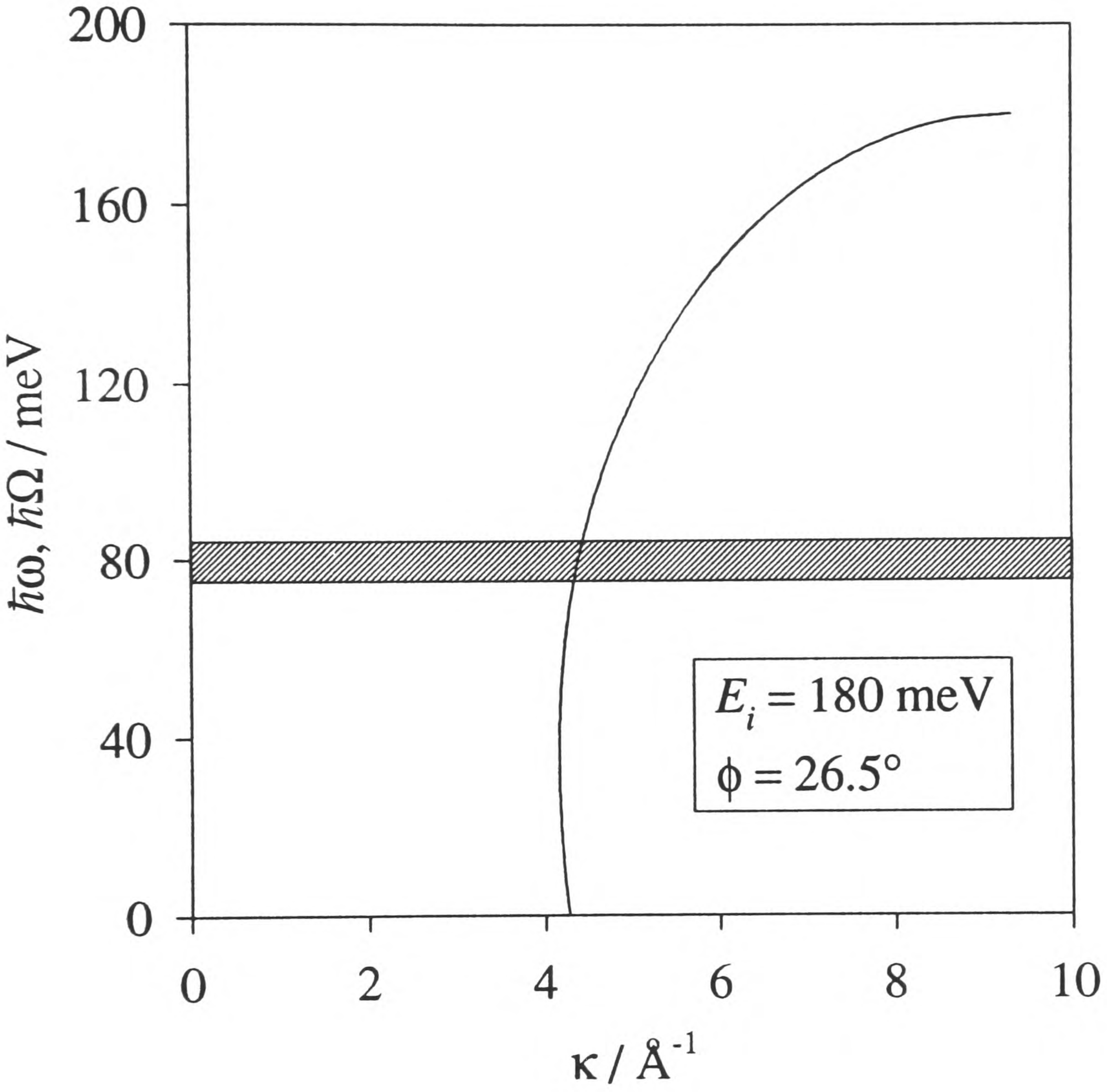

Figure 57: The conservation of energy and momentum in the creation of a single phonon. The solid line shows the neutron dispersion relation $\hbar\omega$ for the given incident energy and detector angle. The shaded region represents an optic phonon dispersion relation $\hbar\Omega$ for different directions of κ.

---

[84] S.W. Lovesey, *Theory of neutron scattering from condensed matter* volume 1, §4.4, Oxford Science Publications (1986).

The second way of deciding if a peak is due to a phonon is to see if a corresponding peak occurs in a 'dummy' sample, discussed below.

Besides single-phonon scattering, single-phonon/elastic multiple scattering and multi-phonon scattering are responsible for the continuous scattering which is essentially a non-magnetic background.

The single-phonon/multiple scattering is simply the situation when a neutron creates (or annihilates) a single phonon as discussed above, and then scatters elastically before it leaves the crystal. Because the probability of a single-phonon process increases as κ^2, such an event is more likely to happen at higher angles (such as 90°) than at lower scattering angles. In experiments, the powder sample is generally mounted as a thin layer perpendicular to the incident beam, and so a neutron scattered through 90° must travel through a large amount of the sample before it leaves, and hence has a significant probability of undergoing a further elastic scattering event.

At high incident energies, the neutron can create more than one phonon simultaneously - this is multi-phonon scattering. Since this is no longer a two-body problem, the conservation laws become much easier to satisfy and so the scattering is continuous with energy.

The best way of estimating the non-magnetic background is to make an identical measurement on a dummy sample. The dummy sample is as near in structure as possible to the sample you're interested in, but with the magnetic ion replaced by a non-magnetic ion. Although this will change some of the scattering lengths and bond strengths, the phonon-related scattering will be broadly reproduced and optic phonons will appear in roughly the same position. Figure 58 shows the spectrum for the dummy sample $YBa_2Cu_3O_7$, which was used as a dummy sample in the experiments on $Y_{0.3}Pr_{0.7}Ba_2Cu_4O_8$.

After trying various methods to subtract the multi-phonon scattering background, I opted for the following. After having subtracted the elastic peak, I would divide the sample spectrum by the dummy spectrum. I would then remove any data points that were from peaks (either crystal-field or single-phonon excitations). What was left would show a roughly linear relationship. I would then fit a straight line to the ratio data, and then use this linear relationship to subtract one spectrum from another. This would effectively remove the multi-phonon scattering, and just leave crystal field excitations and single-phonon processes which had slightly different energies or scattering strengths. I would then use the methods mentioned above to deduce the origins of the peaks.

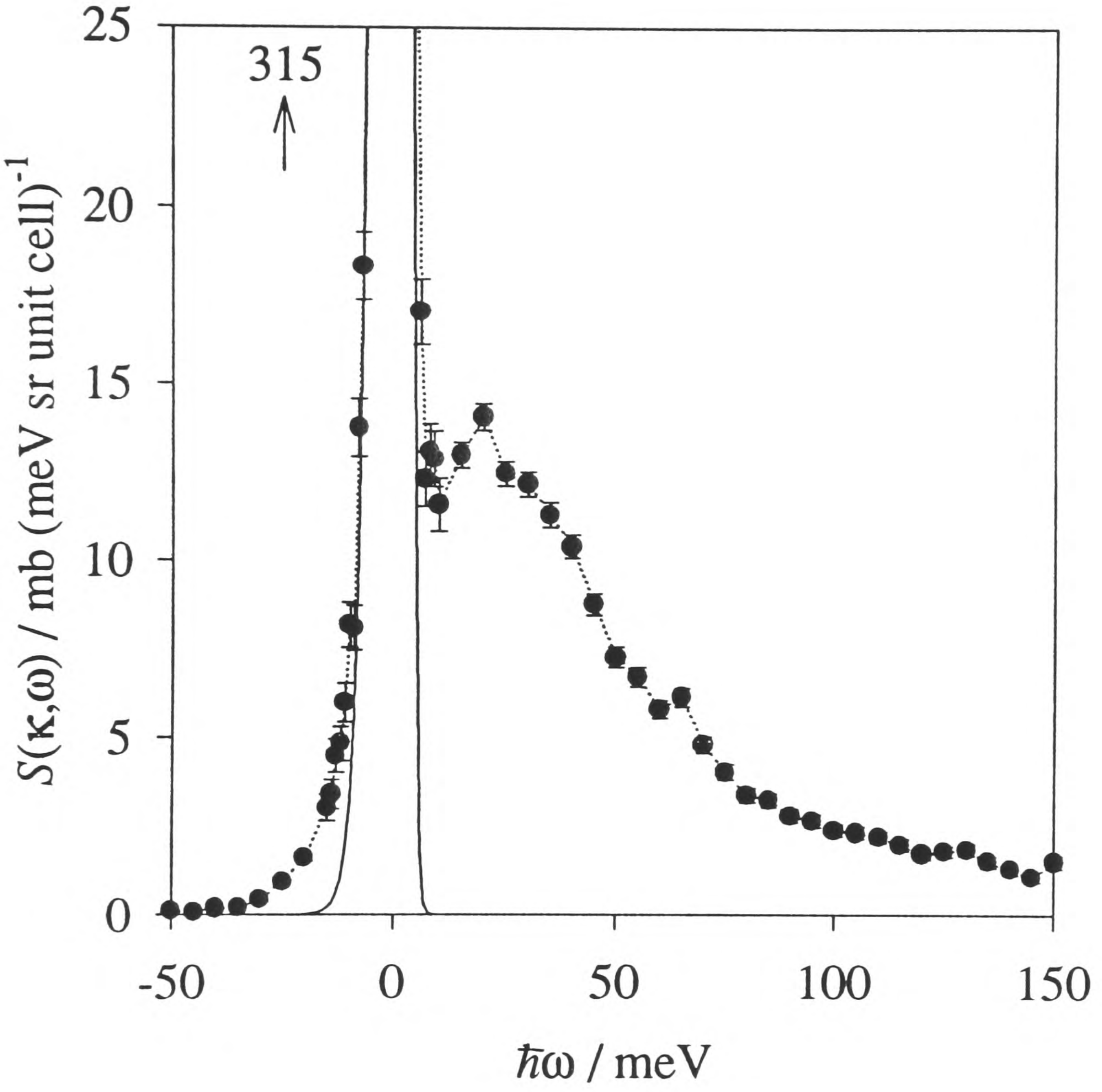

Figure 58: The dummy spectrum observed for $YBa_2Cu_3O_7$, measured at 4.2 K with an incident energy of 180 meV by the detector bank at a scattering angle of $\phi = 5°$. The solid line shows the fit to the elastic line.

3.2 $Y_{0.3}Pr_{0.7}Ba_2Cu_4O_8$

These measurements were made on HET at the Rutherford-Appleton Labs., with a dummy sample of $YBa_2Cu_3O_7$. By comparison with the results of inelastic scattering on $PrBa_2Cu_3O_7$ (see Section *III-2.1*), we expected to see peaks at low energies (<5 meV) and then from 30 meV to 130 meV. For this reason we performed measurements at two incident energies, 20 meV and 180 meV. All measurements were taken at 4.2 K, so that only the ground-state would be occupied. This makes the interpretation of the data easier, since excitations are only occurring from one energy level. (A temperature of 1 K is equivalent to a thermal energy k_BT of 0.086 meV, so this assumes that the first energy level is higher than about 0.36 meV).

3.2a 20 meV data

After removing the elastic line and subtracting the multi-phonon background, peaks were observed at about 2.5 meV, 4.8 meV (although these two may be a single peak) and 9 meV. The peak at 9 meV was interpreted as being caused by single-phonon scattering, as a result of its $|\kappa|$-dependence.

The other two peaks were harder to interpret, being very close to each other and the elastic line (which can never be perfectly subtracted). However, their $|\kappa|$-dependence would suggest that they are magnetic in origin. Figure 59 shows the data measured with the 5° detector bank (this spectrum having the best resolution) after correction for the Pr form factor (using the dipole approximation). The peaks have centres at (2.5 ± 0.4) meV and (4.8 ± 0.4) meV, and intensities (as defined in Appendix *III-4.3*) of (69 ± 10) mb (sr unit cell)$^{-1}$ and (26 ± 8) mb (sr unit cell)$^{-1}$ respectively.

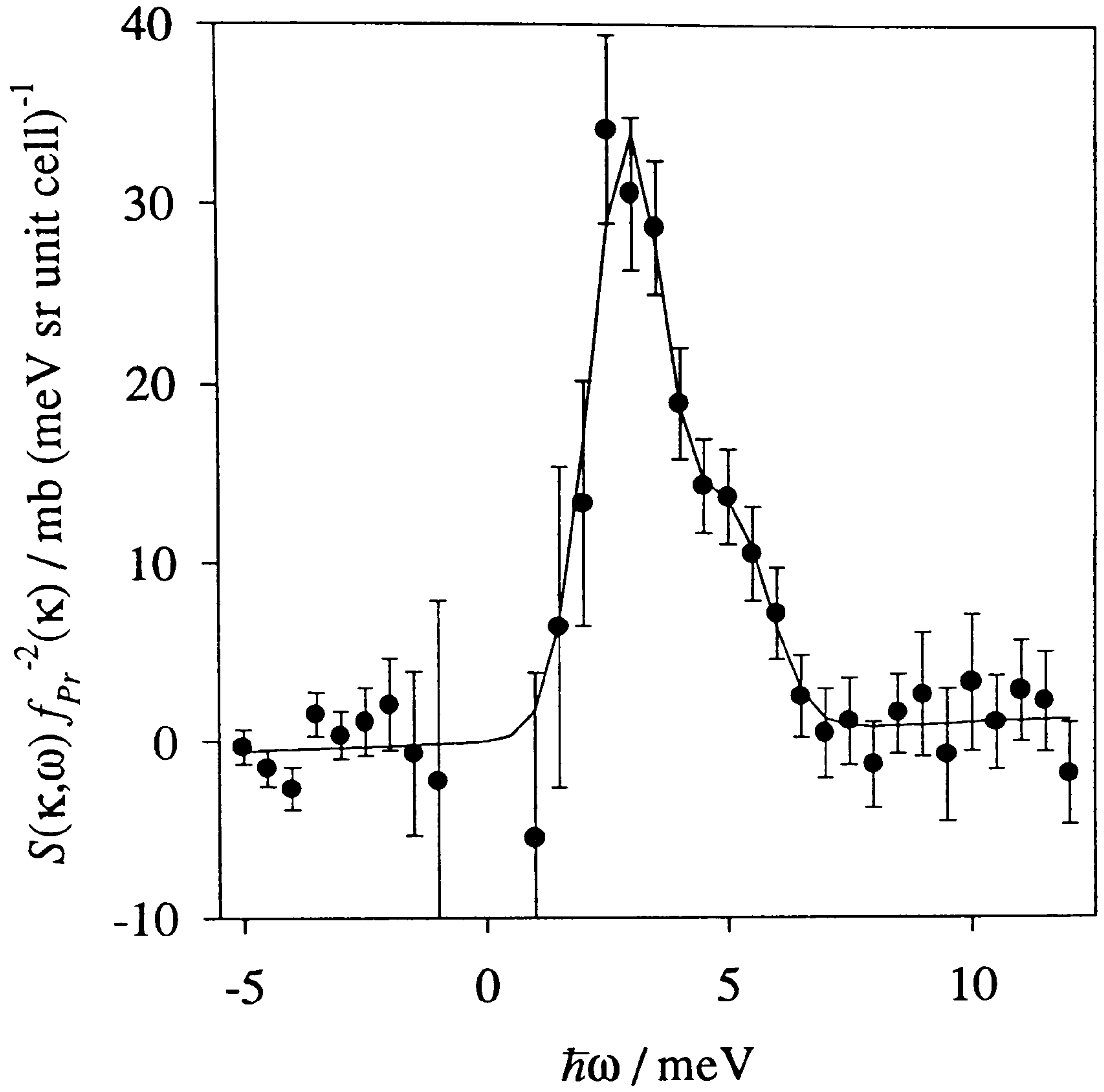

Figure 59: Inelastic scattering measured on $Y_{0.3}Pr_{0.7}Ba_2Cu_4O_8$ at 4.2 K with an incident energy of 20 meV by the detector bank at a scattering angle of $\phi = 5°$. The solid line shows a fit to the data.

3.2b 180 meV data

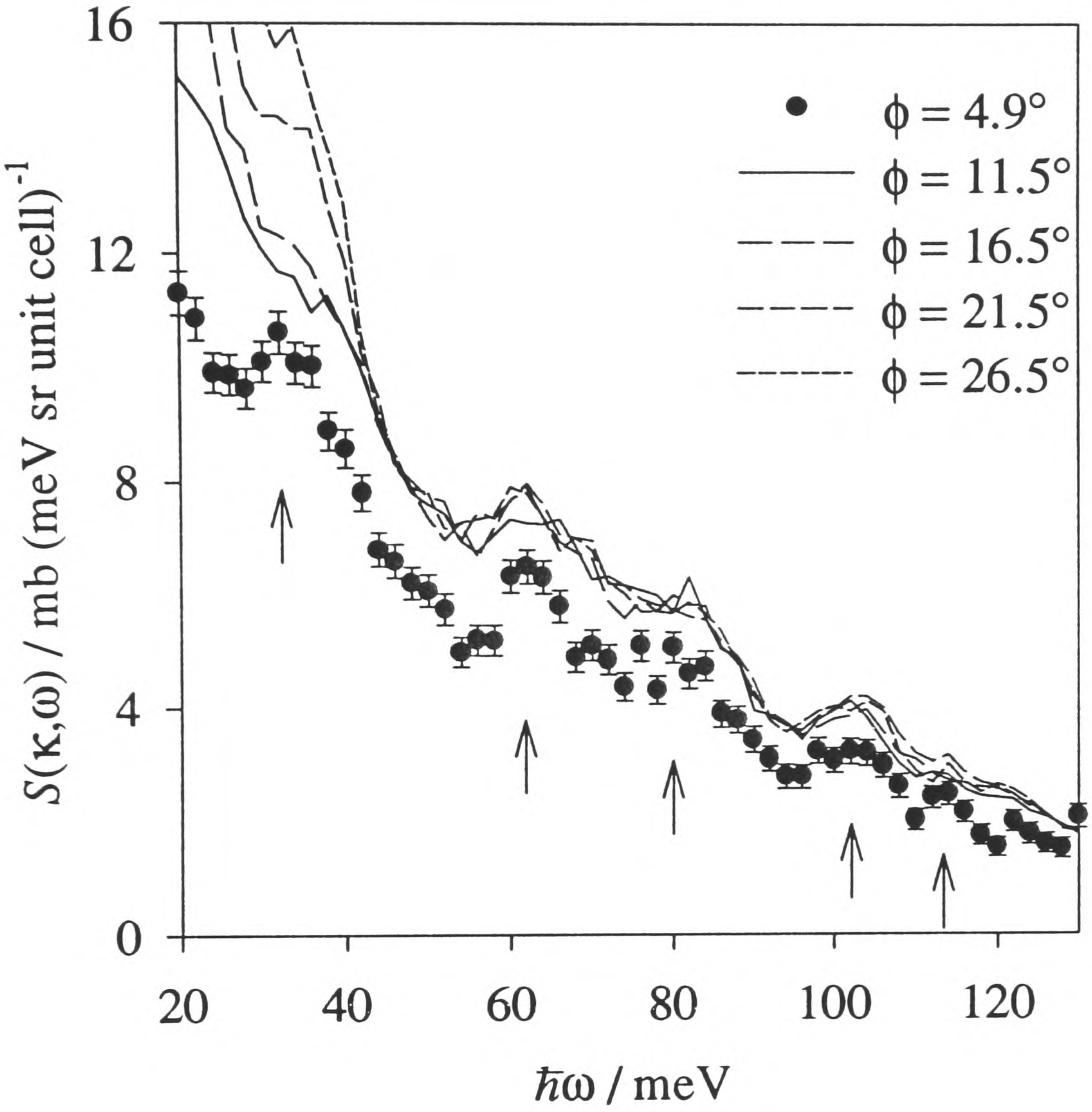

Figure 60: Inelastic scattering measured on $Y_{0.3}Pr_{0.7}Ba_2Cu_4O_8$ at 4.2 K with an incident energy of 180 meV, by the detector banks at scattering angles of $\phi = 5°$ (closed symbols) and $\phi = 11.5°, 16.5°, 21.5°$ and $26.5°$ (lines). Arrows mark possible crystal field excitations.

In these spectra peaks were observed at 33 meV, 62 meV, 80 meV, 102 meV, and 116 meV (see Figure 60). For these peaks, the trend with $|\kappa|$ is clear. The latter four peaks are more pronounced in the $\phi = 5°$ spectrum (which is the scan of lowest $|\kappa|$, see Equation (136)) than in the higher-ϕ spectra. This implies that they are crystal field excitations rather than phonons. The scattering at 33 meV, on the other hand, increases dramatically with ϕ, and hence is due to phonon scattering.

Figure 61 shows the scattering when corrected for the Pr form factor, and Table 33 shows the energies and intensities of the excitations.

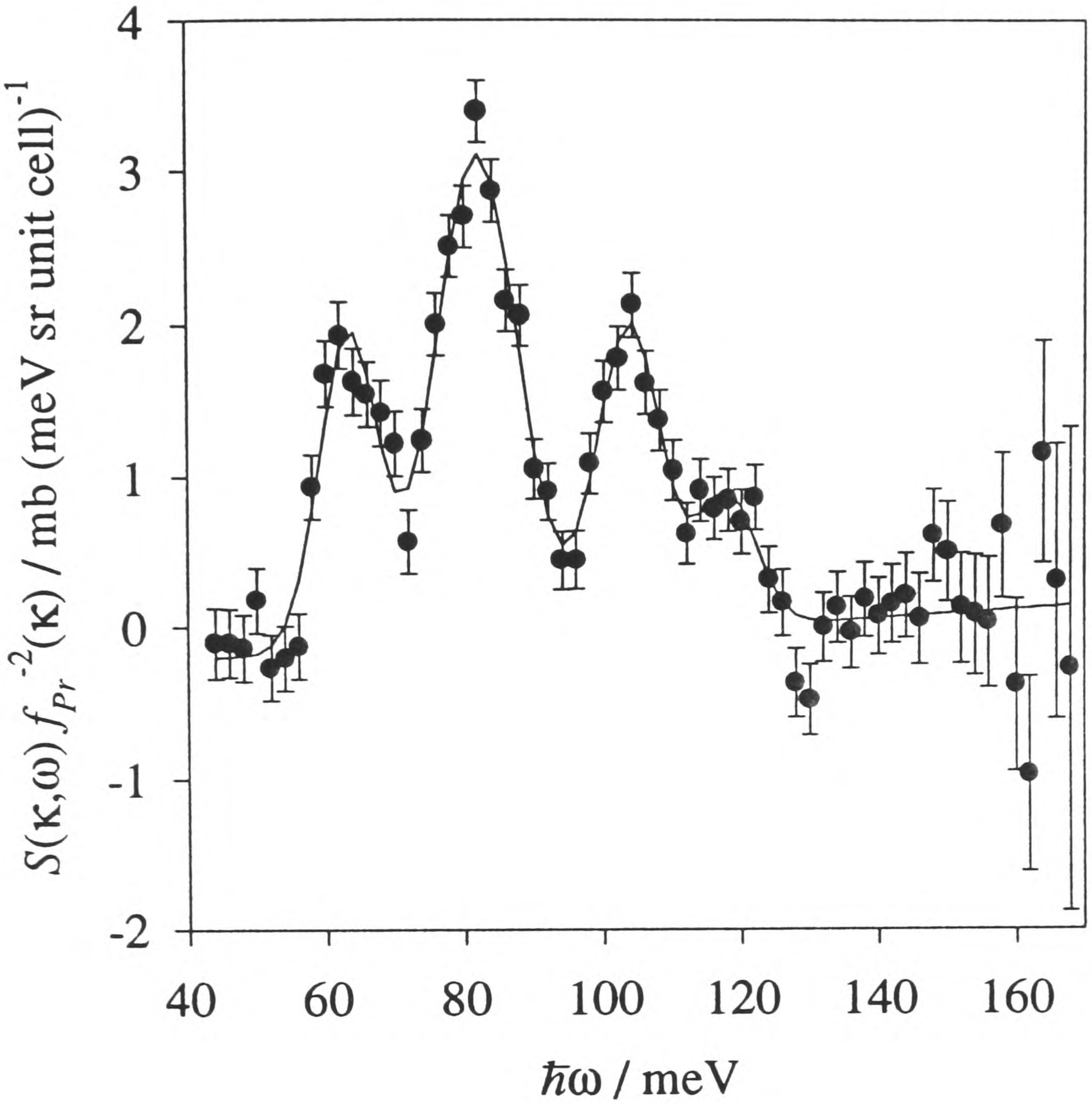

Figure 61: Inelastic scattering measured on $Y_{0.3}Pr_{0.7}Ba_2Cu_4O_8$ at 4.2 K with an incident energy of 180 meV. The data points are the sum of the $\phi = 11.5°$, $\phi = 16.5°$, $\phi = 21.5°$ and $\phi = 26.5°$ spectra. The solid line shows a fit to the data.

Table 33: Energies and intensities of crystal field excitations seen in $Y_{0.3}Pr_{0.7}Ba_2Cu_4O_8$ at 4.2 K with an incident neutron energy of 180 meV.

$\hbar\omega$ / meV	I / mb (sr unit cell)$^{-1}$
61.6 ± 0.4	18 ± 5
80.4 ± 0.2	44 ± 4
102.2 ± 0.4	23 ± 2
116.4 ± 1.0	9 ± 3

3.2c Comparison with $PrBa_2Cu_3O_7$

The crystal field excitations I have observed in $Y_{0.3}Pr_{0.7}Ba_2Cu_4O_8$ agree in certain aspects with some of the measurements on $PrBa_2Cu_3O_7$. Firstly, peak position: I record crystal field excitations at 2.5, 4.8, 62, 80, 102 and 116 meV. This is most similar to the work of Boothroyd *et al*[80], which interpreted previous data as showing crystal field excitations at 3.3, 4.8, 65, 83, 103, 113 and 123 meV. The latter two excitations were assigned to crystal field levels from Pr ions on the Ba site. The crystal field peaks also seem to be broader than the resolution, as has been frequently commented on for $PrBa_2Cu_3O_7$; this can be demonstrated by a comparison with the peaks seen in $HoBa_2Cu_3O_7$.

In terms of observed intensities I again see qualitative agreement, as shown in Table 34 (the cause of the separate normalisation for $PrBa_2Cu_3O_7$ is that the data originally came from two different groups). Hence the spectra for $Y_{0.3}Pr_{0.7}Ba_2Cu_4O_8$ appear to be similar to those of $PrBa_2Cu_3O_7$, and the presence of the structurally well-ordered double chain-layer does not help to resolve the peaks.

Table 34: Energies and intensities of crystal field excitations seen in $PrBa_2Cu_3O_7$ at 5 K[80] and $Y_{0.3}Pr_{0.7}Ba_2Cu_4O_8$ at 4.2 K. For $PrBa_2Cu_3O_7$, the intensities of the first two excitations are normalised to the 5 meV intensity, and the intensities of the remaining excitations are normalised relative to the 83 meV intensity.

$PrBa_2Cu_3O_7$		$Y_{0.3}Pr_{0.7}Ba_2Cu_4O_8$	
$\hbar\omega$ / meV	I	$\hbar\omega$ / meV	I / mb (sr unit cell)$^{-1}$
3.5	> 100	2.5	69 ± 10
5	= 100	4.8	26 ± 8
65	100 ± 30	62	18 ± 5
83	= 100	80	44 ± 4
103	80 ± 30	102	23 ± 2
–	–	116	9 ± 3

3.3 PrO_2

The majority of these measurements were made on HET at the Rutherford-Appleton Labs., with a dummy sample of CeO_2. A few measurements, to investigate scattering close to the elastic line, were also made on a triple axis spectrometer at Risø in Denmark. If the Pr ion is in a stable, unhybridised tetravalent state, then we would expect to see a single, sharp transition, previously reported at 130 meV[83]. However, given the curious behaviour of $PrBa_2Cu_3O_{6+x}$, and the probable hybridisation of its trivalent Pr ion, it seemed worth investigating the much simpler compound of PrO_2 for evidence of any unusual behaviour, such as mixed valency. (If some of the Pr ions, at any instant, are in a trivalent state, then this would produce extra crystal field transitions). Hence we performed measurements with incident energies of 30 meV, 60 meV, 180 meV, 250 meV, 450 meV and 850 meV (the latter two sets of spectra were intended to investigate inter-multiplet transitions), with measurements on CeO_2 at 60 meV, 180 meV, 250 meV and 450 meV.

3.3a The non-magnetic dummy

Figure 62 shows a spectrum measured on the dummy sample of CeO_2 with an incident energy of 180 meV measured at 15 K. The elastic line is fitted as described in Appendix *III-4.2*. Three peaks due to optical phonons can be seen, at 35 meV, 55 meV, and 70 meV, and we would therefore expect to see three similar peaks in the PrO_2 spectra.

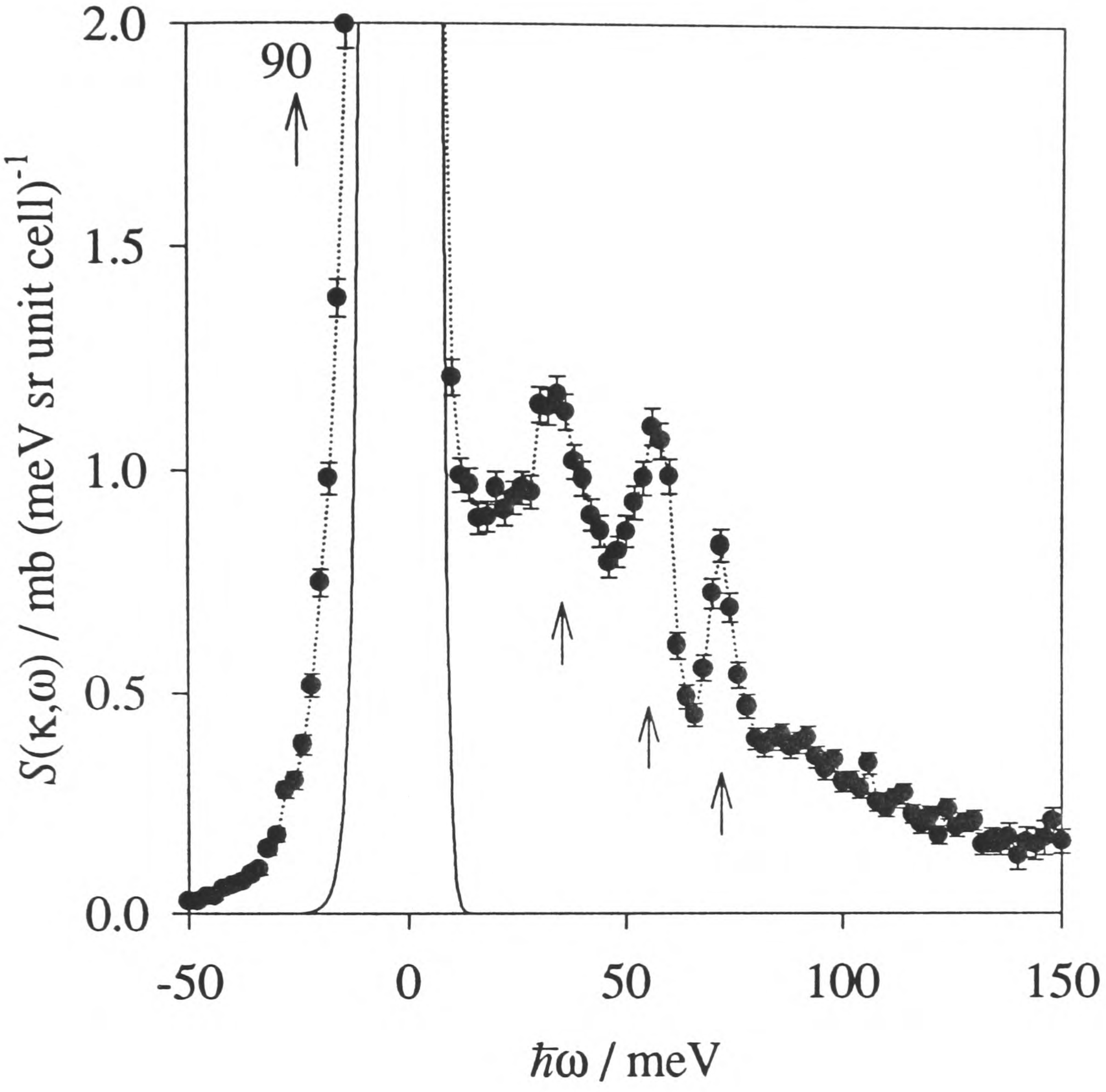

Figure 62: Inelastic scattering measured on CeO_2 at 15 K with an incident energy of 180 meV, summed over the detector banks at scattering angles of $\phi = 11.5°$, $16.5°$, $21.5°$, and $26.5°$. The solid line represents the elastic peak.

3.3b Features observed in PrO_2

A number of features were observed in the spectra measured on the PrO_2 sample. Here we will briefly look at them all, and in the next sections we will examine them in more detail.

Firstly, after we had accounted for the elastic line-shape, scattering was observed in the PrO_2 sample at very low energy transfers (≤ 5 meV), which was not present in the CeO_2 sample (see Figure 63).

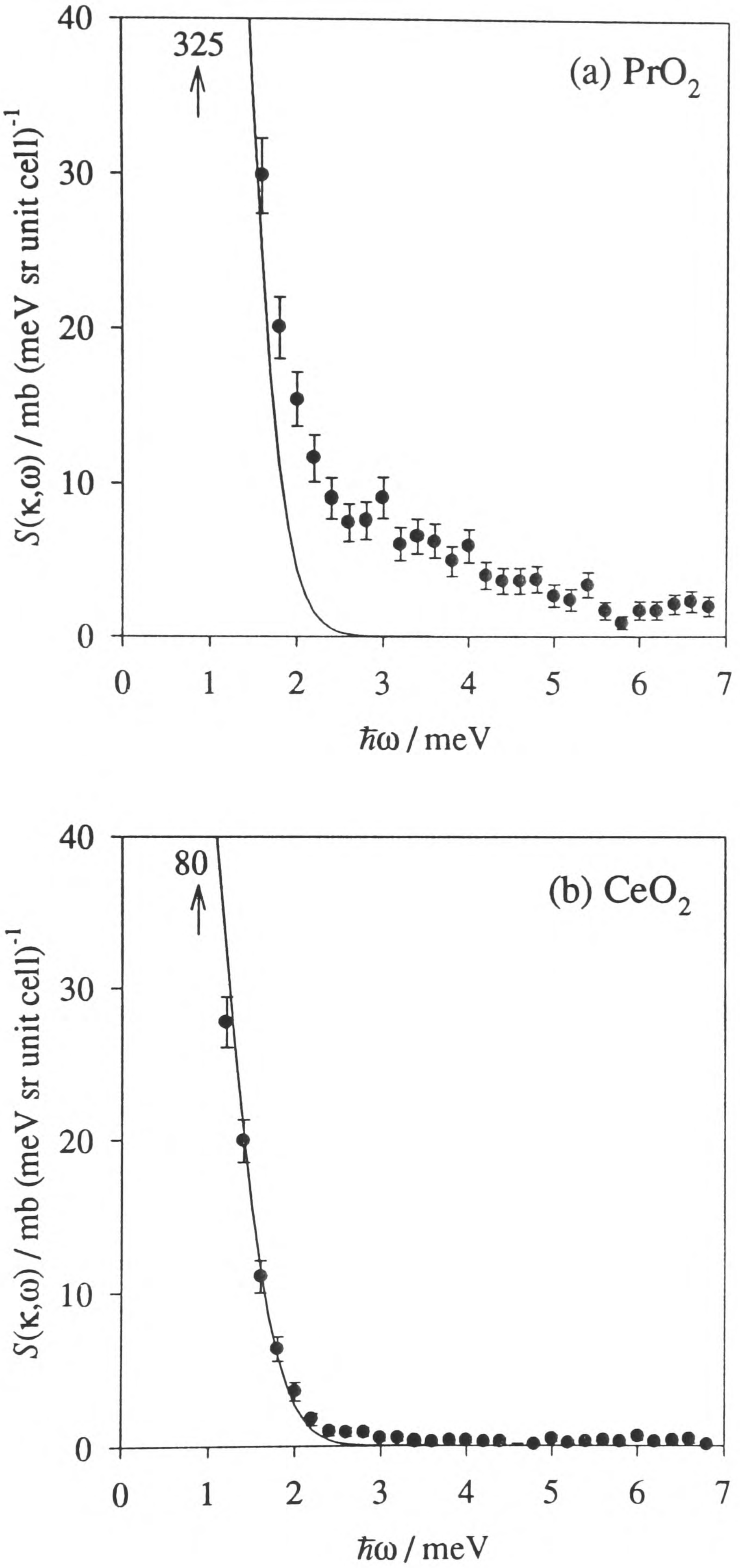

Figure 63: Inelastic scattering measured on (a) PrO_2 and (b) CeO_2 at 15 K with an incident energy of 60 meV by the detector bank at a scattering angle of $\phi = 4.9°$. A region of scattering is present in PrO_2, but not in CeO_2, below about 5 meV.

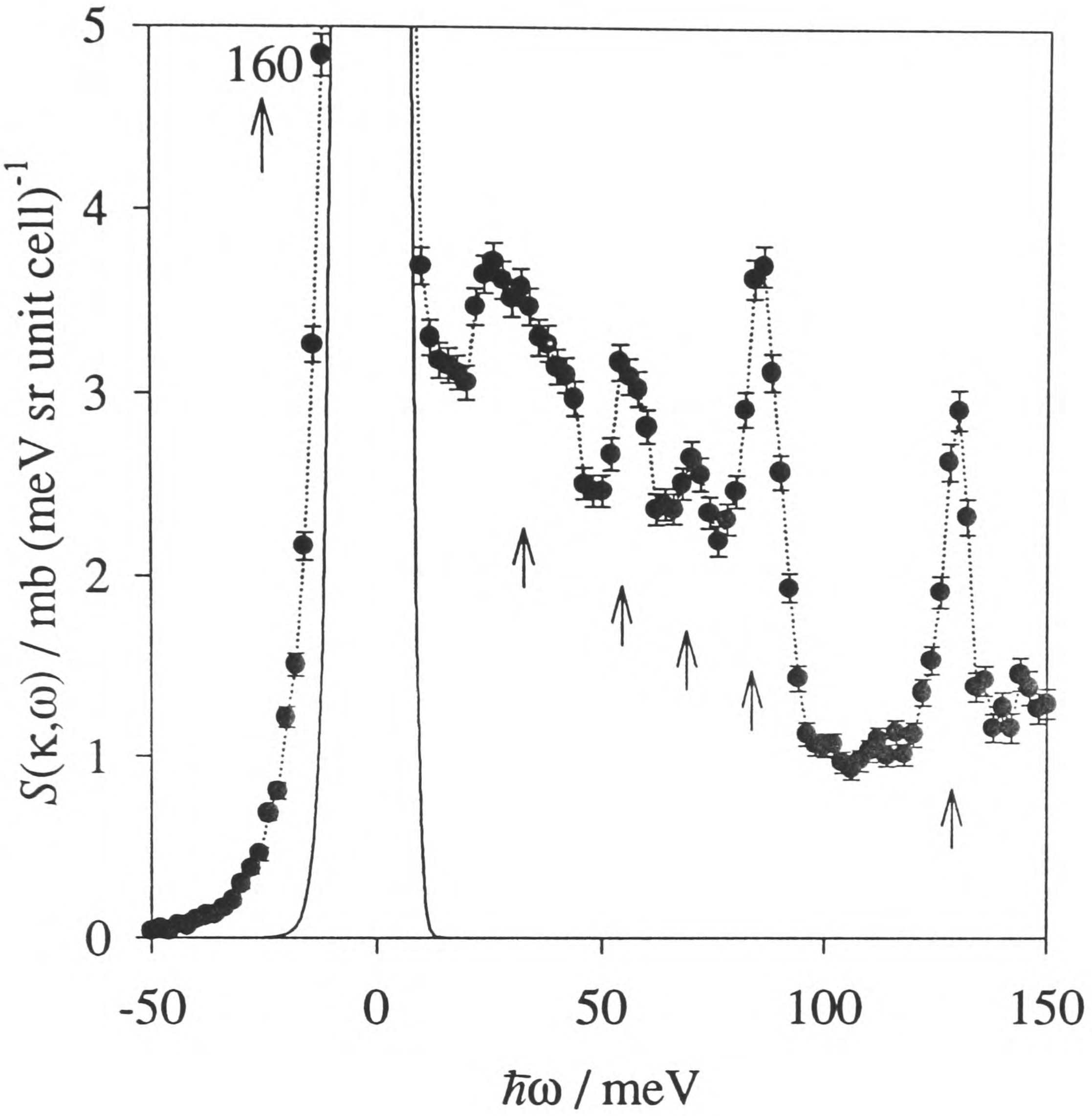

Figure 64: Inelastic scattering measured on PrO_2 at 15 K with an incident energy of 180 meV, summed over the detector banks at scattering angles of $\phi = 11.5°, 16.5°, 21.5°$, and 26.5°. The solid line represents the elastic peak.

A sequence of peaks was then observed at 30 meV, 55 meV, 70 meV, 85 meV, and 130 meV, as shown in Figure 64. Comparing with the equivalent spectra measured on CeO_2 (Figure 62), it would seem reasonable to relate the first three peaks with the optic phonons observed in the dummy sample. This leaves two peaks not observed in CeO_2 (recall that if the Pr ions are stable tetravalent then we only expect to measure one crystal field transition). Also, the 'background' is much higher in the PrO_2 scan, and does not seem to follow the same form as that in CeO_2. (The coherent scattering lengths of Pr and Ce are (4.58 ± 0.05) fm and (4.84 ± 0.02) fm respectively[85], and so we would expect a similar non-magnetic background; the difference in the elastic peak is discussed in Section *III-3.3d*).

Moving to higher energy transfers, the spectra measured with an incident energy of 250 meV showed no additional transitions, and the 450 meV spectra showed no evidence of inter-multiplet transitions. The 850 meV spectra, however, did show a single high energy transfer transition at 445 meV, as shown in Figure 65.

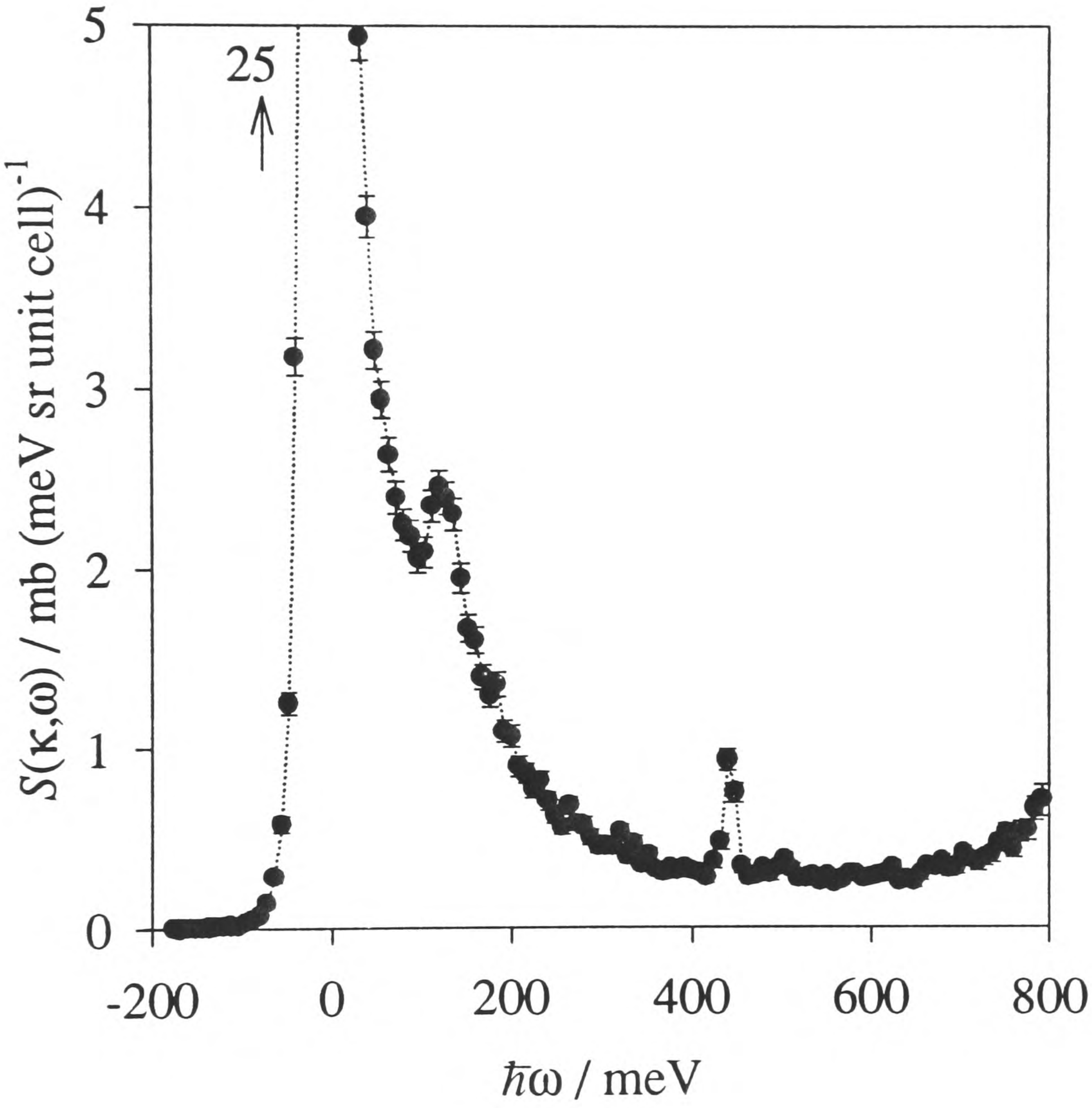

Figure 65: Inelastic scattering measured on PrO_2 at 75 K with an incident energy of 850 meV by the detector bank at a scattering angle of $\phi = 4.9°$. A high energy transfer transition can be seen at 445 meV.

I now examine these features in more detail.

---

[85] V.F. Sears, *Neutron scattering lengths and cross sections*, available from the Rutherford-Appleton Labs.

3.3c Scattering below 5 meV

The measurements on HET indicated that there may be a region of inelastic magnetic scattering below about 5 meV. To investigate this scattering, powder measurements were made on a triple-axis spectrometer in Risø. The scans were made in direct geometry (i.e. the incident neutron energy was fixed) and at constant-κ. Wavevector transfers of $\kappa = (0.8, 0.8, 0), (1.1, 1.1, 0)$ and $(1.7, 1.7, 0)$ were used. Measurements were also made on the CeO_2 dummy sample. The temperature was varied between 1.66 K and 60 K.

Figure 66 shows the scattering at (a) 4.76 K and 18.2 K, and (b) 1.66 K. The presence of an inelastic peak can be seen most clearly at 4.76 K, centred at about 2.6 meV (the '2.6 meV peak' from here on). The integrated scattering function of the 2.6 meV peak follows the square of the form factor (for details of the form factor, see Section *III-3.3f*). As temperature is increased, this peak gradually moves into the elastic line to produce a broad peak of quasi-elastic scattering, as shown in the 18.2 K data. The presence of this inelastic peak therefore seems to be connected to the antiferromagnetic ordering of the PrO_2, which has a Néel temperature of 14 K, i.e. the magnetic interaction appears to have split the crystal field ground-state of the Pr ion.

The 1.66 K data shows an interesting effect - something has filled in the gap between the 2.6 meV peak and the elastic line. Since the 2.6 meV peak remains mostly unaffected, it seems unlikely that this is the result of some change in the magnetic ordering. This additional scattering may be quasi-elastic in origin.

Taking into account the Principle of Detailed Balance, which states that[86]

$$S(\kappa,\omega) = \exp(\beta\hbar\omega)S(-\kappa,-\omega) \qquad (126)$$

the effect of any broadening on the quasi-elastic line can be represented by

---

[86] S.W. Lovesey, *Theory of neutron scattering from condensed matter* volume 1, §3.3, Oxford Science Publications (1986).

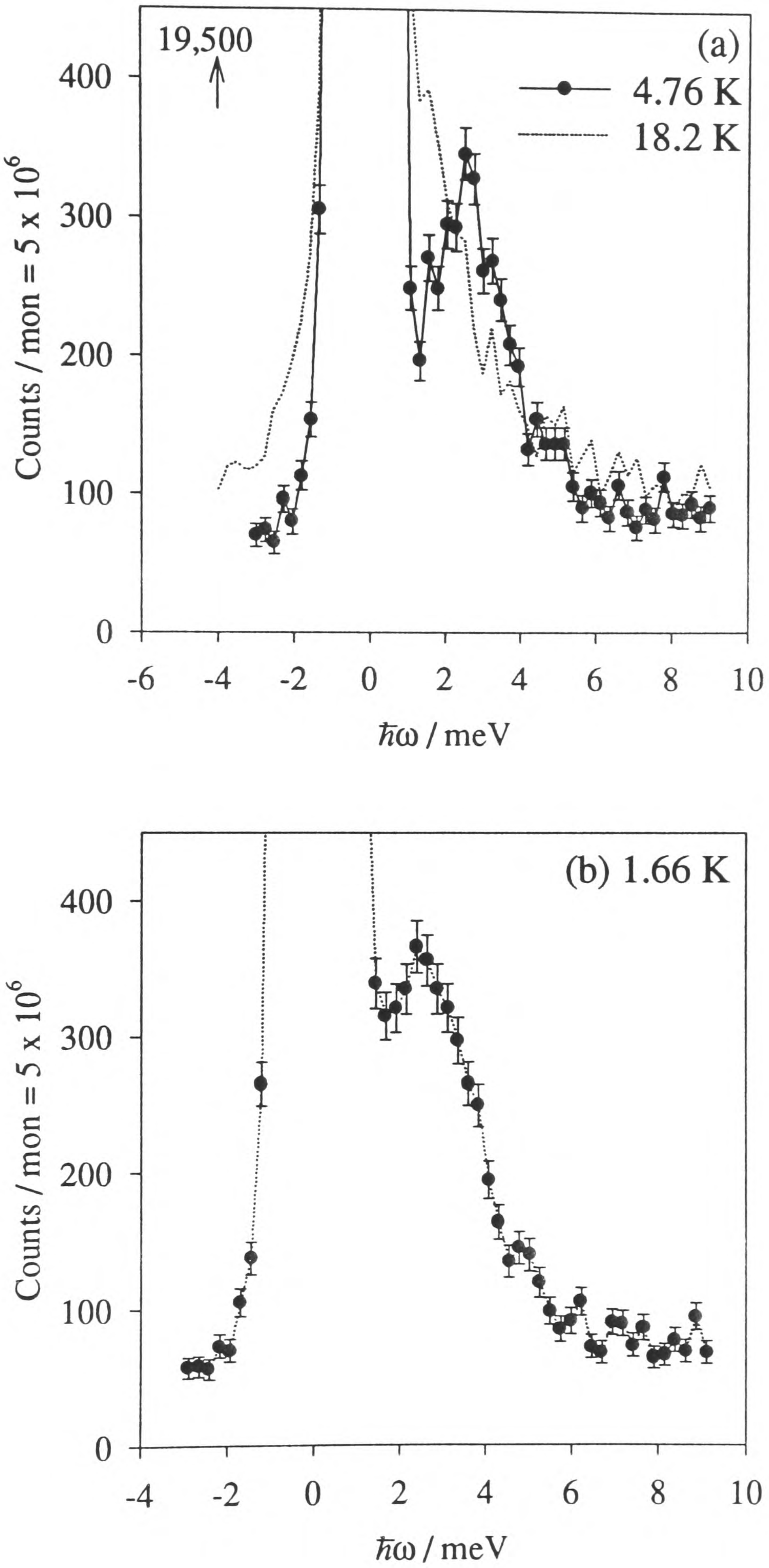

Figure 66: Inelastic scattering measured on PrO_2 with an incident energy of 13.7 meV and wavevector transfer of $\kappa = (1.1, 1.1, 0.0)$ $Å^{-1}$, at (a) 4.76 K (symbols and solid line) and 18.2 K (dotted line), and (b) 1.76 K.

$$\delta(\hbar\omega) \rightarrow \frac{\beta\hbar\omega}{1-\exp(-\beta\hbar\omega)} P(\beta,|\hbar\omega|) \tag{127}$$

where $P(\beta,|\hbar\omega|)$ describes the line-shape and is normalised to unit area. As temperature decreases, the detailed-balance term makes the peak increasingly asymmetric, pushing the centre of mass of the quasi-elastic peak to higher energy losses (greater $\hbar\omega$). This could therefore explain the additional scattering between the elastic peak and the 2.6 meV peak at 1.76 K.

The intensity of the 2.6 meV peak was (23 ± 2) mb (sr unit cell)$^{-1}$. Above the Néel temperature, the intensity of the quasi-elastic scattering was (38 ± 3) mb (sr unit cell)$^{-1}$.

3.3d The 85 meV peak

To definitively decide whether or not a peak is from a crystal field transition or a particularly sharp optic phonon, it is necessary to measure its wavevector dependence. This was done for the 85 meV peak by using the individual detector banks at 4.9°, 11.5°, 16.5°, 21.5°, 26.5°, 118°, and 130°, and incident neutron energies of 105 meV, 130 meV, 180 meV, 250 meV, and 450 meV.

If the peak is from a crystal field transition, it will decrease with κ in proportion to the square of the form factor multiplied by the Debye-Waller factor; if it is from an optic phonon, it will be proportional to $\kappa^2 \exp(-\alpha(T)\kappa^2)$, where the exponential term is the Debye-Waller factor. For a classical harmonic oscillator, $\alpha(T) = k_BT/C$, where C is the spring constant[87]. Normally the Debye-Waller factor is unimportant, so that phonon scattering in the high-angle detector banks is significantly greater than that in the low-angle banks. However, the 85 meV peak was not present in the high-angle banks, and so a more careful study was required.

As can be seen in Figure 67, the integrated scattering function of the 85 meV peak follows the expected κ-dependence for phonon-creation, and not of a crystal field transition. The peak has a very strong Debye-Waller factor. This indicates that low

---

[87] C. Kittel, *Introduction to solid state physics* 6th edition, Appendix A, John Wiley & Sons (1986).

temperatures are sufficient to affect the phonon mode, which in turn implies that the phonon mode is related to weak bonds. On the other hand, the peak is at an unusually high energy, implying that either strong bonds or light elements are involved; the frequency of an optic acoustic mode is proportional to $\sqrt{C/\mu}$, where μ is the reduced mass[88].

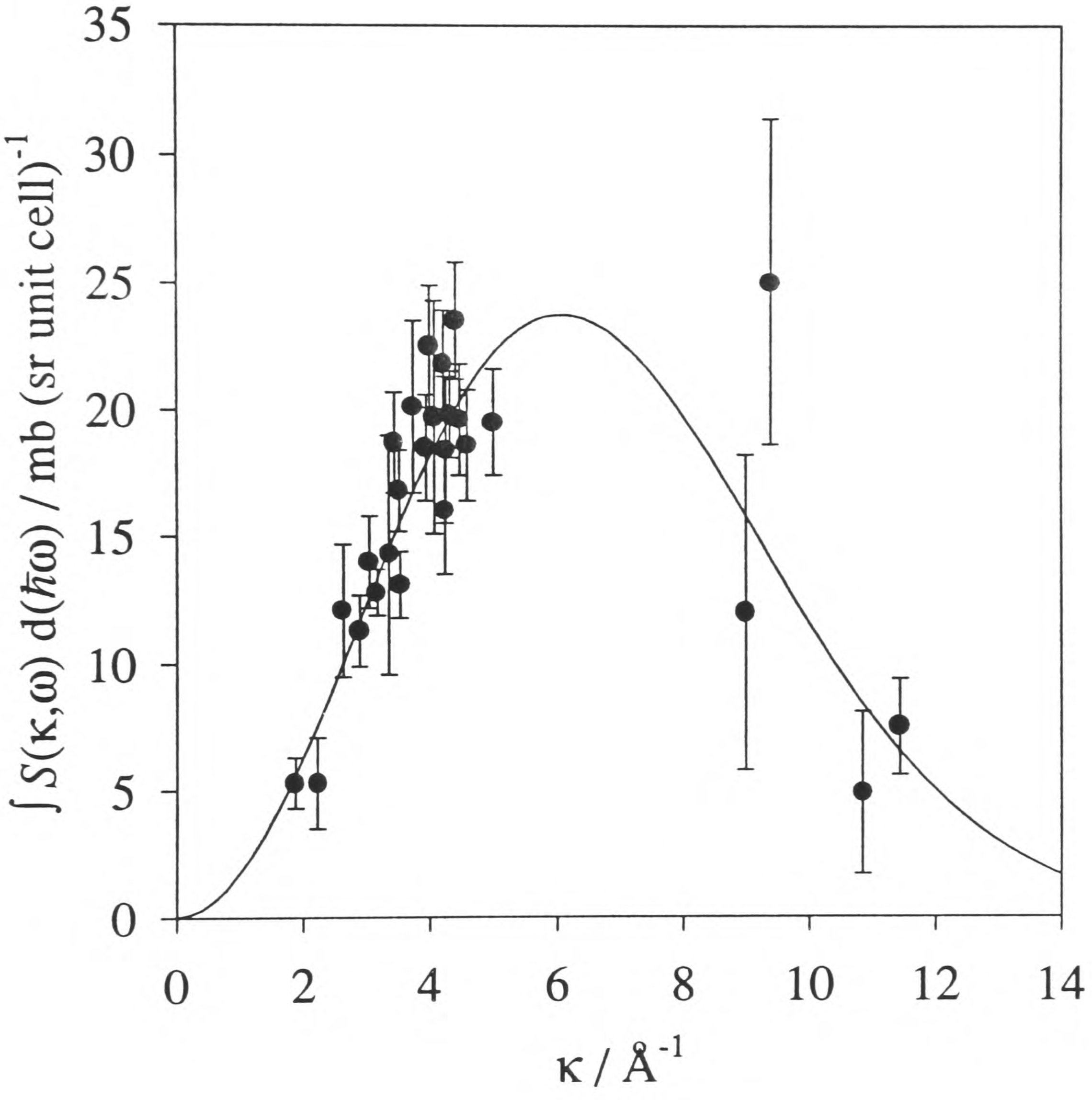

Figure 67: The integrated scattering function of the 85 meV peak measured on PrO_2 at 15 K as a function of wavevector transfer. The solid line shows a fit to the typical phonon wavevector-dependence (see text).

Taken together, these indicate that a very light element is responsible for the peak, for example hydrogen. The first measurements were done with the samples in a

---

[88] C. Kittel, *Introduction to solid state physics* 6th edition, §4, John Wiley & Sons (1986).

displex closed-cycle refrigerator, which can be prone to ice-contamination. To ensure that this was not the cause of the 85 meV peak, subsequent measurements were done in a cryostat, from which it was seen that the peak remained. Additional measurements have shown that an 85 meV peak also occurs in Pr_6O_{11}. It may be that water has contaminated both praseodymium oxides, and that the phonon mode involves weakly bonded hydrogen ions.

An upper limit of the amount of water contamination can be made from the elastic line. In measurements at high wavevector transfer, the integrated scattering function is the same for PrO_2 as for CeO_2, which is to be expected since they have practically the same scattering lengths. However, in measurements at low wavevector transfer there is more scattering from the PrO_2 sample than from the CeO_2 sample. This is also to be expected, since the PrO_2 sample will scatter paramagnetically. However, if there is any water, this would also be a major contribution to the elastic line, since hydrogen has such a big incoherent cross-section. The water would not contribute at high wavevector transfer due to its stronger Debye-Waller factor.

Using the data taken with neutrons of incident energy 60 meV measured in the 4.9° detector bank, the difference in the integrated scattering function between the PrO_2 data and the CeO_2 data is (608 ± 5) mb $(\text{sr unit cell})^{-1}$. Under these conditions, the scattering vector is $\kappa = 0.46$ Å^{-1}. The incoherent cross-section of a water molecule is 161 b[85], and so the differential incoherent cross-section is 12.8 b $(\text{sr})^{-1}$. Hence the upper limit for the water contamination of the sample is approximately 0.048 water molecules per PrO_2 molecule.

3.3e The 30 meV, 55 meV, and 70 meV peaks

As was stated in Section *III-3.3b*, these peaks can be related to corresponding phonon peaks in CeO_2. Figure 68 shows how the scattering changes as you increase the scattering angle (and the wavevector transfer), for an incident energy of 180 meV at 15 K. The broad peak at 30 meV, and the sharper peaks at 55 meV and 70 meV, show the typical phonon behaviour of increasing with κ (this behaviour is most pronounced for the 70 meV peak, which does not even occur in the $\phi = 4.9°$ detector bank). The figure also shows how the strong Debye-Waller factor of the 85 meV peak reduces its intensity in the ϕ = 130° scattering banks, whereas the other phonon peaks are still present.

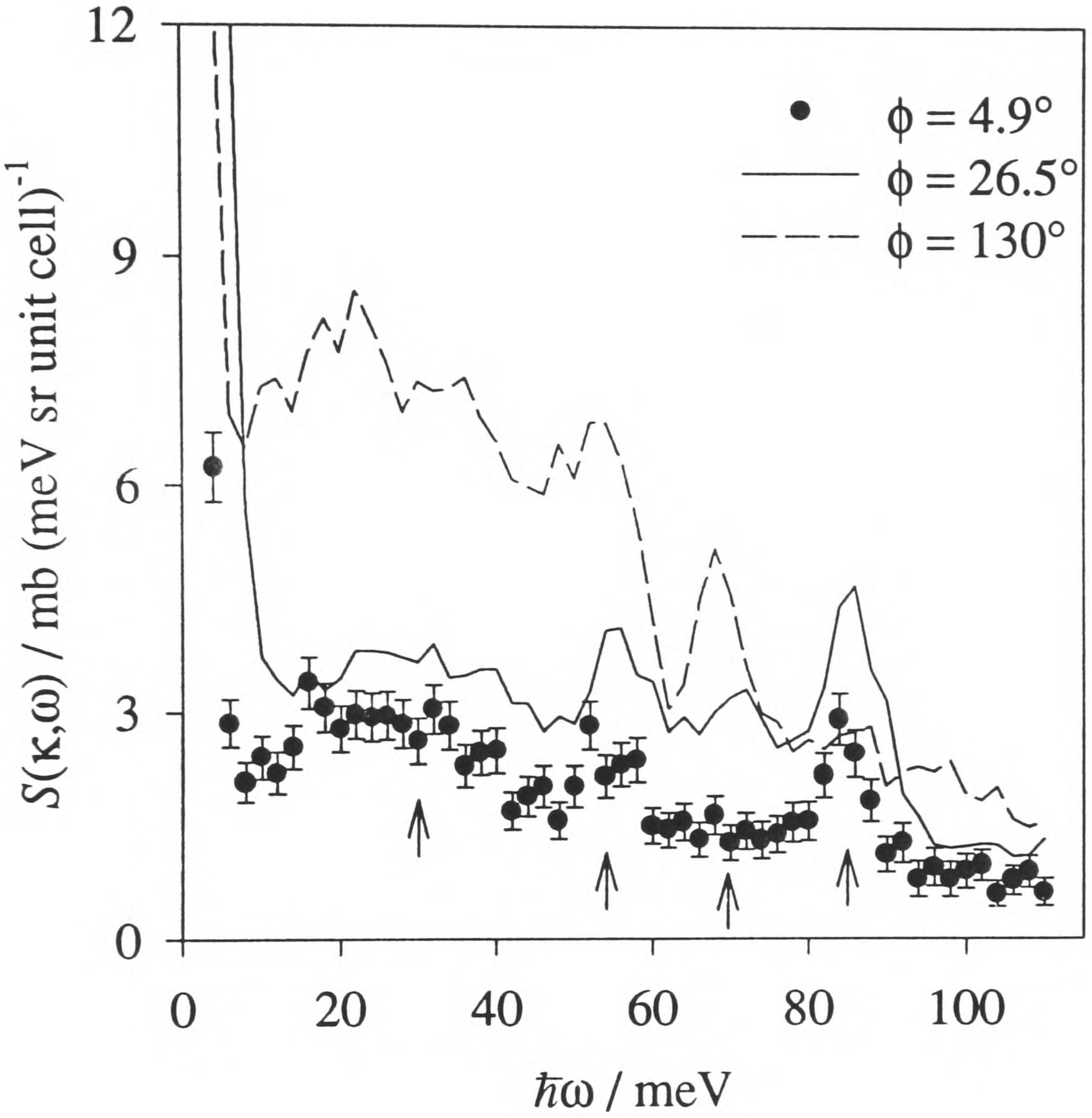

Figure 68: Inelastic scattering measured on PrO_2 at 15 K with an incident energy of 180 meV, by the detector banks at scattering angles of ϕ = 5° (closed symbols), ϕ = 26.5° (solid line), and ϕ = 130° (dashed line).

The high background level also increases strongly with wavevector transfer, indicating that this feature is probably due to phonons. Like the 85 meV peak, the high background is not observed in the CeO_2 sample, and so the two may share a common origin.

3.3f The 130 meV peak

As we have seen, the absence of a peak in the high-angle banks is not necessarily evidence that the peak is magnetic in origin; the 85 meV peak shows this behaviour but is probably due to the creation of an optic phonon. Hence the integrated scattering function for this peak was measured as a function of scattering vector, using the individual detector banks at 4.9°, 11.5°, 16.5°, 21.5°, and 26.5°, and incident neutron energies of 180 meV, 250 meV, and 450 meV.

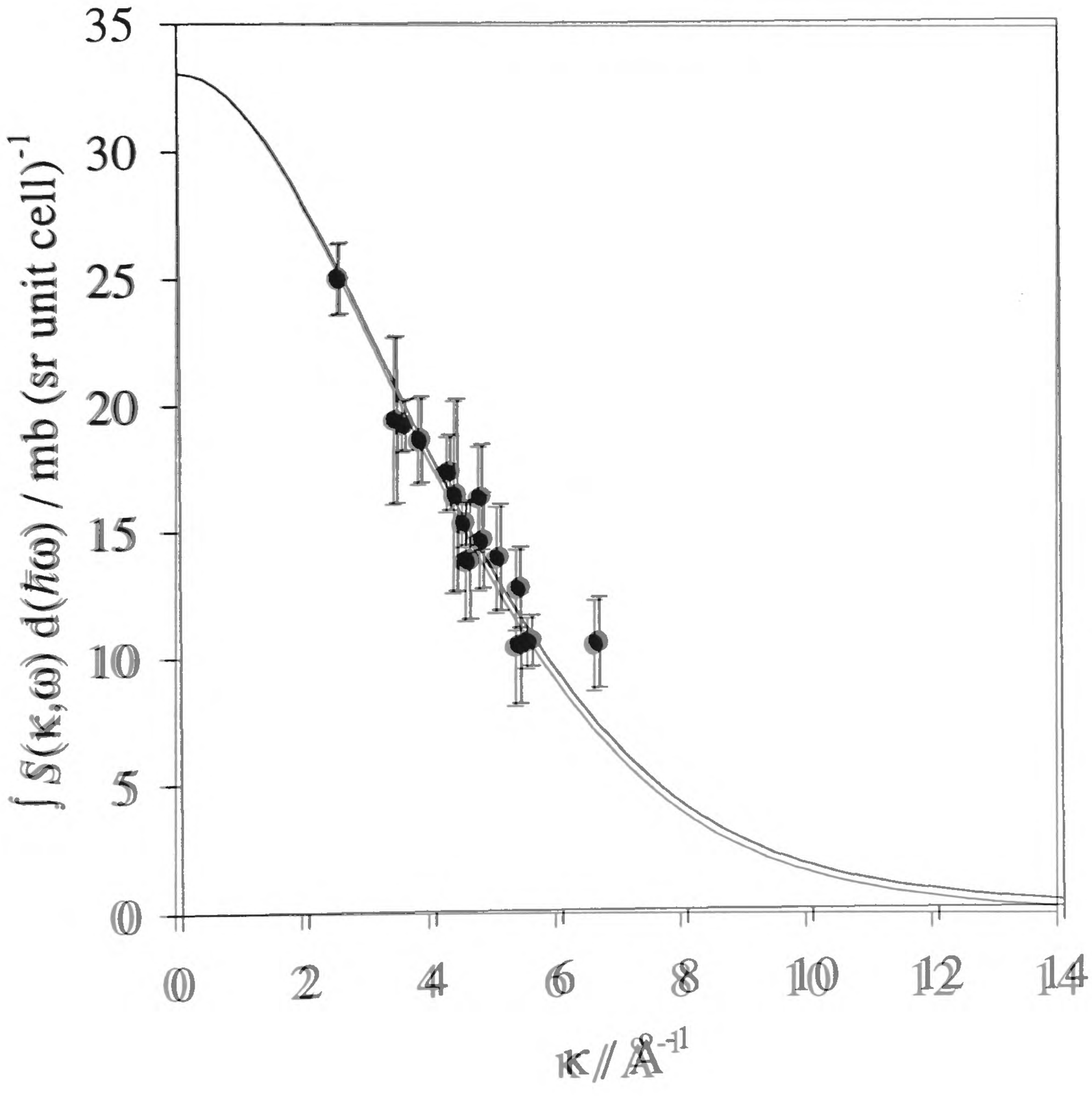

Figure 69: The integrated scattering function of the 130 meV peak measured on PrO_2 at 15 K as a function of wavevector transfer. The solid line shows a fit with an appropriate form factor.

The results are shown in Figure 69, where it can be seen that the integrated scattering function falls off with the square of the form factor. The form factor was calculated using the dipole approximation (see Section *II-1.1c*). The relevant coefficients of $\langle j_n(\kappa)\rangle$ are not tabulated for Pr^{4+}; however, a suitable approximation is to assume that the radial wave function for Pr^{4+} ($4f^1$) is simply contracted compared to Ce^{3+} ($4f^1$) due to the extra ionic charge, and to then stretch the form factor accordingly, as described in Section *II-1.1b*. The amount of radial expansion or contraction, characterised by α (see Equation (22)), can be calculated by

$$(1+\alpha)^n = \frac{\langle r^n\rangle_{Pr^{4+}}}{\langle r^n\rangle_{Ce^{3+}}} \tag{128}$$

A review of tabulated values of $\langle r^n\rangle$ suggests that $\alpha = -0.1$ is a suitable value[89], i.e. Pr^{4+} shows a 10% radial contraction compared to Ce^{3+}. The relevant coefficients for $\langle j_n(\kappa)\rangle$ are given in Table 37, Section *III-3.3g*; it turns out that their is little difference between the expected form factors for Pr^{4+} and Pr^{3+}.

At 15 K, the intensity of the 130 meV peak is (33.1 ± 0.6) mb (sr unit cell)$^{-1}$. However, as temperature increases the peak's behaviour is most unusual: the peak decreases in amplitude, broadens, and moves to lower energy transfers (see Figure 70).

The 130 meV peak was studied at temperatures of 4.2 K, 15 K, 25 K, 75 K, 125 K, 175 K, 225 K, and 250 K, with an incident neutron energy of 180 meV. Although there is some change between 4.2 K and 75 K (Figure 70), the most rapid change occurs between 75 K and 125 K, after which the broadened peak shows little temperature dependence (see Figure 71).

---

[89] W.B. Lewis, *Relativistic calculations of* $\langle r^{-3}\rangle$ *and other* $\langle r^n\rangle$ *parameters encountered in magnetic resonance of rare-earth ions and atoms*, from the proceedings of XVI congress AMPERE, Bucharest, (1971).

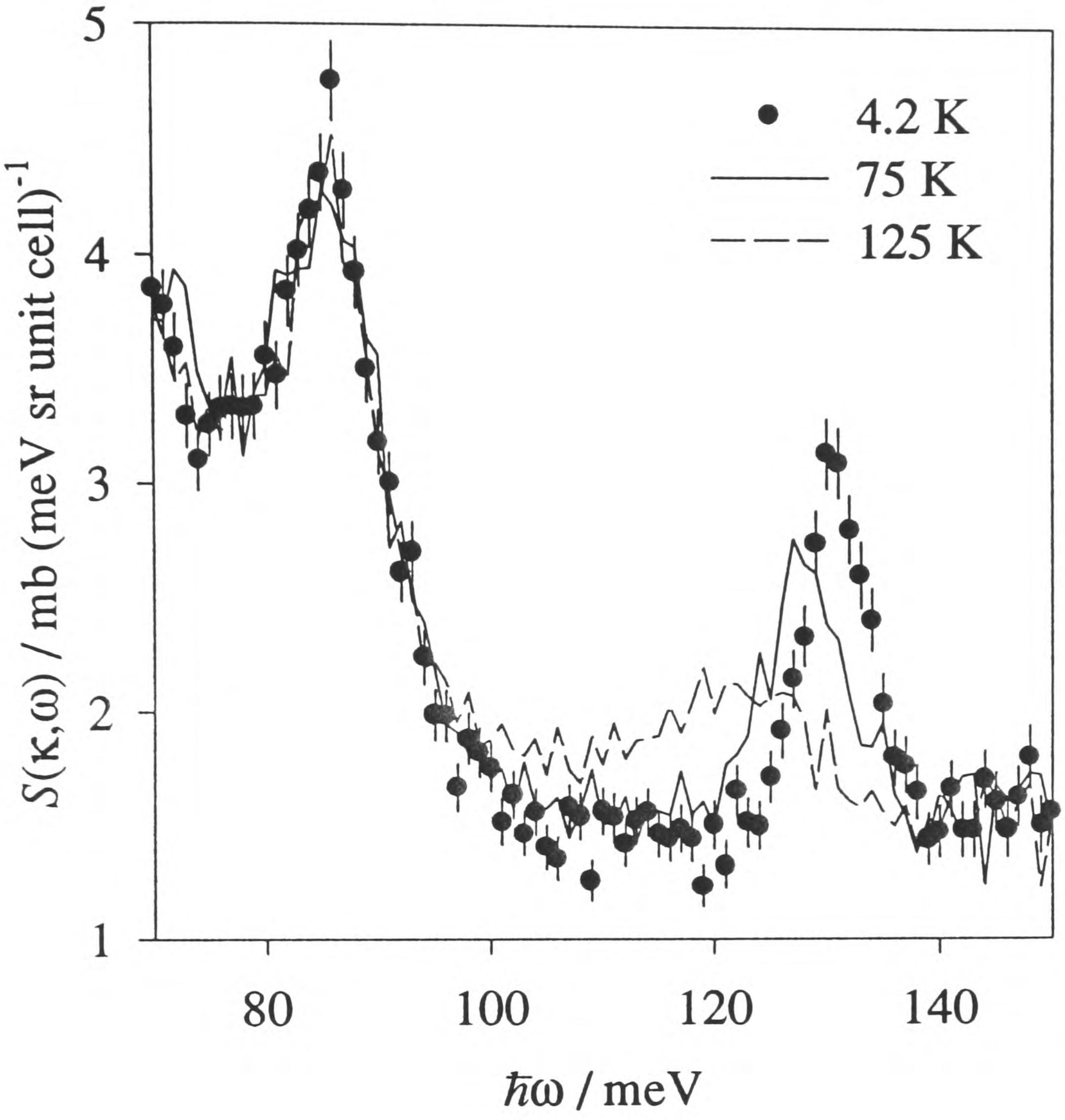

Figure 70: Inelastic scattering measured on PrO_2 with an incident energy of 180 meV, summed over the detector banks at scattering angles of $\phi = 11.5°$, 16.5°, 21.5°, and 26.5°, at 4.2 K (closed symbols), 75 K (solid line) and 125 K (dashed line).

Although the peak is broadening and moving to lower energy transfers (Figure 71 (a)), its integrated scattering intensity remains approximately as it was at 15 K (Figure 71 (b)), where the intensity was (33.1 ± 0.6) mb (sr unit cell)$^{-1}$; to measure the peak area a smooth background was fitted to the 4.2 K data. The curious behaviour of this peak will be the subject of a discussion in Section *III-3.3i*. The fact that the 85 meV peak does not show the same temperature dependence is further evidence that they do not share a common origin.

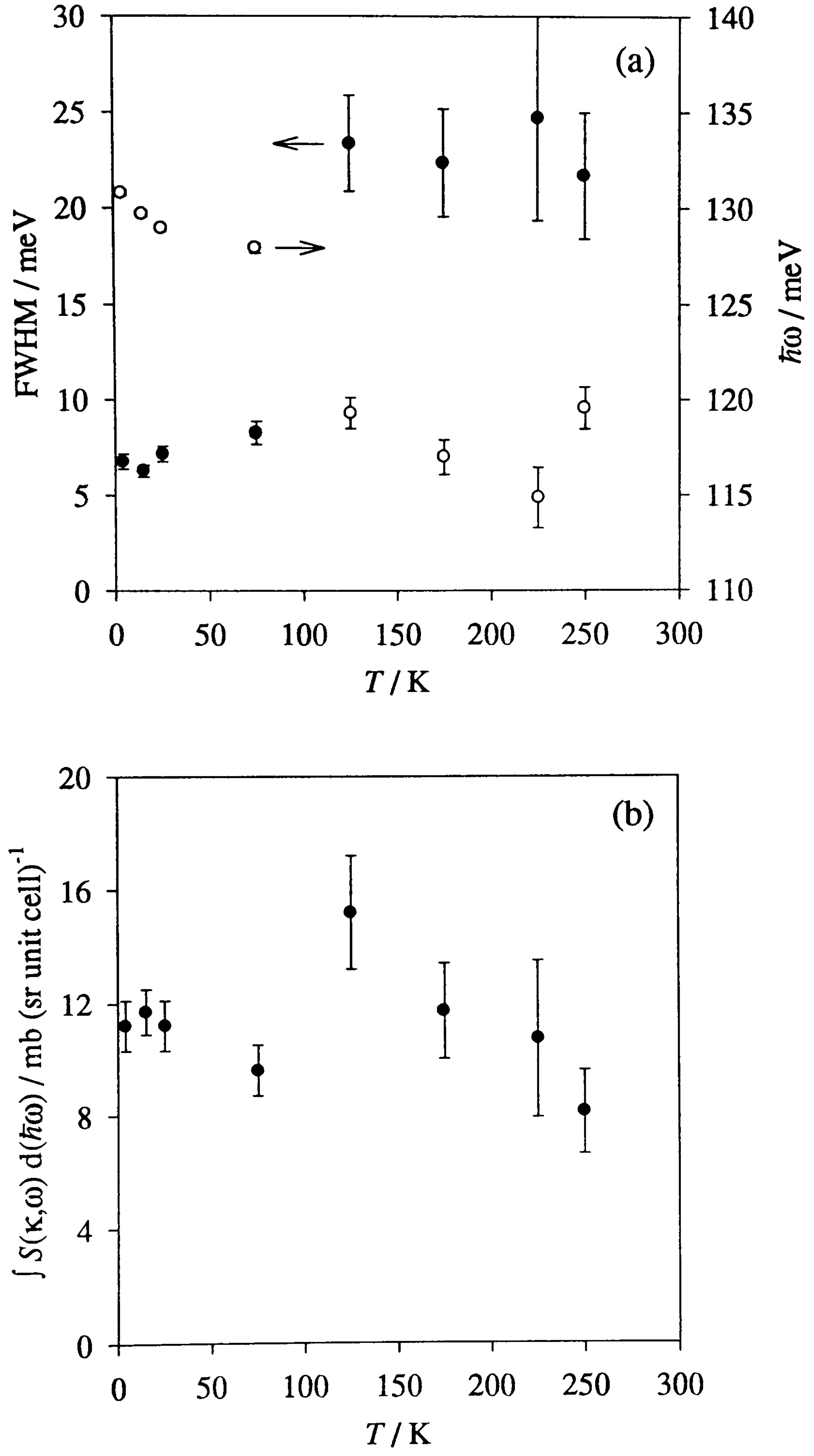

Figure 71: Temperature dependence of the PrO_2 130 meV peak, measured with an incident neutron energy of 180 meV: (a), the FWHM (closed symbols) and peak centre (open symbols), and (b) the integrated scattering function.

3.3g The 450 meV peak

The final peak that was observed occurred at an energy transfer of 450 meV. At such a high energy, this was expected to be an inter-multiplet transition (such transitions have been seen in Pr metal[90]). Transitions within the same J-multiplet have a κ-dependence which can be effectively approximated to the square of the elastic form factor discussed in Section *II-1.1c.* However, a more accurate calculation can be made, for both transitions within the same J-multiplet and for inter-multiplet transitions, which is denoted by $G(\kappa)$[91]. $G(\kappa)$ incorporates the matrix elements, so that the integrated scattering function is

$$\int S(\kappa,\omega)d(\hbar\omega) = 290G(\kappa) \text{ mb (sr unit cell)}^{-1} \tag{129}$$

For transitions within the same J-multiplet, this is, to a very good approximation, related to the elastic form factor by

$$= 72.4 g_J{}^2 \sum_{ij} n_i |\langle j|J_\perp|i\rangle|^2 f(\kappa)^2 \text{ mb (sr unit cell)}^{-1} \tag{130}$$

Inter-multiplet transitions, on the other hand, have a κ-dependence which is distinctly different to the square of the elastic form factor.

$G(\kappa)$ can be expressed in terms of Bessel functions as follows:

$$G(\kappa) = \sum_n g_n \langle j_n(\kappa)\rangle^2 + g_n' \langle j_n(\kappa)\rangle \langle j_{n+2}(\kappa)\rangle \tag{131}$$

Table 35 shows the g_n and g_n' coefficients for the dipole transition Pr^{4+} (or Ce^{3+}) ($4f^1$) $^2F_{5/2} \rightarrow {}^2F_{7/2}$, and Table 36 shows the coefficients for Pr^{3+} ($4f^2$) $^3H_4 \rightarrow {}^3H_5$.

---

[90] A.D. Taylor, R. Osborn, K.A. McEwen, W.G. Stirling, Z.A. Bowden, W.G. Williams, E. Balcar, and S.W. Lovesey, *Intermultiplet transitions in praseodymium using neutron spectroscopy*, Phys. Rev. Letters **61**, 1309-1312, (1988).

[91] E. Balcar and S.W. Lovesey, *Neutron-electron spectroscopy of rare-earth ions*, J. Phys. C **19**, 4605-4611, (1986).

Table 35: Coefficients in the Bessel function expansion of the κ-dependence of the dipole inter-multiplet transition Pr^{4+} (or Ce^{3+}) $(4f^1)\ {}^2F_{5/2} \rightarrow {}^2F_{7/2}$.

n	0	2	4	6
g_n	0.09524	0.42177	0.48474	0.88548
g'_n	−0.09524	−0.01361	−0.00394	–

Table 36: Coefficients in the Bessel function expansion of the κ-dependence of the dipole inter-multiplet transition Pr^{3+} $(4f^2)\ {}^3H_4 \rightarrow {}^3H_5$.

n	0	2	4	6
g_n	0.20000	0.33535	0.09073	0.35376
g'_n	−0.34222	−0.01868	0.00000	–

Hence the Bessel functions are needed for n up to 6. Again, for Pr^{4+}, we must adapt the results tabulated for Ce^{3+}; these are given in Table 37, for use with Equation (19) (Section *II-1.1b*). The corresponding coefficients for Pr^{3+} are given in Table 38.

The coefficients of Table 35 and Table 36 are for the complete $J \rightarrow J+1$ multiplet transitions, and hence take no account of crystal field effects. Figure 72 shows the κ-dependence of the scattering function for inter-multiplet transitions, compared to transitions within the same J-multiplet. The dipole-transition $G(\kappa)$ initially falls quicker than $f(\kappa)^2$, but then becomes levels off whilst $f(\kappa)^2$ continues to fall towards zero.

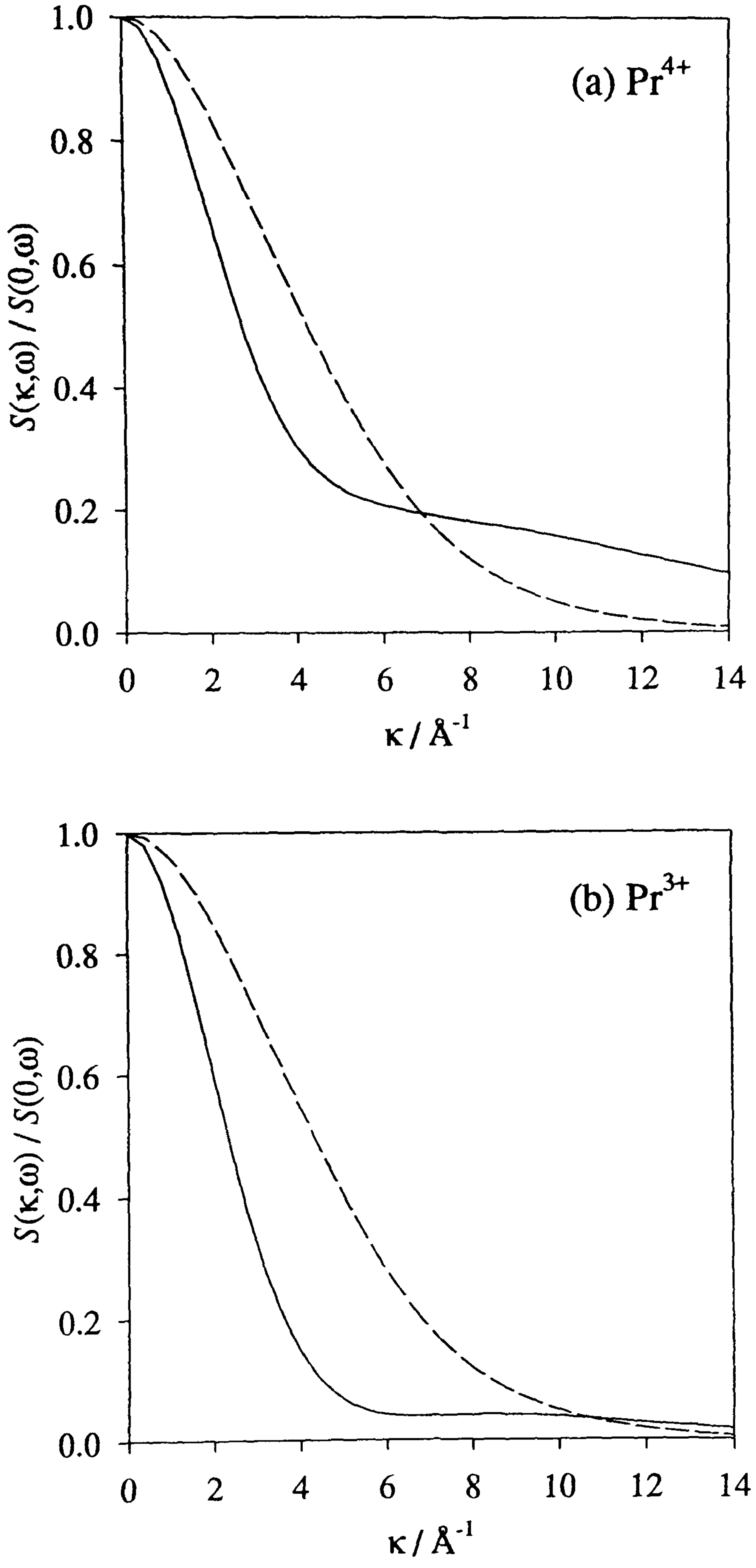

Figure 72: Illustration showing how the scattering function falls off with κ for: (a) Pr^{4+} ($4f^1$) $^2F_{5/2} \rightarrow {}^2F_{7/2}$ (solid line), $^2F_{5/2} \rightarrow {}^2F_{5/2}$ (dashed line); (b) Pr^{3+} ($4f^2$) $^3H_4 \rightarrow {}^3H_5$ (solid line), $^3H_4 \rightarrow {}^3H_4$ (dashed line).

Table 37: Coefficients for $\langle j_n(\kappa)\rangle$, the expectation values of the *n*th Bessel functions, for the Ce^{3+} ion[36]. $C = 0$.

n	A	a	B	b	D
0	0.2291	18.18	0.7897	5.807	−0.0191
2	2.1284	8.9174	1.1229	2.8371	0.01108
4	0.4221	1.7572	−0.4087	14.604	0.01465
6	0.13076	0.8650	−0.15173	5.6704	0.00281

Table 38: Coefficients for $\langle j_n(\kappa)\rangle$, the expectation values of the *n*th Bessel functions, for the Pr^{3+} ion[36]. $C = 0$.

n	A	a	B	b	D
0	0.2277	16.11	0.7923	5.277	−0.0204
2	1.8655	8.1948	1.0779	2.6641	0.01199
4	0.3827	1.5924	−0.3589	12.6798	0.01384
6	0.12917	0.9376	−0.13886	4.1666	0.00793

Although the 450 meV peak was not measured over a broad range of wavevector transfer, it is clear from Figure 73 that the integrated scattering function has a κ-dependence which is much flatter than the elastic $f(\kappa)^2$, and so this would seem to confirm that the 450 meV peak is due to an inter-multiplet transition.

Unlike the elastic form factor, it makes a substantial difference to the intensity whether you assume that the scattering is from Pr^{4+} or Pr^{3+} ions, and so I have not fitted the data to $G(\kappa)$ and extrapolated the result to $\kappa = 0$. The integrated scattering function of the 450 meV peak was approximately constant at (11.8 ± 0.8) mb (sr unit cell)$^{-1}$, in a region of $6 < \kappa < 10$ Å^{-1}.

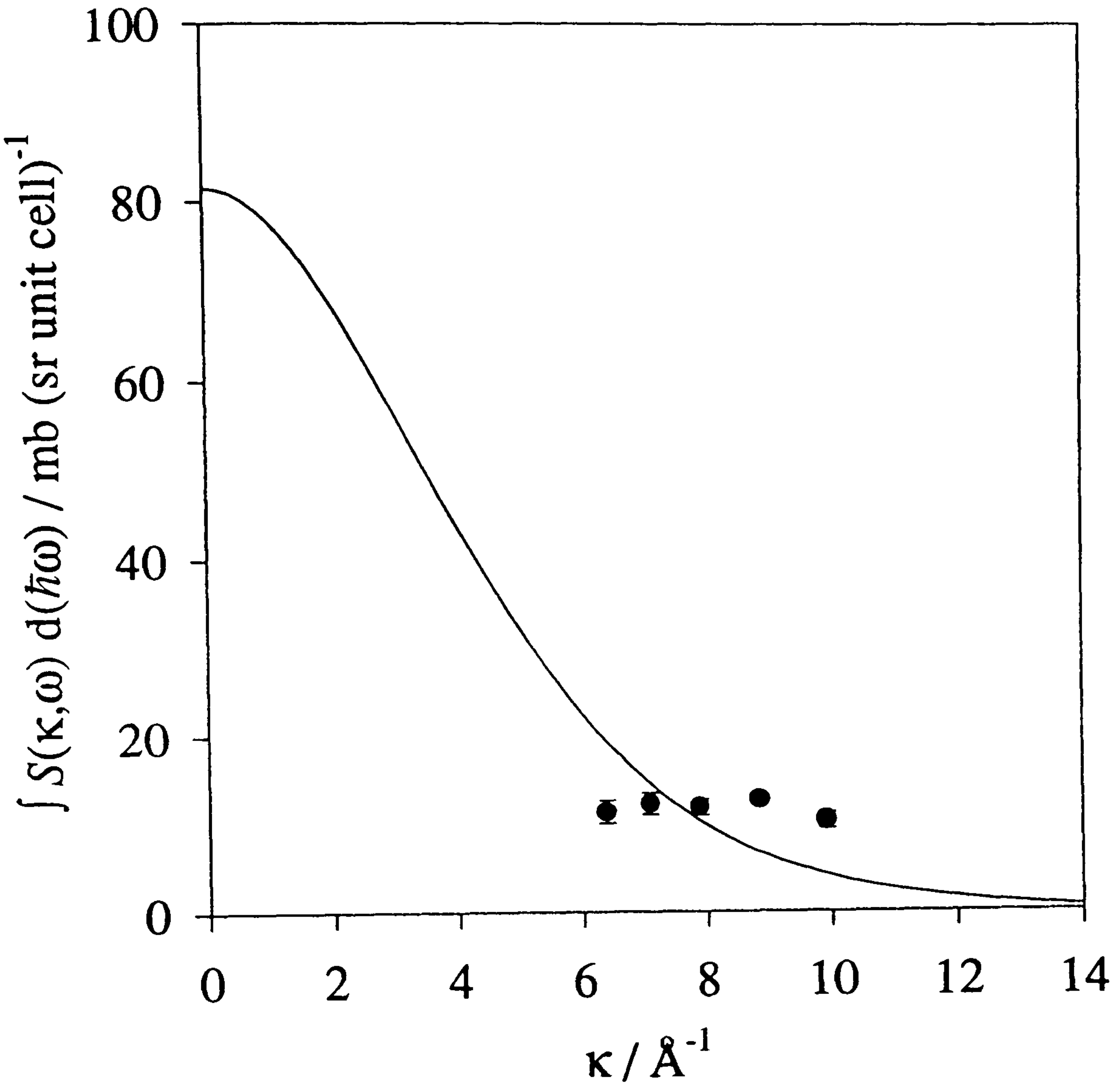

Figure 73: The integrated scattering function of the 450 meV peak measured on PrO_2 at 75 K as a function of wavevector transfer with neutrons with an incident energy of 850 meV. The line shows a fit with the Pr^{4+} elastic form factor. The fit does not reproduce the flatness of the data, implying that this scattering may be from an inter-multiplet transition.

3.3h Expected intensities

In this section I will present the crystal field intensities which you would expect under different circumstances. In Table 39 is a summary of the intensities which were actually measured (the intensity is the integrated scattering function which would be measured if the measurement could be performed at zero wavevector transfer). The 450 meV peak has the appearance of an inter-multiplet transition, the 130 meV peak is caused by the cubic crystal field splitting, and the 2.6 meV peak is probably a result of the magnetic splitting of the crystal field ground-state.

Table 39: Summary of measured intensities. The energy transfers may be temperature dependent, and refer to the temperatures stated (see Sections *III-3.3c,f*, and *g*); the intensities are independent of temperature. The integrated scattering function of the 450 meV peak around 8 Å^{-1} was approximately (11.8 ± 0.8) mb (sr unit cell)$^{-1}$.

$\hbar\omega$	T / K	I / mb (sr unit cell)$^{-1}$
2.6	1.76	23 ± 2
130	4.2	33.1 ± 0.6
450	75	–

If you ignore J-mixing, the wave functions and the intensities of the crystal field transitions within a J-multiplet can be calculated quite straight-forwardly (as a rule of thumb, J-mixing normally only affects the results by about 10%). The effects of symmetry on Pr^{4+} in PrO_2 is examined in detail in Appendix *III-4.5b*. The intensities can then either be calculated from Equation (139) (see Appendix *III-4.3*) directly from the wave functions, or deduced using the tables of matrix elements tabulated from Birgeneau[92]. It should be noted, however, that the matrix elements he lists should be multiplied by the population factor of one of the degenerate initial states (to properly account for the population factor); if all the population is in the ground-state, this is

---

[92] R.J. Birgeneau, *Transition probabilities for f-electron J-multiplets in cubic crystal fields*, J. Phys. Chem. Solids 33, 59-68, (1972).

equivalent to dividing by the degeneracy. The result should then be multiplied by two (to convert J_z^2 to $J_\perp^2$). This number can then be multiplied by g_J^2 72.4 mb (sr unit cell)$^{-1}$ to give the intensity.

Symmetry shows that for Pr^{4+} ($J = {}^5\!/_2$), there should be two energy levels: Γ_7 (a doublet) and Γ_8 (a quartet). The point-charge model predicts that the ground-state should be Γ_8, with intensities of

$$\begin{aligned} I(\Gamma_8 \to \Gamma_7) &= 118 \text{ mb (sr unit cell)}^{-1} \\ I(\Gamma_8 \to \Gamma_8) &= 192 \text{ mb (sr unit cell)}^{-1} \end{aligned} \qquad (132)$$

If any of the Pr sites are occupied by Pr^{3+}($J = 4$), there should be four energy levels: Γ_1 (a singlet), Γ_3 (a doublet), Γ_4 (a triplet), and Γ_5 (a singlet). The point-charge model predicts that the ground-state should be either Γ_1 or Γ_5, with intensities of

$$\begin{aligned} &I(\Gamma_1 \to \Gamma_4) = 618 \text{ mb (sr unit cell)}^{-1}\Big\} \quad \Gamma_1 \text{ ground state} \\ &\left.\begin{aligned} I(\Gamma_5 \to \Gamma_3) &= 124 \text{ mb (sr unit cell)}^{-1} \\ I(\Gamma_5 \to \Gamma_4) &= 108 \text{ mb (sr unit cell)}^{-1} \\ I(\Gamma_5 \to \Gamma_5) &= 386 \text{ mb (sr unit cell)}^{-1} \end{aligned}\right\} \quad \Gamma_5 \text{ ground state} \end{aligned} \qquad (133)$$

It is immediately obvious that none of the transitions between energy levels matches the measured intensity of the 130 meV peak - this will be discussed in Section *III-3.3i*.

To a rough approximation, the position of the inter-multiplet transitions will be determined by the spin-orbit coupling. Measurements on vapour spectra shows that the next J-multiplet for Pr^{4+} is at an energy of 375 meV[93], and 267 meV[94] for Pr^{3+}.

An estimate of the upper limit for the integrated scattering function of the inter-multiplet transitions expected can also be made. The value at $\kappa = 0$ (i.e. the intensity) will have an upper limit of approximately g_∞ 290 mb (sr unit cell)$^{-1}$ (see Section *III-*

---

[93] V. Kaufman and J. Sugar, *The fifth spectrum of praseodymium*, J. Research of National Bureau of Standards 71A, 583-585, (1967).

[94] J. Sugar, *Analysis of the spectrum of triply ionized praseodymium (Pr IV)*, J. Optic. Soc. America 55, 1058-1061, (1965).

3.3g). This is an upper limit because it does not take into account the crystal-field splitting of the upper level; it is approximate because it assumes that the matrix element from the initial states is the same as the matrix element from the unsplit initial *J*-multiplet.

For Pr^{4+}, then, we have $I(^2F_{5/2} \rightarrow {}^2F_{7/2}) < 28$ mb (sr unit cell)$^{-1}$, while for Pr^{3+} we have $I(^3H_4 \rightarrow {}^3H_5) < 58$ mb (sr unit cell)$^{-1}$. From Figure 72, at a wavevector transfer of around 8 Å^{-1}, we expect the integrated scattering function to fall to 0.2 of this value for Pr^{4+}, and to 0.04 for Pr^{3+}. Hence the integrated scattering function at 8 Å^{-1} should be < 6 mb (sr unit cell)$^{-1}$ for Pr^{4+}, and < 3 mb (sr unit cell)$^{-1}$ for Pr^{3+}. Both these values are below the (11.8 ± 0.8) mb (sr unit cell)$^{-1}$ actually measured.

3.3i Discussion

This discussion is concerned with understanding the origin of the 130 meV and 450 meV transitions. The simplest interpretation would be to say that the Pr ions were tetravalent: there is only one transition within the ground-state multiplet at 130 meV (presumably $\Gamma_8 \rightarrow \Gamma_7$), the inter-multiplet scattering is separated by a few hundred meV as expected, and the 2.6 meV transition can be understood in terms of magnetic ordering.

Such an explanation leaves three key points unexplained - why does the 130 meV peak show such strange behaviour as temperature is increased, why is its observed intensity so much smaller than that predicted by theory, and why is the integrated scattering function of the 450 meV peak bigger than expected?

First, let us consider the 450 meV peak. If this really is scattering from a crystal field transition, there must be a reason why the observed integrated scattering function is higher than the estimates. A likely solution is that the predicted form of $S(\kappa, \omega) / S(\kappa, 0)$ (see Figure 72), whilst accurate for a complete dipole transition from one *J*-multiplet to another, may not be accurate once the crystal field has split the multiplets, and may be even less accurate once *J*-mixing has been included in the calculation. Whilst these effects should not have a particularly significant effect on $G(\kappa)$ at zero wavevector transfer, it is conceivable that they could have a pronounced influence on $G(\kappa) / G(0)$ at the higher wavevector transfers at which the peak was measured. This may explain the discrepancy, but a more detailed theoretical calculation is needed.

Now let us consider the behaviour of the 130 meV peak. As temperature is increased, the peak broadens and moves to lower energy transfers, whilst maintaining the same intensity.

Could this be due to a lowering of the symmetry, splitting the crystal field levels so that the 130 meV peak only *appears* to broaden? Any structural lowering of symmetry can only convert a quartet and a doublet into three triplets, which is insufficient to increase the width (FWHM) of the peak from (6.8 ± 0.4) meV at 4.2 K to (22 ± 3) meV at 250 K. To split the doublets further would require a magnetic interaction, which is out of the question since the Néel temperature for PrO_2 is only 14 K.

Another possibility which should be considered is the population of a broad level, centred at about 13 meV and with a width of about 21 meV (these numbers have been chosen to produce the necessary changes in position and width). Although there is no evidence of a peak in this region, it could be that there is no matrix element to it from the ground state. However, Pr^{4+} can not have three energy levels in cubic symmetry, it is very difficult to think of a physical reason why this level should be broad whilst the 130 meV level is sharp, and (worst of all) the 130 meV transition should remain visible because some population will always remain in the ground state.

Having discounted the two theories which allow the 130 meV state to stay as a sharp level (or levels) as temperature is increased, we are left with theories which introduce intrinsic broadening into the 130 meV level.

If there were a distribution of crystal field parameters, then there would be a broadening of the energy levels - this is a static broadening, as opposed to life-time broadening (which is considered below). To have a distribution of crystal field parameters requires there to be a distribution of charge-geometries. For example, suppose oxygen were to leave the sample as it was heated: the crystal field potential in which the Pr ions sat would decrease, lowering the mean energy loss of the scattering neutron; and different Pr ions would have slightly different surroundings, producing the necessary distribution in crystal field parameters. However, at 75 K the 130 meV peak is already showing significant movement from its position at 4.2 K, which would seem to be much too small a temperature to produce oxygen-hopping on the necessary scale.

Before I move on to the final possible theory, I would like to come back to the low intensity of the 130 meV peak, (33.1 ± 0.6) mb (sr unit cell)$^{-1}$, compared to the expected 118 mb (sr unit cell)$^{-1}$. Two explanations immediately spring to mind. Firstly, the discrepancy could be a result of error on my behalf - whilst I believe that the intensity should be correct within the limits stated, I have to accept error as a possibility. I can only say that I have attempted to make the possibility as remote as possible. Secondly, it may be that the influence of J-mixing has affected the intensities by significantly more than the 10% rule-of-thumb value. However, we have investigated this possibility, using the method of Tensor operators (see Section *III-1.4*), and this does not seem to be the case.

There is, then, one more theory. It has the advantage that it not only explains the behaviour of the 130 meV peak, it also explains its missing intensity. It requires that the Pr ions exhibit mixed valency.

The question of the valency of Pr ions in PrO_2 is not a new one; Ogasawara *et al* have presented evidence that 'there is a strong mixing between $4f^1$ and $4f^2\underline{v}$ in the ground state of PrO_2, where $\underline{v}$ denotes a hole in the oxygen $2p$ valence band'[95], i.e. a mixing between ionic Pr^{4+} and covalent $Pr^{(3+v)+}$. These results supported an earlier publication[96] which showed that the number of $4f$ electrons resident on each Pr ion was approximately $n_f = 1.6$. The interpretation of the X-ray absorption spectra is that there are two possible states with different $4f$ occupancies - one state which is essentially tetravalent $4f^1$, and one state which is hybridised with the O $2p$ ligand. The amount of hybridisation increases with pressure[97].

---

[95] H. Ogasawara, A. Kotani, K. Okada, and B.T. Thole, *Theory of x-ray-absorption spectra in PrO_2 and some other rare-earth compounds*, Phys. Rev. B **43**, 854-859, (1991).

[96] A. Bianconi, A. Kotani, K. Okada, R. Giorgi, A. Gargona, A. Marcelli, and T. Miyahara, *Many-body effects in praseodymium core-level spectroscopies of PrO_2*, Phys. Rev. B **38**, 3433-3437, (1988).

[97] Z. Hu, S. Bertram, and G. Kaindl, *X-ray-absorption of PrO_2 at high pressure*, Phys. Rev. B **49**, 39-43, (1994).

How do these observations relate to the crystal field measurements? Well, if only a fraction x of the Pr ions are tetravalent, then we would only expect to measure the same fraction of the intensities calculated for pure Pr^{4+}. Assuming that the Pr^{4+} ions are in the Γ_8 ground state, the fraction is approximately $x = 33.1/118 = 0.28$. Hence we have 28% Pr^{4+} ($4f^1$), 72% $Pr^{(3+v)+}$ ($4f^{2-v}$) per Pr ion site. Now using the X-ray observation that $n_f = 1.6$, we have $1.6 = 0.28(1) + 0.72(2 - v)$, giving $v = 0.17$.

Further evidence comes from the magnetic moment measured per Pr ion. Kern *et al*[83] measure ~ 0.6 μ_B, whereas the calculated magnetic moment for the Pr^{4+} Γ_8 ground state is 1.57 μ_B or 1.37 μ_B (for (100) or (110) moment directions respectively). This loss of magnetic moment may be caused by the magnetic splitting of the Γ_8 level, or it may be caused by a fraction of the Pr ions not being tetravalent. If the ground state of the $Pr^{(3+v)+}$ ions were approximately Γ_1, then there would be no magnetic moment from these ions (see Equation (133)).

Hence the presence of covalent Pr ions can explain the intensity of the 130 meV peak, which is independent of temperature. But why should the peak broaden as temperature is increased? As temperature varies, the same number of Pr ions must be tetravalent at any instant since the peak area remains the same (Figure 71 (b)). However, this can happen in two ways: either 28% of the Pr ions are stable and tetravalent all of the time; or each Pr ion is tetravalent 28% of the time. In the former case, the Pr ion is in a stable state and the measured peak will be sharp (this situation corresponding to the low temperature measurements); in the latter case, the Pr ion is in an unstable state, and the peak will show lifetime broadening (corresponding to the high temperature measurements).

A quick calculation can estimate the lifetime of the high temperature states. The width of the peak increases with temperature from about 6.8 meV to about 22 meV. Taking the 6.8 meV width as the resolution width, the intrinsic width of the high temperature peak is about 21 meV, since when two Gaussians are convoluted to produce another Gaussian the widths add as squares. Hence the intrinsic width of the ground state and 130 meV levels is about 15 meV each. The lifetime of the tetravalent state is then given by $\tau \sim \hbar / 15 \text{ meV} \sim 10^{-13}$ s.

If the charge surrounding the Pr ions has changed from a stable distribution to one in which covalent electrons are continually rebonding with different atoms, then this may also explain why the peak moves to lower energy transfers - it is possible to imagine that the dynamically-moving charge of the covalent bonds is shielded more from the Pr atoms and so has a smaller effect on the crystal field potential, reducing the separation between the crystal field levels.

There is just one question remaining concerning this mixed valency theory - where are the crystal field transitions from the nearly-trivalent Pr ions? No matter what the ground state, there should be at least one observable crystal field transition for a Pr^{3+}. However, it would not be surprising if the effect of their covalent interaction with the O ions, the dynamical sharing of an electron, produced a broadening in the crystal field levels. The peaks may have been broadened to the extent where they could not be seen among the high phonon background below about 80 meV (see Figure 62 and Figure 64), or even so much that they produced an essentially flat magnetic background. Both of these eventualities would make the observation of the crystal field transitions very difficult.

This mixed valency theory, although based on a certain amount of speculation and hypothesis, does at least attempt to explain the more perplexing details of the measured PrO_2 spectra. It should be noted, however, that it increases the difficulty posed by the 450 meV peak having an unexpectedly high integrated scattering function, since a lower population reduces still further the expected upper limits of possible inter-multiplet scattering. Clearly, it would be constructive to see how these question may be resolved.

To begin with, it might be useful to repeat the experiment with a PrO_2 sample which has been prepared and kept in a dry, inert atmosphere. At the very least, this would confirm (or disprove) the theory that the 80 meV peak and the high background were due to phonons involving hydrogen. It may also reveal, through the improved signal-to-noise, the presence of broadened crystal field transitions from the $Pr^{(3+\nu)+}$ ions.

A true description of how the inter-multiplet scattering varies with wavevector transfer, including J-mixing and crystal field effects, would clarify the measurements at 450 meV, and calculations in this area are now being carried out.

Finally, measurements on an instrument with higher resolution at low energies, such as IRIS at the Rutherford-Appleton Labs., may help to measure the quasi-elastic broadening and the effects of the magnetic ordering.

3.4 Conclusions

Inelastic crystal field measurements have been made on both $Y_{0.3}Pr_{0.7}Ba_2Cu_4O_8$ and PrO_2. These materials were chosen since they would approximately reproduce the electrical surroundings of the Pr ion in $PrBa_2Cu_3O_{6+x}$. Since it was possible that these 'model' systems would be simpler to measure and understand than their counterpart in $PrBa_2Cu_3O_{6+x}$, through perhaps less Pr-O hybridisation, it was hoped that light may be shed on the difficult task of interpreting the crystal field spectra for $PrBa_2Cu_3O_{6+x}$.

In a sense, then, the measurements failed. While the spectra from $Y_{0.3}Pr_{0.7}Ba_2Cu_4O_8$ reproduced the spectra from $PrBa_2Cu_3O_{6+x}$, they did not do much to improve the interpretation of the spectra. Furthermore, having (perhaps naively) expected PrO_2 to contain Pr^{4+} ions, the spectra from this 'model system' produced more questions than answers, apparently showing mixed valency effects with temperature dependent lifetime effects.

However, a way forward has emerged. Applying the results of the elastic measurements on pure and Al-contaminated $PrBa_2Cu_3O_{6+x}$ crystals (see Section *II-3.6*), it seems possible that a deliberately Al-contaminated powder sample of $PrBa_2Cu_3O_{6+x}$ would exhibit less hybridisation and would therefore be easier to analyse. And learning more about the hybridisation of the Pr ions in PrO_2, initially through inelastic neutron scattering on chemically dry PrO_2 samples, can only increase our understanding of how the Pr ions interact with their surroundings. These experiments are now being considered.

4. Appendix

4.1 The spallation source

Section *II* describes the elastic measurements which have been made. All those measurements were performed on a reactor neutron source, at Risø in Denmark (see Appendix *II-4.1*). The inelastic measurements, on the other hand, were made both on the reactor source at Risø and a 'spallation' source, the ISIS neutron source at the Rutherford-Appleton Laboratories (RAL), Didcot.

A spallation source produces neutrons in a different way to a reactor source. Rather than the neutrons being the by-products of a self-sustaining fission reaction, the neutrons are produced in short (0.6 μs) bursts when accelerated protons hit a ^{238}U target. In all neutron sources, one of the limiting factors in neutron flux is removing all of the heat generated by the neutron production, especially since it is desirable to have a spatially small neutron source to increase the flux of neutrons per solid angle. At a spallation source, less heat is produced per usable neutron (55 MeV rather than 180 MeV), and the fact that the beam is pulsed also aids the removal of heat. At ISIS the uranium plates are cooled by heavy water.

The beam is pulsed because of the way in which the protons are delivered: H^- ions are accelerated to 70 MeV in a linear accelerator, then the electrons are stripped off and the protons stored in a synchrotron ring, by the use of magnetic fields. The synchrotron ring then accelerates the protons to 800 MeV; this is not the heat generated per usable neutron, since many neutrons are produced per incident proton. Controlling the protons is then a tricky business, and so a few protons are removed by short, sharp 'kicks' at regular intervals - 50 Hz - and it is this that determines the frequency of the neutron pulses. The removed protons are then guided to the uranium target.

The neutrons so produced have energies of around 2 MeV, although some take a much bigger fraction of the proton energy, up to a few 100 MeV. The neutrons are then moderated down to the required energies. This is done by a series of thin moderators, which contain neutron-absorbing 'poisons', in an effort to prevent the sharp pulse being broadened by repeated collisions (the process of moderation is deliberately left incomplete). The moderators are cooled, to increase the number of cold neutrons.

After moderation there is a range of neutron energies, as there is in a reactor source. However, the simplest way of monochromating the beam at a pulsed source is to use a 'chopper'. A chopper is essentially a rotating drum, which only allows neutrons to pass through in one position, rotating at 50 Hz (or some multiple thereof) but phased to slightly lag the creation of the neutrons. Only the neutrons which travel from the uranium target in the correct time to coincide with the chopper's transmission position get through the chopper, and so the chopper acts as a velocity (and hence an energy) selector.

This means that the monochromated beam (with neutron energies around E_i) which strikes the sample is also pulsed. The inelastic measurements which were performed at ISIS were done on the HET (High Energy Transfer) instrument. A bank of ^{3}He neutron detectors (see Appendix *II-4.2*) is arranged to measure the angle of the scattered neutrons, and their time of arrival, and from this you can calculate both the energy transfer $\hbar\omega$ and the wavevector transfer κ.

E_f is deduced from the time taken for the neutrons to arrive at the detector, and $\hbar\omega = E_i - E_f$. The wavevector of the initial neutrons then follows from

$$E_i = \frac{\hbar^2 k_i^2}{2m} \tag{134}$$

and similarly for the final neutrons. The wavevector transfer can then be deduced, as a function of the detector angle (which is therefore the scattering angle) ϕ, from the cosine rule on the scattering triangle:

$$\kappa^2 = k_i^2 + k_f^2 - 2k_i k_f \cos\phi \tag{135}$$

This means that a given incident energy and detector angle allows simultaneous measurements in (κ,ω)-space along a locus of points given by

$$\frac{\hbar^2\kappa^2}{2m} = 2E_i - \hbar\omega - 2\sqrt{E_i\left(E_i - \hbar\omega\right)}\cos\phi \tag{136}$$

This is both the advantage and the disadvantage of a pulsed spallation source. Although the peak flux of a pulsed spallation source is quite high, comparable to the best reactor sources, the mean flux is quite low. If you wish to measure a large section of (κ,ω)-space, then the low mean flux is not serious since you are measuring all points on Equation (136) simultaneously. If, on the other hand, you are only interested in a small region of (κ,ω)-space, then you are left with a low mean flux and no compensating advantage.

4.2 The lineshape on HET

There are three main contributions to the intrinsic lineshape of peaks measured on HET. The first two are contributions from the effect of under-moderation. In order to maintain as far as possible the sharpness of the neutron pulse, the neutrons are 'under-moderated', i.e. do not come completely to thermal equilibrium with the moderators. There is therefore a Maxwell-Boltzmann character to the neutrons, for those which do come close to thermal equilibrium, which can be represented by a Gaussian; and an 'epithermal' (high-energy) character, for those which remain mostly unaffected by the moderators, which can be represented by a cut-off exponential (see Figure 74 (a)). The overall effect of the moderator is therefore a convolution of a cut-off exponential and a Gaussian.

The third contribution is from the chopper, which has a transmission which is Gaussian. The total resolution is therefore a convolution of all three contributions. The two Gaussian contributions (σ_{mod} and σ_{chop}) can be convoluted to a single Gaussian ($\sigma^2 = \sigma^2_{mod} + \sigma^2_{chop}$) (Figure 74 (b)), and so the final lineshape is just the convolution of a cut-off exponential with a Gaussian:

$$\int_{-\infty}^{E_0} \exp\left(\frac{E' - E_0}{\varepsilon}\right) \exp\left\{-\left(\frac{\hbar\omega - E'}{\sigma}\right)^2\right\} dE' \qquad (137)$$

The parameters ε and σ can best be determined by fitting to a 'clean' elastic peak. Vanadium, with its very high incoherent scattering and very small coherent scattering, provides just such a clean peak. Knowing accurately the shape of the resolution is especially useful in detecting inelastic scattering very close to the elastic peak, since the elastic peak can be accurately subtracted.

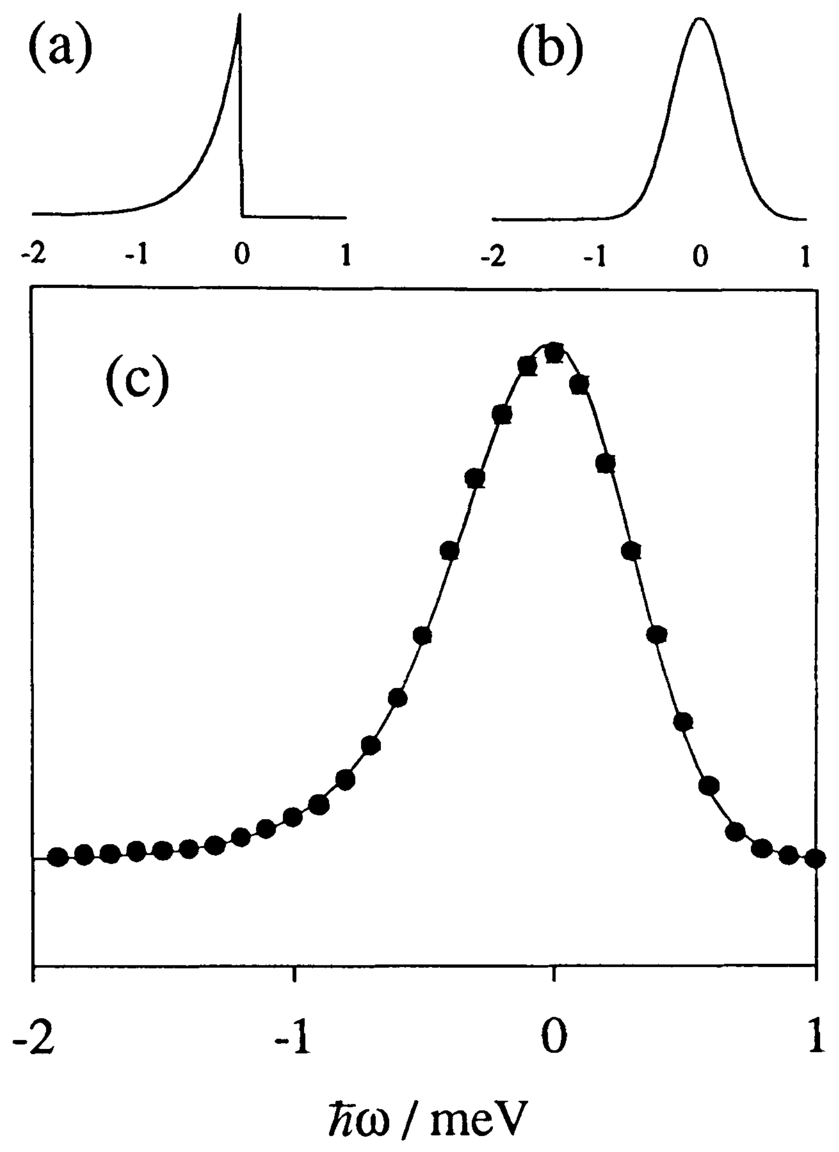

Figure 74: The resolution of HET, for $E_i = 20$ meV and the bank of detectors 11.5° < $\phi < 26.5°$. (a), epithermal contribution, $\varepsilon = 0.30$ meV; (b), Gaussian contribution from moderator and chopper, $\sigma = 0.38$ meV; (c), resolution fitted to the vanadium elastic peak, $E_0 = 0.18$ meV.

4.3 The intensity

The differential cross-section is the universal expression for all scattering processes which can happen in an experiment. The neutron arrives with energy E and wavevector $\mathbf{k}$; the differential cross-section then gives the probability, per unit incident flux, of observing a neutron in a solid angle $d\Omega$ centred around wavevector $\mathbf{k}'$ with an energy between E' and $E' + dE'$ (the neutron having imparted an energy $\hbar\omega = E - E'$ to the sample). The differential cross-section can be written

$$\frac{d^2\sigma}{d\Omega dE'} = \frac{k'}{k} NS(\kappa,\omega) \tag{138}$$

where N is the number of scattering objects in the crystal, and $S(\kappa,\omega)$ is the scattering function of those objects. In the case of inelastic scattering from crystal field levels, the scattering objects are individual atoms, and the scattering function (if the crystal field levels are discrete and of good quantum number J) is

$$S(\kappa,\omega) = \left(\frac{1.91r_e}{2}\right)^2 g_J^{\,2} f(\kappa)^2 \exp(-2W_D) \sum_{ij} n_i \left|\langle j|J_\perp|i\rangle\right|^2 \delta\left(E_j - E_i - \hbar\omega\right) \tag{139}$$

where $J_\perp$ is the component of the atom's angular momentum J perpendicular to κ, n_i is the Boltzmann occupation factor of the initial atomic state $|i\rangle$,

$$n_i = \frac{\exp\left(-E_i/k_B T\right)}{Z} \tag{140}$$

and r_e is the classical electron radius. The 'characteristic' scale of cross-sections is therefore

$$\left(\frac{1.91r_e}{2}\right)^2 = 72.4 \text{ mb} \tag{141}$$

where a millibarn (mb) is 10^{-31} m^2. Note that measurements are normally made on powders, in which case measurements are made as a function of $|\kappa|$. This means that form factors which approximate the magnetisation density as being spherically symmetric are quite accurate, for example the dipole approximation for rare earth ions (see Section *II-1.1c*).

The atomic states can be written in terms of the angular momentum eigenvectors, i.e.

$$|i\rangle = \sum_{m=-J}^{J} a_m |J,m\rangle \tag{142}$$

for the initial atomic state, and similarly for the possible final atomic states $|j\rangle$. The coefficients a_m can be calculated by a suitable model, for instance the point-charge model (see Section *III-1*).

The matrix elements of interest are, for a powder,

$$\begin{aligned} |\langle j|J_\perp|i\rangle|^2 &= \frac{2}{3}|\langle j|J|i\rangle|^2 \\ &= \frac{2}{3}\left(|\langle j|J_x|i\rangle|^2 + |\langle j|J_y|i\rangle|^2 + |\langle j|J_z|i\rangle|^2\right) \end{aligned} \tag{143}$$

The first step results from the powder averaging, and J^2 is then split into its orthogonal components. J_x and J_y can be written in terms of raising and lowering operators,

$$\begin{aligned} J_x &= \frac{J_+ + J_-}{2} \\ J_y &= \frac{J_+ - J_-}{2i} \end{aligned} \tag{144}$$

and so all that is now required are the results of operating with the raising and lowering operators, and the eigenvalues of J_z:

$$\begin{aligned} J_+|J,m\rangle &= \sqrt{(J-m)(J+m+1)}\,|J,m+1\rangle \\ J_-|J,m\rangle &= \sqrt{(J+m)(J-m+1)}\,|J,m-1\rangle \\ J_z|J,m\rangle &= m|J,m\rangle \end{aligned} \tag{145}$$

The observed intensity of an inelastic peak is defined as

$$I(\omega) = \int \frac{S(\kappa,\omega)}{f(\kappa)^2}\, d(\hbar\omega) \tag{146}$$

where the integral is along the dispersion relation given in Equation (136), i.e. it is the integrated scattering function you would measure if you could perform the measurement at zero wavevector transfer.

The total intensity within a *J*-multiplet can be found from the Sum Rule, which is valid for a powder average with no broadening of the transitions. Suppose you put all of the population into the ground state. Then the sum of all the matrix elements multiplied by the population factors will be

$$\begin{aligned}\sum_j n_0 \left|\langle j|J_\perp|0\rangle\right|^2 &= \tfrac{2}{3}\sum_j \left|\langle j|J|0\rangle\right|^2 \\ &= \tfrac{2}{3}\sum_j \langle j|J|0\rangle\langle 0|J|j\rangle \\ &= \tfrac{2}{3}\left|\langle 0|J|0\rangle\right|^2 \\ &= \tfrac{2}{3}J(J+1)\end{aligned} \tag{147}$$

Since it does not matter which particular state is the ground-state, it follows that the same result holds no matter how the population is distributed. Hence the total intensity within the J-multiplet will be

$$I = 72.4 {g_J}^2 \tfrac{2}{3} J(J+1) \text{ mb (sr unit cell)}^{-1} \tag{148}$$

4.4 Normalisation of intensities

In essence, the normalisation of the observed spectra into absolute $S(\kappa,\omega)$ (i.e. in units of mb meV^{-1} sr^{-1} per unit cell) is quite straightforward. You first measure the elastic vanadium peak for a known mass of vanadium. Because this scattering is mostly incoherent, it has no κ-dependence, and so the absolute intensity just depends on the amount of vanadium present. Then a knowledge of the mass of your sample, and the mass of each unit cell, is sufficient to calculate the scattering function per unit cell. At RAL this procedure, as well as many other corrections, can be performed automatically.

4.5 Using symmetry

Symmetry is a very powerful and elegant tool in condensed matter physics: from a knowledge of symmetry, it is possible in a crystal field experiment to know how many states to expect, what the degeneracy should be, the form of the crystal field wave functions, which transitions are allowed, and which crystal field parameters are needed to describe the crystal field.

Symmetry is also difficult for the unacquainted to use, not because the arithmetic processes involved are very hard (they are, in fact, very simple), but because the subject has methods and jargon not otherwise encountered. This section is not intended to be a complete explanation or derivation of the methods of symmetry, but rather a demonstration of how to use symmetry to your advantage.

4.5a $Pr^{3+}Ba_2Cu_3O_7$

I will use the example of the Pr^{3+} ion in $PrBa_2Cu_3O_7$ as my first example. The first task is to determine the (point-group) symmetry of the site, i.e. what symmetry operations can be applied, with the Pr ion as the origin, which leave the crystal in an identical arrangement? An inspection of Figure 1 should be sufficient to see that the operations are:

E,	a rotation of 360° (which leaves positions unchanged)
C_2 (2_z),	a two-fold rotation about the z-axis
C_2' (2_y),	a two-fold rotation about the y-axis
C_2'' (2_x),	a two-fold rotation about the x-axis
I,	inversion symmetry
σ_{xy} (m_z),	a mirror plane perpendicular to the z-axis
σ_{xz} (m_y),	a mirror plane perpendicular to the y-axis
σ_{yz} (m_x),	a mirror plane perpendicular to the x-axis.

An inspection of the appendix of a suitable book on symmetry[98] will reveal that this symmetry defines the symmetry group which is called *mmm* in 'International notation', or D_{2h} in 'Schoenflies notation'. This is an orthorhombic point-group, and also shown is its *character table*. The structures and symmetries of the more common crystals of thirty years ago can be found in Wyckoff[99]; however, the point-group symmetry of the chemical unit cell is only necessarily the same as the point-group symmetry of the atom of interest if the atom is at the origin of Wyckoff's structure.

---

[98] For instance, V. Heine, *Group theory in quantum mechanics*, International Series of Monographs on Pure and Applied Mathematics vol. 9 (1960), 448-455.

[99] Wyckoff, *Crystal structures*, Interscience Publications (1965).

The fact that the symmetry is orthorhombic can immediately produce some results. Walter[100] has tabulated the J-multiplet splitting expected for different crystal field symmetries, and from this it is apparent that we expect 9 singlets, i.e. a total lifting of the $2J + 1$ degeneracy. Furthermore, Walter has tabulated which crystal field parameters will be needed: for D_{2h}, they are B_{20}, B^c_{22}, $B_{40}, B^c_{42}, B^c_{44}$, $B_{60}, B^c_{62}, B^c_{64}$, and B^c_{66}, with the crystal field axis of quantisation being the z-axis of the point group symmetry. This z-axis is normally the axis with the highest rotational symmetry; in the absence of rotational symmetry, it is perpendicular to the mirror plane, as in C_s (*m*), and in the case of cubic symmetry it is parallel to a two-fold axis, for example in T (*23*).

To proceed further, I need to explain some of the technical language associated with symmetry. Consider a rotation about the z-axis by an angle ϕ_z (a proper rotation); this *operation* could be written as $R(\phi_z)$. The operator can act on *basis functions* φ_i with results shown by the *representation* D_{ij},

$$R\varphi_j = D_{ij}\varphi_i \tag{149}$$

So, for $R(90°)$, suitable basis functions could be $\varphi_1 = x$, $\varphi_2 = y$, and $\varphi_3 = z$. The corresponding representation in matrix form could then be given by

$$D_{ij}(90°) = \begin{pmatrix} 0 & 1 & 0 \\ -1 & 0 & 0 \\ 0 & 0 & 1 \end{pmatrix} \tag{150}$$

so, for example,

$$Ry = D_{12}x = -x \tag{151}$$

(the indices of D_{ij} read column, then row).

A representation's *character* is then the sum of the diagonal elements of the representation D_{ij}, which in the case of $R(90°)$ would be 1.

In the case of spherical symmetry, for states of well-defined angular momentum $|J,m\rangle$ the representation for $R(\phi_z)$ is

---

[100] U. Walter, *Treating crystal field parameters in lower than cubic symmetries*, J. Phys. Chem. Solids 45, 401-408, (1984).

$$D_{ij}(\phi_z)=\begin{pmatrix} \exp(iJ\phi_z) & 0 & \cdots & 0 \\ 0 & \exp(i(J-1)\phi_z) & \cdots & 0 \\ \cdots & \cdots & \cdots & 0 \\ 0 & 0 & 0 & \exp(-iJ\phi_z) \end{pmatrix} \tag{152}$$

with a character of

$$\chi_D(R)=\begin{cases} \dfrac{\sin(J+\frac{1}{2})\phi}{\sin\frac{1}{2}\phi}, & \phi\neq 0 \\ 2J+1, & \phi=0 \end{cases} \tag{153}$$

for all proper rotations. Improper rotations are proper rotations followed by an inversion (or a reflection in Schoenflies notation): for instance, a mirror plane in *xy* can be considered to be a two-fold rotation about *z* followed by an inversion, and is therefore an improper rotation. The characters for improper rotations are $\pm\,\chi_D(R)$, '+' for wave functions of even parity and '–' for wave functions of odd parity, where R is the corresponding proper rotation.

Shown in Table 40 is part of the character table for the point group D_{2h} (*mmm*) which I mentioned earlier. For this, I use the character table of Koster *et al*[101], Table 23. These authors used a $\Gamma_i^{\pm}$ notation for representations (the ± refers to even and odd parity). Because Pr^{3+} ($4f^2$, $^3H_4$) has even parity (since $\sum l = 3+3=6$ is even), only the representations with even parity ($\chi(I)>0$) need to be considered. Across the top are the operations, down the left are the representations, down the right are the basis functions, and in the main body of the table are the characters (the $\Gamma_5^{\pm}$ representations in Koster *et al*'s table are to do with half-integer spin and are discussed in Appendix *III-4.5b*).

We can also apply the same operations to the case of spherical symmetry, which represents the Pr atom in the undistorted state (see Table 41). For this we use Equation (153). This information can also be found in Koster *et al*[101], Table 2.

---

[101] G.K. Koster, J.O. Dimmock, R.G. Wheeler, and H. Statz, *Properties of the thirty-two point groups*, M.I.T. Press (1966).

Table 40: Part of the character table for the point-group D_{2h} (*mmm*).

D_{2h} (*mmm*)	E	C_2 (2_z)	C_2' (2_y)	C_2'' (2_x)	
Γ_1^+ (A_g)	1	1	1	1	
Γ_2^+ (B_{2g})	1	−1	1	−1	S_y
Γ_3^+ (B_{1g})	1	1	−1	−1	S_z
Γ_4^+ (B_{3g})	1	−1	−1	1	S_x

Table 41: Characters for relevant D_{2h} (*mmm*) operations on a spherical atomic wave function with $J = 4$.

D_{2h} (*mmm*)	E	C_2 (2_z)	C_2' (2_y)	C_2'' (2_x)	
D^+ ($J = 4$)	9	1	1	1	

Now, for a given symmetry operation, the sum of the characters for all the wave functions remains the same as the distortion occurs. Hence, on going from spherical symmetry to D_{2h} (*mmm*) symmetry, the representations of the wave functions undergo the following transformation,

$$D^+(J=4) \rightarrow 3\Gamma_1^+ + 2\Gamma_2^+ + 2\Gamma_3^+ + 2\Gamma_4^+ \tag{154}$$

since

$$\chi_{D^+(J=4)}(E) = 3\chi_{\Gamma_1^+}(E) + 2\chi_{\Gamma_2^+}(E) + 2\chi_{\Gamma_3^+}(E) + 2\chi_{\Gamma_4^+}(E) \tag{155}$$

i.e. 9 = 3(1) + 2(1) + 2(1) + 2(1), and similarly for the other symmetry operations besides E.

Hence there should be three states with symmetry corresponding to the Γ_1^+ representation, two corresponding to Γ_2^+, two corresponding to Γ_3^+, and two corresponding to Γ_4^+. Koster *et al*[101] also contains tables showing how the representations for spherical wave functions (the full rotation group) transform to the representations in the lower symmetry group; for D_{2h}, (*mmm*), see Koster *et al*, Table 21.

The next place where symmetry can help is in determining which transitions are symmetry-forbidden. In general, the matrix element for a transition will be given by

$$M_{ij} = \langle \varphi_i | V | \varphi_j \rangle \tag{156}$$

If the representations of φ_i, φ_j, and V are Γ_i, Γ_j, and Γ_V respectively, then the representation of M_{ij} can be written as a *product representation*

$$\Gamma_M = \Gamma_i \times \Gamma_V \times \Gamma_j \tag{157}$$

and the character of this representation can be calculated by

$$\chi_M = \chi_i \chi_V \chi_j . \tag{158}$$

χ_M can then be expressed as the sum of the characters of the point-group's representations, and if it includes the representation Γ_1^+ (which is the representation for a scalar symmetry element) then the transition is allowed; if not, the transition is symmetry forbidden.

For instance, suppose that $\Gamma_M = \Gamma_2^+ \times \Gamma_3^+ \times \Gamma_4^+$. It is then possible, using the character table in Table 40, to calculate the characters of Γ_M, as in Table 42, from which it can be seen that $\Gamma_M = \Gamma_1^+$ and hence the transition is allowed by symmetry. Multiplication tables can also be found in Koster *et al*[101]; for D_{2h}, (*mmm*), see Koster *et al*, Table 18.

Table 42: Characters for $\Gamma_2^+ \times \Gamma_3^+ \times \Gamma_4^+$, for the relevant operations in the point-group D_{2h} (*mmm*).

D_{2h} (*mmm*)	E	C_2 (2_z)	C_2' (2_y)	C_2'' (2_x)	
$\Gamma_2^+ \times \Gamma_3^+ \times \Gamma_4^+$	1	1	1	1	

For crystal field transitions, the potential is proportional to the magnetic moment operator μ. This transforms like a spin, which has basis functions S_x, S_y, and S_z, and so in the D_{2h} (*mmm*) point-group transforms like Γ_4^+, Γ_2^+, and Γ_3^+ respectively. It can be shown that the only product representations that can be formed containing Γ_1^+ are $\Gamma_1^+ \times \Gamma_1^+ \times \Gamma_1^+$, $\Gamma_1^+ \times \Gamma_2^+ \times \Gamma_2^+$, $\Gamma_1^+ \times \Gamma_3^+ \times \Gamma_3^+$, $\Gamma_1^+ \times \Gamma_4^+ \times \Gamma_4^+$ and

$\Gamma_2^+ \times \Gamma_3^+ \times \Gamma_4^+$. Hence the symmetry-allowed transitions are $\Gamma_i^+ \leftrightarrow \Gamma_j^+$, $i \neq j$. Assuming that the ground-state is fully occupied, this means that we should see a maximum of 6 transitions if a Γ_1^+ state is the ground-state, and 7 transitions otherwise.

Finally, symmetry can predict the form of the wave functions produced by the crystal field. Each wave function will be the sum of angular momentum eigenvectors (see Equation (142)), and symmetry can determine the phase relation between these angular momentum eigenvectors. To do this, it is necessary to know how the angular momentum eigenvectors transform under the symmetry operations.

The problem of determining how the angular momentum eigenvector $|J,m\rangle$ transforms under proper and improper rotations has been dealt with by Wigner[102]. A general proper rotation can be defined by Euler angles α, β, and γ, meaning that the rotation can be decomposed into a rotation about z by γ, a rotation about y' by β, and a rotation about z'' by α. Under such a rotation $R(\alpha\beta\gamma)$, $|J,m\rangle$ transforms as

$$R(\alpha\beta\gamma)|J,m\rangle = \sum_{m'} D^J_{m'm}(\alpha\beta\gamma)|J,m'\rangle \tag{159}$$

where

$$\begin{aligned} D^J_{m'm}(\alpha\beta\gamma) &= \sum_{p=-2J}^{2J} a^{Jp}_{m'm} A^{Jp}_{m'm}(\alpha\beta\gamma) \\ a^{Jp}_{m'm} &= (-1)^p \frac{\sqrt{(J+m)!(J-m)!(J+m')!(J-m')!}}{(J-m'-p)!(J+m-p)!\,p!\,(p+m'-m)!} \\ A^{Jp}_{m'm}(\alpha\beta\gamma) &= \mathrm{e}^{im'\alpha} \cos^{2J+m-m'-2p}\left(\tfrac{1}{2}\beta\right) \sin^{2p+m'-m}\left(\tfrac{1}{2}\beta\right) \mathrm{e}^{im\gamma} \end{aligned} \tag{160}$$

Some simplifications can be made. For a proper rotation about the z-axis by an angle ϕ, this reduces to

$$R(\phi 00)|J,m\rangle = e^{im\phi}|J,m\rangle \tag{161}$$

Furthermore, for integer J, $|J,m\rangle$ transforms under proper rotations in the same way as the spherical harmonic Y_J^m does.

---

[102] E.P. Wigner, *Group theory and its application to the quantum mechanics of atomic spectra*, Academic Press (1959).

For an improper rotation (i.e. a proper rotation followed by an inversion), $|J,m\rangle$ transforms in the same way as for its corresponding proper rotation multiplied by the parity of the state. The effects of the symmetry operations on $|4,m\rangle$ are shown in Table 43.

Table 43: Description of the relevant D_{2h} (*mmm*) operations in terms of Euler angles, and the effects on the angular momentum eigenfunctions for Pr^{3+}, $J = 4$.

D_{2h} (*mmm*)	E	C_2 (2_z)	C_2' (2_y)	C_2'' (2_x)
(α, β, γ)	(0, 0, 0)	$(\pi, 0, 0)$	$(0, \pi, 0)$	$(\pi, \pi, 0)$
$J = 4, \|m\rangle$	$\|m\rangle$	$(-1)^m\|m\rangle$	$(-1)^m\|-m\rangle$	$\|-m\rangle$

From this, it is possible to construct four different types of wave functions (i.e. four different combinations of angular momentum eigenvectors) which are basis functions of the symmetry operators. The wave functions can then be related to the representations by studying the effects of the symmetry operations and comparing the results with the characters in Table 40.

The four wave functions (irrespective of parity) are:

$$\begin{aligned}
\Gamma_1&: \; a_4|-4\rangle + a_2|-2\rangle + a_0|0\rangle + a_2|+2\rangle + a_4|+4\rangle \\
\Gamma_2&: \; -b_3|-3\rangle - b_1|-1\rangle + b_1|+1\rangle + b_3|+3\rangle \\
\Gamma_3&: \; -c_4|-4\rangle - c_2|-2\rangle + c_2|+2\rangle + c_4|+4\rangle \\
\Gamma_4&: \; d_3|-3\rangle + d_1|-1\rangle + d_1|+1\rangle + d_3|+3\rangle
\end{aligned} \tag{162}$$

4.5b $Pr^{4+}O_2$

The case for Pr^{4+} follows fairly analogously to the case of Pr^{3+}, with a slight complication due to the fact that the total angular momentum is non-integer. It can be seen, either by inspection (see Figure 55) or from Wyckoff[99], that the relevant symmetry is the cubic point-group O_h (*m3m*). From Walter[100], this means that we expect one doublet and one quartet, and that the necessary crystal-field parameters are

B_{40}, B^c_{44}, B_{60} and B^c_{64}. Because Pr^{4+} ($4f^1$, ${}^2F_{5/2}$) has odd parity, only the representations with odd parity ($\chi(I) < 0$) need to be considered.

The fact that J is half-integer produces an interesting effect: the character of a 360° rotation (operation E) is, by Equation (152), $\chi_D(E) = -1$. This is because an electron's function of position is spinor (rather than scalar), and rotating by 360° changes the sign of a spinor. An additional rotation by 360° returns the system to its original state, and hence the operation of rotating by 720° is given the symbol $\overline{E}$. Likewise, every other operator has a barred equivalent, which corresponds to the same physical rotation with a change of sign of spinors. The presence of these additional operators introduces additional basis functions and representations, which are the appropriate subjects for wave functions of half-integer angular momenta (i.e. for odd numbers of electrons).

The relevant section of the character table for O_h ($m3m$) (Koster *et al*[101], Table 87), as well as the characters for the same operations in the case of spherical symmetry ($J = 5/2$), are shown in Table 44, from which it can be seen that the representations of the wave functions undergo the following transformation,

$$D^-(J = 5/2) \rightarrow \Gamma_7^- + \Gamma_8^- \qquad (163)$$

($6C_4$ means that there are six equivalent four-fold axes, *etc.*).

Table 44: Part of the character table for the point-group O_h ($m3m$), and characters for the operations on a spherical atomic wave function with $J = 5/2$.

O_h ($m3m$)	E	$8C_3$ (3)	$3C_2$ (2_z)	$6C_4$ (4_z)	$6C_2'$ (2_d)
Γ_6^-	2	1	0	$\sqrt{2}$	0
Γ_7^-	2	1	0	$-\sqrt{2}$	0
Γ_8^-	4	-1	0	0	0
D^- ($J = 5/2$)	6	0	0	$-\sqrt{2}$	0

The appropriate representation for the magnetic moment operator is Γ_4^+ and so, using the method of product representation demonstrated above, it can be shown that

$\Gamma_7^- \times \Gamma_4^+ \times \Gamma_7^-$, $\Gamma_7^- \times \Gamma_4^+ \times \Gamma_8^-$, and $\Gamma_8^- \times \Gamma_4^+ \times \Gamma_8^-$ all contain Γ_1^+ and hence all transitions are allowed.

The case of a cubic crystal field raising the degeneracy of $2J + 1$ multiplets has been considered in detail by Lea, Leask, and Wolf[103]. This comprehensive paper contains Equation (163), but also shows that, in the point-charge model, the ground-state is Γ_8 (irrespective of parity) for $J = {}^5\!/_2$. Furthermore, the atomic wave functions are listed,

$$\begin{aligned} \Gamma_7:&\quad a\left|\pm\tfrac{5}{2}\right\rangle - b\left|\mp\tfrac{3}{2}\right\rangle, \quad a = \sqrt{\frac{1}{6}} \\ \Gamma_8:&\quad \begin{cases} b\left|\pm\tfrac{5}{2}\right\rangle + a\left|\mp\tfrac{3}{2}\right\rangle \\ \left|\pm\tfrac{1}{2}\right\rangle \end{cases}, \quad b = \sqrt{\frac{5}{6}} \end{aligned} \tag{164}$$

and so it is possible to calculate the transition probabilities exactly using the methods discussed in Appendix *III-4.3*. It is also possible to predict the effects of an applied magnetic field (or an effective mean field from magnetic ordering) on the energy levels, and to predict the magnetic moment of the ion.

The fact that the coefficients of the angular momentum eigenvectors are fixed in Equation (164) is a result of the fact that the three-fold symmetry axis transforms the eigenvectors into a linear combination of states of all m (see Table 45).

Table 45: Description of the relevant O_h ($m3m$) operations in terms of Euler angles, and the effects on the angular momentum eigenfunctions for Pr^{4+}, $J = {}^5\!/_2$. For the three-fold rotation, $D_{m'm}$ is a full J by J matrix which can be calculated by Equation (160).

O_h ($m3m$)	E	$8C_3$ (3)	$3C_2$ (2_z)	$6C_4$ (4_z)	$6C_2'$ (2_d)
(α, β, γ)	$(0, 0, 0)$	$(0, -\frac{\pi}{2}, -\frac{\pi}{2})$	$(\pi, 0, 0)$	$(\frac{\pi}{2}, 0, 0)$	$(\frac{\pi}{2}, \pi, 0)$
$J = {}^5\!/_2$, $\lvert m\rangle$	$\lvert m\rangle$	$\sum D_{m'm}\lvert m\rangle$	$i^{2m}\lvert m\rangle$	$i^{m}\lvert m\rangle$	$i^{m+1}\lvert -m\rangle$

---

[103] K.R. Lea, M.J.M. Leask, and W.P. Wolf, *The raising of angular momentum degeneracy of f-electron terms by cubic crystal fields*, J. Phys. Chem. Solids 23, 1381-1405, (1962).

IV - Summary

1. Elastic magnetic scattering

Previous publications concerned with the magnetic ordering in $PrBa_2Cu_3O_{6+x}$ have not provided a unified picture: quoted oxygen contents were dubious in the single crystal work; sample purity was not investigated; the Pr ordering was often interpreted on the basis of just two reflections; and Néel temperatures, magnetic moments and magnetic couplings rarely agreed.

I have succeeded in performing a much more systematic and thorough investigation of the magnetic ordering. Comparisons with previous publications have been made, and discrepancies understood in terms of sample preparation. Several phenomena, previously unnoticed in neutron diffraction work, were observed, including:

- a clear interaction between the Pr ions and the Cu-O_2 planes, shown by the reduction in the Cu(2) moment when the Pr ions order magnetically
- the tilting of the Pr moments away from the *c*-axis. This has been observed previously by Mössbauer spectroscopy, but never before measured by neutron scattering. Evidence has also been presented of a deviation of the Pr form factor from the prediction of the dipole approximation.
- true two-dimensional ordering is observed in the Al-containing crystals, evidenced by the existence of Bragg rods.

Due to the systematic nature of this work, trends in the magnetic ordering with Al- and O-content were observed. I showed that these trends could be understood in terms of the redistribution of electronic charge, which in turn supports the theory that the Pr^{3+} ion exhibits hybridisation.

In the single crystal measurements performed, a range of intrinsic peak-shapes were encountered, due to long-range *3D* order, short-range *3D* order and *2D* order. The necessary formalism for extracting intensities from this data, by taking into account the spectrometer resolution, sample mosaicity, and the intrinsic peak-shapes, was developed.

2. Inelastic scattering and crystal field excitations

The crystal field determines the wave function of the 4*f* electrons of the Pr ions, and these in turn determine its magnetic properties. Hence crystal field measurements are a valuable tool in understanding the behaviour of the Pr ion.

Because of the difficulties previously encountered in measuring crystal field transitions in $PrBa_2Cu_3O_{6+x}$, I have used instead the compounds PrO_2 and $Y_{0.3}Pr_{0.7}Ba_2Cu_4O_8$, which contain Pr in a chemically similar environment. The hope was that these measurements might aid an interpretation of the spectra observed in $PrBa_2Cu_3O_{6+x}$. This hope was not realised, but the measurements were not in vain.

The spectra of $Y_{0.3}Pr_{0.7}Ba_2Cu_4O_8$ showed similar broadening effects to $PrBa_2Cu_3O_{6+x}$, and so are just as difficult to interpret. However, this at least confirmed that the broadening of the peaks is probably not related to partial oxidation or disorder in the Cu-O chain layers in $PrBa_2Cu_3O_{6+x}$, since the double chains of $Y_{0.3}Pr_{0.7}Ba_2Cu_4O_8$ are fully oxygenated. It is proposed to perform an experiment on a deliberately Al-contaminated powder sample of $PrBa_2Cu_3O_{6+x}$, to see if this reduces the Pr hybridisation with a corresponding sharpening of the measured spectra.

The measurements on PrO_2 revealed many interesting features. Observed intensities do not correspond with those expected, and from the unusual effects of temperature on the spectra, it seems possible that the Pr ion is in a state of mixed-valency, with temperature-dependent lifetime effects. The spectra measured also showed features which indicated the possibility of water contamination, and this made the spectra more difficult to interpret. This compound clearly warrants further investigation, and experiments are proposed on dry samples, with the aim of removing contamination signals from the spectra.

The application of symmetry considerations and the point-charge model to the crystal field measurements is considered in some detail. The usefulness of the point-charge model is demonstrated, using Pr_2NiO_4 and Nd_2NiO_4. The application of symmetry, although enormously powerful, can also be difficult for the casual user to master, and the sections describing how symmetry can be applied to the structures in question were an attempt to bridge the gap between theory and application.